ATLAS Inner Detector alignment and analysis of the Wtb vertex structure with single top quarks

Javier Jiménez Peña

Director:

Salvador Martí García

Doctorat en Física
Juliol 2018

Facultat de Física
Departament de Física Atòmica, Molecular i Nuclear

VNIVERSITAT DE VALÈNCIA

Dr. Salvador Martí García
Investigador Científico del Consejo Superior de Investigaciones Científicas

CERTIFICA:

Que la presente memoria, ***"ATLAS Inner Detector alignment and analysis of the*** Wtb ***vertex structure with single top quarks"***, ha sido realizada bajo mi dirección en el *Departament de Física Atòmica, Molecular i Nuclear* de la *Universitat de València* por Javier Jiménez Peña y constituye su tesis para optar al grado de doctor en Física.

Y para que así conste, en cumplimiento de la legislación vigente, firmo el presente certificado.

Firmado

Dr. Salvador Martí García

A las maravillosas personas que he conocido durante estos años.
Sin duda, lo mejor del doctorado.

Contents

Part I

General introduction

Chapter 1

Theoretical motivations

The top quark is the heaviest known elementary particle. Postulated in 1973, together with the bottom quark, by Makoto Kobayashi and Toshihide Maskawa [1] in order to explain the observed charge-parity violations in the kaon decay, was finally discovered in 1995 by the CDF and D0 experiments at Fermilab [2, 3]. This chapter presents a short summary of the current understanding of the fundamental interactions and set a theoretical basis for the work presented in this thesis.

Single top quark is the only source of polarised top quarks at the LHC and thus, it becomes a powerful tool to test the Standard Model.

1.1 The Standard Model

The Standard Model (SM) of particle physics is the theory describing three of the four known fundamental forces in nature: the electromagnetic force and the weak and strong interactions. Only the gravitational force, which is described with the General Theory of Relativity, is not included in the SM. Additionally, the SM also classifies all known elementary particles of the universe. Developed in the early 1970s, it has successfully explained almost all experimental results and precisely predicted a wide variety of phenomena. Over time and through many experimental test, the SM has become a well established physics theory.

Figure 1.1 summarises all the components of the SM: Matter is made of fundamental fermions, which interact among them through the interchange of the gauge bosons. The Higgs boson (H) is the last piece of the SM, which was finally discovered by the ATLAS and CMS experiments in 2012 [4, 5].

1.1.1 Matter particles

According to the SM, all matter around us is made of a small number of elementary particles of spin $\frac{1}{2}$ called fermions, the building blocks of matter. In particle physics, a fermion is a particle that follows Fermi–Dirac statistics.

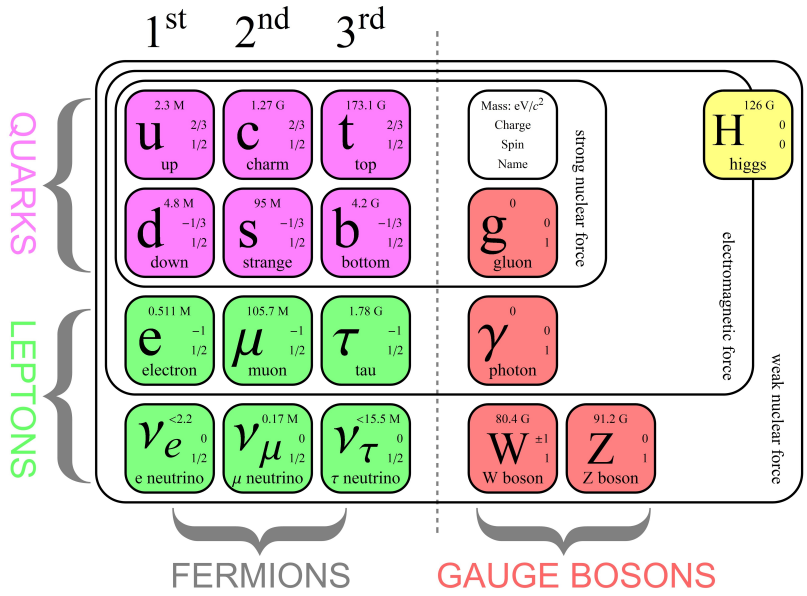

Figure 1.1: The SM of elementary particles, with the three generations of matter, gauge bosons in the fourth column, and the Higgs boson in the fifth.

These particles obey the Pauli exclusion principle. Fermions occur in two basic types called quarks and leptons. Each group consists of six particles, which are related in pairs, or generations. Table 1.1 summarises the symbols and charges of the elementary fermions that exist in nature according to the SM.

Particle	Flavour			$Q/\|e\|$
leptons	e	μ	τ	-1
	ν_e	ν_μ	ν_τ	0
quarks	u	c	t	+2/3
	d	s	b	-1/3
Generation	1st	2nd	3rd	

Table 1.1: All known fundamental fermions in nature. They are ordered from left to right in generations, having the lightest fermions at the left side.

The three charged leptons are the electron (e), the muon (μ) and the tau (τ), and all of them have a charge of minus one unit. The charge of the electron with the changed sign is used to define the charge unit. Every charged lepton has a neutral partner called neutrino with no electrical charge and a null mass within the SM. The electrically charged leptons and neutrinos are related to each other through their weak isospin charge, which both charged and neutral leptons carry. The pair formed by the electron and the electron neutrino compounds the first generation of fermions. The muon and the tau are heavier partners of the electron. They are both unstable and decay spontaneously.

On the other hand, all the quarks have a fractional electric charge, that can

either be of +2/3 or -1/3. The six quarks are paired in three generations: the up quark (u) and the down quark (d) form the first generation, followed by the charm quark (c) and strange quark (s), and ending with the top quark (t) and bottom (or beauty) quark (b).

All stable matter in the universe is made from particles that belong to the first generation. Any heavier particles quickly decay to the next most stable level. While leptons exist as free particles, quarks only appear in nature forming bound states called hadrons. The protons and neutrons composing all atoms nuclei are bounded states of quarks. The proton is composed of two up quarks and a bottom quark, what gives a total electric charge of one positive unit. The neutron is composed of an up quark and two bottom quarks, with a null total charge. The fact that quarks do not appear as free particles in nature is due to the characteristics of the strong interaction, responsible of the colour confinement. The two main types of hadrons are the baryons, formed by three quarks, and the mesons, formed by a quark and an antiquark. Two examples of baryons and mesons are the proton (p) and the pion (π) respectively.

Every fundamental fermion described in table 1.1 has a partner with the same properties except from the electrical charge, with has opposite sign. These 'copies' are called antiparticles. For example, the antiparticle of the electron (e^-) is the positron (e^+). Quarks also have its corresponding antiparticles, the antiquarks, which apart from having the opposite electrical charge than their corresponding particles, have opposite colour charge, the charge of the strong interaction. When a particle and its antiparticle collide, they annihilate mutually, producing energy. The amount of the released energy is proportional to the total mass of the particle-antiparticle system, in accord with the mass–energy equivalence equation, $E = mc^2$. Analogously, particle-antiparticle pairs can be created from the vacuum if there is enough energy to produce them, through a process called pair production. Pair production requires an initial boson to create the pair.

1.1.2 Interactions mediators

Interactions in particles physics are the ways that particles influence other particles. At macroscopic level, electromagnetism can be explained via electric and magnetic fields. At microscopic level, the SM explains such forces as resulting from the exchange of the gauge bosons between matter particles. The gauge bosons can also be referred to as force mediating particles. When a gauge boson is exchanged between two particles, at macroscopic level the effect is equivalent to a force influencing both of them, and the particle is therefore said to have mediated that force.

There are four fundamental forces at work in the universe: the strong force, the weak force, the electromagnetic force, and the gravitational force. They work over different ranges and have different strengths. Gravity is the weakest but it has an infinite range. The electromagnetic force also has infinite range but it is many times stronger than gravity. The weak and strong forces are effective only over a very short range and dominate only at the level of subatomic particles. Despite its name, the weak force is much stronger than gravity but it is indeed

the weakest of the other three. The strong force, as the name suggests, is the strongest of all four fundamental interactions.

	Force	Field particles	Spin	$Q/\|e\|$
Gauge bosons	strong	g	1	0
	weak	$W^{\pm}$	1	± 1
	weak	Z	1	0
	electromagnetic	γ	1	0
Scalar boson		H	0	0

Table 1.2: The bosons of the SM listed with their spin and electrical charge

Three of the fundamental forces result from the exchange of force-carrier particles, which belong to a broader group called bosons. In particle physics, a boson is a particle with an integer spin that follows Bose–Einstein statistics. Particles of matter transfer discrete amounts of energy by exchanging bosons with each other. Table 1.2 list all the fundamental boson included in the SM. Each fundamental force has its own corresponding boson or bosons:

- The electromagnetic force is the physical interaction that occurs between particles that carry electrical charge. The electromagnetic force is carried by the photon (γ), a massless particle without electrical charge.

- The strong interaction is the mechanism responsible for the strong nuclear force. It holds the protons and neutrons together in the atomic nuclei, as also the quarks and gluons forming the protons, neutrons and other hadrons. The strong force is carried by the gluon (g), a massless boson, electrically neutral and that carries colour charge, the charge of the strong interaction. Apart from the gluons, only quarks carry colour charge, meaning that only them are sensitive to the strong force. As gluon carry colour charge, they not only interact with quarks but also among themselves, what makes this interaction to behave quite different from the other ones, as it induces asymptotic freedom.

- The weak interaction is the mechanism responsible of the radioactive decay. The weak force is mediated with the W and Z bosons, which in contrast to the gluon or the photon, are massive gauge bosons. The W bosons are electrically charged and the Z boson is neutral.

Gravity, the fourth force known in nature is not part of the SM. The quantum theory used to describe the microscopic world, and the general theory of relativity used to describe the macroscopic world, are difficult to fit into a single framework. Luckily for particle physics, when it comes to the minuscule scale of particles, the effect of gravity is so weak as to be negligible. Only when matter is in bulk, at the scale of the human body or of the planets for example, does the effect of gravity dominate. So the SM still works well despite its reluctant exclusion of one of the fundamental forces.

1.1.3 Mathematical framework of the SM

The dynamics and kinematics of the SM are controlled by a Langrangian based on the symmetry group:

$$SU(3)_C \otimes SU(2)_L \otimes SU(1)_Y \tag{1.1}$$

where C indicates the colour charge, L the weak isospin and Y the hypercharge. The SM is a quantum gauge field theory, built from the principle that physics should be invariant under local gauge transformations. Roughly, the three factors of the gauge symmetry give rise to the three fundamental interactions. The strong interaction, also known as Quantum Chromodynamics (QCD), is associated with the local $SU(3)_C$ symmetry. The local symmetry $SU(2)_L \otimes SU(1)_Y$ is associated with the electroweak interaction, which was proposed by Glashow, Salam and Weinbergh [6, 7], unifying the electromagnetic and weak interactions.

The last piece of the SM is the Higgs field and its corresponding Higgs boson. In order to maintain invariance under the electroweak $SU(2)_L \otimes SU(1)_Y$ local gauge transformations, mass terms for fermions and gauge bosons are not admitted in the Lagrangian of the electroweak sector, what enters in conflict with the experimental observations. This problem was solved in the 60's by Brout-Englert-Higgs (BEH) which proposed the Electroweak Spontaneous Symmetry Breaking mechanism [8, 9]. With this mechanism, the introduction of a $SU(2)_Y$ complex field spontaneously breaks the gauge symmetry of the electroweak part into the electromagnetic group $U(1)_Q$, where Q is the electrical charge. In this way, a mass is given to the weak interaction force carriers bosons ($W^{+/-}, Z$), leaving the photon massless. This mechanism introduces an additional scalar boson, the Higgs boson (H). Also, with the BEH mechanism, the fermions acquire a mass proportional to the vacuum expectation value of the Higgs field, through the Yukawa interaction.

The complete Lagrangian of the SM can be factorised in terms that describe the electroweak interactions, the Higgs sector, the Yukawa terms for the fermion masses and the strong interactions:

$$\mathcal{L}_{SM} = \mathcal{L}_{EW} + \mathcal{L}_{H} + \mathcal{L}_{strong} + \mathcal{L}_{Yukawa} \tag{1.2}$$

Only the term corresponding to the electroweak sector is going to be further discussed, as it is the most relevant for this work, focused in the study of the single top quark, whose production and decay is mediated by the electroweak interaction.

1.1.4 Electroweak interaction

The electroweak Lagrangian $\mathcal{L}_{EW}$ includes several terms accounting for the charged-current interaction, the neutral-current interaction and the gauge self interactions [10]. The charged-current interaction is mediated by the W^+/W^- bosons, while the neutral-current interaction is mediated by the Z and γ bosons. We are interested here in the charged-current interaction, as it is the one meditating the production and the decay of single top quarks. The Lagrangian of the charged-current is given by

$$\mathcal{L}_{CC} = -\frac{g}{2\sqrt{2}} \left\{ W_\mu^\dagger \left[\sum_{ij} \bar{u}_i \gamma^\mu (1-\gamma_5) V_{ij} d_j + \sum_l \bar{\nu}_l \gamma^\mu (1-\gamma_5) l \right] + \text{h.c.} \right\} \tag{1.3}$$

where g is the coupling constant of the weak isospin and $W_\mu^\dagger$ is the complex-conjugate of the weak boson field. The term of the left in the sum refers to the quark sector: $\bar{u}_i$ and d_j are the up (u, c, t) and down (d, s, b) type quarks and V_{ij} is the CKM matrix, which couples any up type quark with all down type quark. The term of the right refers to the lepton sector: $\bar{\nu}_l$ and l are the neutrino and the lepton, where l runs all over the three generations (e, μ, τ). γ^μ are the Dirac matrices.

While the W boson mediates interactions between leptons of the same generation only, there is also coupling across generations in the quark sector via the CKM matrix. It is for this reason that the only stable particles we observe in nature in the quark sector comprise up and down quarks, the members of the lightest generation. The inter-generational coupling is characterised by the Cabibbo-Kobayashi-Maskawa (CKM) matrix [1, 11], a matrix whose individual elements represent the probability of given quark family (d, s, or b) transitioning to another.

For the top quark, V_{tb} is close to one, while the terms V_{ts} and V_{td} are almost null, meaning that the top quark almost only interacts through the Wtb vertex. Therefore, neglecting the terms V_{ts} and V_{td}, the Lagrangian of the weak interactions of the top quarks is given by

$$\mathcal{L}_{Wtb} = -\frac{g}{2\sqrt{2}} \left\{ W_\mu^\dagger \bar{t} \gamma^\mu (1-\gamma_5) V_{tb} b + \text{h.c.} \right\} \tag{1.4}$$

1.2 Successes and limitations of the SM

The SM theory has been exhaustively tested in several experiments. The measurements and searches performed so far seem to be consisted with the theory, and no hints of new physics are observed. Collider experiments have tested the SM predictions in a wide range of energy: from the $\sqrt{s} \sim 200$ GeV of LEP, to the $\sqrt{s} \sim 1.9$ TeV of Tevatron. Currently, with the LHC, the SM is being tested to an energy of $\sqrt{s} = 13$ TeV. Figure 1.2 shows the results of cross-section measurements of several SM processes performed with the ATLAS detector with data from LHC Runs I and II [12]. An overall good agreement between data and predictions is seen for more than ten orders of magnitude. Figure 1.3 shows a fit to the masses of the W boson, the top quark and the Higgs boson. With the current experimental precision, measurements are compatible with the SM predictions [13].

Despite the great success of the SM describing the subatomic world dynamics through the strong and electroweak interactions, the SM is an incomplete theory. There are several open questions and fundamental physical phenomena in nature that the SM is not able to explain:

- **Strong-electroweak Unification**: The SM does not unify the strong

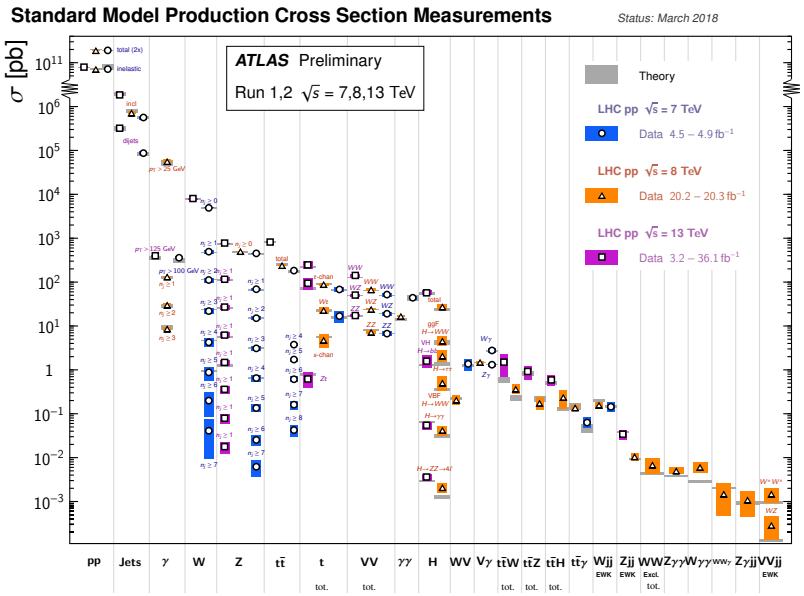

Figure 1.2: Summary of several SM total and fiducial production cross section measurements, corrected for leptonic branching fractions, compared to the corresponding theoretical expectations. All theoretical expectations were calculated at NLO or higher. The measurements have been performed with the ATLAS detector at $\sqrt{s}$ =7, 8 and 13 TeV. The luminosity used for each measurement is indicated close to the data point.

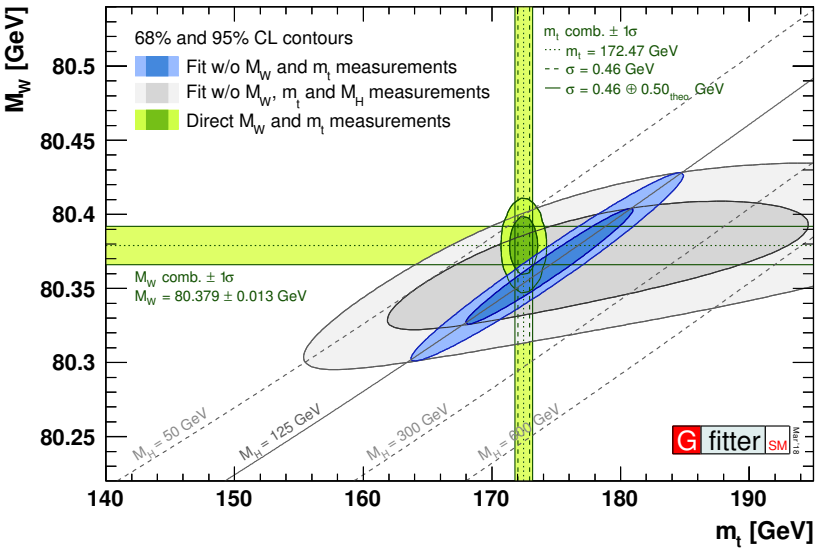

Figure 1.3: Contours of 68% and 95% confidence level obtained from scans of fits with fixed variable pairs M_W vs. m_t. The narrower blue and larger grey allowed regions are the results of the fit including and excluding the M_H measurement, respectively. The horizontal bands indicate the 1σ regions of the M_W and mt measurements.

and electroweak interactions, as was done with the electromagnetic and weak interaction. Theories that unify the SM symmetries in this way are called Grand Unified Theories (or GUTs), and the energy scale at which the unified symmetry is broken is called the GUT scale. GUT theories predict the existence of magnetic monopoles and the instability of the proton. None of these predictions has been observed in nature.

- **Hierarchy problem**: While the EW scale is of the order of 10^2 GeV, the Plank scale, where the gravitational force becomes important is of the order of 10^{19} GeV. This huge gap between both scales is known as the hierarchy problem. The fact that the Higgs boson mass is well below the Planck seems to either require new physics between the EW and the Planck scale or an incredible fine tuning to cancel out the radiative corrections to the Higgs boson mass.

- **Gravity**: The SM does not includes gravity. The underlying theories of the SM and the General Relativity, the most successful theory of gravity to date, seem to be incompatible.

- **Cosmological discrepancies**: Cosmological measurements lead to the conclusion that the SM particles only account for about the 5% of the matter/energy present in the universe. The missing 95% would be composed of dark matter (26%) and dark energy (70%). Dark matter is proposed to explain various gravitational effects that can not be explained with the visible matter, such as the rotation speeds of galaxies or the gravitational lensing. Dark matter is believed to be formed by non-baryonic matter which does not interact electromagnetically. Its name comes from the fact that it does not interact with light and, therefore, is invisible. The SM does not provide any candidate particle that can account for dark matter. The dark energy is an unknown form of energy that is hypothesised to permeate space. Dark energy is proposed as an explanation of the accelerated expansion of the universe. The SM does not propose any candidate for the dark energy either.

- **Neutrino masses**: According to the SM, neutrinos are supposed to be massless particles and to exist only in one helicity state: neutrinos are left-handed, while antineutrinos are right handed. However, neutrino oscillation experiments have shown that neutrinos do have mass. Although mass terms for the neutrinos can be added to the SM, these lead to new theoretical problems. The problem can be solved either by adding sterile neutrinos, which have right-handed chirality and only interact gravitationally, or through the Majorana mechanism, that states that the neutrino is its own antiparticle. For example, the mass terms need to be extraordinarily small and it is not clear if the neutrino masses would arise in the same way that the masses of other fundamental particles do in the SM.

- **Matter–antimatter asymmetry**: The SM determines that matter and antimatter should have been created in (almost) equal quantities, but the universe we see today is completely made of matter only. Although the SM has some violations of CP in the quark sector, these are not large enough to explain the absence of antimatter in our universe.

- **Fermion masses hierarchy problem**: The masses of the SM fermions vary over a wide range, including several orders of magnitude, from the top quark mass (172.4 GeV) to the electron mass (511 KeV). That is without taking into account the neutrino masses. The SM does not provide any explanation about the values of the fermion masses. It can not explain just either why fermions are grouped in three generations.

1.3 Top quark physics

In the 1970s, the discovery of the tau-lepton and the Y-Meson (comprising a bottom and antibottom-quark) led to the conclusion that a sixth quark (the top quark) could be discovered restoring the picture of a symmetry between the lepton and quark generations. The top quark was then finally discovered in 1995 by the CDF and D0 collaborations at the Tevatron collider.

The extraordinarily large mass of the top quark causes the top quark to decay almost immediately. The lifetime of the top quark is approximately $0.5 \cdot 10^{-24}$ s, which is why no bound states containing top quarks are formed. The short lifetime of the top quark grants the opportunity for measurements which are impossible to be performed on lighter quarks. Such as polarisation measurements. In bound states the spin of the quarks is depolarised by QCD interactions. Due to its high mass, and therefore large Yukawa coupling, the top quark might play a special role in electroweak symmetry breaking. A comprehensive understanding of top quark physics is also important for future physics beyond the SM since top quark decays will be a large source of background for new physics processes.

At hadron colliders, top quarks are produced predominantly in pairs ($t\bar{t}$) via the flavour-conserving strong interaction, but can also be produced singly through charged-current electroweak processes involving a Wtb vertex. Three sub-processes contribute to single top quark production at leading-order (LO) in perturbation theory: the associated production of a top quark with a on-shell W boson (Wt), or the exchange of a virtual W boson either in the s-channel or in the t-channel, being this last one also referred to as Wg fusion channel in the literature (figures 1.4 and 1.5). At next-to-leading-order (NLO) in QCD, there is no interference between the t-channel and the s-channel and are thus well defined at that order.

1.3.1 Single Top quark physics

An important difference between single top quark and paired top quark production is that that the first ones are produced with a high degree of polarisation in the appropriate reference frame. This is due to the vector-axial nature of the Wtb vertex, which in the SM is completely left-handed, implying large correlations between the W helicity and the top quark and b-quark polarisations. This is not the case for top quark pairs, which are produced mainly from a gg initial state via strong interaction, and do not dominantly populate a single spin configuration in any reference frame.

At the LHC, the t-channel exchange is the dominant production process of single top quarks, accounting for about 75% of the predicted cross-section at the centre-of-mass energy $\sqrt{s} = 8$ TeV. In the t-channel, the exchange of a space-like W boson produces a top quark and a forward light-quark (called spectator quark) in the final state. The Feynman diagram corresponding to this 2→2 process ($q+b \to q'+t$ - five-flavour scheme considering the quarks u, d, s, c and b in the initial state) is displayed in Figure 1.4(a). The t-channel single top quark production can also be represented through a 2→3 process ($q+g \to q'+t+\bar{b}$ - four-flavour scheme considering only the quarks u, d, s and c in the initial state) [14], in which an initial-state gluon splits into two b-quarks and one of them scatters with an incoming light-quark. In that case, an additional forward and soft b-quark (called second b-quark) appears in the final state. The corresponding Feynman diagram is shown in Figure 1.4(b). Both figures include the leptonic decay of the top quark through weak interaction.

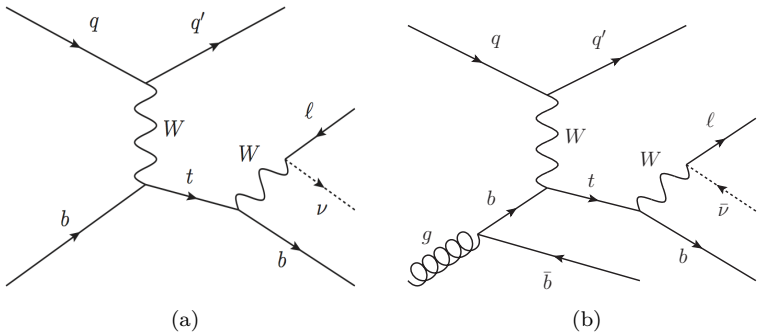

Figure 1.4: LO Feynman diagrams for t-channel production of single top quarks in pp collisions (a) 2→2 process (five-flavour scheme) and (b) 2→3 process (four-flavour scheme). The leptonic decay of the top quark ($t \to Wb$ with $W \to \ell\nu$) is also displayed.

It has been shown [15] that the d-quark direction of motion is maximally correlated with the top quark spin. For top production, the spectator-quark is generally a d-quark that comes from one of the valence u-quarks of the incoming proton. This defines the so-called spectator basis in which the top quark spin direction is taken along the spectator-quark momentum, boosted to the top quark rest frame. The overall fraction of spin-up top quarks in the spectator basis at 8 TeV is predicted to be 0.91.

The case of antitop quark production is different, as the d-quark is generally the valence d-quark of one of the incoming protons, corresponding the spectator jet with the scattered light-quark. Hence, at first sight, it could be concluded that the spectator basis chooses the wrong direction most of the times for antitop quark production. However, the transference of momentum between the incoming quark and the spectator jet is very small, resulting in almost parallel momentum vectors for both quarks. Then, the degree of spin polarisation for antitop quarks is not degraded much in the spectator basis. In the spectator basis, the degree of polarisation calculated at NLO for top-antiquark production is -0.86, just slightly smaller than the value predicted for top quark production, 0.91 [16].

Since the majority of the time the down-quark comes from one of the two

beams, another basis can be defined in addition to the spectator basis. The beam line basis is defined by decomposing the antitop quark spin along the direction of the beam that is providing the initial down-quark. The decision of which of the two beams is providing the light-quark can not be made unambiguously, but as already explained, the spectator quarks typically follows the direction of the incoming down-quark, so it can be used to choose among the two beams. It has been shown that this choice gives the correct answer for $dg \to q't\bar{b}$ 98% of the time [17].

In proton-proton colliders as the LHC, single top quarks produced via Wt-channel or s-channel do not show a high degree of polarisation in any basis. The Feynman diagrams at LO for both processes are shown in figure 1.5. In the s-channel production, the d-quark appears only in the initial state, coming from one of the valence d-quarks of the incoming protons, but unlike in the t-channel production, there is not a spectator jet that allows to choose among the two beams. This makes impossible to find a basis in which the top quarks populate dominantly a single spin configuration. In the other hand, there is not any d-quark involved in the Wt-channel production, as the initial state is composed by a b-quark and a gluon.

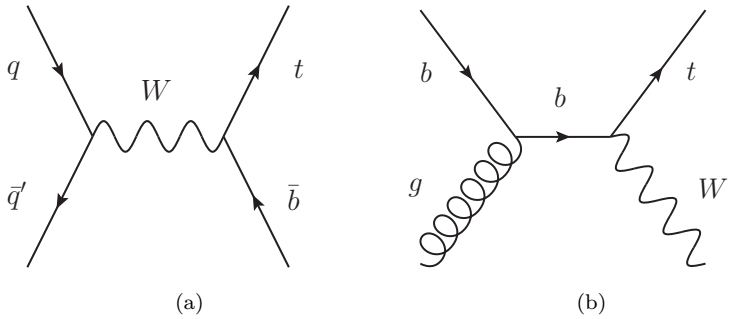

Figure 1.5: LO Feynman diagrams of single top quarks production in pp collisions for the s-channel (a) and for the Wt-channel (b). The Wt-channel production has a second Feynman diagram contributing in which the gluon emits a real top quark plus a virtual antitop quark that merges with the b-quark to emit a W boson.

As said before, one consequence of the large top quark mass is that its decay time scale is much shorter than the typical time needed for QCD interactions to depolarise its spin. Therefore the spin of the top quark by the time of its decay is the same one as it was produced. This information can thus be obtained from its decay products. Within the SM, the top quark decays almost exclusively through electroweak interaction into a W boson and a b-quark. The W boson immediately decays into a lepton and a neutrino, or into a pair of quarks. As with the d-quark, it has been shown that the lepton direction of motion is maximally correlated with top quark spin direction [18, 19]. These correlations can be used to determine probabilistically whether the top quark is spin up or down. The produced W boson also possesses a polarisation that can be extracted from angular distributions of its decay products through the measurement of spin-dependent observables.

1.3.2 Wtb anomalous couplings

Measuring the top quark polarisation and the W boson spin observables in t-channel single top quark production provides a powerful tool for studying the Wtb vertex in both top quark production and decay. New physics effects resulting in corrections to the Wtb vertex would affect the top quark and W boson polarisations. Within the SM, the Wtb coupling is purely left-handed at tree level (equation 1.4), and its strength is given by the V_{tb} element of the CKM matrix, which can be directly extracted from cross-section measurement in single-top production.

In new physics models, deviations from the SM prediction $V_{tb} \simeq 1$ are possible, as well as new radiative contributions to the Wtb vertex. These corrections can be parameterised with the effective operator formalism, with the radiative corrections to the vertex being absorbed into a small number of non-renormalisable effective couplings called anomalous couplings. Within this framework, the most general Wtb Lagrangian can be written as [20]:

$$\mathcal{L}_{Wtb} = -\frac{g}{\sqrt{2}}\bar{b}\gamma^{\mu}\left(V_{\mathrm{L}}P_L + V_{\mathrm{R}}P_R\right)tW_{\mu}^{-} - \frac{g}{\sqrt{2}}\bar{b}\frac{i\sigma^{\mu\nu}}{M_W}q_{\nu}\left(g_{\mathrm{L}}P_L + g_{\mathrm{R}}P_R\right)tW_{\mu}^{-} + \mathrm{h.c.} \tag{1.5}$$

In this expression g is the weak coupling constant, M_W and q_ν are the mass and the four-momentum of the W boson, respectively, $P_L \equiv \frac{1}{2}(1-\gamma^5)$ and $P_R \equiv \frac{1}{2}(1+\gamma^5)$ are the left- and right-handed projection operators, and $\sigma^{\mu\nu} = [\gamma^{\mu}, \gamma^{\nu}]/2$. The constants $V_{L,R}$ and $g_{L,R}$ are the left- and right-handed vector and tensor couplings. In the SM at tree level, the coupling V_L is the V_{tb} element of the CKM matrix, with a value close to one, while all the anomalous couplings V_R and $g_{L,R}$ are all zero. Deviations from this values would provide hints of physics beyond the SM. Complex values of the couplings would imply a CP-violating component in the top quark decay.

Of particular interest is the imaginary part of g_R (Im g_R), that can be measured with the best precision in t-channel top quark production [21]. Limits on Im g_R have been set already at the LHC by the ATLAS collaboration at a centre-of-mass energy of 7 TeV from the analysis of the double-differential angular decay rates of the produced t-channel single-top quark-events [22]. Searches for anomalous Wtb couplings in single top quark production and decay at 7 and 8 TeV have been also published by the CMS Collaboration [23, 24].

Chapter 2

The LHC and the ATLAS detector

The Large Hadron Collider (LHC) [25] is the biggest and most powerful particle accelerator of the world. Located at CERN (Organisation Européenne pour la Recherche Nucléaire), near to Geneva and across the border between France and Switzerland, the LHC is the final step of the CERN accelerator complex. The accelerating ring of the LHC has a 27 km circumference, and it is hosted in the same tunnel that formerly housed the Large Electron-Positron collider (LEP). The LHC is a proton accelerator, that makes protons to circulate in two circular beams going in opposite directions. The LHC can also accelerate heavy nuclei. The LHC consists of eight crossing points connected by straight tunnels. The eight straight sections contain the experiments, beam dumps, cleaning and RF cavities. The arcs consist of focusing and bending magnets. This geometry is an artefact of the LEP collider, where the straight sections would compensate for synchrotron radiation losses that are more significant for a circular lepton collider. Unlike a particle-antiparticle collider, the counter-rotating beams must be circulated in two separate rings. Due to limited space in the LHC tunnel, which has a radius of 3.7 m, a twin-bore superconducting magnet design was developed, consisting of two sets of coils and beam channels within the same magnetic and mechanical structure and cryostat.

In total, the LHC is made up of 1232 superconducting Niobium-Titanium dipole magnets (shown in figure 2.1) that bends the beam in a circular path, 392 quadrupole magnets for focusing the beam, and additional complex magnet systems for beam corrections and squeezing the beams at the collision points. The acceleration and the creation of proton bunches is accomplished by the oscillating electromagnetic field inside radio-frequency (RF) cavities. The LHC has 16 RF cavities (8 per beam) operating at 400 MHz in a super-conducting state. Protons that are perfectly synchronised with the oscillating RF cavities will see no acceleration while protons with slightly different energies will be accelerated or decelerated until they are synchronised. The process also forms and maintains bunches of protons. The LHC is designed to handle 2808 proton bunches with a 25 ns bunch-spacing.

The cryostat that houses the beam pipe and magnets is maintained at a temperature of 1.9 K using super-fluid liquid helium. The LHC is designed to operate at a proton-proton centre of mass energy of $\sqrt{s} = 14$ TeV. In order to reach this energy, 11850 A of electrical current is required to create an 8.33 T magnetic field in the superconducting dipole magnets. The beam pipes are maintained under vacuum conditions with pressures below 10^{-13} atmospheres. The LHC beams have not reached the designed energy yet. During Run-I, the LHC ran with a centre of mass energy of 7 TeV in 2011 and 8 TeV in 2012. Since Run-II, which started in 2015, the LHC has ran at a centre of mass energy of 13 TeV.

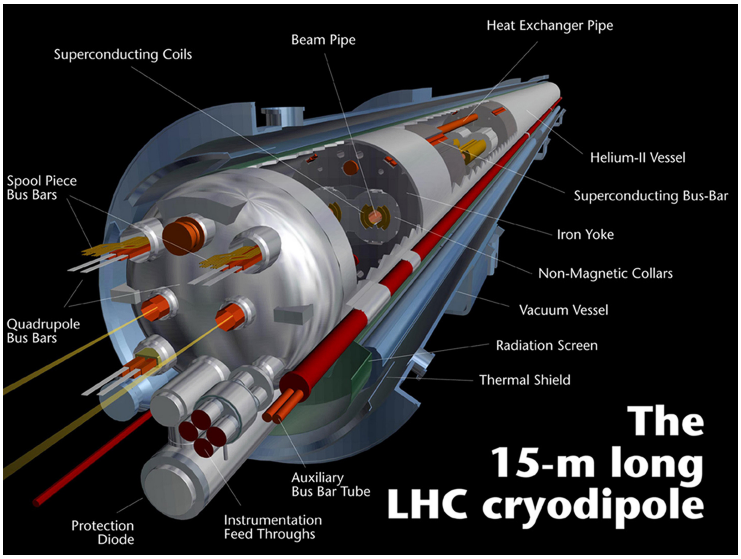

Figure 2.1: Diagram of one of the 1232 dipoles used in the LHC [26].

Figure 2.2 show the CERN accelerator complex and the route protons take before colliding at e.g. the ATLAS site. After having been separated from its electron in the hydrogen state, the protons are in sequence accelerated through the LINAC-2, PSB1, PS, SPS and LHC accelerators. In this context, each of the accelerators before LHC is used to accelerate the protons up to its maximum energy, before passing the beams to the next accelerator in the chain. The energy reached by each step is: 50 MeV (LINAC-2), 1.4 GeV (PSB), 25 GeV (PS) and 450 GeV (SPS). The LHC is finally able to boost the individual protons from 450 GeV up to a maximum of 7 TeV.

Most of the other accelerator in the chain have experimental halls where the beams are used for other experiments at lower energies. The accelerator complex includes the Antiproton Decelerator (AD) and the ISOLDE radioactive ion beam facility. It also produces neutrinos for the Gran Sasso (CNGS) and feeds the nTOF and the Compact Linear Collider (CLIC) test area. LHC is also able to accelerate ions. A source of Vaporised lead is accelerated in the LINAC-3 before being collected and accelerated in the Low Energy Ion Ring (LEIR). After, ions follow the same route than the protons.

Four large experiments collect and record data of the LHC collisions: AT-

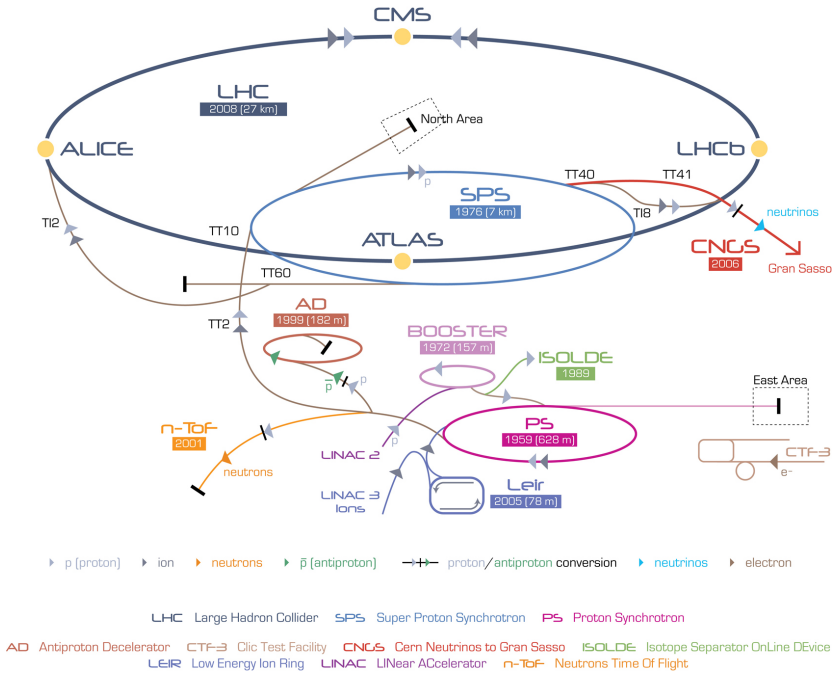

Figure 2.2: Schematic representation of the CERN accelerator complex, of which the LHC is the final step.

LAS, ALICE, CMS and LHCb. ATLAS is explained in detail in section 2.1. A brief description of the other three is given here:

- **CMS**: Together with ATLAS, the Compact Muon Solenoid is one of the two general purpose detectors of the LHC. It is designed to investigate a wide range of physics, including SM tests, Higgs physics and searches of new physics as SUSY or extra dimensions. It has the same scientific goals than the ATLAS experiment, but uses different techniques and design. It is built around a huge super conducting solenoid magnet able to generate a field of 4 T. With a weight of 15000 tons, it is the heaviest LHC experiment.

- **LHCb**: The Large Hadron Collider beauty experiment focus on flavor physics of the b-quark, investigating the slight differences between matter and antimatter. The LHCb experiment is a one-arm like experiment, built close to the beam line in one direction from the collision point and is able to reconstruct tracks in the very forward region, optimal for heavy flavour physics.

- **ALICE**: A Large Ion Collider Experiment is designed to study the physics of strongly interacting matter at high energy densities, where a phase of matter called quark-gluon plasma forms. It focus on heavy-ion physics, mostly on Pb-Pb collisions and is designed to reconstruct a higher track multiplicity at higher resolution compared to the ATLAS and CMS experiments. Higher resolution comes at the cost of a slower response.

- **Other experiments**: Three additional and smaller experiments are allo-

cated at the LHC. LHCf, where the f stands for forward, is a experiment that measures particles produces very close to the beam direction. The motivation is to test models used to estimate the primary energy of the ultra high-energy cosmic rays. It has the detectors 140 m from the ATLAS collision point. TOTEM focus on the measurement of the proton cross-section at the LHC. It is placed near the collision point of the CMS experiment. MoEDAL is a experiment that performs direct searches of magnetic monopoles and other highly ionising stable massive particles, near the LHCb detector.

The event production rate of a particular physics process in a collider is given by $N_{\text{event}} = L \cdot \sigma_{\text{event}}$, where L is the instantaneous luminosity provided by the collider, the LHC in this case, and σ_{event} is the production cross section of the process, what depends on the centre of mass energy. The latest is determined by nature, while L depends only on the beam parameters. Assuming a Gaussian profile for the beams, the luminosity at the interaction points is characterised using the following relationship:

$$L = \frac{N_p^2 n_b f_{\text{coll}} \alpha_r}{4\pi \epsilon_n \beta^*} F \tag{2.1}$$

where N_p is the number of protons per bunch, n_b is the number of bunches circulating in each beam, f_{coll} is the collision frequency, α_r is the relativistic Lorentz factor of the beam, ϵ_n is the normalised transverse beam emittance, F a geometric reduction factor due to the crossing angle of the beams at the interaction point, and β^* is the beta function, which measures the beam focus.

There are three main ways of increasing the luminosity in a collider. Squeezing the beams down to a smaller transverse size, increasing the number of circulating bunches, or increasing the number of protons in each bunch. Squeezing the beams or increasing the number of protons per bunch also leads to an increase in the number of proton-proton interactions within the same bunch, called in time pile-up- In the other hand, increasing the number of bunches (decreasing the space between them) leads to an increase in the out of time pile-up. The LHC and the high luminosity ATLAS and CMS detectors are designed to operate at a peak luminosity of $L = 10^{34}$ cm^{-2}s^{-1} with proton beams, corresponding to a bunch collision rate of 40 MHz and an average of 22 simultaneous proton-proton interactions. Already in 2016, the LHC surpassed the nominal design instantaneous luminosity, reaching a peak luminosity of $L = 20.9 \cdot 10^{33}$ cm^{-2}s^{-1} in 2017. Figure 2.3 shows the distribution of the mean number of interactions per crossing for LHC Run-I (left) and Run-II (right).

The instantaneous luminosity L can be integrated over time, providing the total amount of data used in the physics analyses. Figure 2.4 shows the cumulative distributions of the integrated luminosity as a function of time for the 2011-2018 campaigns.

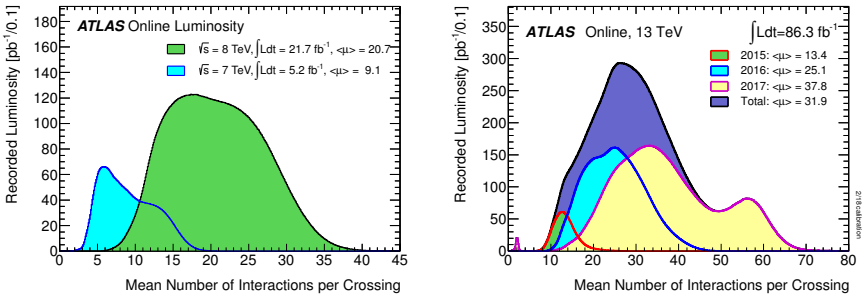

(a) (b)

Figure 2.3: Luminosity-weighted distributions of the mean number of interactions per crossing for Run-I (a) and Run-II (b). Run-I consists of the data recorded in 2011 and 2012 at a centre of mass energy of 7 and 8 TeV respectively. Run-II includes the data recorded from 2015 to 2017 at a centre of mass energy of 13 TeV. [27]

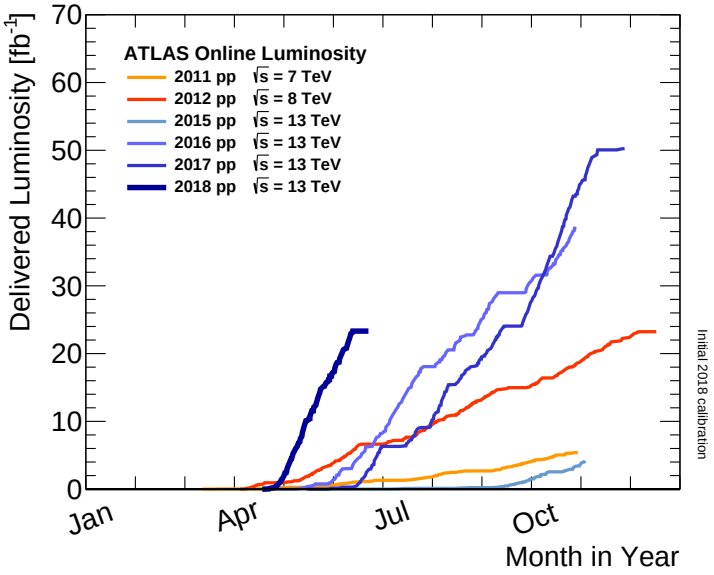

Figure 2.4: Cumulative luminosity versus day delivered to ATLAS during stable beams and for high energy p-p collisions. Data from years 2011-2018 is included in the plot. Data from 2018 goes only up to mid June, as the data taking was on going by the time this plot was made. [27]

2.1 The ATLAS experiment

ATLAS [28] (A Toroidal LHC ApparatuS) is a general-purpose particle physics experiment run by an international collaboration and, together with CMS, is designed to exploit the full discovery potential and the huge range of physics opportunities that the LHC provides. It investigates a wide range of physics phenomena, from precision SM physics measurements to searches of physics beyond the SM like SUSY, extra dimensions, black holes, dark matter, etc. Being 25 m in height and 44 m in length, ATLAS is the largest collider detector ever built. It is installed in a cavern along the LHC tunnel at CERN's main site in Meyrin, Switzerland. ATLAS comprises more than 3000 members from about 182 institutions around the world, representing 38 countries.

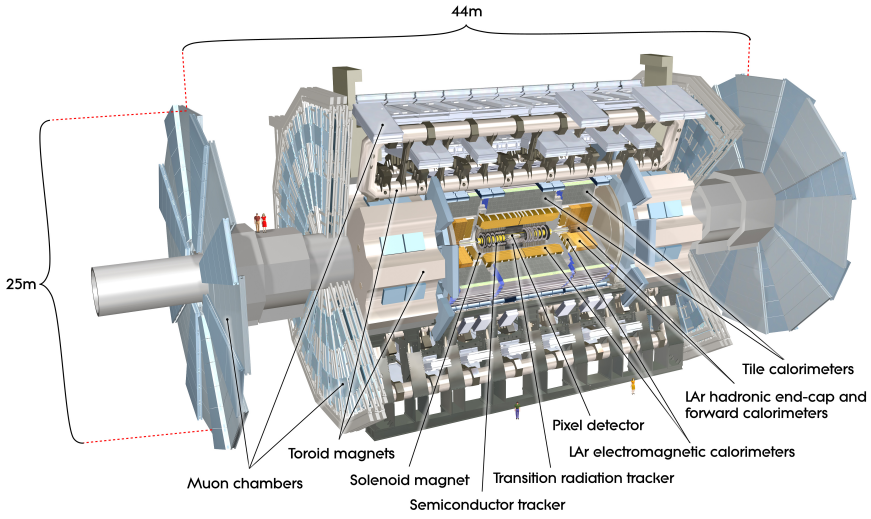

Figure 2.5: A cut-away view of the ATLAS detector, displaying its major subsystems. Some people are drawn together with the detector to show the real scale of the detector [29].

ATLAS is composed of several layers of sub detectors with forward-backward cylindrical geometry that is nominally symmetric about the interaction point. Each layer is designed to measure signals left by certain particles and collectively they build a detailed description of each collision event. A cut-away view of the ATLAS detector is shown in Figure 2.5. Each subdetector is composed of a barrel and two end caps. The barrel has cylindrical shape, and is placed around the LHC beam pipe. The end caps close the cylinder by its sides in the forward region. The closest subdetector to the beam is the Inner Detector (ID), made up of silicon and gas-based particle tracking devices. It composes the ATLAS tracking system, reconstructing the path of the electrically charged particles produced in the collisions. A solenoid magnet surrounds the ID, bending the trajectories of the charged particles, what allows to measure its momentum. The calorimeters surround the tracking system and measure energy deposits from neutral and charged particles. ATLAS has two different calorimeter. The innermost one is the electromagnetic calorimeter, designed to

measure the energy of photons and electrons. The hadronic calorimeter, placed just afterwards, is intended to measure the energy deposited by hadrons. Finally the Muon Spectrometer forms the outermost layers, recording the outer part of the muon trajectories. A large toroid magnet spanning the barrel region and two smaller toroids in the end caps provide the magnetic field for muon momentum measurement. Figure 2.6 illustrates the pass of different kind of particles through the ATLAS detector and how they are identified. The figure is simplified, as hadrons deposit energy also in the electromagnetic calorimeter. These subdetectors are further described in next sections, focusing more in the ID details, as this thesis describes the ID alignment procedure.

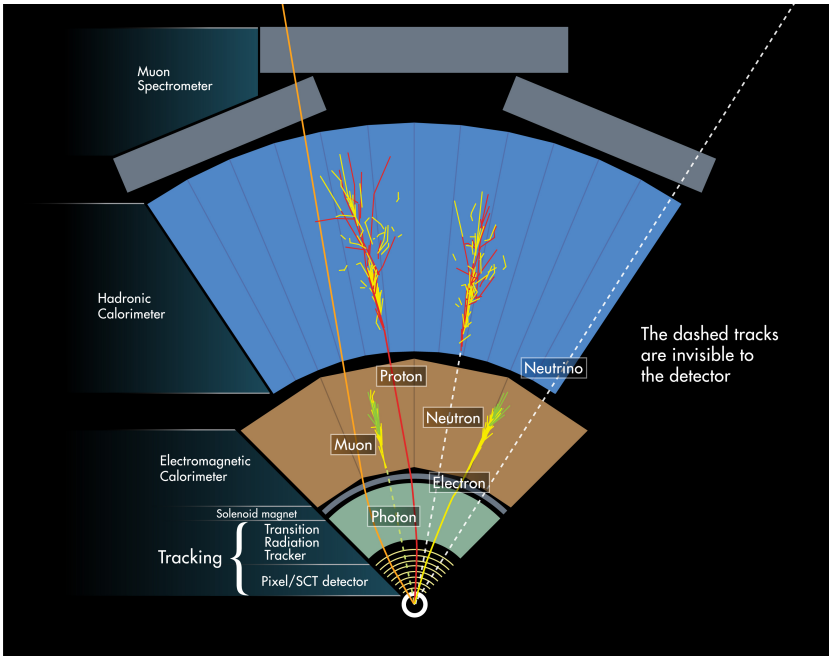

Figure 2.6: Diagram showing the interactions that suffer different kinds of particles while traversing the ATLAS detector [30].

2.1.1 The ATLAS coordinate system

The ATLAS detector is described with a right handed cartesian reference system centred in the ATLAS nominal interaction point of the proton-proton collisions. The z-axis goes along the LHC beam axis, with the same orientation than the solenoid magnetic field. The x-y plane is transverse to the beam, with the x-axis pointing to the centre of the LHC ring and the y-axis pointing upwards to the sky. It is often more convenient to describe detector signals and reconstructed physics objects with polar coordinates: r, ϕ and θ or η. In this case, r is the radial distance to the z-axis and ϕ the azimuthal angle measured in the x-y plane ($\phi \in [-\pi, \pi]$, with $\phi = 0$ in the x-axis and $\phi = \pi/2$ in the y-axis). Finally, θ is the polar angle with respect the z-axis, taking values from 0 at the positive z-axis to -π at the negative z-axis. The polar direction of physics objects is

frequently measured in terms of rapidity, y, defined as:

$$y = \frac{1}{2} \ln \frac{E + p_z}{E - p_z} \tag{2.2}$$

The rapidity has the property that the difference between the rapidities of two particles is invariant with respect to Lorentz boosts along the z–axis. In the ultra relativistic regime limit, where the particle's mass can be neglected, the rapidity is approximately equal to the pseudo-rapidity, η, defined as:

$$\eta = -\ln \tan \theta/2 \tag{2.3}$$

Often the total angular separation between two objects is expressed in terms of $\Delta R = \sqrt{\Delta\eta^2 + \Delta\phi^2}$.

2.1.2 The Inner Detector

The ID, the subdetector closest to the interaction point, composes the tracking system of the ATLAS detector. The primary aim of the ID is to precisely measure trajectories, also often referred to as 'track', of charged particles in the region closest to the beam pipe. As the ID is immersed in a magnetic field of known strength and polarity, the momentum and charge sign of a particle can be determined by measuring the track radius of curvature. Primary and secondary decay vertices can be reconstructed by extrapolating the tracks to their common origins.

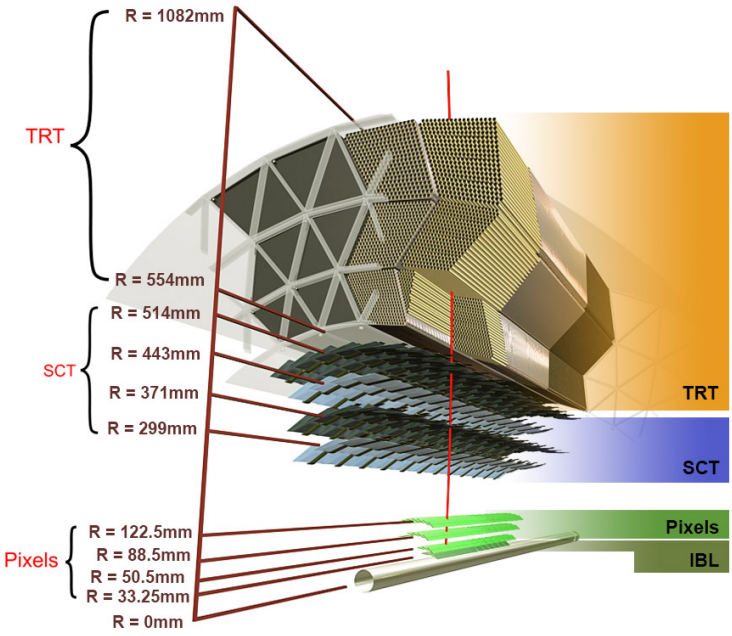

Figure 2.7: A 3D visualisation of the structure of the barrel of the ID. In the picture are shown the beam pipe, the IBL, the Pixel layers, the four cylindrical layers of the SCT and the 72 straw layers of the TRT [31].

In total, the ID has a length of 7 m and a diameter of 2.3 m, and it is placed surrounding the beam pipe. Its layout is shown in figure 2.7. The ID is made from different subdetectors, which use different technologies. Table 2.1 summarises the characteristic of each subdetector.

Subdetector	Element size [μm]	Intrinsic resolution [μm]	Radius barrel layers [mm]
IBL	50×250	8×40	33.2
Pixel	50×400	10×115	50.5, 88.5, 122.5
SCT	80	17×580	299, 371, 443, 514
TRT	4000	130	from 554 to 1082

Table 2.1: Summary of the main characteristics of the ID subdetectors. The intrinsic resolution of the IBL, the Pixel and the SCT is reported along r-ϕ and z, while for TRT is only along r-ϕ. For SCT and TRT the element sizes refers to the spacing of the readout strips and the diameter of the straw tubes, respectively.

The combination of precision silicon trackers at small radii with the TRT in the outermost part of the ID provides robust and high precision pattern recognition in both r-ϕ and z coordinates. The silicon detectors allow precise measurements of the impact parameter as well as high accuracy for primary and secondary vertices, what is very important for example in the identification of jets originating from b-hadrons.

Pixel

Made of pixels detectors, it was the closest detector to the interaction point and the one with the finest granularity during LHC Run-I. It provides full coverage in the azimuthal angle ϕ and within a pseudorapidity range of $|\eta| < 2.5$. It is composed of 1774 pixel detectors, with 47232 silicon pixels on each, distributed in three barrel layers and in six end cap disks, three for each side. A schematic drawing of the ATLAS Pixel Detector is shown on figure 2.8. The barrel layers are concentric cylindrical layers around the beam axis, while the end cap disks have wheel shape mounted in the x-y plane. For the most part, the pixels have a size of 50×400 μm^2, what translates into intrinsic resolutions of 10 μm in r-ϕ and 115 μm along z. The system ensures three precisely measured hits for each track. The closeness of the Pixel detector to the interaction point together with its high resolution enables it to reconstruct the interaction vertices very precisely.

During the LHC Long Shutdown 1 (LS1) that took place between Runs I and II, the Pixel was dismounted from its position in order to perform some interventions in the detector to prepare it for the harder conditions expected for LHC Run-II: more radiation damage and higher pile-up. Several damaged modules were replaced, reducing the fraction of dead modules and improving the data speed transmission with optical fibbers for the second layer. Additionally, a new layer of pixels detectors has been added to the ID, the Insertable B-Layer, described below.

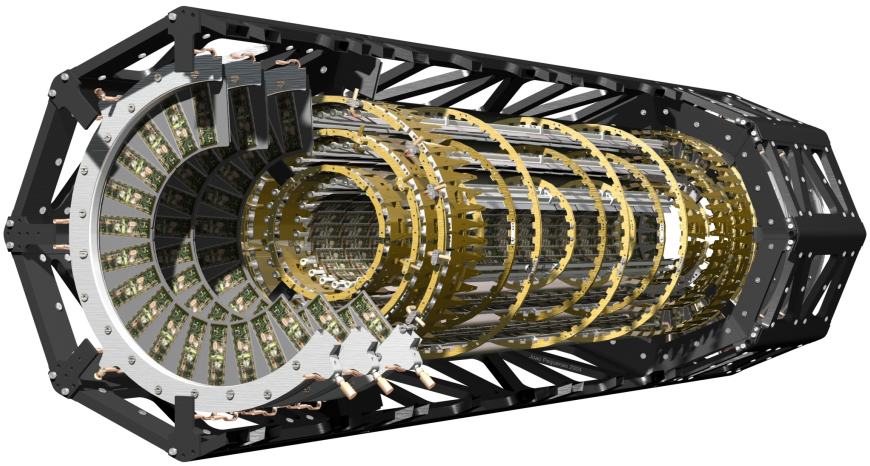

Figure 2.8: Schematic drawing of the ATLAS Pixel Detector [28].

IBL

The Insertable B-Layer is placed closer to the interaction point thanks to a new thinned beam pipe, reducing the distance from the interaction point to the first tracking layer. It consists of 280 silicon pixel modules arranged on 14 azimuthal carbon fibber staves surrounding the beam pipe at a mean radius of 33.2 mm. The staves distribution ensures a full hermetic coverage in ϕ, with an overlapping angle between the staves of 1.82°. Each stave is instrumented with 12 two-chip silicon planar modules, covering the region of $|\eta| < 2.7$, and 8 single chip modules with silicon 3D sensors, four at each end of the stave ($2.7 < |\eta| < 3$). Figure 2.9 shows a schematic view in the r-ϕ plane of the IBL. Mechanically, it is attached to the new beam pipe and not to the rest of the Pixel detector. The expected hit resolution is 8 μm in r-ϕ and 40 μm in z. Further details about the IBL mechanical structure are given in section 5.

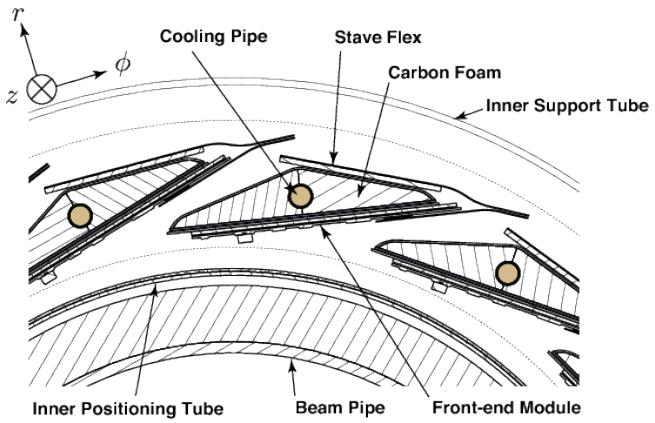

Figure 2.9: Transverse view of 3 of the Insertable-B-Layer (IBL) staves, located directly on the beam pipe [32].

SCT

The SemiConductor Tracker (SCT) surrounds the Pixel detector, providing additional precision tracking but using silicon microstrip sensor technology, more cost-effective than the pixel sensors. It has a similar geometry to the Pixel, consisting of 4088 silicon strip modules, arranged in four barrel layers and two end caps with nine wheels each. It has full coverage in ϕ and up to 2.5 in η. The barrel layers consist of silicon detector units of 780 readout strips each with a pitch of 80 μm, while the end cap disk detector units are similar but with a tapered geometry. Each detector unit consists of two back-to-back silicon microstrips planes with a relative 40 mrad offset between the two planes, as can be seen in figure 2.10. Both measurements are combined such that the coordinate along the module axis can be measured, allowing the determination of the z coordinate. The system provides eight precisely measured hits for each track. The intrinsic resolution of the SCT modules is 17 μm in r-ϕ and 580 μm in z.

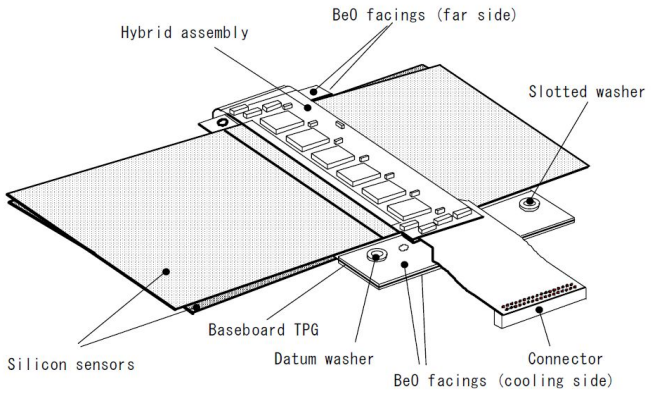

Figure 2.10: SCT module structure [28].

TRT

Instead of pixels or strips, the Transitional Radiation Tracker (TRT) consists of a large number of gas filled tubes. The TRT relies both on the collection of primary ionisation charge and the collection of secondary ionisation charge arising from transition radiation to measure passage of charged particles. Each tube, functioning as a cathode, has an anode wire in the centre. When a charged particle passes through the gas mixture, freed electrons drift toward the anode wire and generate an electrical signal. The TRT also provides discrimination between electrons and pions. Minimum-ionising charged particles like pions generate a much smaller signal than electrons, that emit transition radiation in the form of x-ray photons as they pass through the inhomogeneous TRT material. These photons are absorbed by the xenon gas and result in a larger avalanche of freed electrons toward the anode wire.

The TRT barrel covers the radius of 56-108 cm and $|\eta| < 1$, while the combined barrel and end cap cover up to $|\eta| < 2$. Within this region of coverage particles with $p_{\mathrm{T}} > 0.5$ GeV will traverse roughly 35 drift tubes providing continuous tracking. Wires are arranged longitudinally to the beam axis in the barrel region and radially in the end caps. In total, the TRT is made of 350848 gas-filled straw tubes with a single hit resolution of 130 μm in r-ϕ. It does not have sensitivity along the z coordinate.

2.1.3 The calorimeter system

A calorimeter is a device that aims to stop and fully absorb an incident particle, and in doing so convert some fraction of its energy into a measurable signal. Calorimeters are composed of two kind of components.

- **Passive material**: where the incident particles interact. They are made of layers of dense material to absorb incident particles. As charged particles traverse the dense absorber layers, they interact and loose energy, producing secondary particle showers.
- **Active material**: that register the signal of the particles of the shower. They measure an output signal proportional to the input energy.

The calorimetry requirements of ATLAS are fulfilled by two different types of calorimeters: electromagnetic and hadronic calorimeters. The ATLAS calorimeter is composed of two subdetectors: the Liquid Argon Calorimeter (LAr) and the Tile Calorimeter (TileCal), which jointly cover the region $|\eta| < 4.9$. Whereas TileCal is fully a hadronic calorimeter, the LAr calorimeter comprises a set of detectors: the Electromagnetic LAr (EM LAr), the LAr hadronic end caps (HEC) and the LAr forward calorimeter (FCal).

The calorimeters are designed to contain as much of the resulting shower as possible in order to ensure the best measurement of a particle's total energy. The depth of the calorimeter has enough radiation lengths to avoid the occurrence of punch-through effect, particles that could escape from the calorimeter. Punch-through can compromise the performance of the surrounding muon system. An overview of the full calorimeter system of ATLAS, showing all its components, is shown in figure 2.11.

The Liquid Argon Calorimeter

The EM LAr calorimeter is a lead-liquid argon detector whose main purpose is the detection and measurement of energy deposits left by electromagnetic interacting particles, such as electrons and photons. It consists of accordion-shaped kapton electrodes and lead absorber plates. As 2.12 shows, it is divided in two main parts, the barrel region ($|\eta| < 1.475$) and the end caps ($1.375 < |\eta| < 3.2$). The barrel part is located surrounding the central solenoid, in which the ID is placed. The barrel calorimeter consists of two identical halves, separated by a small gap (4 mm) at $z = 0$, whereas each end cap calorimeter is mechanically divided into two coaxial wheels: an outer wheel covering the region

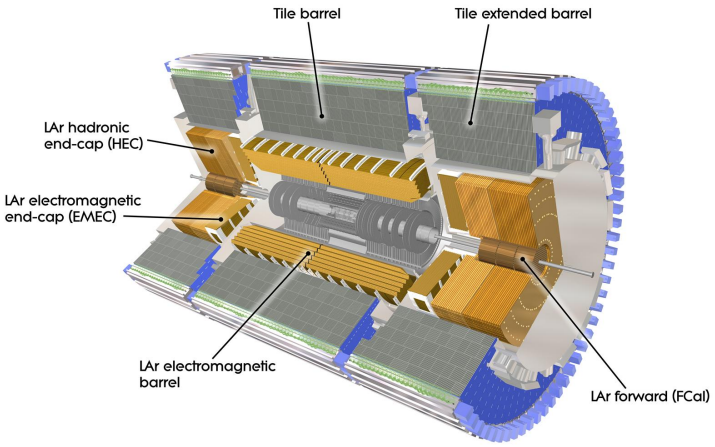

Figure 2.11: Diagram showing the Calorimeter system of the ATLAS detector. The LAr calorimeter system, the closest to the beam pipe, that includes the LAr EM part, HEC and FCal, is drawn in orange colour. TileCal is situated in the outer part of the cylinder and is drawn in blue colour [33].

$1.375 < |\eta| < 2.5$, and an inner wheel, covering the region $2.5 < |\eta| < 3.2$. Over the region devoted to precision physics (coverage of the precision ID tracking, $|\eta| < 2.5$), the EM calorimeter is segmented in three sections in depth as shown in figure 2.13(a). For the end cap inner wheel, the calorimeter is segmented in two sections in depth and has a coarser lateral granularity than for the rest of the acceptance. In the region of $|\eta| < 1.8$, a presampler detector is used to correct for the energy lost in the ID, solenoid and cryostat wall by electrons and photons upstream of the calorimeter. The presampler consists of an active LAr layer without lead, of thickness 1.1 cm in the barrel region and 0.5 cm in the end cap region. The expected energy resolution of the EM calorimeter is $\frac{\sigma_E}{E} = \frac{10\%}{\sqrt{E}} \oplus 0.7\%$.

The LAr detector includes also two hadronic end cap detectors, the Hadronic end cap Calorimeters (HEC). They consist of two independent wheels per end cap, located directly behind the end cap electromagnetic calorimeter and sharing the same cryostats. To reduce the drop in material density at the transition between the end cap and the forward calorimeter (around $|\eta| = 3.1$), the HEC extends out to $|\eta| = 3.2$, thereby overlapping with the forward calorimeter. Similarly it also overlaps with TileCal ($|\eta| < 1.7$) by extending to $|\eta| = 1.5$. HEC has an expected energy resolution of $\frac{\sigma_E}{E} = \frac{50\%}{\sqrt{E}} \oplus 3\%$ for single pions.

Finally, the Forward Calorimeter (FCal) is placed in the forward region (high η) at each side of the ID. It is placed inside the LAr end cap calorimeters, surrounding the beam pipe, as can be observed in 2.12. The FCal consists of three modules in each end cap: the first, made of copper, is optimised for electromagnetic measurements, while the other two, made of tungsten, measure predominantly the energy of hadronic interactions. Each module consists of a metal matrix, with regularly spaced longitudinal channels. The channels are filled with the electrode structure consisting of concentric rods and tubes parallel

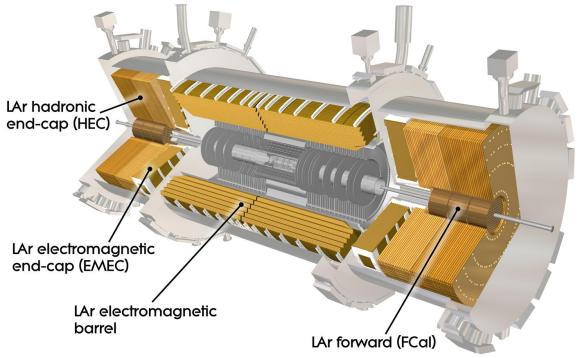

Figure 2.12: Diagram showing the structure of the ATLAS LAr system, including the Electromagnetic barrel (EM LAr) and end caps (EMEC), the LAr hadronic end caps (HEC) and the LAr Forward detector (FCal). The ID is shown in grey inside the EM LAr barrel [34].

to the beam axis. The FCal is integrated into the end cap cryostats, as this provides clear benefits in terms of uniformity of the calorimetric coverage as well as reduced radiation background levels in the muon spectrometer. The expected energy resolution for FCal is $\frac{\sigma_E}{E} = \frac{100\%}{\sqrt{E}} \oplus 10\%$ for single pions.

The Tile Calorimeter detector

The Tile Calorimeter (TileCal) is a hadronic sampling detector that uses steel as absorber and tiles of plastic scintillator as active medium. Its main purpose is the absorption of the hadronic particles produced in the collisions and the measurement of their energy.

As figure 2.11 shows, TileCal is placed surrounding the LAr system, in the region $|\eta| < 1.7$. The detector is divided in two parts: a central barrel, named *Long Barrel* (LB), which covers the region $|\eta| < 1.0$, and two Extended Barrels (EB), which cover the region $0.8 < |\eta| < 1.7$. Each barrel is a cylinder with an inner radius of 2.28 m and an outer radius of 4.25 m.

However, the TileCal is not totally hermetic, as there is a 0.6 m gap between the LB and the EB, which is needed for the ID and LAr services (figure 2.12). A stepped calorimeter structure is placed in the gap region, which tries to maximise the active material in this region while leaving enough space for cables and services. The special cells covering the region between $1.0 < |\eta| < 1.6$, are called gap scintillators ($1.0 < |\eta| < 1.2$) and crack scintillators ($1.2 < |\eta| < 1.6$).

Each partition is divided in the transverse plane in 64 wedge-shaped modules starting at $\phi = 0$, as shown in figure 2.13(b). Each of the modules is composed of a steel structure with interlaced plastic tiles of scintillator material. The light produced in the scintillators is collected at the two edges of each tile using wavelength-shifting fibbers. The fibbers are grouped together and coupled to the

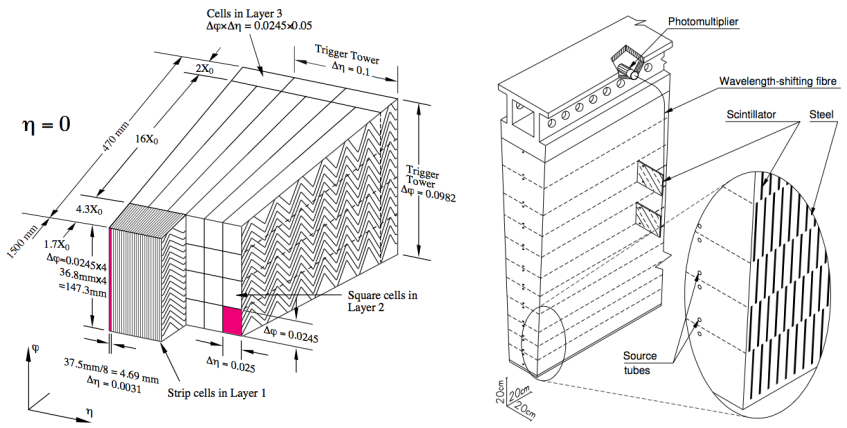

(a) (b)

Figure 2.13: The left figure is a schematic section of the EM barrel detector, displaying the granularity of the three samplings regions. The right figure is a schematic longitudinal cut of the Tile Calorimeter, showing the cell structure of the LBA and EBA partitions

read-out photomutipliers (PMTs), which are housed at the outer edge of each module. The fibber grouping is used to define a three-dimensional cell structure which has dimensions $\Delta\eta \times \Delta\phi = 0.1 \times 0.1$ in the first two layers and 0.2×0.1 in the last layer. TileCal has an expected energy resolution of $\frac{\sigma_E}{E} = \frac{50\%}{\sqrt{E}} \oplus 3\%$.

2.1.4 The Muon Spectrometer

As muons behave like minimum ionising particles, they typically deposit only a few GeV of energy in the calorimeters before escaping from them. In the other hand, muons leave tracks in the ID. The outermost layers of the ATLAS detector are dedicated to the detection, triggering and identification of muons. The Muon Spectrometer (MS), shown in figure 2.14, is composed of different types of detectors that either provide precise tracking or fast triggering. It has full coverage in ϕ and within $|\eta| < 2.7$. The central part of the MS is enclosed by the coils of three toroidal magnets, a large one for the barrel and a smaller one for each end cap, that provide an azimuthal magnetic field within the MS with a bending power that varies between 1 to 7.5 Tm, depending on the η region. The spectrometers immense size and high bending power yield a high momentum resolution. The nominal resolution of the MS standalone transverse momentum measurement is below 4% for central muons with $p_{\mathrm{T}} < 200$ GeV, increasing to 10% for muons with $p_{\mathrm{T}} = 1$ TeV.

The MS is formed by three barrel layers and six end cap disks, which are built using four different types of detectors, optimised for different purposes. Two of them provide precision muon tracking while the other two are used for triggering muon candidates.

- **MDT**: The Monitored Drift Tubes provide muon tracking in a wide η

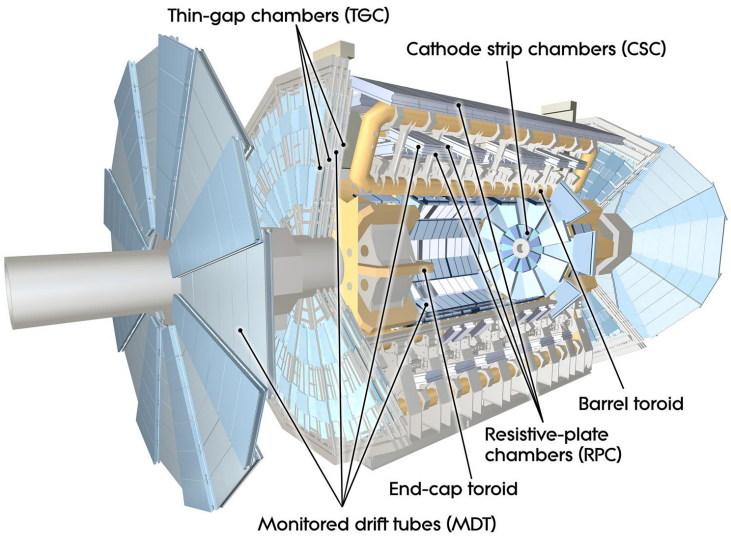

Figure 2.14: Cut away view of the ALTAS Muon Spectrometer [35].

region ($|\eta| < 2.7$). They consist of drift tubes that measure the distance of a muon track to the wire located in the centre of the tube, providing high precision measurements of the tracks in the principal bending direction of the field. In order to avoid crack regions, the individual modules are slightly overlapping. They are placed in three layers in the barrel region and in two disks in the end caps.

- **CSC**: The Cathode Strip Chambers serves as the other system for high precision muon tracking. It is situated as the innermost layer of the barrel region in front of the MDT, covering the forward region, $2 < |\eta| < 2.7$, where a higher muon flux is expected. They are multi-wire proportional chambers which provide a position resolution better than 60 μm.

- **RPC**: The Resistive Plate Chambers are gaseous detectors placed in the barrel region that provide trigger signals. They count with a time resolution of 1.5 ns. They are arranged in layers with the MDT, sandwiched in between, covering the range $|\eta| < 1.5$.

- **TGC**: The Thin Gap Chambers are multi-wire proportional chambers as the CSC, but have a smaller time resolution as they are designed for triggering purposes. They are located in the forward region, covering $1.05 < |\eta| < 2.7$.

2.1.5 The ATLAS magnet system

The ATLAS magnet system consists of the central solenoid and the toroid system. The central solenoid provides the magnetic field for the ID. The purpose of the solenoid is to bend the charged particles trajectories inside the ID such that their charge and transverse momentum can be measured form the track

curvature. It is designed to provide a 2 T magnetic field inside the ID volume: 2.5 m in diameter and 5.3 m in length.

The toroid system is composed of eight large scale air-core superconducting toroids, divided in the barrel and end cap toroids. The toroid system is placed together with the Muon Spectrometer. The barrel toroid has a total length of 25 m, with an inner bore of 9.4 m and a outer one of 20.1 m. The two end cap toroids are inserted in the barrel at each side of the detector and have a length of 5 m, with an internal (external) bore of 1.65 m (10.7 m). The toroid provides a magnetic field of 3 Tm in the barrel and 6 Tm in the end caps in average.

2.1.6 The Trigger system

At its nominal values, the LHC is able to provide a collision rate of 40 MHz. Additionally, due to the in time pile up, more than one proton-proton collision takes place every time the two beams cross, as can be seen in figure 2.3. These experimental conditions make impossible to record every single event and a online selection of the processes of interest has to be performed.

ATLAS trigger system is designed to reduce the LHC beam crossing rate rate down to an event rate that can be handled by the data acquisition system (DAQ). This large reduction is achieved with the trigger system. The trigger rejects events with no interesting physics signatures, after what the event recording rate is reduced to a few hundreds Hz. During Run-I, the ATLAS trigger system was divided into three different levels: the Level-1 and Level-2 triggers (L1 and L2 respectively) and the Event Filter (EF).

The L1 trigger is a completely hardware based trigger, integrated in the hardware of the detectors. It uses coarse information from the electromagnetic and hadronic calorimeters as well as from the Muon Spectrometer trigger chambers, reducing the event rate to 75 kHz. The processing time of the L1 trigger is 2.5 μs. Fast trigger algorithms search for high transverse momentum muons, electrons, photons, jets, and hadronically decaying tau leptons, defining regions of interest (RoIs) in the η-ϕ region around the identified physics objects. L1 can also trigger on a large imbalance in the transverse momentum or large total transverse energy.

The RoIs are then passed to the L2 trigger, a software based system that performs a partial event reconstruction of the information contained within the RoI. At this step, the full detector granularity is used. The events that pass the L2 trigger are then sent to the EF. Both L2 and EF are similar in that they both run reconstruction algorithms that are designed to be as close as possible to the final offline reconstruction. The main difference between them is that the L2 only considers RoIs provided by L1 (roughly 1-2 % of the event size), while the EF examines the full detector. The L2 is designed to to reduce the event rate to approximately 3.5 kHz, with a 40 ms latency, while the EF reduces the event rate up to 200 Hz, with an average single event processing time of four seconds.

During the LS1, the ATLAS trigger system was upgraded in order to cope with the increased detector occupancy expected for LHC Run-II. The L1 trig-

gering rules have been changed such that an output rate of 100 kHz and a 2.5 μs latency are ensured despite the more challenging conditions. This has been achieved by raising the selection thresholds and by adding hadronic or electromagnetic isolation requirements. Additionally, a L1 Topological processor has been introduced, allowing for topological selections between L1 trigger objects. The L2 and EF have been merged over a single computing farm, named High Level Trigger (HLT), for better resource sharing and overall simplification. Once HLT is passed, the event is accepted and written into data streams. For Run-II, the nominal event rate after the selection is of 1 kHz.

Being ATLAS a multipurpose detector, it is designed to record events from very different processes, whose cross-sections may vary in several orders of magnitude. To prevent the data from processes of interest with large cross-sections from completely filling the trigger bandwidth, prescales are introduced in the trigger system. Events fulfilling a determined trigger category are only written in tape with a scaled rate controlled with the prescale factors. That is, if a determined process has a prescale of 1000, only one event out of 1000 will accepted.

2.1.7 Computing System

Large amounts of data are produced every year at the LHC. Only for 2018, 50 petabytes of data are expected. These data needs to be stored, easily retrieved and analysed by physicists all over the world. This requires massive storage facilities, global networking, immense computing power, and, of course, funding. As CERN does not have the computing or financial resources to crunch all of the data on site, the Grid computing technology [36] was developed to share resources with computer centres around the world. This was the origin of the Worldwide LHC Computing Grid (WLCG) [37], a distributed computing infrastructure arranged in tiers that gives a community of over 10,000 physicists access to LHC data.

The WLCG presents a hierarchy structure of sites called Tiers (figure 2.15), which go from 0 to 3, where each Tier provides a specific set of services. Tier 0, the first layer of the WLCG, is the CERN Data Centre. All data from the LHC passes through the central CERN hub, but CERN provides less than 20% of the total computing capacity. Tier 0 is responsible for the safe-keeping of the raw data (first copy), first pass reconstruction, distribution of raw data and reconstruction output to the Tier 1s, and reprocessing of data during LHC down-times. After this first pre-processing, the data is distributed between the 13 Tier 1 sites around the world. Tier 1 are responsible of the full reconstruction of the data, and also of the safe-keeping of a proportional share of raw and reconstructed data. They also manage the distribution of data to Tier 2s and safe-keeping of a share of simulated data produced at these Tier 2s. The Tier 2s are typically universities and other scientific institutes, which can store sufficient data and provide adequate computing power for specific analysis tasks. They handle analysis requirements and proportional share of simulated event production and reconstruction. By 2018, there are around 160 Tier 2 centres around the world. Finally, the last level of the WLCG are the Tier 3 sites, local computing resources used to perform the analysis.

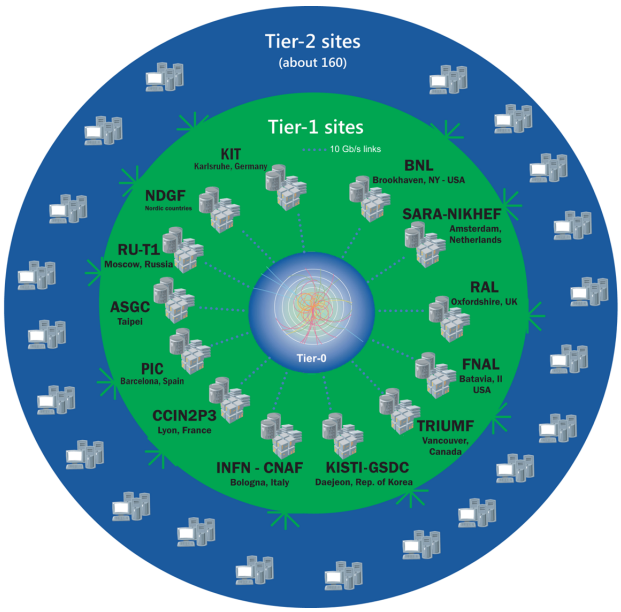

Figure 2.15: Schematic view of the WLCG hierarchy, which is distributed in different tiers [37].

2.2 Simulated samples

Monte Carlo (MC) simulated samples are extensively used in particle physics experiments, both for detector performance testing purposes and for modelling and studying the signal and backgrounds processes in physics analysis. Moreover, in physics analysis, they are used to study the detector response against different physics processes, to optimise the selection criteria and for a better understanding of the signal and the backgrounds events. The production of simulated MC samples follows three main steps: generation, detector simulation and digitisation.

- The first step is to generate the events from the matrix elements according to the theoretical calculations. Different event generators interfaced to various parton showering codes are used to produce the samples of generated events.
- The second step is to simulate the interaction of the events with the detector. In ATLAS, this step is done using GEANT4 framework for the simulation of the passage of particles through matter using MC techniques. The whole ATLAS detector has been modelled in GEANT4 and the events generated in the first step are passed through it [38]. Additionally, there is a second simulation available, called `ATLFAST-II`, that allows for a faster simulation, as the response of the electromagnetic and hadronic calorimeters is parameterised [39]. Minimum-bias events are overlaid to simulate the effects of multiple additional pp collisions in the same and nearby bunch crossings (pile-up). In order to properly include the pile-up effects in the simulated samples, the events are re-weighted by using the average

number of inelastic interactions per collision, in order to reproduce the data conditions.

- The last step in the production of MC samples consists of the digitisation, in which the output of the detector simulation is converted into raw format data, such that it can run through the ATLAS trigger system as if they were real data. All simulated events are then processed using the same reconstruction and analysis chain as for collision data.

2.3 Physic objects reconstruction at ATLAS

This section describes briefly the procedures used to reconstruct, calibrate and select the physical objects (electrons, muons, jets, b-tagged jets and missing transverse momentum) required by the generic ATLAS analysis. However, some anticipation of the criteria to identify top quark events from the t-channel is also given. Further details about the object selection and calibration can be found in [40, 41].

2.3.1 Electrons

Offline candidates are reconstructed from an isolated electromagnetic energy deposit (cluster) matched to an Inner Detector track and passing tight identification requirements [42]. Electron candidates must have a transverse momentum $p_{\mathrm{T}} > 25$ GeV and a pseudorapidity $|\eta| < 2.47$, excluding the calorimeter barrel-end cap transition regions, corresponding to $1.37 < |\eta_{\mathrm{cluster}}| < 1.52$, in which there is limited instrumentation. A longitudinal impact parameter z_0 from the primary vertex smaller than 2 mm is also required.

Possible background sources are: hadronic jets faking an electron, electrons from heavy-flavour decays and photon conversions. Since signal electrons from W boson decay are typically isolated from jet activity, these backgrounds can be suppressed via an isolation criteria which requires minimum calorimeter activity (calorimeter isolation) and only few tracks in an η-ϕ cone around the electron (track isolation). The isolation cut thresholds are chosen such that the efficiency on the reconstruction of selected electron candidates in $Z \to ee$ events is 90%.

Another category of electrons, with relaxed identification criteria and with no isolation cuts applied, is also used in the analysis for the data-driven estimate of fake and real electron selection efficiencies. This category is also used to reject dileptonic background events, for which the transverse energy threshold is lowered to 10 GeV.

2.3.2 Muons

Muon candidates are reconstructed by combining track segments found in the ID and in the MS, and must pass tight identification requirements [43, 44]. They must have a transverse momentum $p_{\mathrm{T}} > 25$ GeV and a pseudorapidity $|\eta| < 2.5$. Selected muons must additionally satisfy a series of requirements on the number

of track hits present in the various tracking subdetectors. As for the electron candidates, the longitudinal impact parameter z_0 of the muon candidates with respect to the primary vertex is required to be smaller than 2 mm. Isolation criteria are applied in order to reduce contamination from events in which a muon is produced from a hadron decay. E.g. heavy-flavour quarks that decay leptonically and result in a muon inside a jet.

The muon triggering and identification efficiencies are measured from Z boson data samples using the tag-and-probe method, and corrections factors to match the simulation to the data are extracted as a function of the pseudorapidity and azimuthal angle of the muon.

As in the case of the electron selection, a second category of muons is defined in order to estimate the fake and real selection efficiencies in the muon channel, for which no isolation cuts are applied. Non-isolated muon candidates, with a p_{T} threshold lowered to 10 GeV, are also considered for the dileptonic veto.

2.3.3 Jets

Jets are reconstructed using the anti-k_t algorithm [45] with a radius parameter of 0.4 from topological calorimeter clusters, calibrated with a local cluster weighting method which partially corrects for detector response due to the non-compensating nature of the calorimeters [46]. The jets out of the cluster have a dedicated calibration which includes the jet area pile-up suppression, and scale factors based on MC simulations which bring the measured jet p_{T} to the particle level [47].

With the anti-k_t algorithm, the recombination of pseudojets is performed around high-p_{T} pseudojets and grow concentrally around them. This create jets with conical edges, making their energy calibration easier. This algorithm has been adopted as the default one in the ATLAS collaboration.

In order to reject jets from pile-up events, low momentum jets with $p_{\mathrm{T}} < 50$ GeV and $|\eta| < 2.4$ are required to pass the so-called jet vertex fraction criterion: at least 50% of the scalar p_{T} sum of the tracks associated with the jet is required to be from tracks compatible with the primary vertex. Furthermore, a jet cleaning is applied and events which contain at least one jet with a transverse momentum greater than 10 GeV and reconstructed from noisy calorimeter cells are removed.

Jets overlapping with selected electron candidates within a cone of radius $\Delta R = 0.2$ are removed from events, as the jet and the electron are very likely to correspond to the same physics object (only the jet closest to an accepted electron is rejected). If a remaining jet with $p_{\mathrm{T}} > 25$ GeV is found close to an electron within a cone of radius $\Delta R = 0.4$, then the electron is discarded (the electron efficiency corrections are only valid for $\Delta R > 0.4$).

Finally, jets considered in this analysis should have $p_{\mathrm{T}} > 30$ GeV and $|\eta| < 4.5$. To remove some mis-modelling in the transition region between the central and forward hadronic calorimeters, the p_{T} threshold is raised to 35 GeV for the jets having a pseudorapidity $2.7 < |\eta| < 3.5$.

2.3.4 b-tagged jets

For the top quark identification analysis, it is crucial to distinguish between jets originated by a b-quark (referred to as b-tagged jets or b-jets) and all the other jets, as the top quark decays exclusively through the $t \to Wb$ process. MV1 b-tagging algorithm [48] is used to identify b-jets. This algorithm is based on a neural network exploiting the long life-time of b-quarks, that results in significant flight path lengths leading to tracks with large impact parameters and measurable secondary and tertiary vertices. The MV1 algorithm takes as input the response of three high performance taggers: IP3D, JetFitter and SV1 algorithms. The used MV1c b-tagging algorithm is a version of the MV1 algorithm that is optimised to reject c-quark induced jets, as W boson production in association with c-quarks is one of the main backgrounds of the analysis. The threshold value applied to the MV1c output (value > 0.9195) corresponds to a b-tagging efficiency of 50% measured in $t\bar{t}$ events [49]. The corresponding mis-tagging rates for the charm-quark and light-flavour jets are 3.9% and 0.07%, respectively [48].

A relaxed b-tagging requirement is used to define a validation region enriched in W+jets events (section 9.4). In that case, the efficiency of the b-tagging algorithm is raised to 80%, corresponding to a threshold value of 0.4051 in the MV1c algorithm.

The detector can only identify b-jets in the central pseudorapidity region, $|\eta| < 2.5$, the region covered by the ATLAS ID, as the tracking information is needed for the discrimination. Therefore, in the following, the forward candidate jets ($|\eta| > 2.5$), as well as the central jets not passing the b-tagging requirement, are referred to as non b-tagged jets or non b-jets.

2.3.5 Missing transverse momentum

The missing transverse momentum ($E_{\mathrm{T}}^{\mathrm{miss}}$) is defined as the momentum imbalance in the transverse plane to the beam axis, where the total initial momentum is null. The imbalance is associated to undetected particles, such as neutrinos, that leave the detector without interacting with it, but also includes energy losses due to detector inefficiencies, as the $E_{\mathrm{T}}^{\mathrm{miss}}$ is reconstructed from transverse component of the vector sum of all clusters of energy deposits in the calorimeters. The calorimeters are calibrated at the electromagnetic scale. High momentum jets, $p_{\mathrm{T}} > 20$ GeV, and electrons are further calibrated using their respective energy corrections. Contributions from the p_{T} of the muons are also taken into account [50].

Part II

ATLAS Inner Detector alignment

Chapter 3

Inner Detector Alignment

The Inner Detector (section 2.1.2) of the ATLAS experiment comprises its tracking system, used for the reconstruction of the charged particles trajectories. The accuracy of the trajectory reconstruction is determined by the intrinsic precision of the detector elements, the amount of material in the detector and the precision of the alignment of the detector elements. Misalignments of the detector modules may also lead to systematic biases in the measured trajectories and to a degraded resolution of the measured track parameters. Therefore, a precise knowledge of the position of the detector elements in the ID is crucial for an optimal performance and operation of the tracking system. This chapter presents the basis of the alignment algorithm for the ATLAS ID.

3.1 Alignment coordinate systems

Two different ATLAS coordinate systems are relevant for the alignment of the ID: the Global coordinate frame, used to describe the position of the detector modules in space, and the Local coordinate frame, which is defined for each module and is used for the reconstruction of the hits of the tracks. Figure 3.1 shows both the global coordinate frame (x, y, z), common for all ID components, and the local coordinate frame (x', y', z') of the different ID devices.

Global coordinate frame

The global coordinate frame is the right handed Cartesian reference described in section 2.1.1. The z-axis goes along the LHC beam axis, the x-axis points to the centre of the LHC ring and the y-axis points towards the sky. The data base describing the detector geometry uses this coordinate frame.

Local coordinate frame

The local coordinate frame is a local right handed Cartesian reference system that is defined for each detector module of the ID. While the origin is usually located at the geometrical centre of the module, the axes definition depends on the characteristics of each technology, varying for pixels, strips and straws detectors:

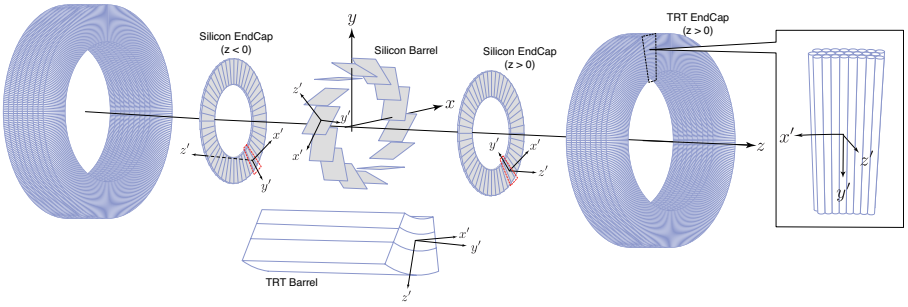

Figure 3.1: Schematic representation of the ATLAS global coordinate frame. The different local coordinate frames of silicon and TRT barrel and end cap devices are also displayed.

- For IBL and Pixel modules, the x' and y' axes are defined within the detector plane. The x'-axis is defined along the most precise measurement direction of the pixel, corresponding to the direction in which the pixel module is shorter. The y'-axis is defined perpendicular to the x'-axis, along the long size of the pixel modules. For a nominal geometry, the x'-axis is orientated along the global ϕ-axis for barrel modules, while the y'-axis is parallel to the global z-axis. The local z'-axis points out of the detector plane.
- For the SCT modules, the global frame is defined similarly to the case of the pixel modules. The x'-axis is in the module plane, perpendicular to the strip direction, which is the most precise measurement direction. In general, strip technology only provides a measurement in that direction, but as was mentioned in section 2.1.2, the SCT modules are composed of two wafers assembled back to back, with the strips orientated in slightly different directions, making the modules sensitive along the strip direction. The y'-axis is oriented along the strip direction. As for the pixels modules x' and y' axes match the global ϕ and z axes for barrel modules. The local z'-axis points out of the detector plane.
- In the TRT straws, the y'-axis points along the wire, which is the less precise measurement direction. The x'-axis is perpendicular both to the wire direction and the radial direction from the origin of the global frame to the straw centre. For barrel modules, the x'-axis is orientated along the global ϕ-axis.

3.2 Track parameters and reconstruction

The trajectory of a charged particle in a uniform magnetic field is a helical trajectory that can be parameterised using five parameters. The representation chosen in ATLAS is

$$\boldsymbol{\tau} = (d_0, z_0, \phi_0, \theta, q/p) \tag{3.1}$$

which makes use of the perigee, defined as the point of the trajectory closest

to the global z-axis. [1] The transverse and longitudinal impact parameters, d_0 and z_0, are defined as the distances from the perigee in the transverse plane and along the z-axis respectively. The angles ϕ and θ correspond with the azimuthal and polar angles at the perigee. Finally, q/p, the charge of the particle over its momentum measures the curvature of the track. Figure 3.2 shows a graphical interpretation of the track parameters at the perigee.

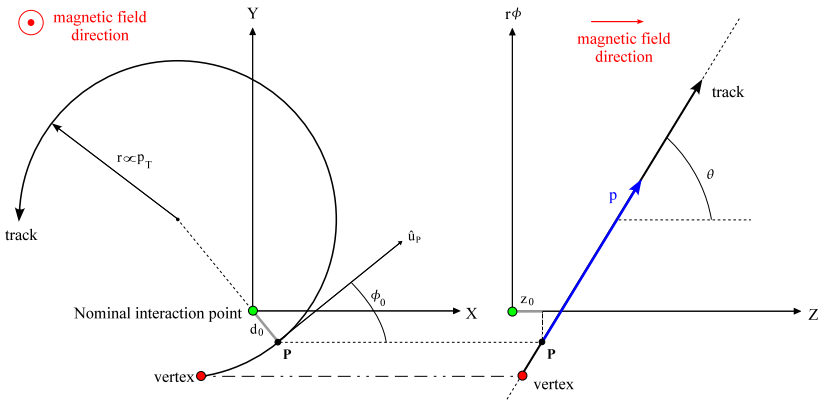

Figure 3.2: Graphical interpretation of track parameters at perigee, **P**.

Signals of the different ID modules produced by the impact of particle are referred to as hits, which are reconstructed using the local coordinate frame of each module. The IBL, Pixel, SCT and TRT hits from a specific ATLAS event are combined using different algorithms in order to reconstruct the charged particles trajectories or tracks happening in the event.

3.3 Alignment parameters

The position and orientation of a rigid body in the space can be described with 6 dof: 3 translations along the 3 axes of the global coordinate frame, defined as T_x, T_y and T_z respectively, and 3 rotations around these same axes, R_x, R_y and R_z. In the ID alignment framework, each alignable object can be aligned in these 6 dof.

3.4 Track-to-hit residuals

Within the tracking and the alignment context, a residual is the distance between a hit and the predicted intersection point of the reconstructed track with the sensor. Mathematically, it can be expressed as

$$\mathbf{r} = (\mathbf{m} - \mathbf{e}(\boldsymbol{\tau}, \mathbf{a})) \tag{3.2}$$

where $\mathbf{m}$ are the local measurements of the sensor and $\mathbf{e}(\boldsymbol{\tau}, \mathbf{a})$ the vector to the predicted track, which depends both on the track parameters $\boldsymbol{\tau}$ and on

[1] The perigee is currently defined with respect the beam spot

the detector geometry (in other words: its alignment parameters $\mathbf{a}$). For a detector which is well aligned, in which the predicted position of the track and the actual hit position are close, the residual distributions will be centred at zero. The presence of misalignments can make these distributions broader and shift their mean values.

In the alignment framework, two different kind of residuals can be defined, named as biased and unbiased residuals respectively:

- Biased track-to-hit residuals: the hit under test is used in the track fitting, so all available information is used. These residuals are employed by both the track fitting and the alignment.
- Unbiased track-to-hit residuals: the hit under test is removed from the track, which is then refitted without that hit. These residuals are used for monitoring purposes.

3.5 Track based alignment

The main goal of the alignment is to determine with a high level of precision the position and the orientation of each detector module composing the ID such that no degradation in the track parameter resolution is introduced due to a wrong description of its geometry. The actual geometry of the ID differs from the nominal one. The ID assembly itself or the operation of the ATLAS detector introduces misalignments and deformations in the ID and therefore its geometry needs to be updated over time. Since the ID had not been accessible after its installation, indirect measurements have to be performed in order to determine the proper description of the ID geometry. This can be achieved using track based algorithms.

Figure 3.3 shows a schematic description of the procedure followed to determine the ID geometry. The ATLAS alignment code is a track based alignment algorithm, which consists in the minimisation of a χ^2 function defined by the track-to-hit residuals. Two different approaches can be used in the minimisation: the Global χ^2 and Local χ^2 algorithms. These two methods are presented in detail below.

3.6 Global χ^2 algorithm

This algorithm consists in the minimisation of the χ^2 function, which is built from the track-to-hit residuals as

$$\chi^2 = \sum_t \sum_{h \in t} \left(\frac{r_{th}(\boldsymbol{\tau}, \mathbf{a})}{\sigma_{th}} \right)^2 \tag{3.3}$$

where t are the tracks used to perform the alignment, h are the hits of each track, r_{th} is the residual of the hit and σ_{th} its associated hit error. Using vector

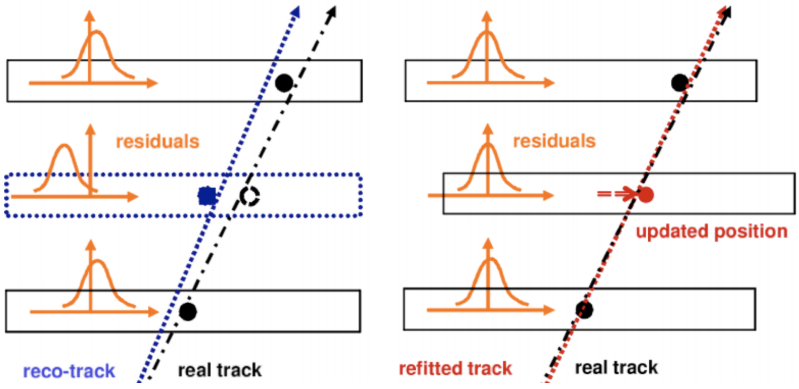

Figure 3.3: Schematic view of the alignment process. In the left figure, the layer at the centre is displaced from its nominal position. When the biased position is used in the track reconstruction, it leads to shifts of the residual distributions of all layers. With the alignment of the detector, the position of the second layer is updated to match its real position. Once aligned, all the residual distributions are well centred in zero.

notation, the previous equation can be written in a more convenient way

$$\chi^2 = \sum_t \mathbf{r}(\boldsymbol{\tau}, \mathbf{a})^T V^{-1} \mathbf{r}(\boldsymbol{\tau}, \mathbf{a}) \tag{3.4}$$

being $\mathbf{r}$ is a vector with all the residuals that the system can provide. With this notation, the hit error can be decoupled from the residual vector, and expressed with the covariance matrix V, a matrix containing the detector measurements uncertainty. Usually, V is not a diagonal matrix, as the multiple coulomb scattering introduces correlations between the accuracy of a measurement in a determined module with the hit on the previous module.

As said before, the alignment of the ID is achieved by minimising the residual distributions with respect the alignment parameters. Therefore, introducing the minimum condition in 3.4 leads to

$$\frac{d\chi^2}{d\mathbf{a}} = 0 \rightarrow \sum_t \left[\left(\frac{d\mathbf{r}}{d\mathbf{a}} \right)^T V^{-1} \mathbf{r} \right]^T + \sum_t \left[\mathbf{r}^T V^{-1} \left(\frac{d\mathbf{r}}{d\mathbf{a}} \right) \right] = 0 \tag{3.5}$$

in which $\mathbf{r}(\boldsymbol{\tau}, \mathbf{a})$ has been simplified to $\mathbf{r}$. Using the fact that V^{-1} is a symmetric matrix, after a convenient transposing, equation 3.5 can be rewritten as

$$2 \sum_t \left(\frac{d\mathbf{r}}{d\mathbf{a}} \right)^T V^{-1} \mathbf{r} = 0 \tag{3.6}$$

From equation 3.3, it can be seen that the residuals depends both on the track parameters $\boldsymbol{\tau}$ and on the alignment parameters $\mathbf{a}$. Therefore, its differential is given by

$$d\mathbf{r} = \frac{\partial \mathbf{r}}{\partial \boldsymbol{\tau}} d\boldsymbol{\tau} + \frac{\partial \mathbf{r}}{\partial \mathbf{a}} d\mathbf{a} \tag{3.7}$$

and $d\mathbf{r}/d\mathbf{a}$ can be calculated as

$$\frac{d\mathbf{r}}{d\mathbf{a}} = \frac{\partial \mathbf{r}}{\partial \boldsymbol{\tau}} \frac{d\boldsymbol{\tau}}{d\mathbf{a}} + \frac{\partial \mathbf{r}}{\partial \mathbf{a}} \frac{d\mathbf{a}}{d\mathbf{a}} = \frac{\partial \mathbf{r}}{\partial \boldsymbol{\tau}} \frac{d\boldsymbol{\tau}}{d\mathbf{a}} + \frac{\partial \mathbf{r}}{\partial \mathbf{a}} \tag{3.8}$$

The term $d\mathbf{r}/d\boldsymbol{\tau}$ can be calculated in equivalent way, but in this case it can be assumed that the alignment parameters do not depend on the track parameters ($d\mathbf{a}/d\boldsymbol{\tau} = 0$), as one would not expect that the ID geometry, which is described at a final stage by the alignment parameters, has any dependence on the tracks traversing it. Thus

$$\frac{d\mathbf{r}}{d\mathbf{a}} = \frac{\partial \mathbf{r}}{\partial \boldsymbol{\tau}} \tag{3.9}$$

Inserting the expression 3.8 in equation 3.6 leads to

$$\sum_t \left(\frac{\partial \mathbf{r}}{\partial \boldsymbol{\tau}} \frac{d\boldsymbol{\tau}}{d\mathbf{a}} + \frac{\partial \mathbf{r}}{\partial \mathbf{a}} \right)^T V^{-1} \mathbf{r} = 0 \tag{3.10}$$

From this equation, it is clear that the dependence of the track parameters with the alignment parameters, $d\boldsymbol{\tau}/d\mathbf{a}$, together with the dependence of the residuals with the track parameters, $\partial \mathbf{r}/\partial \boldsymbol{\tau}$, have to be calculated in order to solve the equation. This requires a previous step: to find the track parameters from a collection of track-to-hit residuals.

3.6.1 Track parameters fitting

The idea now is to obtain the track parameters $\boldsymbol{\tau}$ when reconstructing the tracks with a given detector geometry $\boldsymbol{a}$. In the same way that is done for the alignment constants, the track parameters that best describe a collection of hits is obtained by minimising the χ^2 function with respect the track parameters. Following the same steps described above for the derivation with respect the alignment parameters and taking into account equation 3.9, it can be seen that minimum condition can be expressed as

$$\frac{d\chi^2}{d\boldsymbol{\tau}} = \sum_t \left(\frac{\partial \mathbf{r}}{\partial \boldsymbol{\tau}} \right)^T V^{-1} \mathbf{r} = 0 \tag{3.11}$$

Using a Taylor expansion, the residuals $\mathbf{r}(\boldsymbol{\tau}, \mathbf{a})$ can be expanded around a set of initial track parameters $\boldsymbol{\tau_0}$ that are close to the solution, such that $\boldsymbol{\tau} = \boldsymbol{\tau_0} + \delta\boldsymbol{\tau}$ minimises the χ^2 function. If higher orders of the Taylor expansion are rejected, the residual are given by

$$\mathbf{r}(\boldsymbol{\tau}, \mathbf{a}) = \mathbf{r}(\boldsymbol{\tau_0}, \mathbf{a}) + \frac{\partial \mathbf{r}}{\partial \boldsymbol{\tau}}\Big|_{\boldsymbol{\tau}=\boldsymbol{\tau_0}} \delta\boldsymbol{\tau} \tag{3.12}$$

Generally, the initial set $\boldsymbol{\tau_0}$ will not be close to the solution and the final solution will be obtained by iterating until convergence is reached. Combining equations 3.12 and 3.11 and defining

$$E \equiv \frac{\partial \mathbf{r}}{\partial \boldsymbol{\tau}}\Big|_{\boldsymbol{\tau}=\boldsymbol{\tau_0}} \tag{3.13}$$

the track parameter conditions can be extracted from

$$\sum_t E^T V^{-1}[\mathbf{r}(\boldsymbol{\tau_0}, \mathbf{a}) + E\delta\boldsymbol{\tau}] = 0 \tag{3.14}$$

In order to make a more compact notation, the matrix $\mathcal{Q} \equiv E^T V^{-1} E$ and the vector $\mathbf{s} \equiv E^T V^{-1}\mathbf{r}$ can be defined, and isolating the term $\delta\boldsymbol{\tau}$ from previous equation, the corrections to the track parameters for an arbitrary track become

$$\delta\boldsymbol{\tau} = -\mathcal{Q}^{-1}\mathbf{s} \tag{3.15}$$

and the final track parameters are given by $\boldsymbol{\tau} = \boldsymbol{\tau_0} - \mathcal{Q}^{-1}\mathbf{s}$.

Now, the derivative of the track parameters with respect the alignment parameters can be finally calculated

$$\frac{d\boldsymbol{\tau}}{d\mathbf{a}} = \frac{d\boldsymbol{\tau_0}}{d\mathbf{a}} - \frac{d}{d\mathbf{a}}[(E^T V^{-1} E)^{-1} E^T V^{-1}\mathbf{r}(\boldsymbol{\tau_0}, \mathbf{a})] \tag{3.16}$$

Considering that $d\boldsymbol{\tau_0}/d\mathbf{a}$, $dV/d\mathbf{a}$ and $dE/d\mathbf{a} = \partial^2\mathbf{r}/\partial\mathbf{a}\partial\boldsymbol{\tau}$ are null or can be neglected and assuming that $d\mathbf{r}/d\mathbf{a}|_{\boldsymbol{\tau}=\boldsymbol{\tau_0}} = \partial\mathbf{r}/\partial\mathbf{a}|_{\boldsymbol{\tau}=\boldsymbol{\tau_0}}$ as $\boldsymbol{\tau}$ is a fixed value, previous equation results in

$$\frac{d\boldsymbol{\tau}}{d\mathbf{a}} = -\mathcal{Q}^{-1} E^T V^{-1} \frac{\partial\mathbf{r}}{\partial\mathbf{a}}\Big|_{\boldsymbol{\tau}=\boldsymbol{\tau_0}} \tag{3.17}$$

3.6.2 Alignment parameters fitting

At this point we can go back to equation 3.10 and introduce the $d\boldsymbol{\tau}/d\mathbf{a}$ term from equation 3.17, considering that the alignment corrections are calculated for the initial track parameters $\boldsymbol{\tau_0}$.

$$\sum_t \left[\left(I - E\mathcal{Q}^{-1}E^T V^{-1}\right)\frac{\partial\mathbf{r}}{\partial\mathbf{a}}\right]^T V^{-1}\mathbf{r} = 0 \tag{3.18}$$

being I the identity matrix. In order to make a more compact notation, the matrix $\mathcal{G} = E\mathcal{Q}^{-1}E^T V^{-1}$ is defined, and the equation above can be expressed as

$$\sum_t \left[(I - \mathcal{G})\frac{\partial\mathbf{r}}{\partial\mathbf{a}}\right]^T V^{-1}\mathbf{r} = \sum_t \left(\frac{\partial\mathbf{r}}{\partial\mathbf{a}}\right)^T \left(I - \mathcal{G}^T\right) V^{-1}\mathbf{r} = 0 \tag{3.19}$$

and a last matrix can be defined in order to compact even more the notation: $W = \left(I - \mathcal{G}^T\right) V^{-1}$, such that

$$\sum_t \left(\frac{\partial\mathbf{r}}{\partial\mathbf{a}}\right)^T W\mathbf{r} = 0 \tag{3.20}$$

Here, it is important to remark the important role that E has in the Global χ^2 method, as it introduces correlations between all the modules that participate in the reconstruction of a common track. For each track in the summatory,

the residual derivatives from different modules are calculated with respect the same track parameters, meaning that these modules will be correlated and their movements constrained. If E is null or neglected, $\mathcal{G}$ becomes null and W is directly the hit correlation matrix V^{-1}.

In order to compute the alignment corrections, the same approach that was followed for the track parameters fit (section 3.6.1) is followed: A Taylor expansion of the residuals is done around a set of initial alignment parameters, $\mathbf{a_0}$, that are supposed to be close to the minimum condition. The goal is to find the set of alignment corrections, $\delta\mathbf{a}$, such that $\mathbf{a} = \mathbf{a_0} + \delta\mathbf{a}$ minimises the χ^2 function. Only first order terms are kept and it is assumed that the residual change linearly with $\delta\mathbf{a}$. Thus

$$\mathbf{r}(\boldsymbol{\tau_0}, \mathbf{a}) = \mathbf{r}(\boldsymbol{\tau_0}, \mathbf{a_0}) + \frac{\partial \mathbf{r}}{\partial \mathbf{a}}\Big|_{\mathbf{a}=\mathbf{a_0}} \delta\mathbf{a} \tag{3.21}$$

which can be combined with equation 3.19, obtaining that

$$\sum_t \left(\frac{\partial \mathbf{r_0}}{\partial \mathbf{a}}\right)^T W \left[\mathbf{r_0} + \frac{\partial \mathbf{r_0}}{\partial \mathbf{a}}\delta\mathbf{a}\right] = 0 \tag{3.22}$$

where, in order to simplify a bit the notation, $\mathbf{r_0}$ denotes $\mathbf{r}(\boldsymbol{\tau_0}, \mathbf{a_0})$ and $\partial\mathbf{r_0}/\partial\mathbf{a}$ means $\partial\mathbf{r}/\partial\mathbf{a}|_{\mathbf{a}=\mathbf{a_0},\boldsymbol{\tau}=\boldsymbol{\tau_0}}$. The alignment corrections can be isolated from the above equation, obtaining that

$$\delta\mathbf{a} = -\left[\sum_t \left(\frac{\partial \mathbf{r_0}}{\partial \mathbf{a}}\right)^T W \left(\frac{\partial \mathbf{r_0}}{\partial \mathbf{a}}\right)\right]^{-1} \sum_t \left(\frac{\partial \mathbf{r_0}}{\partial \mathbf{a}}\right)^T W \mathbf{r_0} \tag{3.23}$$

The previous expression can be written in a more compact way by defining a new matrix, called the big matrix $\mathcal{M}$, and a new vector, the big vector $\mathbf{v}$

$$\mathcal{M} = \sum_t \left(\frac{\partial \mathbf{r_0}}{\partial \mathbf{a}}\right)^T W \left(\frac{\partial \mathbf{r_0}}{\partial \mathbf{a}}\right) = \sum_t \left(\frac{\partial \mathbf{r_0}}{\partial \mathbf{a}}\right)^T \left(I - \mathcal{G}^T\right) V^{-1} \left(\frac{\partial \mathbf{r_0}}{\partial \mathbf{a}}\right) \tag{3.24}$$

$$\mathbf{v} = \sum_t \left(\frac{\partial \mathbf{r_0}}{\partial \mathbf{a}}\right)^T W \mathbf{r_0} = \sum_t \left(\frac{\partial \mathbf{r_0}}{\partial \mathbf{a}}\right)^T \left(I - \mathcal{G}^T\right) V^{-1} \mathbf{r_0} \tag{3.25}$$

so equation 3.23 becomes simply

$$\delta\mathbf{a} = -\mathcal{M}^{-1}\mathbf{v} \tag{3.26}$$

and the new set of alignment parameters are obtained from

$$\mathbf{a} = \mathbf{a_0} - \mathcal{M}^{-1}\mathbf{v} \tag{3.27}$$

Obtaining the alignment corrections requires the filling of the big vector $\mathbf{v}$ and the big matrix $\mathcal{M}$ and the inversion of the big matrix $\mathcal{M}$. In order to fill them, it is needed first to calculate the partial derivatives of the residuals with respect the track parameters for a fixed geometry, followed by the calculation of the partial derivatives of the residual with respect the alignment parameters once the track reconstruction has been performed. As the steps of filling $\mathbf{v}$ and $\mathcal{M}$ and of inverting $\mathcal{M}$ can be done independently, the alignment procedure has been divided into two different steps in ATLAS:

- **Accumulation**: In this step, the tracks are refitted using the initial geometry, calculating the partial derivatives of the residuals with respect the track parameters first and with respect the alignment parameters after, filling both the big vector and the big matrix. Different track selections can be applied at this stage depending on the objectives of the alignment.
- **Solving**: The solving step takes care of the big matrix inversion. Once this is done, the alignment corrections are obtained with equation 3.27.

As was commented before, the approximation made in 3.21, in which it was supposed that the initial alignment parameters were already close to the correct ones is usually not true. The way to overcome this approximation is to iterate with the alignment until null corrections are obtained. Equation 3.27 can be then rewritten as

$$\mathbf{a}_{\mathrm{IterN}} = \mathbf{a}_{\mathrm{IterN}-1} - \delta\mathbf{a}_{\mathrm{IterN}-1} \tag{3.28}$$

Although it goes beyond the scope of this thesis, it can be proven [51, 52] that the $\mathcal{M}^{-1}$, the inverse matrix of the big matrix, is indeed the covariance matrix of the alignment parameter corrections, so when the big matrix is inverted, not only the alignment corrections are obtained but also their errors and correlations.

The size of the big matrix can be very big if the number of objects to align is high, making the handling, storing and inversion of the matrix quite challenging from the computational side. When only large structures of the detector are aligned, such as the whole SCT barrel and end caps or individual layers of the SCT barrel are considered for example, the Global χ^2 method is preferred, as it correctly takes into account the correlations between the different objects to align. However, for a module level alignment of the ID, the size of the big matrix is huge and its inversion is prohibitive in terms of CPU consumption. In these cases, the Local χ^2 algorithm is preferred, as it produces sparse matrices which are much easier to invert.

3.7 Local χ^2 algorithm

As commented above, the inversion of the big matrix can become prohibitive if the number of objects to align is too large. The Local χ^2 algorithm can be seen as a particular case of the global one, in which it is assumed that the track parameters do not depend on the alignment ones, or mathematically, that $d\boldsymbol{\tau}/d\mathbf{a} = 0$. Going back to the section 3.6.1, this last assumption implies that equation 3.10 simply becomes

$$\sum_t \left(\frac{\partial \mathbf{r}}{\partial \mathbf{a}}\right)^T V^{-1}\mathbf{r} = 0 \tag{3.29}$$

so all the terms proportional to E can be dropped from equation 3.18 and then W just becomes equal to the covariance matrix, V^{-1}. Equivalent big matrix and vector can be defined for the Local χ^2 case

$$\mathcal{M}' = \sum_t \left(\frac{\partial \mathbf{r_0}}{\partial \mathbf{a}}\right)^T V^{-1}\frac{\partial \mathbf{r_0}}{\partial \mathbf{a}} \tag{3.30}$$

$$\mathbf{v}' = \sum_t \left(\frac{\partial \mathbf{r_0}}{\partial \mathbf{a}} \right)^T V^{-1} \mathbf{r_0} \tag{3.31}$$

With the Local χ^2 algorithm, the produced big matrix is $N \times N$ diagonal in blocks, where N is the number of alignment degrees of freedom used for every block. This sparse matrices are much less computing resources demanding than the ones produced with the Global χ^2 method. In the other hand, as the correlation between the different structures is dropped, the convergence is slower and more iterations are needed.

3.8 Alignment levels

This section describes the different alignment degrees of freedom (dof) used in ATLAS and the alignment hierarchy followed during the alignment derivation.

The total number of individual modules of the ID is bigger than 300k, distributed between the IBL, the Pixel, the SCT and the TRT. The large number of sensitive elements makes the ID alignment a challenging task. In order to reduce the number of dof to align, the alignment framework has been organised in levels of alignment that mimic the assembly structure of the detector. Big structures as the individual barrels and end caps are aligned first. Next levels focus on the internal structure of the largest structures, as the individual disks conforming a SCT end cap. Finally, up to individual modules can be aligned with the last alignment levels. Although the alignment level definition can be as arbitrary as desired, three main levels are defined within the ATLAS ID alignment framework:

- **Level 1**: The first layer of the alignment hierarchy. It considers only as alignable objects the big ID structures. SCT and TRT barrels and end caps are treated as individual objects. Pixel barrel and end caps, unlike SCT or TRT, are mounted together in a single structure, so it is expected that they move collectively at first approximation, and therefore, the whole Pixel is aligned together. Since the IBL installation, L1 has been generalised to L11, in order to include the IBL in the alignment framework as an individual object. The reason for that is that the IBL is not attached mechanically to the Pixel but to the beam pipe.
- **Level 2**: Here, the internal substructure of each L1 object is considered in the alignment. For example, the SCT is composed of 4 barrel layers and 9 end cap disks at each side, which are all treated independently in a L2 alignment. Pixel and TRT are treated in a similar way. As the IBL is composed of a single layer, it is not treated differently at L2.
- **Level 3**: This is the last and more detailed level of alignment. On it, each individual module is aligned by its own. Due to the large number of alignable objects at L3, usually the Local χ^2 method is used at this point.

The level-hierarchy of the alignment procedure also ensures that collective movements and deformations of parts of the ID are treated correctly. Lets

consider a vertical displacement of the inner barrel layer of a detector as the one represented in figure 3.4. The residuals of tracks going parallel to the barrel displacement are not affected, while an important bias will appear on the residual of tracks going out in the perpendicular direction. If this displacement is corrected with a L3 alignment, the position of the modules around the direction of motion will not vary, while the ones at the sides will be displaced in order to remove the bias in the residuals, distorting the shape of the barrel layer. Aligning the whole barrel layer as single object (L2) ensures that its shape is maintained, and the vertical displacement is corrected. For this reason, the ID alignment has always to be done in steps of increasing complexity, starting at low levels of the alignment, and moving only to higher levels once all the collective movements have been corrected.

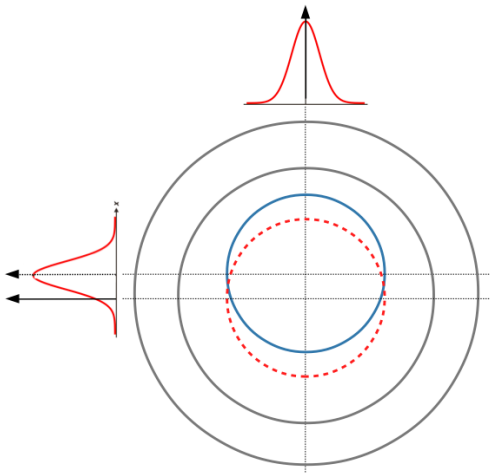

Figure 3.4: Schematic representation of how a vertical displacement of a barrel layer will reflect on the residual distributions. The real position of the inner layer is painted with a blue circle. If the detector is not aligned, it is assumed that the layer is at its nominal position (red dashed circle) for the track reconstruction, what introduces a shift of the residuals distributions in the direction transverse to the displacement.

The alignment framework is fully configurable, meaning that different levels can be assigned to different parts of the ID. For example, a L2 alignment of the IBL and Pixel can be done together with a L1 alignment of the SCT and TRT. Similarly happens with the alignment dofs, that can be configured differently for different subdetectors. One example of this is the T_z of the TRT. The TRT modules are not sensitive to translations along the beam axis. Due to that, in order to avoid the introduction of fake or misdetermined displacements of the TRT, its T_z is always excluded from the alignment.

As was commented before, as many alignment levels as wanted can be defined within the alignment framework. The ones defined in ATLAS are usually well motivated from the assembly structure of the ID. Some additional levels that are often used and are referred to in this thesis are:

- **Level 15**: The Pixel detector is built from two half shells, that are joined together to form the full Pixel cylinder. L15 is identical to the L1, but

each Pixel half shell is aligned independently.

- **Level 16**: This alignment level is similar to the L11, but each stave of the IBL is aligned on its own.
- **Level 27**: the same idea behind level 16 but extended to all the barrel layer staves of the Pixel and SCT.

3.9 Alignment weak modes

The track based alignment method is not sensitive to certain kind of movements or deformations of the ID known as weak modes, as they correspond to 'near-singular' modes of the solution to the alignment problem. Both the global and the Local χ^2 methods rely on the χ^2 function minimisation. Therefore, movements or deformations of the ID that leave the χ^2 function almost unaltered can not be detected (and thus corrected) with the only use of this kind of methods. Examples of this kind of deformations are global translations, or expansions of the whole ID. These kind of deformations maintain an helical shape of the tracks, leaving the χ^2 function value unaltered.

Although weak modes preserve the track model, they may introduce systematic biases on the track parameters that can not be determined and removed by just checking the quality of the track fit. The biases on the track parameters lead to biased physics measurements, such as the measurement of the invariant mass of the Z boson. The track parameters most affected by the weak modes are the impact parameters d_0 and z_0 and the charge over momentum q/p_{T}. Two examples of weak modes affecting the track momentum are shown in figure 3.5. Here has to be noted that such distortions of the ATLAS ID geometry can arise from real deformations of the ID or from artefacts introduced during the alignment derivation.

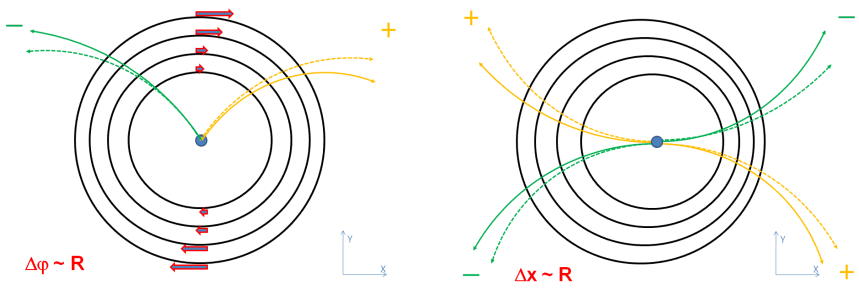

(a) (b)

Figure 3.5: Examples of basic distortions affecting the measured particle momentum. The left picture represents a curl of the detector, a charge-antisymmetric distortion, and the right picture represents a radial translation, a charge-symmetric distortion. The detector deformation as well as the impact on the reconstructed particle momenta are shown schematically. The true particle trajectories are shown as dashed lines, and the reconstructed trajectories as continuous lines [53].

The alignment framework can be extended in order to introduce further constraints in the alignment such that the weak modes can be detected and corrected. The constraints can be introduced in the alignment algorithm by to means: adding extra terms to the χ^2 function with different dependencies for the residuals or using Lagrange multipliers. For the first case, a generic new residual-like vector can be defined as $\mathbf{R}_{\boldsymbol{\tau}} = \mathbf{R}_{\boldsymbol{\tau}}(\boldsymbol{\tau})$, which only depends on the track parameters. With it, the original χ^2 function can be extended to

$$\chi^2 = \sum_t \mathbf{r}(\boldsymbol{\tau}, \mathbf{a})^T V^{-1} \mathbf{r}(\boldsymbol{\tau}, \mathbf{a}) + \sum_t \mathbf{R}_{\boldsymbol{\tau}}(\boldsymbol{\tau})^T S^{-1} \mathbf{R}_{\boldsymbol{\tau}}(\boldsymbol{\tau}) \tag{3.32}$$

where S is a matrix defining the tolerances on the track constraints. Following the same procedure used with the original χ^2 function, it can be proven [51, 52] that the alignment solutions for this equation have of the following shape:

$$\delta\mathbf{a} = -{\mathcal{M}_\tau}^{-1}(\mathbf{v}_{\boldsymbol{\tau}} + \mathbf{w}_{\boldsymbol{\tau}}) \tag{3.33}$$

being $\mathbf{w}_{\boldsymbol{\tau}}$ an additional new big vector. In previous equation, all terms depend on $F_\tau = \partial\ \mathbf{R}_{\boldsymbol{\tau}}/\partial\boldsymbol{\tau}$. Different kinds of constraints can be included in the algorithm varying the dependencies of the vector $\mathbf{R}_{\boldsymbol{\tau}}$ with $\boldsymbol{\tau}$. Some of the most commonly used constraints are presented below.

3.9.1 Track parameters constraints

The simplest case that can be defined is to consider a residual like $\mathbf{R}_{\boldsymbol{\tau}}(\boldsymbol{\tau}) = \boldsymbol{\tau} - \hat{\boldsymbol{\tau}}$, where $\boldsymbol{\tau}$ is the original value of the track parameter and $\hat{\boldsymbol{\tau}}$ is the external constraint for the track parameters. With this constrain the track parameters are forced to vary by the desired quantity, what allows for example to recover a bias in any of the track parameters.

The decay of known resonances as the muonic decay of a Z-boson can be used to derive corrections maps for d_0 and z_0. It is expected for both muons, which came from the same vertex, to share the same impact parameters, differences are due to systematic distortions of the ID geometry. Examples of $\delta d_0 = d_0^+ - d_0^-$ and $\delta z_0 = z_0^+ - z_0^-$ maps can be found in section 7.2

3.9.2 Beam spot constraint

The alignment algorithm can be extended in order to use of the beam spot position information during the alignment derivation. The idea behind is that all particles are generated in the beam spot vicinity. This specially constrains the transverse impact parameter, d_0. Since the spread of the beam spot along the beam axis is quite large, z_0 is not much constrained by the beam spot position. In order to include the beam spot information in the algorithm, the following relation between its position and the impact parameters is considered

$$d_0 = -(x_{\mathrm{BS}} + z_0\alpha_{\mathrm{BS}})\sin\phi_0 + (y_{\mathrm{BS}} - z_0\beta_{\mathrm{BS}})\cos\phi_0 \tag{3.34}$$

in which x_{BS} and y_{BS} are the beam spot global coordinates and α_{BS} and β_{BS} are the tilts of the beam spot along the global z-axis.

3.9.3 Mass resonances

The decay of well known resonances, also known as standard candles, can be exploited in order to constrain the momentum scale of the ID. Some weak modes result in a shift of the reconstructed track momentum, what bias the reconstructed mass. There are two main types of weak modes depending on how they affect particles with different charges. The first ones, called charge-symmetric distortions, affect in the same manner to positive and negative particles. By contrast, the charge-antisymmetric distortions have a different impact depending on the charge of the particle. Figure 3.5 illustrates two weak modes that introduce biases in the reconstructed track momentum. The figure of the left correspond to a curl of the detector, which is charge-asymmetric, while the one at the right represents a radial translation, which is a charge-symmetric distortion.

In order to understand the possible bias that can be introduced through weak modes in the measurement of particle transverse momentum, let's consider the simple case of a cylindrical detector of radius R, with a uniform magnetic field B along the cylinder axis. In such detector, the transverse momentum of a charged particle with charge q can be written as

$$p_{\mathrm{T}} = 0.3\ q\ B\ \rho\ =\ 0.3\ q\ B\ \left(\frac{R^2}{8s} + \frac{s}{2}\right) \tag{3.35}$$

where s is the sagitta of the trajectory. In many cases, for medium and large p_{T}, the sagitta is much smaller than the detector radius (R), so the above expression becomes simply

$$p_{\mathrm{T}} = 0.3\ q\ B\ \frac{R^2}{8s} \tag{3.36}$$

At this point, it can be seen that the p_{T} measurement can be biased through three different sources: the magnetic field B, the radius of the detector R, and the sagitta of the trajectory, s. Weak modes concerning a wrong description of the magnetic field where studied and measured in ATLAS during Run-I [53] and will not be further discussed here. The other two distortions are known as radial and sagitta distortions.

Considering the case of the decay of a boson into two muons, the mass of the boson is

$$m^2_{\mu\mu} = 2p_1p_2(1 - \cos\Delta\phi) \tag{3.37}$$

being p_1 and p_2 the total momentum of each muon and $\Delta\phi$ the opening angle between them. As the effects on the track parameters of both kind of weak modes is different, they are discussed separately.

Radial distortions: the most generic radial distortion is the one in which all points of a trajectory gets expanded/contracted proportionally to their radial location ($\Delta R \propto r$) as it is represented in figure 3.6.

The radial distortion biases the reconstructed transverse and longitudinal momenta, as well as the reconstructed $\cot\theta$, such that

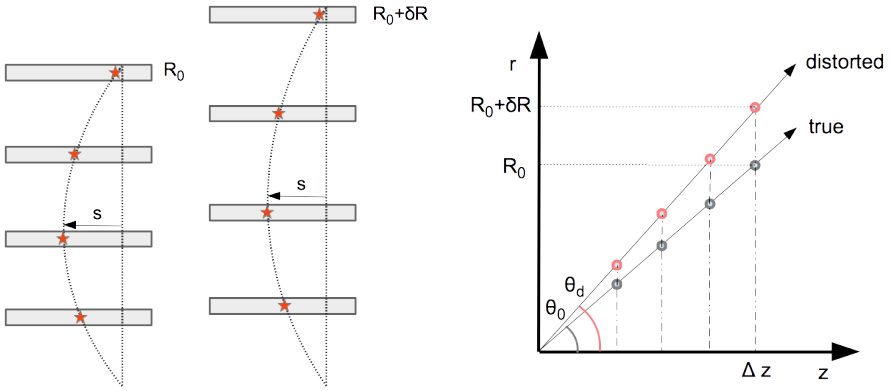

(a) (b)

Figure 3.6: Schematic representation of how the radial distortion leaves invariant the sagitta of the track, left, while modifying the $\cot\theta$ of the track, right. In the left figure, the reconstructed points are located at different radii, but at the same transverse distance than the true ones. In the right diagram, true points are given in grey, while the reconstructed points with the distorted geometry are shown in red. In this model, the z coordinate of the points is preserved and the r coordinate is changed proportionally to the true radius.

$$\begin{aligned} p_{\mathrm{T}} &\to p_{\mathrm{T}}(1+2\epsilon) \\ p_z &\to p_z(1+\epsilon) \\ \cot\theta &\to \cot\theta(1+\epsilon)^{-1} \end{aligned} \tag{3.38}$$

where $\epsilon = \delta R/R_0$ is the magnitude of the radial distortion.

Introducing previous results in equation 3.37, the relationship between the reconstructed mass $\tilde{m}_{\mu\mu}$ and the true mass $m_{\mu\mu}$ can be obtained

$$m^2_{\mu\mu} = \tilde{m}^2_{\mu\mu} + 2A\ \epsilon(\eta^+,\phi^+) + 2B\ \epsilon(\eta^-,\phi^-) \tag{3.39}$$

being

$$\begin{aligned} A &= \left[\tilde{\mathbf{p}}^+\tilde{\mathbf{p}}^- + \tilde{\mathbf{p}}^+_{\mathbf{T}}\tilde{\mathbf{p}}^-_{\mathbf{T}} - \tilde{E}^-/\tilde{E}^+\left((\tilde{E}^+)^2 + (\tilde{p}^+_T)^2\right)\right] \\ B &= \left[\tilde{\mathbf{p}}^+\tilde{\mathbf{p}}^- + \tilde{\mathbf{p}}^+_{\mathbf{T}}\tilde{\mathbf{p}}^-_{\mathbf{T}} - \tilde{E}^+/\tilde{E}^-\left((\tilde{E}^-)^2 + (\tilde{p}^-_T)^2\right)\right] \end{aligned} \tag{3.40}$$

where $\tilde{\mathbf{p}}$ and $\tilde{E}$ are the momentum and energy of the muons reconstructed with the distorted geometry,and the $+$ and $-$ superscripts refer to the positively- and negatively-charged muons.

The true mass $m_{\mu\mu}$ can be either be determined from a MC simulation or either be taken as the last published Particle Data Group [54]. The effect of using one or the other has already been evaluated, and it can be neglected.

The radial distortion coefficients $\epsilon(\eta,\phi)$ are computed following an iterative procedure. The momentum of each muon is left uncorrected in the first iteration, and corrected with the current values of $\epsilon(\eta,\phi)$ in the following iterations. The reconstructed invariant mass distribution, computed with the corrected muon

momenta, is binned corresponding to the (η, ϕ) values of each lepton, and the value of $\tilde{m}^2_{\mu\mu}$ in each bin is estimated with a Gaussian fit to the peak of the invariant mass spectrum. The differences between $\tilde{m}^2_{\mu\mu}$ and $m^2_{\mu\mu}$ are used to compute the $\epsilon(\eta, \phi)$ coefficients of the two muons according to equation 3.39. Unfortunately, there is an ambiguity, as it is not possible a priory to determine which of the two muons is biased. A way out of this issue is through an iterative procedure in which half of the correction is applied to each muon. The procedure starts with the assumption of null ϵ for each muons and keeps iterating until the convergence of the ϵ values.

The presence of radial distortions in the ATLAS ID has been measured recently using the decay into two muons of various bosons: Z, J/ψ and Υ. The full study can be found in [55]. Figure 3.7 shows the main result of the study: the presence of a radial distortion of the ID with $\epsilon = \delta R/R_0 \sim$ -0.05%.

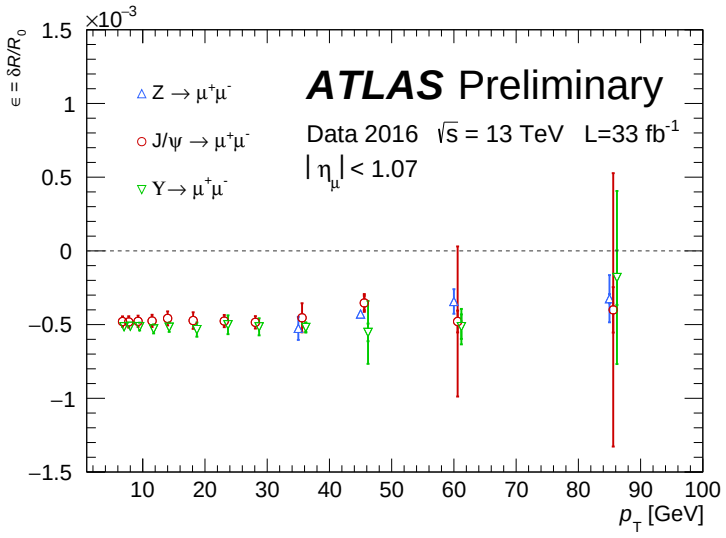

Figure 3.7: Results of the measurement of the radial distortion coefficient $\epsilon = \delta R/R_0$ as a function of the track p_{T} for 2016 data. The vertical bars represent the quadratic sum of statistical and systematic uncertainties [55].

Sagitta distortions: For cylindrical shape trackers, this distortion can be induced by a rotation of the layers or curl as shown in figure 3.8. They alter the track curvature in a asymmetric way, such that

$$q/p_{\mathrm{T}} \rightarrow q/p_{\mathrm{T}}(1 + q p_{\mathrm{T}} \delta_{\mathrm{sagitta}}) \tag{3.41}$$

meaning that the reconstructed mass of the boson in a detector with a sagitta distortion is

$$\tilde{m}^2_{\mu\mu} = m^2_{\mu\mu}[1 - (p_1 q_1 \delta_{\mathrm{sagitta},1} + p_2 q_2 \delta_{\mathrm{sagitta},2})] \tag{3.42}$$

where $\tilde{m}^2_{\mu\mu}$ denotes the reconstructed mass and $m^2_{\mu\mu}$ its true value. From this last equation, the values of $\delta_{\mathrm{sagitta}}$ of each muon can be estimated. Unfortunately, there is an ambiguity, as it is not possible a priory to determine which of the two muons is biased. A way out of this issue is through an iterative procedure in which half of the correction is applied to each muon. The procedure

starts with the assumption of null δ_{sagitta} for each muons and keeps iterating until convergence is reached.

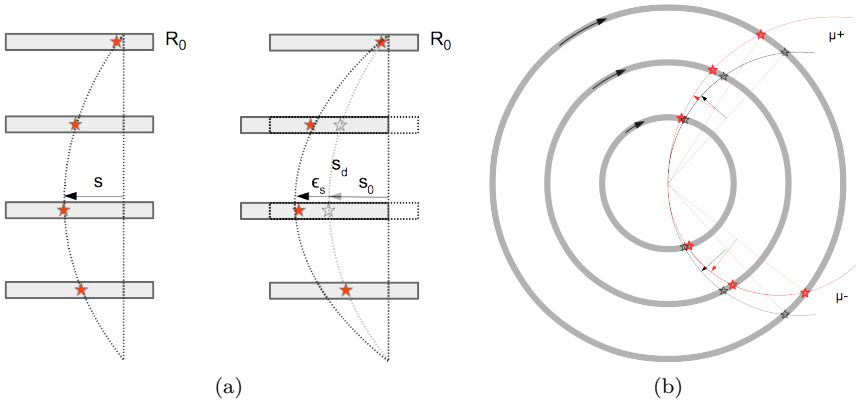

(a) (b)

Figure 3.8: Schematic representation of how a relative shift of the detector layers affects the sagitta of the track. In the left figure, the simple case of shifting two layers in the plane transverse to the direction of the track illustrates how sagitta is biased, while leaving the track radii unaltered. In the right diagram, a more realistic curl distortion of a cylindrical detector is shown. The bias is such that for the μ^+ the apparent (distorted) sagitta is smaller than the true one, thus the reconstructed$\tilde{p}_T$ is larger than the real one ($\tilde{p}_T > p_{\text{T}}$). For the μ^-, the effect is just the contrary. For both diagrams, true points are given in grey, while the reconstructed points with the distorted geometry are shown in red.

Just as for the radial distortion case, the δ_{sagitta} corrections are derived through an iterative process in order to overcome the ambiguity of the correction assignment. As the distortions vary depending on the detector region, they are derived in the form of $\delta_{\text{sagitta}}(\eta, \phi)$ maps. An example of a δ_{sagitta} map obtained with 2017 data of the decay of Z bosons can be seen in section 7.2.

3.9.4 E/p method

Another method that can be used for the detection and correction of bias in the momentum scale of the ID is the so called E/p method, in which the energy E measured by the electromagnetic calorimeter is compared to the total momentum measured for electrons coming from the decay of a Z boson. As the mass of such an electron is negligible with respect to its total momentum, the approximation $E \sim p$ is in general a good one. An advantage of the E/p method with respect mass resonance one is that there is no ambiguity when assigning the correction to each of the electrons, as they are calculated independently.

Additionally, the response of the calorimeter is independent of the charge, meaning that the same measurement is given for e^- and e^+ of equal energy. In the other hand, the reconstructed trajectory can be charged dependent, as explained before. Therefore, cases in which $(E/p)^- \neq /E/p)^+$, are due to the presence of ID weak modes.

Despite of that, this method does not provides corrections for d_0 and z_0 and therefore, it is used as crosscheck of the maps derived with the $Z \to \mu^+\mu^-$

method. Also, the electron tracking is more complicated than the muon tracking, as they interact more with the material of the detector.

3.10 Soft mode cuts

All the alignment constraints explained above are included through the introduction in the χ^2 function of a residual-like vector $\mathbf{R}_{\boldsymbol{\tau}}$ that depends on the track parameters. Similarly, constraints in the alignment parameters can be included by adding an extra residual vector, $\mathbf{R}'_{\mathbf{a}} = \mathbf{R}'_{\mathbf{a}}(\mathbf{a})$, which depends only on the alignment parameters this time. Another peculiarity is that this term is only evaluated once per data sample, and not for every track

$$\chi^2 = \sum_t \mathbf{r}(\boldsymbol{\tau}, \mathbf{a})^T V^{-1} \mathbf{r}(\boldsymbol{\tau}, \mathbf{a}) + \mathbf{R}'_{\mathbf{a}}(\mathbf{a})^T G^{-1} \mathbf{R}'_{\mathbf{a}}(\mathbf{a}) \tag{3.43}$$

where G is a generic covariance matrix. Although $\mathbf{R}'_{\mathbf{a}}$ and G can be as generic as desired, we are interested here in the particular case in which the residuals are $\mathbf{R}'_{\mathbf{a}} = \mathbf{a} - \mathbf{a_0}$ and the covariance matrix is $G^{-1} = 1/\sigma^2$, where $\mathbf{a_0}$ are the initial set of alignment parameters and σ represents the allowed tolerances on the alignment parameter corrections. With this choice, the added constrains represent penalty terms, also known as soft mode cuts, which are very useful as they can be used to avoid large alignment corrections. With the specific choice mentioned above, it can be shown [51, 52] that the alignment solutions minimising equation 3.43 is the same one than the unconstrained one (equation 3.27) but with the addition of an additional diagonal matrix to $\mathcal{M}$

$$\mathbf{a} = \mathbf{a_0} - (\mathcal{M} + G^{-1})^{-1} \mathbf{v} \tag{3.44}$$

During a L3 alignment, it can occur that, due to large correction uncertainties, large corrections are obtained for some modules with low statistics. The covariance matrix $G^{-1} = 1/\sigma^2$ sets a maximum size for the alignment corrections through the individual constraints σ, which can be defined specifically for different modules and dofs.

3.11 Error scaling

As can be seen in equation 3.3, the χ^2 function depends on the uncertainties of the detector measurements. Each detector hit has a finite intrinsic resolution and particles traversing the ID suffer from multiple scattering. All this makes that, even for a perfectly aligned detector, the residual distributions of each detector follow a Gaussian distribution of a certain width. For an ID in which both the ID geometry and ID material structure are well modelled, the pull of the track-to-hit residuals should follow a normal distribution of null mean and width equal to 1.

However, the ID residual pull distributions often do not follow the exact closure. In order to recover the closure, the detector measurement uncertainty

entering in equation 3.3 is not directly the intrinsic resolution of each hit, σ_{int}, but a scaled uncertainty given by

$$\sigma'^2 = (a\sigma_{\text{int}})^2 + c^2 \tag{3.45}$$

where the terms a and c transform σ_{int} to a scaled resolution σ'. Although in principle, the term a is enough to perform the scaling, it is usually reserved as the correction of the intrinsic position resolution, while c is used to take into account anything else, including unaccounted misalignment. For cases in which the pull width is smaller than 1, only the term a can be used to recover the perfect closure.

Chapter 4

Pixel vertical displacement

This chapter presents the studies performed with Run-I data relative to the observed beam spot vertical displacement at the beginning of the data taking that led to the finding of the Pixel vertical movements. During Run-II an additional slower but longer drift of the Pixel has been detected. The alignment framework has been upgraded, minimising the impact of the drift on the data quality.

4.1 Beam spot vertical displacement

During the LHC Run-I, a pronounced drop in the vertical position of the beam spot of about 10 μm was observed typically during the first hour of a run [56]. Examples of this behaviour can be seen in figure 4.1, where the evolution over time of the horizontal and vertical positions of the beam spot are shown for three different LHC fills. A clear drop of the vertical position (y_{BS}) at the beginning of each run is seen while the horizontal position (x_{BS}) does not show any pronounced changes during the data taking period. The plots corresponding to the longitudinal (along the beam axis) position of the beam spot (z_{BS}) are not shown, but as in x_{BS} case, no relevant displacements are usually seen.

Of particular interest was LHC fill number 3032 (ATLAS run 209812) to understand the effect. The two bottom plots of figure 4.1 show the horizontal (left) and vertical (right) beam spot position evolution during this fill. LHC first declared stable beams around 16:00 CET, but two hours later, it had to adjust the beam, dropping the stable beams flag. Stable beams operations were resumed again about 15 minutes after, around 18:30 CET. For safety reasons, the Pixel and SCT detectors are set into standby mode whenever LHC stable beams flag is down. Once the stable beams returned, both detectors where brought back from standby and, as can clearly be seen in figure 4.1, a second drop of the beam spot vertical position y_{BS} was observed. As usual the horizontal x_{BS} and longitudinal z_{BS} (not shown) positions do not show any particular displacement during the same periods.

Although it was already quite improbable, the presence of a second beam

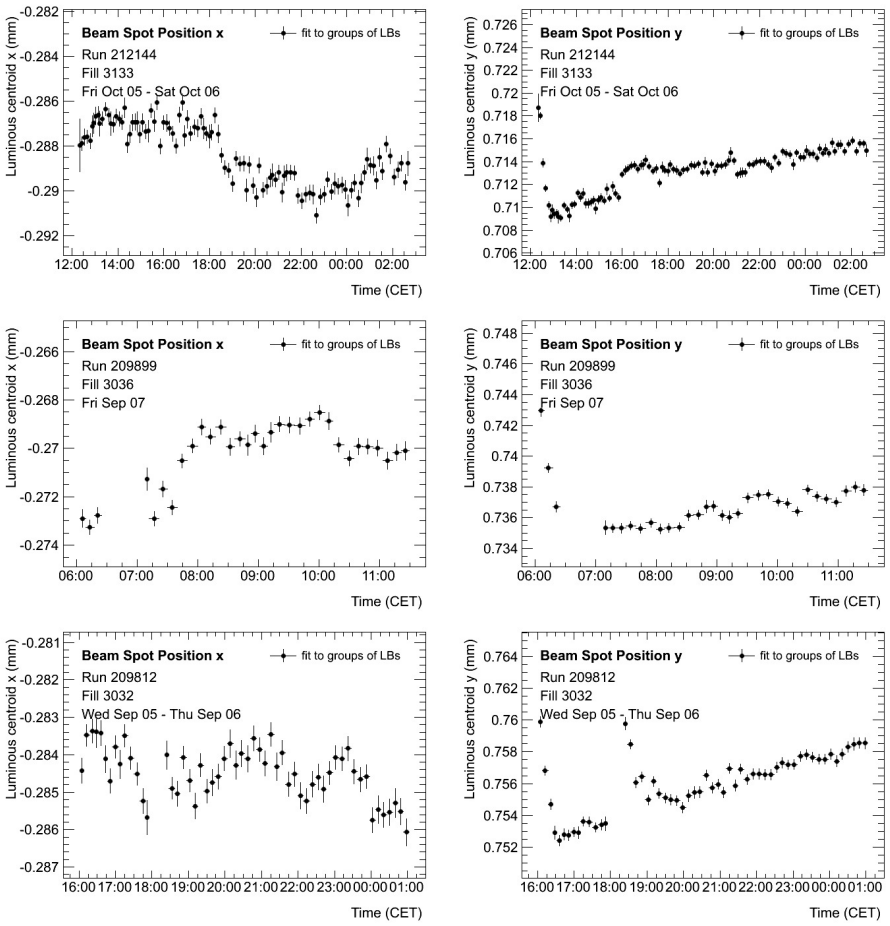

Figure 4.1: Evolution of the horizontal (left) and vertical (right) position of the beam spot during three different fills of the LHC during 2012 from top to bottom. In all cases a pronounced drop in the vertical position of the beam spot is observed at the beginning of the run, while a much more stable behaviour is seen in the horizontal axis. During fill 3032 (the two bottom plots) the beam were adjusted for 15 minutes in the middle of the run, and a second drop is seen when stable beams operations resumed [56].

spot drop in the same fill discarded the LHC beams themselves as the cause of a genuine beam spot movement at the beginning of the collisions and it pointed to the ATLAS ID as the origin of the measured beam spot displacements.

4.2 Alignment studies

During LHC Run-I, the ATLAS ID alignment was monitored with the calibration loop alignment (section 6.1). The alignment corrections used in the reconstruction were assumed to be constant over time, and only if large displacements were observed for a new run in the alignment monitoring, the baseline alignment was updated in order to correct for the measured misalignments. Therefore, fixed set of alignment constants were used over large periods of time, including several ATLAS runs, as a good stability of the ID was seen. This can be seen in figure 4.2, where the translations along the ATLAS $\hat{x}$-axis of the ID subdetectors during the whole 2012 data taking campaign are shown. The shown corrections are relative to the Pixel detector, which is used as a reference to derive the alignment. SCT and TRT barrels and end caps are aligned at L1.

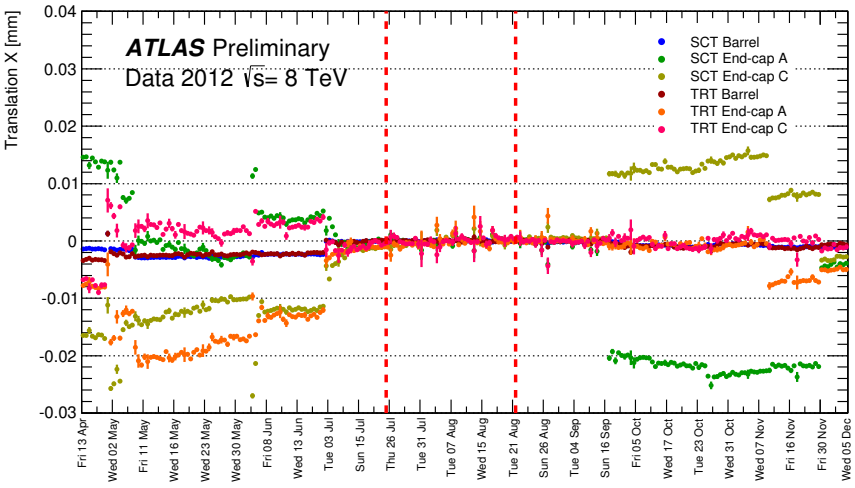

Figure 4.2: The corrections to the global X position (T_x) of all ID sub-detectors with respect to the Pixel detector during 2012. Errors shown are statistical uncertainties on determined alignment parameter [57].

Long stable periods can be seen along the year, in which the geometry does not change from run to run. Only *seismic events* as cooling system power cuts or shutdowns of the toroid magnet seemed to cause a change in the the detector geometry. There was no reason therefore to suspect for movements of the ID within a run. Once the alignment team was aware of the suspicious vertical displacement of the beam spot at the beginning of each run, first studies were performed to determine if it was a genuine beam displacement, or alternatively, if it were reflecting a time dependent movement of the ID. For the beam spot determination, the ID was assumed to have an stable geometry, meaning that the presence of ID movements would translate into displacement of the beam

spot position. It has to be noted that all these studies were performed during May 2014, two years after the end of LHC Run-I.

Due to the peculiarities of LHC fill 3032 (ATLAS run 209812), in which the beam spot drop was seen twice, it was selected to perform time-dependent alignment studies. The run was divided into groups of 10 lumiblocks (LB) each performing an individual alignment for each group. Each group corresponds to a time window of 10 minutes approximately. This configuration was chosen as it resulted in a good compromise between the accumulated statistics and a proper time-tracking of the possible detector movements.

In the first performed study, the first hour of run 209812 was analysed, performing a time-dependent alignment of the SCT and the TRT with respect the Pixel detector. Results of this study would reveal if there were any time dependency in the obtained corrections. Results are shown in figure 4.3, where the translations T_x and T_y for the barrels of the SCT and TRT are shown as a function of the time. While T_x corrections are stable on time within the statistical uncertainties, a clear dependence with time is seen for the T_y corrections of both detectors, although it is more significant in the case of the SCT due to smaller statistical uncertainties. Corrections are relative to the Pixel position.

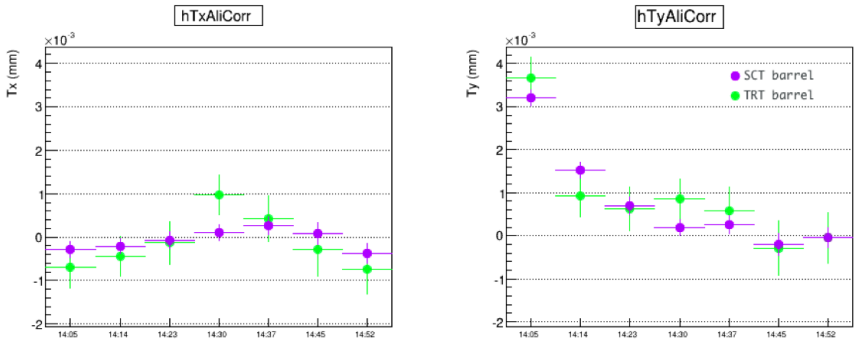

Figure 4.3: T_x and T_y alignment corrections for SCT and TRT barrels with respect the Pixel as a function of time during the first hour of data taking of run 209812. While T_x corrections are compatible with zero (within the statistics) during the whole period, a clear drop in T_y over time can be seen for the SCT barrel. TRT T_y follows the same trend but is statistically less significant.

The fact that SCT and TRT barrels show a coherent movement during the run indicates that it is the Pixel detector what is moving instead. In addition, as the Pixel detector is closer to the ATLAS interaction point, a displacement thereof would have a bigger impact in the beam spot position than a similar displacement of the SCT and the TRT. For these reasons, the alignment strategy was changed for the rest of studies, fixing the SCT barrel as a reference and letting the Pixel to move and rotate along the three ATLAS axis. Additionally, the Pixel detector is constructed in two half-shells, so each half was aligned independently in order to test if they moved together or not. Results of this test are shown in figure 4.4(a), together with the corrections of the SCT with respect the Pixel obtained in previous test. As expected, opposite signed corrections were obtained when the reference is the SCT instead of the Pixel. The results

also imply that both half-shells move coherently. A more detailed alignment has also been performed, allowing each layer of the Pixel barrel and each disk of the Pixel end cap to move independently, what corresponds to a L2 alignment of the Pixel. From the results of this study, shown in figure 4.4(b), it can be concluded that within the available statistics, the whole Pixel detector moves as a single object, without relative movements between layers or disks.

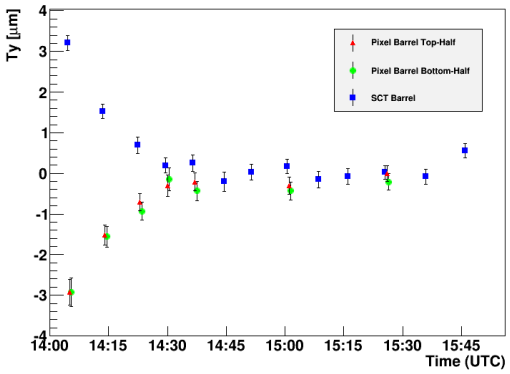

(a)

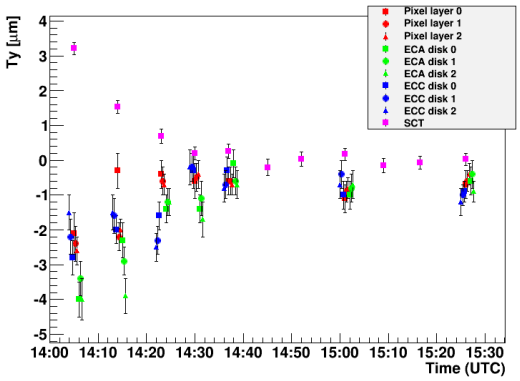

(b)

Figure 4.4: T_y alignment corrections evolution over time for (a) each of the Pixel half-shells (L15) and (b) each of the Pixel barrel layers and end cap disks (L2) with respect to the SCT, which is fixed as a reference. The SCT barrel T_y alignment corrections with respect to the Pixel are also shown in both plots for comparison. The opposite sign between SCT and Pixel corrections is expected as both detectors switch roles as the fixed reference detector. The first two hours of run 209812 data has been used in the plot.

In the following, for an easier comparison between the beam spot dropping and the Pixel lifting, results will be shown as a function of $\Delta T_y = T_y^i - T_y^0$ where T_y^0 is the lumiblock group with the smaller correction and T_y^i are each of the corrections. Figure 4.5 show the evolution of ΔT_y for the Pixel detector together with the change in the vertical position of the beam spot, as a function of the time. Here, the study was extended for all the length of run 209812 in

order to check if the second drop in the beam spot position was also detected by the alignment. It can be seen that the Pixel vertical displacements match both beam spot drops, but after the initial displacements, the Pixel detector remains stable with respect the rest of the ID, while the beam spot steady rises during the run. This last and slower component has nothing to do with relative displacements of the ID.

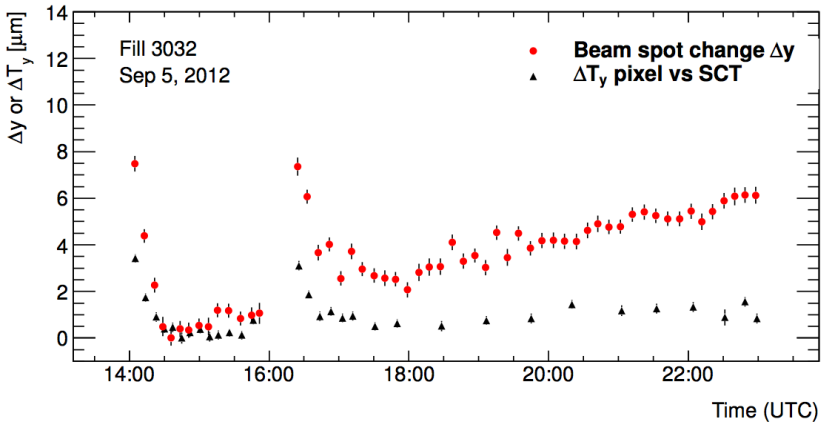

Figure 4.5: Comparison of the change of the vertical position of the beam spot $\Delta y = y_{\mathrm{BS}} - min(y_{\mathrm{BS}})$ with the change in the vertical alignment correction of the Pixel ΔT_y for ATLAS run 209812 (LHC fill 3032). As both are normalised quantities, the amplitude of the movements can be directly compared.

Another conclusion that can be extracted from figure 4.5 is that the drop of the beam spot is bigger in magnitude than the lifting of the Pixel detector: while beam spot drops around 8 μm, the Pixel detector only moves around 4 μm. This magnification in principle could be explained due to a level arm effect, although a naive expectation from the radii of the detector layers gives a magnification factor between 1.1 and 1.65, not enough to cover the observed factor of $\sim$2. In order to determine more precisely the magnification factor, two different approaches were used.

The first one consists in a basic toy MC, in which the barrel layers of Pixel and SCT have been placed at their nominal radii, and a relative translation between the Pixel and the SCT has been introduced. Figure 4.6(a) shows the configuration of the toy MC. By a linear fit to the positions of the layers, the extrapolated position of the beam spot can be extracted. The intrinsic resolutions of the Pixel and SCT modules has been used as error for the layers. For a vertical displacement of 20 μm, the extrapolated position of the beam spot is $24 \pm 11 \mu$m, meaning that the magnification factor is 1.2 ± 0.5.

A more precise estimation has been done by aligning a MC sample in which the Pixel vertical position has been displaced. Here again, a 20 μm displacement is introduced. The beam spot vertical and horizontal positions can be determined from the transverse impact parameter d_0 and the azimuthal angle ϕ, as they are related through

$$d_0 = -x_{\mathrm{BS}} \sin\phi + y_{\mathrm{BS}} \cos\phi \quad . \tag{4.1}$$

Using the tracks from the MC sample with the distorted geometry, the mean impact parameter has been plotted as a function of the azimuthal angle, and the beam spot horizontal and vertical positions have been extracted from a fit. Results of this test are shown in figure 4.6(b). While a null value is obtained for the horizontal position ($x_{\mathrm{BS}} = 0.06 \pm 0.10$ μm) the vertical one is $y_{\mathrm{BS}} = 22.7 \pm 0.1$ μm, clearly far away from zero. For the same sample, the obtained alignment vertical correction is $T_y = 19.16 \pm 0.13$ μm. The magnification factor is just the ratio of both, obtaining a value of 1.185 ± 0.013. The obtained value is compatible with the previous estimation, but not with the observed ratio in real data, for which a value close to 2 is observed. This could point to the presence of an additional global movement of the whole ID. A movement of this kind could also explain the steady rise of the beam spot position seen in figure 4.5, but this hypothesis cannot be verified from alignment studies, as the method is only sensitive to relative movements within the ID.

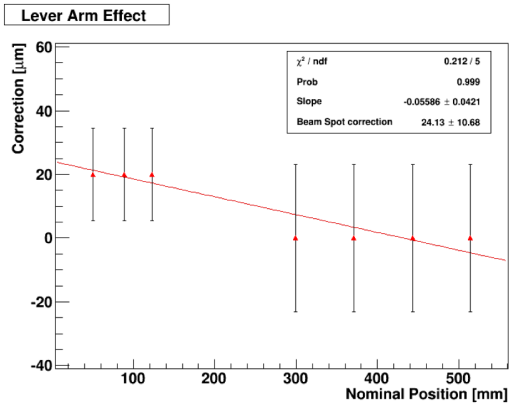

(a)

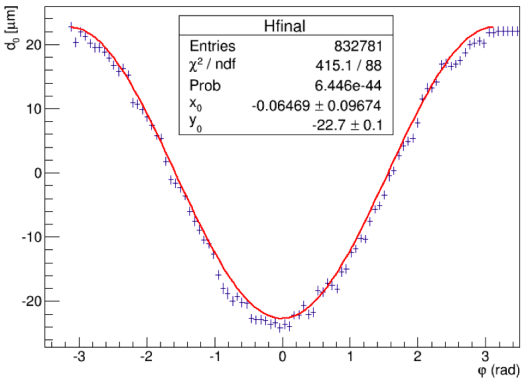

(b)

Figure 4.6: Estimation of the level arm effect between the Pixel and beam spot displacements from two methods. The first one (a) uses a toy MC that places the Pixel and SCT layers at their nominal radii and includes a relative transverse displacement between both detectors. The beam spot position is extracted from a linear fit. The second method (b) exploits equation 4.1 and a MC sample with a distorted geometry in order to extract the beam spot position.

In order to test the hypothesis in which it is the SCT and not the Pixel what moves, same test was repeated with a MC sample in which the SCT was displaced 20 μm vertically. In this case, the obtained magnification factor is -0.182 ± 0.007. This result supports the hypothesis of a movement of the Pixel against a movement of the SCT and TRT, as the lever arm effect between between the SCT and the beam spot is not only smaller but negative, meaning that the beam spot would displace in opposite direction to the SCT.

Although the reasons behind the Pixel detector movements at the start of a run are not understood in detail, it has been suggested that it could be caused by a change in the cooling liquid mass between the standby and ready modes of the Pixel detector. The evaporative cooling system of the Pixel detector uses a gas heater in the exhaust line that heats non-evaporated C_3F_8 cooling liquid plus gas to a constant temperature of 20 °C. When the detector is fully turned on, the total power dissipation increases, more C_3F_8 evaporates inside the detector, and therefore the gas heater power drops as can be seen in figure 4.7. Because the Pixel detector volume heats up gradually, the decrease in gas heater power is not instantaneous but has a time constant of about 30 to 40 min. Figure 4.7 shows the comparison between the evolution of the Pixel gas heater power and the evolution of the vertical position of the Pixel detector through the whole run. A strong correlation is clearly seen between both quantities.

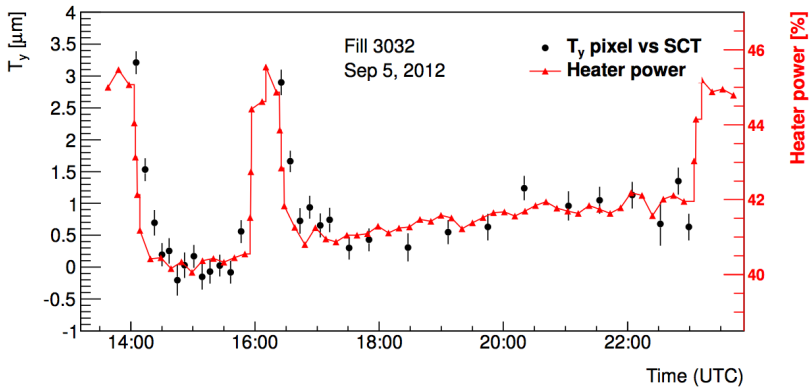

Figure 4.7: Comparison of the Pixel gas heater power with the vertical alignment corrections T_y from time dependent L1 alignment of the Pixel detector with respect the SCT during ATLAS run 209812 (LHC fill 3032). The very high correlation of the two quantities over the full course of the fill is evident.

4.3 Pixel movements on Run-II

The studies performed with Run-I data showed that the Pixel detector moves vertically during the first minutes of data taking, but during the rest of the run remains stable at the level of a micron. This behaviour was confirmed during 2015, the first year of LHC Run-II. Figure 4.8 shows the evolution of the horizontal and vertical alignment corrections of the IBL, Pixel and TRT barrel detectors during ATLAS run 284285, one of the longest runs recorded

in 2015. All subdetectors are aligned with respect the SCT barrel, which has been used as reference for the alignment derivation since 2015. It can be seen that while the Pixel detector is quite stable in the horizontal axis (T_x), it suffers a fast displacement of the order of 5 μm when the detector starts collecting data for a given run. A slower displacement in the opposite direction to the initial displacement of the Pixel detector is seen during the rest of the run. The magnitude of this second displacement is smaller, at the micron level.

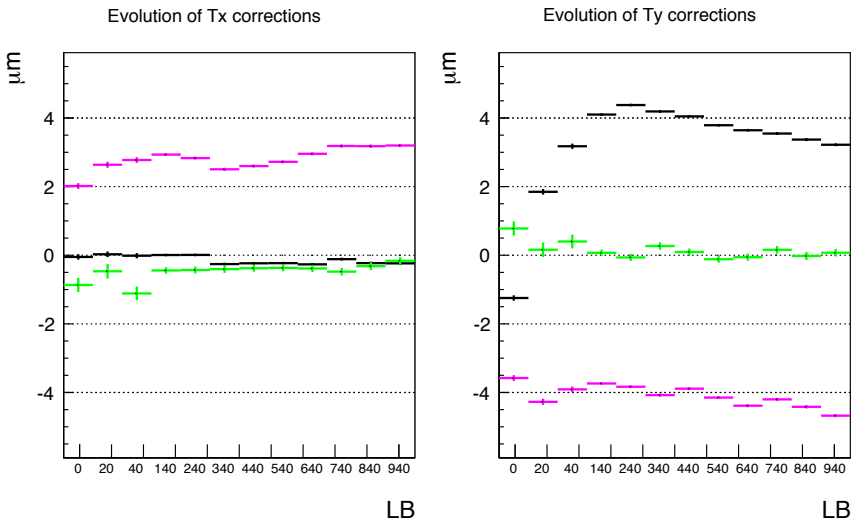

Figure 4.8: Corrections to the IBL (pink), Pixel (black) and TRT barrel (green) positions with respect the SCT barrel during a typical run of 2015. The Pixel lift is visible on the right plot (T_y) corrections.

The IBL is detached mechanically from the Pixel detector. Therefore, it is aligned independently from the Pixel, as an individual object. In figure 4.8, it can be seen that the IBL detector does not show any significant displacement either in the horizontal or vertical axes during the whole run. Same behaviour is seen for the TRT barrel. This confirms, once again, that it is the Pixel detector what moves at the beginning of every run and the main responsible for the beam spot vertical drift.

During 2016, as the LHC increased its luminosity, the second and slower drift of the Pixel detector became larger in magnitude. Figure 4.10 shows the evolution of the relative vertical position of the Pixel during an ATLAS run of 2016. An alignment every 10 lumiblocks (∼10 minutes) has been derived during the whole length of the run. The detector quickly rises around 6 μm during the first hour of data taking, followed with a gentle descend during the rest of the run, falling a total of ∼3 μm. Together with the relative displacement of the Pixel, figure 4.10 shows the instantaneous luminosity of the corresponding LHC fill. A big correlation between both quantities is observed. Figure 4.11 shows that the speed of the Pixel descent is correlated to the peak luminosity of the LHC fill.

The instabilities of the Pixel detector, together with the IBL bowing described in chapter 5, forced the implementation of a "dynamic" scheme for the

alignment. Details about this implementation are given in section 6.2.1. Figure 4.9 shows the impact that a vertical displacement of ∼6 μm of the Pixel has on the residual distributions of the IBL and on the first layer of the Pixel detector, the B-layer, when the misalignment is not corrected. The plots also show how a good performance in the residual distributions can be recovered by introducing a time-dependent alignment.

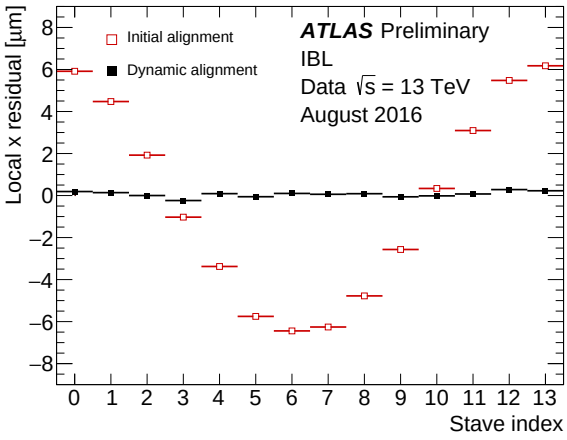

(a)

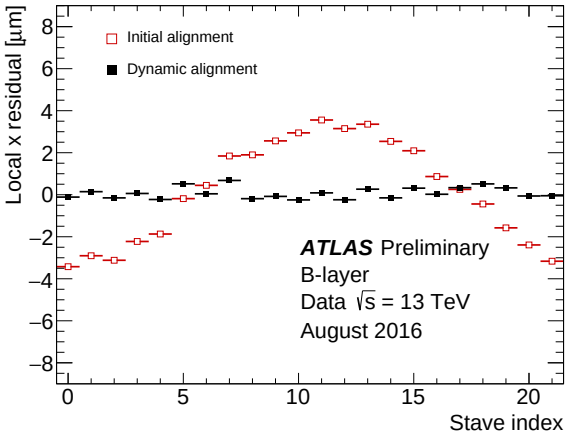

(b)

Figure 4.9: Mean local x unbiased residual of the (a) IBL and (b) B-layer per stave. The stave index is ordered in ϕ. This plot is made from the second hour of data set of a fill recorded in August, where the displacement is maximum. The initial alignment is obtained from the first 20 minutes of the fill and is corrected for general detector displacement and the IBL bowing. The red points show the residuals using the initial alignment and the black points show the residuals after the dynamic alignment has been applied. This illustrates the extreme impact that a vertical displacement of the Pixel of ∼6 um would have in that portion of the data if not aligned dynamically. Given the definition of the residuals, a movement in the Pixel detector is expected to induce a deformation in the IBL residuals and vice versa [58].

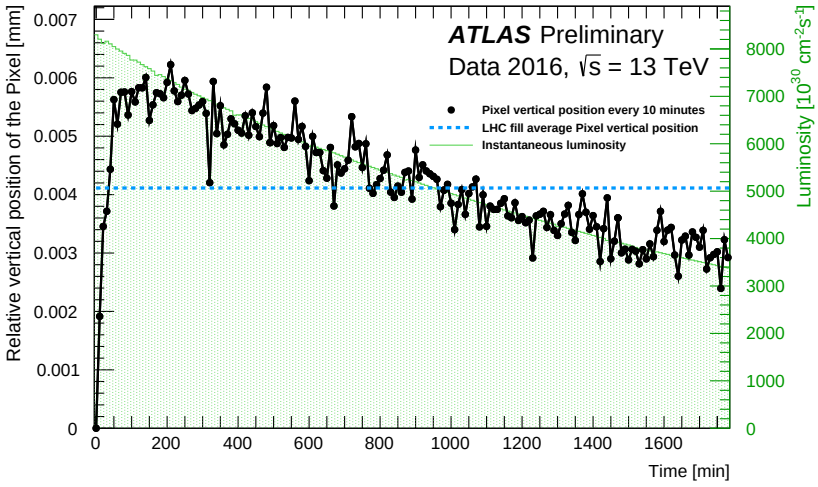

Figure 4.10: Short time scale movements of the Pixel detector during a fill. Every time the Pixel detector is switched on it rises fast during a transitory regime until it reaches a maximum. Afterwards (in a high luminosity LHC fill) the Pixel detector goes down following closely the behaviour of the luminosity of the beams. The black points correspond to the vertical position of the Pixel detector as a function of time (every 10 min) and relative to the initial measurement, whereas the instantaneous luminosity is plotted in the green area histogram. The relative normalisation of both histograms allows a straight comparison. The dashed blue line corresponds to the average vertical position that would be computed from the entire range [59].

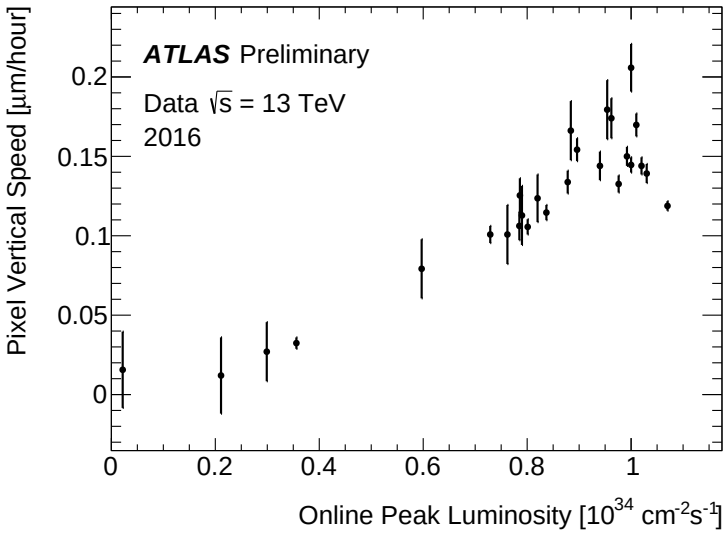

Figure 4.11: Vertical speed of the Pixel package as a function of the peak luminosity of the fill extract from the alignment corrections. The vertical speed is determined as the average speed of the Pixel package excluding the first one hour after the start of the data taking. Only fills longer than 8 hours were used [58].

Chapter 5

Bowing of the IBL staves

This chapter discusses how the bowing of the IBL staves was find out, its impact on the general performance of the ID and how the alignment framework was upgraded in order to correct it.

5.1 IBL first alignment with cosmic-ray data

Data recorded by ATLAS during the 2014 and 2015 cosmic-ray campaigns were used to perform the first alignment of the detector after the LS1 and to test the performance of the new inserted IBL detector. The very first alignment of the ID after ATLAS Run-I was performed using data recorded during two periods of commissioning, named M6 and pre-M7 in which ATLAS was operating without magnetic field, as the solenoid was off. B-field off data is valid for alignment although it gives lower quality results, as it is not possible to filter the tracks by its momentum in order to remove low-momentum tracks from the selection. These are more affected by multiple scattering effects, worsening the alignment performance. During LS1, the Pixel detector was removed from ATLAS for the performance of maintenance and put back in place with a precision from the survey of $\sim$100 μm. The IBL was installed during LS1 for the first time, so there was no previous experience from Run-I. The SCT and TRT barrels were not moved during LS1, so it was expected that they would be in the same position as at the end of Run-I. Because of that, the first detector alignment was focused in the Pixel and the IBL. Issues with the IBL geometry were found with this first alignment:

- A significant displacement along the beam axis of the IBL with respect its nominal position was corrected, as shown in figure 5.1(a). The IBL was displaced around 2 mm in the local-y direction.
- The cause of the 2 mm shift of the IBL comes from a wrong description in the simulated IBL geometry model of a closing flange in the sealing cone, which was simulated with a thickness of 48 mm while in reality it is 50 mm thick. The real and simulated pieces are shown in figure 5.1(b) (green

colour flange of right plot).

- Hits with residuals 5 times bigger than the nominal detector resolution are not considered for the track reconstruction. With an intrinsic resolution of 40 μm in the local-y direction for the IBL modules, hits displaced by 2 mm were initially discarded for the alignment. In order to recover the IBL hits, a large error scaling (section 3.11) factor had to be applied.

- It was also discovered that there was a mismatch between the real and simulated IBL geometries in the tilt of the IBL staves (figure 2.9).

- ATLAS ID simulated geometry (section 2.2) was updated to correctly describe the real geometry of the IBL.

- Figure 5.2 shows the number of IBL hits before and after the alignment. The improvement achieved with the alignment is evident. The sinusoidal structure in ϕ direction is expected, as cosmic-ray events come from the sky and traverse the detector from top to bottom.

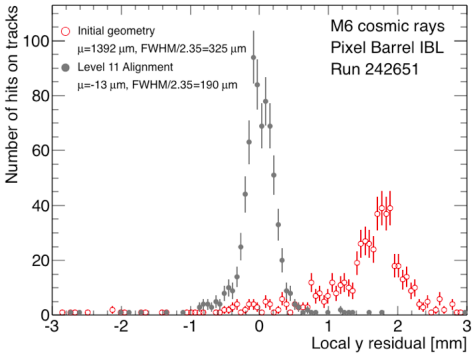

(a)

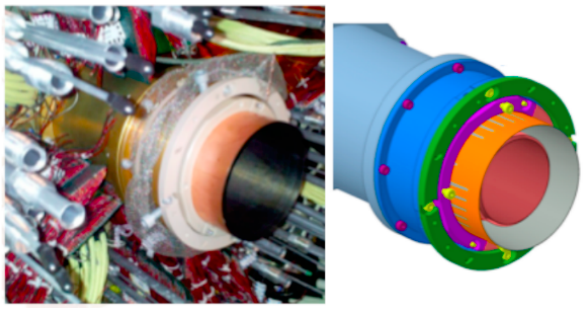

(b)

Figure 5.1: IBL local-y residual distribution (a) when hits were reconstructed with its nominal geometry (in red) and after correcting a large shift of the IBL along the beam axis (in grey). A wrong description of a beam pipe closing-flange was the origin of the shift. A photography of the real piece is shown (b), together with its simulation for the ATLAS GeoModel. The corresponding piece is coloured in green.

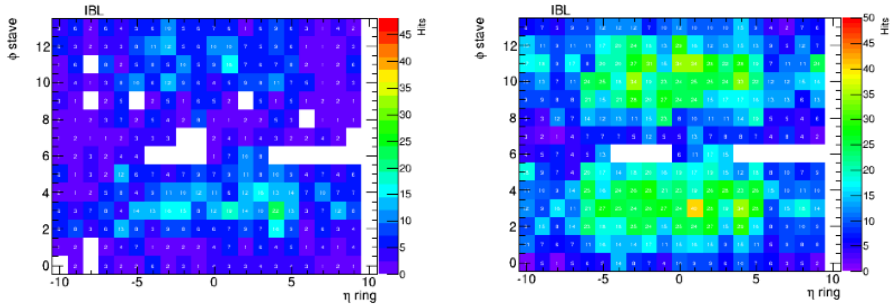

(a) (b)

Figure 5.2: Map of hits in the IBL before (a) and after (b) correcting a shift of 2 mm of the IBL. Each cell corresponds to a single IBL module, and they are shown as function of their η and ϕ module identifiers. Data used are from the pre-M7 commissioning period.

After performing a first alignment with the solenoid off data of M6 and pre-M7 commissioning periods, a more detailed alignment was performed gradually with data of three additional periods, M7, M8 and M9, recorded between December 2014 and March 2015. The data used was recorded with the solenoid on, meaning that the momentum of the tracks was accessible and low momentum tracks could be rejected. The analysis of data up to M8 can be found here [31]. Figure 5.3 show the improvements in the residual distributions of the IBL and the Pixel achieved with the February (M8) and March (M9) alignment campaigns. The track selection used in both periods was the following:

- $N^{\text{Pixel}} \geq 1$: at least one hit in the Pixel detector.
- $N^{\text{SCT}} \geq 8$: at least eight hits in the SCT detector.
- $N^{\text{SCT}}_{\text{top}} + N^{\text{Pixel}}_{\text{top}}$ and $N^{\text{SCT}}_{\text{bottom}} + N^{\text{Pixel}}_{\text{bottom}} \geq 2$: at least two hits both in the top and bottom half shells of the silicon detector.
- $N^{\text{TRT}} \geq 25$: at least twenty five hits in the TRT detector.
- $p_{\text{T}}^{\text{Track}} \geq 2$ GeV

During the commissioning period, it was possible to perform a module by module alignment of the IBL (L3). Figure 5.4 shows the mean of the local-x and local-y residual distributions as a function of the module location along the stave (η index). It can be seen on both plots that the red distribution, which are made with tracks reconstructed with the nominal IBL geometry, are not flat, meaning that the real IBL geometry is different from its nominal one. The distribution of the local-x residuals mean indicates an in-plane deformation of the IBL staves in the negative local-x direction. The distribution in local-y indicates a systematic displacement of the modules along the global z-axis of the IBL staves. The L3 alignment is able to correct for both observed stave deformations. In both cases, the distributions are integrated over all 14 IBL staves.

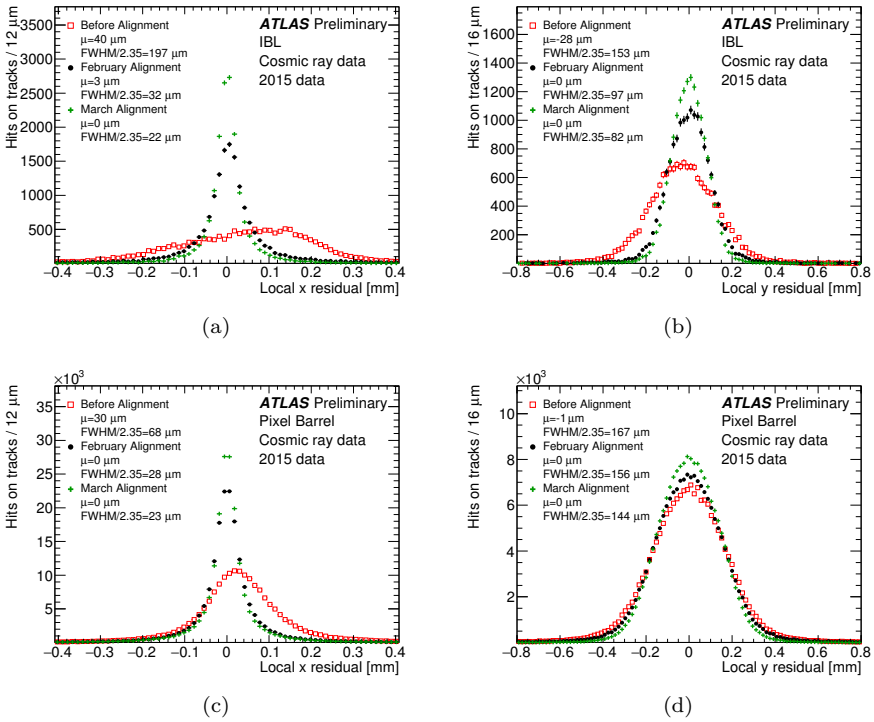

Figure 5.3: The IBL (top) and Pixel (bottom) local-x (left) and local-y (right) residual distribution for the cosmic-ray data sample reconstructed before (red) and with February (black) and March (green) alignments. The distributions are integrated over all hits associated to tracks (hits-on-tracks) in IBL/Pixel modules. The parameter μ represents the mean of the distributions. March distribution has been re-scaled to February's number of entries [60].

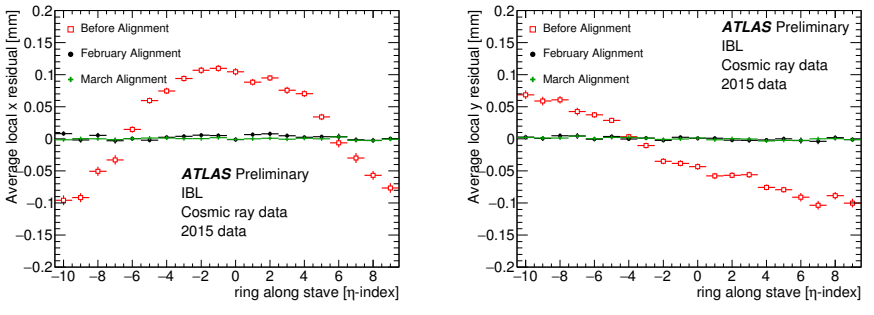

Figure 5.4: The IBL mean of the local-x (a) and local-y (b) residual distributions as a function of the η position of the module, before alignment (red) and with February (black) and March (green) alignments [60].

The split-track method was used to test the goodness of the alignment. Cosmic tracks, which traverse the whole detector, are divided into upper and lower segments, and each one is reconstructed independently. The technique is illustrated in Figure 5.5. Since both tracks come originally from the same particle, their track parameters at the perigee must be the same. The differences in the reconstructed track parameters ($\Delta\tau$) arise from the track parameter detector resolution, σ_τ. Both quantities are related through $\sigma_\tau = \delta\tau/\sqrt{2}$.

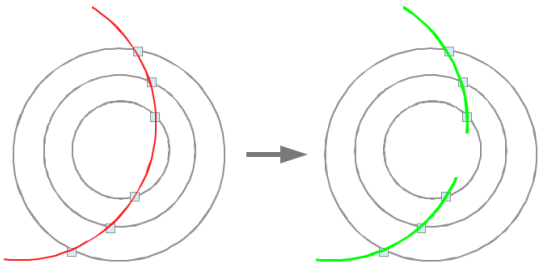

Figure 5.5: Diagram illustrating the split-track method. In red it is shown a full cosmic-ray track reconstructed in the ID, while in green are shown the two reconstructed segments, if the track is split in the top and bottom parts.

Figure 5.6 shows the distributions of Δd_0, Δz_0 and $\Delta q/p_{\mathrm{T}}$ at different stages of the alignment. Biases of -19 μm in Δd_0, of -7 μm in Δz_0 and of -9.4 TeV^{-1} in $\Delta q/p_{\mathrm{T}}$ were corrected with the alignment. The resolution of these track parameters was improved from 97 to 40 μm for d_0, from 227 to 135 μm for z_0 and from 4.9 to 1.2 TeV^{-1} for q/p_{T}.

5.2 First evidence of the IBL stave bowing

During the commissioning of the IBL, it was observed that the IBL staves exhibit a distortion of the shape from the design geometry (figure 5.4). The distortion was found to depend on the detector conditions, as it presented variations between the different data taking periods. First, a possible deformation due to the switching on/off of the solenoid field was suspected. But a detailed analysis of the M8 data, recorded with and without magnetic field, already discarded that the B-field played any role on the distortion, as no geometry changes were observed between data with the solenoid on or off.

In order to find out if the operation temperature had an impact in the IBL staves shape, the following commissioning week, M9, was organised to record data with the IBL operated at different temperatures. A wide range in temperature was covered, going from room temperature (+15 °C) to the IBL nominal operation temperature (-20 °C). The selected temperature set points were: +15 °C, +7 °C, 0 °C, -10 °C, -15 °C and -20 °C. Figure 5.7 shows the residual mean local-x and local-y residuals as a function of the modules position along the stave for the different temperatures at which IBL was operated. For all data sets, the same alignment constants are used to derive the residual distributions:

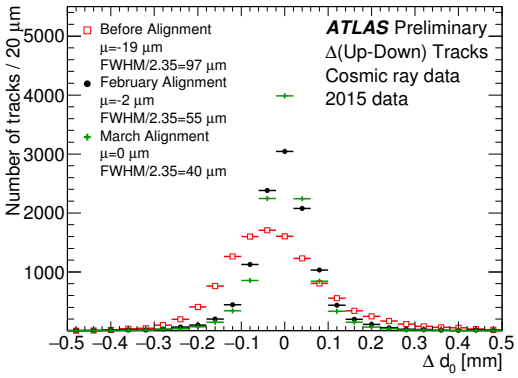

(a)

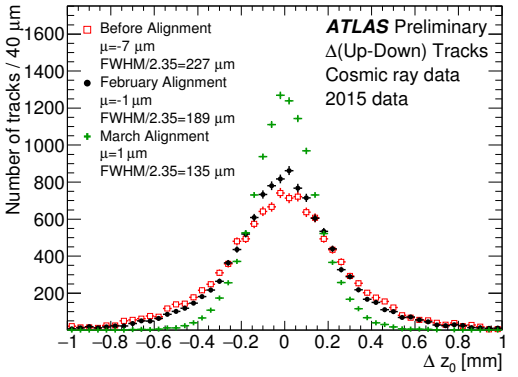

(b)

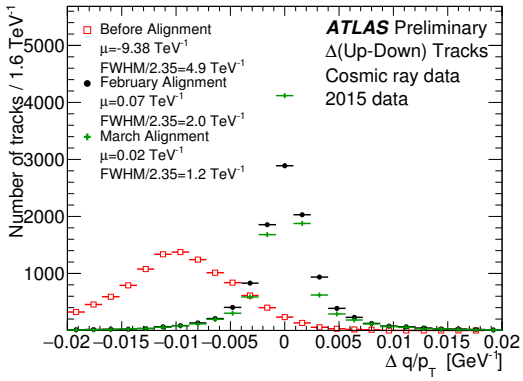

(c)

Figure 5.6: Distribution of the difference of the reconstructed transverse impact parameter Δd_0 (a), of the difference of the reconstructed longitudinal impact parameter Δz_0 (a) and of the difference of the reconstructed track charge over transverse momentum $\Delta q/p_{\mathrm{T}}$ using tracks reconstructed in the top part of the inner detector with respect to track reconstructed in the bottom part [60].

the alignment corrections derived at -20 °C, the planned operational temperature for the IBL. The IBL shape dependence with temperature is evident for local-x. The distortion introduced by changing the IBL temperature from room temperature to -20 °C is bigger than 300 μm at the centre of the staves. No dependence with the temperature in local-y is seen.

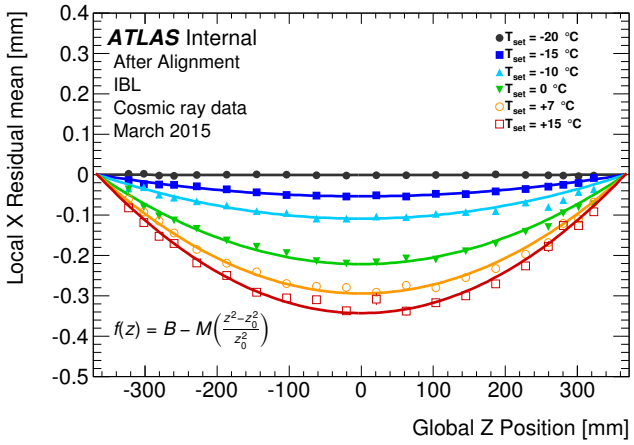

(a)

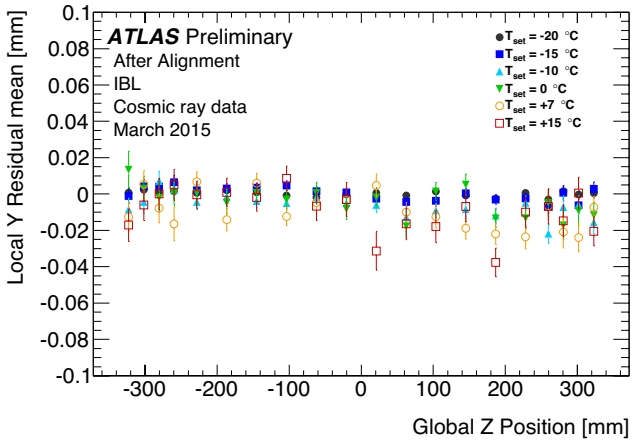

(b)

Figure 5.7: The track-to-hit residual mean in the local-x direction (a) and in the local-y direction (b). The residual mean is averaged over all hits of modules at the same global-z position. The alignment corrections derived at -20 °C are applied to the local positions in the module frames. For local-x, each data set is fitted to a parabola which is constrained to match to the baseline $B = 0$ at $z = \pm 366.5$ mm, where the IBL ends are fixed [61].

Some of the temperature points were recorded in two different passes in order to test the presence of any hysteresis effect of the IBL distortion. The temperature evolution at the end of M9 was the following: -10 °C → -15 °C → -20 °C → -15 °C → -20 °C. No significant differences were observed between the two passes so a hysteresis effect with the temperature was discarded, with

a residual precision of 20 μm.

A second order polynomial function has been used to perform a fit to each temperature point data set, as it was seen that it gives a proper parameterisation of the IBL bowing. The fitting function is defined as

$$f(z) = B - M\left(\frac{z^2 - z_0^2}{z_0^2}\right) \tag{5.1}$$

where z is the position of the module along the z-axis, $z_0 = 366.5$ mm corresponds to the fixing points of the stave at each end, B is the baseline describing a global translation along the local-x direction of the whole stave, and M is the bowing magnitude, defined as the transverse amplitude of the distortion at the centre of the stave. For the fit, the baseline B has been fixed to zero for all temperatures as the ends of each stave are fixed mechanically. Therefore, the bowing magnitude M is the only free parameter in the fit, and it is used to quantify the size of the distortion.

Figure 5.8 shows the obtained bowing magnitude M as a function of the operating temperature. A linear dependence of the bowing magnitude with the temperature is observed. The slope extracted with a linear fit to the collection of points is

$$\frac{\mathrm{d}M}{\mathrm{d}T} = -10.6 \pm 0.7\ [\mu\mathrm{m/K}] \tag{5.2}$$

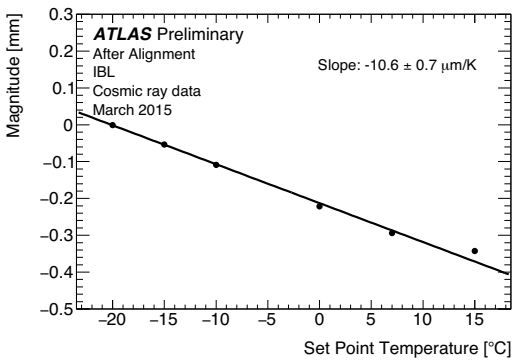

Figure 5.8: The magnitude of the distortion as a function of the temperature set point. Each data point is a best fit of a parabola to the local-x residual mean as function of the global-z of the module position (equation 5.1). The alignment corrections derived at -20 °C are applied to the local positions in the module frames [61].

The distortion consists in a bowing of the staves by their centres, which moves along the modules local-x direction, while both ends of each stave remain at their nominal positions.

Once the IBL stave bowing dependence with the temperature was well stated, the IBL Distortion Task Force was formed for understanding the peculiar distortion of the IBL with temperature, its stability and reproducibility. The study was done together with another task force, named the IBL Mechanics Task Force. It was carried out in parallel by engineers, focusing on understanding the mechanism of the distortion and its risk assessment of the detector

integrity based on the finite element analysis (FEA) simulation as well as experiments in the laboratory. The carried studies and the obtained results are reported in detail in [61, 62]. Here, only a brief summary is given.

The IBL bowing is caused by a mismatch between the coefficients of thermal expansion (CTE) of the components in the IBL staves. While the CTE of the carbon foam composing the bare stave structure is almost zero ppm, the polyimyde flex bus line glued on one side of the stave, has a CTE of several tens of ppm, making the whole system asymmetric (figure 2.9). This mismatch on the materials CTE, together with the asymmetric placement of the stave flex, induces a tension force when the staves are cooled down to the operational temperature. Figure 5.9 shows the results of the FEA, what helps to visualise the shape of the distortion. Results of the simulation are compatible with the observed distortion in real data. The FEA also predicts radials distortions of the stave, out of the module plane, but the alignment has low sensitivity on that direction.

5.3 The IBL stave bowing on collisions

It is clear that the distortion of the IBL and its impact on the ID residual distributions has a consequence on the general ID performance as well as on the ATLAS object reconstruction. In particular, being the IBL the closest detector to the interaction point it is expected that the measurement of the track impact parameters is largely affected by an uncorrected IBL bowing. Using a $Z \rightarrow \mu^+\mu^-$ MC sample, the impact of the IBL distortion on the transverse impact parameter d_0 has been evaluated by implementing different artificial misalignments that mimic the IBL bowing. Five different bowing magnitude values have been used: ΔM = 0.0, 2.1, 5.4, 10.7 and 21.4 μm, corresponding to ΔT = 0.0, 0.2, 0.5, 1.0 and 2.0 K. The average deviation of the transverse impact parameter, d_0^{rec}, from its true value, d_0^{tru}, as a function of the transverse momentum p_{T} for the different simulated bowing magnitudes is shown in figure 5.10. For an uncorrected bowing magnitude of 21.4 μm, the magnitude of the d_0 significance increases with p_{T}, approaching approximately 1.5 σ for $p_{\mathrm{T}} > 10$ GeV. The size is linear with the uncorrected distortion magnitude ΔM. More details about these studies can be found in [63].

From the studies reported on [61] about the mechanical stability of the IBL, it was measured that the variations on the IBL staves temperature during the same cosmic-ray run were less than 0.2 K. The expected bias on d_0 for such a temperature change is of the order of 1 μm, small when compared to the expected d_0 resolution, of the order or 15 μm. Therefore, as long as the IBL temperature remained stable at that level, no significant biases will be introduced in the impact track parameters.

During the first months of *pp* collisions data taking of 2015, the temperature of the IBL staves remained stable, with temperatures fluctuations below 0.2 K. Therefore, the IBL bowing distortion also remained stable and the IBL distortion problem could be well controlled with a static alignment correction. Since the end of September 2015, as the LHC luminosity increased, a new effect was

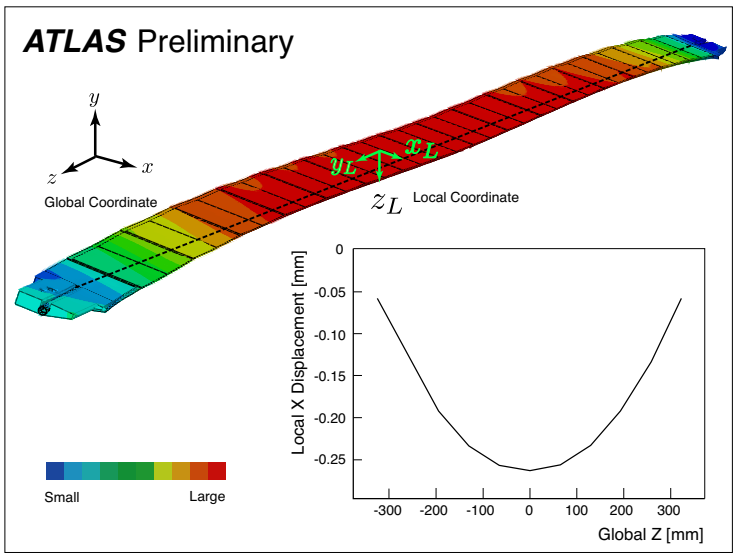

(a)

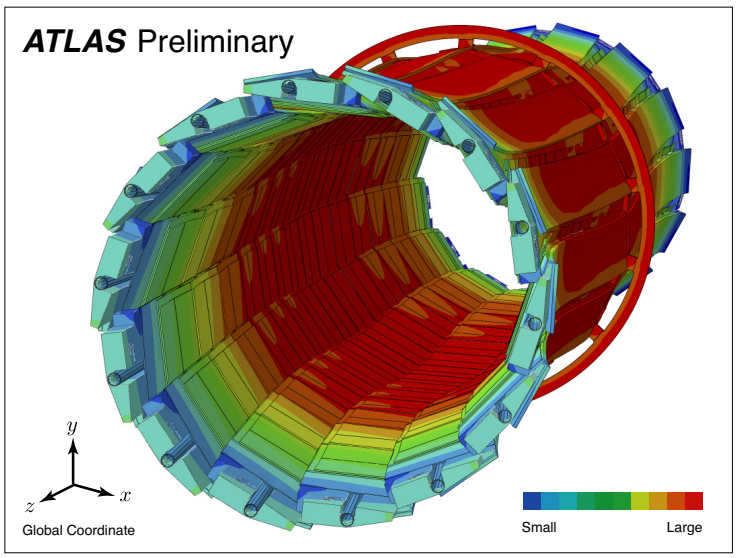

(b)

Figure 5.9: (a) Visualisation of the distorted stave with magnified distortion size. The size of the distortion is magnified for visualisation. The colour represents the magnitude of the displacement. The right bottom graph shows the relative displacement size in local-x direction (x_L) as a function of the global z-position at the face plate surface of the stave. (b) Full package of the IBL staves with the central ring simulated by the 3D FEA representing the distortion. The size of the distortion is magnified for visualisation. The colour represents the relative size of the local displacement. The temperature is set at ΔT = -60 K uniformly from the nominal temperature. The distortion is magnified by a factor 20. [61]

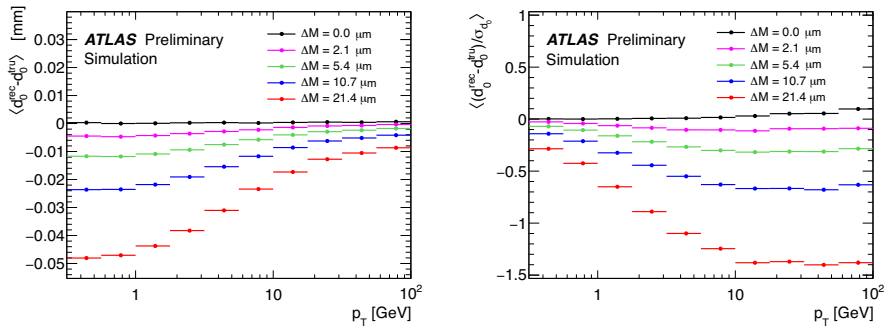

(a) (b)

Figure 5.10: Average deviation of transverse impact parameter d_0 as a function of the transverse momentum p_{T}, for different values of the IBL bowing magnitude, in absolute value (a) and weighted by the intrinsic resolution at each p_{T} (b). [64]

observed: the staves bowing became unstable, changing during the data taking, even within a run. This additional bowing was caused by an increased power consumption of the modules induced by irradiation, known as total ionisation dose effect. With the change of the power consumption, the temperature of IBL modules also changed. The change of the thermo-mechanical conditions of the IBL resulted in changes of the IBL distortion magnitude. Figure 5.11 shows the evolution of the low-voltage current of IBL modules during a month and a half of data taking around the end of 2015. Further details about these studies can be found in [65].

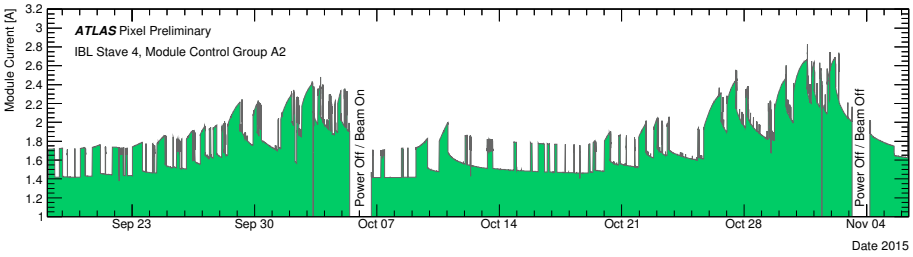

Figure 5.11: An example of the low-voltage current drift of IBL modules from the middle of September until the beginning of November 2015 [65].

Figure 5.12 shows the evolution of the average IBL bowing for a typical ATLAS run in 2015 with unstable IBL distortion (a) and the impact that it has on the residual distributions if left uncorrected (b). It shows the presence of variations up to 10 μm between the maximum and the minimum observed IBL bowing, ranging between 15 and 25 μm. As already mentioned, MC studies determined that distortions of these sizes have a large impact on the detector performance, and thus, have to be corrected.

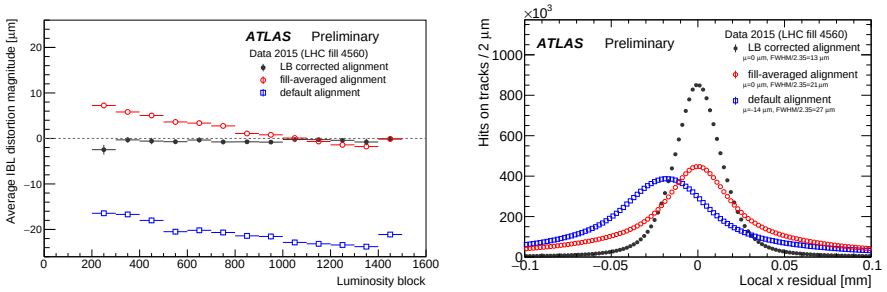

(a) (b)

Figure 5.12: Figure 5.12(a) shows the IBL distortion magnitude in the transverse plane per luminosity block range (LB) averaged over all 14 IBL staves. In blue (open squares) the distribution obtained with the default alignment compared with the one obtained with the fill-averaged alignment (open red circles) and after LB corrected alignment (solid black circles). Figure 5.12(b) shows the distribution of local-x residual [64].

5.4 IBL bowing corrections: data base updates

In the usual alignment scheme, as explained in section 3.8, alignable objects have six degrees of freedom: three translations $T_{x,y,z}$ and three rotations $R_{x,y,z}$. Within this scheme, the IBL bowing can only be corrected with a module level alignment (L3) in which every module is treated individually. This approach needs a large amount of statistics and takes longer to solve than lower level alignments due to the large amount of dofs in the alignment matrix. In order to cope with the new observed characteristics of the IBL bowing, the alignment scheme was extended with a new dof to correct for the collective distortion of the staves. As seen in figure 5.7, the stave distortion is well parameterised with the parabolic function 5.1. The first derivative of the track-to-hit residual with respect to the IBL bowing distortion magnitude is

$$\frac{\partial r_x}{\partial M} = \frac{z^2 - z_0^2}{z_0^2} \tag{5.3}$$

being r_x the local-x residual of the alignable module, z its position along the beam axis in the alignment frame and M the IBL stave bowing alignment parameter. The distance between the centre of the stave and the IBL fixation points at the stave ends is $z_0 = 366.5$ mm. The baseline B in equation 5.1 was not introduced in the alignment as it can be correctly corrected by the usual six alignment dofs. In particular a rotation along the beam axis, R_z matches perfectly the baseline. No impact of the IBL bowing on the local-y has been seen so its derivative with respect the bowing magnitude was set to zero. This new dof has been implemented in two different alignment levels:

- $L11$: a common bowing magnitude is derived for the average of the 14 staves distortion.
- $L16$: an individual bowing magnitude is derived for each of the staves.

With the introduction of the bowing magnitude in the alignment derivation, it is possible to correct for the IBL distortion in a run by run basis and also to provide time-dependent corrections within each run. The IBL performance with the default alignment (blue), with a fill-averaged bowing correction (red) and with time-dependent bowing corrections (black) are compared in figure Figure 5.12. In the time-dependent alignment case, an individual alignment has been derived for every 100 LB ($\sim$ 100 minutes). The impact on the IBL performance is clearly seen in the residual distributions.

A time-dependent alignment including IBL bowing corrections was implemented in the Calibration Loop alignment towards the end of 2015. More details about the CL alignment are given in chapter 6. The new procedure completely mitigates the impact on the track parameter resolution of the IBL shape distortion. Figure 5.13 shows the relative bowing magnitude of the IBL staves, averaged over its 14 staves and computed with the default alignment (blue dots) and with respect to the aligned geometry including time-dependent bowing corrections (red open circles).

The IBL operation temperature T_{set} for each period is also shown. A dedicated default baseline alignment was derived for each period as the IBL geometry strongly depends on the operation temperature. The baseline alignment is usually derived at the beginning of each period of data taking. An example of the derivation of a baseline alignment is given in chapter 7. T_{set} has been set depending on the data taking periods from -20 °C to +15 °C. During 2015 T_{set} was -10 °C. During 2016, T_{set} was +15 °C at the beginning of the year, later lowered down to +5 °C in June. Figure 5.14 shows the change in the IBL bowing derived from the variations in T_{set} in 2015-2016. Since 2017 T_{set} has been changed back to the nominal IBL operation temperature, -20 °C.

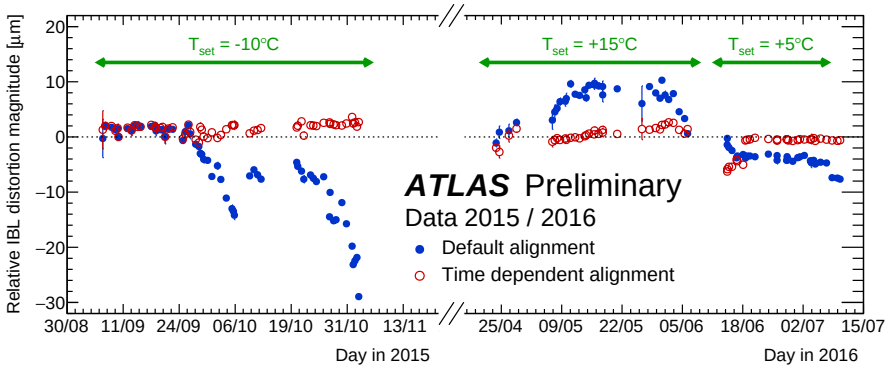

Figure 5.13: Averaged bowing magnitude evolution during 2015 and 2016 for two set of geometries: the default alignment of each period (blue dots) and after the calibration loop alignment (open red circles) [66].

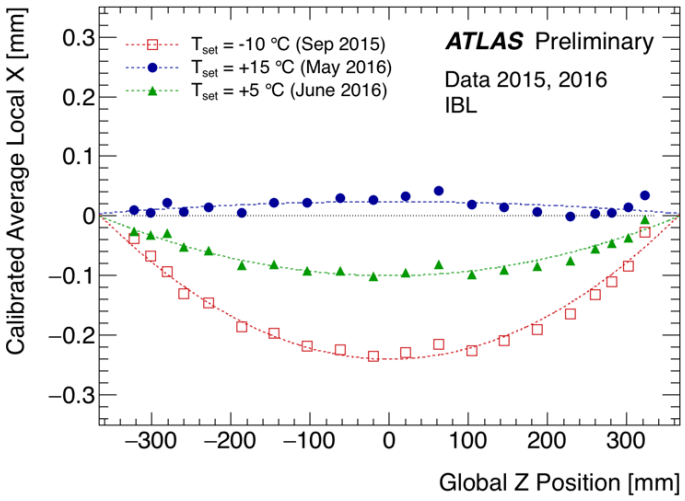

Figure 5.14: IBL local-x correction in the transverse plane averaged over all 14 IBL staves for 2015 data (red open squares), and for 2016 data using different T_{set} (+15 °C, solid blue circles; +5 °C, solid green triangles) [66].

Chapter 6

Calibration Loop alignment and Tier-0 machinery

Data collected by the ATLAS experiment are promptly processed at the CERN's Tier-0 [67] to provide fast access to high quality data for physics analysis. The high quality of the data is achieved by a so-called *Calibration Loop*, CL, that relies on the detector calibrations becoming available within 48 hours based on a selected subset of the data, the `express_express` stream, designed to allow detailed data investigations.

ID alignment has been one of the tasks included in the CL since LHC Run-I, providing a powerful tool to monitor the status of the ID alignment and to update if needed the geometry of the detector.

6.1 Calibration Loop alignment in Run-I

Already in LHC Run-I, an automatic alignment was implemented to run on the CL just after the reconstruction of the beam spot ended. It made use of a specific 50 Hz stream of high p_{T} tracks selected by the High Level Trigger called `calibration_IDTracks`. The implementation of the alignment in the calibration loop allowed the detection *on the fly* of movements or deformations of the different subdetectors so that these could be corrected before the start of the bulk data reprocessing: reconstruction of the full data set that starts after the end of the CL 48 hours afters the data taking. In any case, the detector geometry was not corrected online. It would only be updated after the end of the run if large misalignments were found. During Run-I, the ID presented a quite stable behaviour between runs, as can be seen in figure 4.2. Only *big events* as cooling system failures, power cuts or ramp up and down of the magnetic fields led to significant movements of the sub-detectors.

The alignment configuration in Run-I consisted of two iterations of $L1$ alignment with respect the Pixel detector, which was kept fixed as reference. Parallel to the CL alignment derivation, a web site was developed to monitor the results

of the CL alignment. The decision on updating or not the ID geometry before the bulk reconstruction was done by the ID shifter based on the results shown on the web site, that allowed the user to produce plots on demand as subdetector residual distributions and alignment corrections evolution between runs. The website is allocated in `https://atlasalignment.cern.ch/webapp/` and it is still used in Run-II.

6.2 Calibration Loop alignment in Run-II

The CL alignment at Tier-0 has been maintained for LHC Run-II, based on the machinery available from Run-I, but it have suffered so many structural changes to adapt it to the new needs that have appeared during Run-II that currently it has little in common with the Run-I version. Moreover, updates of its software and configuration are introduced as demanded by the ATLAS operations. The version described on this section is the one available at the beginning of 2018. The CL alignment described here is indeed a more restrained and simplified case of a fully configurable Tier-0 alignment tool described in section 6.3.

In general, the ID alignment in ATLAS is performed in three distinct steps. The first two match the accumulation and solving steps described in section 3.6.2. The last one produces a set of histograms that allow to monitor the alignment results. This applies to every alignment job run for ALTAS and not only to the specific case of the CL alignment. The three steps that conform a complete alignment iteration are:

- **Accumulation**: It is the process of reconstructing tracks and calculating the track-to-hit residuals, usually starting from raw data. It creates the χ^2-matrix elements of the corresponding data, referred to as `AlignmentTFile.root`. A monitoring file of the reconstructed tracks is also produced with the name `monitoring.root`. This task is coordinated through the script `Accumulate_tf.py`.
- **Solving**: It is the process to add all produced `AlignmentTFile.root` by the accumulation jobs, and calculate the alignment constants from the inversion of the alignment big matrix. The main output data is a database file with the new geometry of the ATLAS ID. It also produces some text log files with the alignment results that allow to monitor the obtained corrections. This task is coordinated through the script `Solve_tf.py`.
- **Merging**: It is a process to merge the individual `monitoring.root` files into a single `TotalMonitoring.root` file. This task is coordinated through the script `Merge_tf.py`.

Figure 6.1 shows a diagram explaining the job structure followed at Tier-0 to complete an iteration of the alignment. Due to Tier-0 requirements, an accumulation job is run for every raw data file, corresponding each to a single lumiblock (LB). The reconstruction of the tracks is performed over the geometry resulting from previous iteration or from the baseline alignment in case of the first iteration. Accumulation jobs run in parallel. Once all accumulation jobs

are completed, the solving and merging jobs are run, obtaining an updated geometry and a set of monitoring plots. The process continues until all iterations are completed.

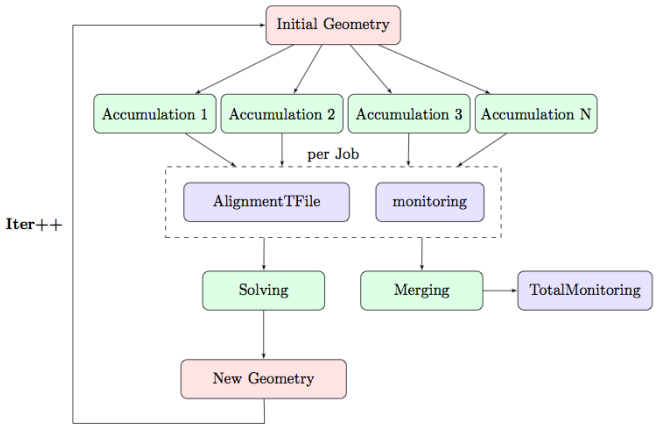

Figure 6.1: Diagram of the job structure for a full alignment iteration at Tier-0.

There are two main conceptual differences between Run-I and Run-II CL alignments. The first one is that due to the presence of sub-detector movements and deformations within a LHC fill such as the Pixel drift (chapter 4) and the IBL bowing (chapter 5), a time-dependent alignment is derived. The second one is that the ID geometry is updated automatically after the end of every new run. Actually, as the IBL and the Pixel suffer from large time-dependent misalignments, the beam spot calculation at the CL has been re-scheduled to be executed after the detector alignment, as its results are strongly dependent on the IBL and Pixel positions. An important implication of having an automatic upload of the ID geometry is that CL alignment has to be robust: the alignment configuration has to be done such that no biases or weak modes are introduced during the alignment. Additionally, a set of automatic tests on the alignment output have been set to avoid the update of a wrongly determined geometry, due to lack of statistics for example.

Since 2016, the alignment configuration used in the CL alignment is the following: the alignment of every new run starts from the defined baseline (chapter 7). Then, four iterations are performed in total. Two iterations of L11, followed by another two of L16 (section 3.8). The details about the configuration are given in table 6.1. Tier-0 is configured to start the alignment of every new run with `calibration_IDTracks` stream. A configurable cut in the transverse momentum is used in the track selection. Typically, 3 GeV are used.

6.2.1 Time-dependent alignment at the Calibration Loop

The Tier-0 alignment machinery has been prepared to allow a time-dependent alignment. The runs are segmented into groups of LBs in order to detect sub-detector displacements or deformations that occur during the run. Due to the Tier-0 requirements, the splitting of the run into groups of LBs has to be done

Level	IBL	Pixel	SCT barrel	SCT EC	TRT barrel	TRT EC
L11	all but R_z	all	fixed	all but T_z	all but T_z	all but T_z
L16	M	fixed	fixed	fixed	fixed	fixed

Table 6.1: Alignment configuration for the CL since 2016. Two iterations of each level are run. Both at L11 and L16, the bowing magnitude dof, M, described in section 5.4 is included in the alignment. L11 includes a single M dof for the whole IBL. L16 includes one for each stave.

internally: The solving task get as input the full list of `AlignmentTFile` files and divides it in groups of LBs. An `Athena` alignment job is run for each LB group, one after the other, until all groups have been processed, producing an individual set of alignment constants for each. Next iteration is only signed if each group solving succeeds. The merging task proceeds in the same way. The accumulation task handles the matching of every raw file with its corresponding LB group alignment constants from previous iteration. This is done with the help of two auxiliary files that record the list of available LB files such that the LB splitting can be coordinated between the accumulation, solving and merging tasks.

Due to the characteristics of the Pixel drift, the scripts have been prepared to allow for two different 'speeds' for the alignment during the run. Currently, at the CL, the first 60 LBs of the run are split into three groups of 20 LBs each. The remaining LBs of the run are grouped into bunches of 100 LBs. These configuration was found to provide a proper tracking of the Pixel drift. Figure 18.9 shows an example of the LB splitting performed at the CL for a typical LHC fill during 2016. The vertical drift of the Pixel detector (in black) is tracked with the time-dependent alignment of T_y. A finer binning is performed during the first hour of data taking. The Pixel drift can be compared with the stable behaviour of IBL T_y (in pink) through the whole run.

Updating the database DB means uploading all the constants to the DB. Just for the silicon part of the ID (IBL, Pixel and SCT), the DB has 36k entries, including the corrections from L1 to L3. Nevertheless, in the CL alignment, only $\sim$60 corrections are calculated. It is not efficient to upload 36k values, when only 60 of them are changed. As it was need to do frequent uploads of the ID geometry DB, it was split into two files. One contains the $L3$ DB and remains untouched during long periods of time. The other one contains the $L1$ and $L2$ DB and it is uploaded for every new run processed at the CL. The DB includes an interval of validity (IOV) that allows to update time-dependent alignments by assigning different geometries to different LB ranges. The TRT DB has also been divided in the same way.

6.3 Tier-0 fully configurable alignment tool

Traditionally, the alignment has been run in the `lxplus` batch system, making use of the ATLAS queues system. Both public queues as the `1nh` or `8nh` and

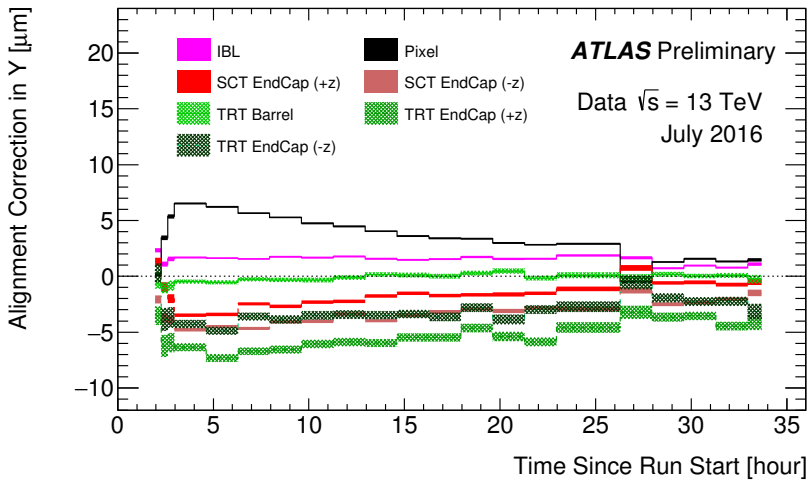

Figure 6.2: Correction in the y (vertical) direction for the ID components as a function of time. Bands indicate statistical uncertainty. End caps on both sides of the detector are shown separately. SCT barrel is kept fixed as a reference during the derivation of the alignment constants. For the first hour of collisions, the ID is aligned each ∼20 minutes. Later on, the frequency of the alignment is decreased to once each ∼100 minutes [58].

calibration-dedicated queues (as the `atlasb1`) have been used. Although the batch system provides a good framework for alignment studies, it does not perform optimally in cases in which a large amount of alignment jobs have to be run in a short period of time, as usually a fraction of the jobs fail and queues may be busy, implying waiting periods. Examples of these urgent alignment cases are the derivation of a new alignment baseline due to new detector conditions or the derivation of weak-mode-free alignment at the end of each year for the data reprocessing.

In order to profit the Tier-0 resources, a fully configurable alignment machinery compatible with the Tier-0 specifications has been derived during 2016-2017. This tool, referred to as TZ-tool in the following, has been used extensively during 2017, resulting in a very reliable and fast machinery. All baseline derivations during 2017 have been done using TZ-tool, both for online alignment and for the reprocessing of the data. Examples of these derivations are given in chapter 7. As in the CL case, TZ-tool allows for the derivation of a time-dependent alignment and two different *speeds* during the run can be selected.

TZ-tool also follows the workflow described in figure 6.1, being composed of the same three steps: accumulation, solving and merging. The scripts of TZ-tool controlling these steps are Tier-0 transformations meaning that their coding structure have to comply with the Tier-0 rules. They can get input only through a JSON file [68], what provides a reduced amount of information as the run and iteration numbers, or the stream of raw data to use. All remaining details about the alignment configuration are controlled by two external files, which are loaded at running time:

- **ConfigurationFile.py** : Provides information to the Tier-0 transformations as the LB splitting configuration, the number of events to process or to skip, the input constants, dynamic database or bowing database.

- **alignConfig.X.py** : This file configures all the alignment details that are common between iterations and for all LB groups: which subdetectors and DOF to align or the level of the alignment are just two examples. It is read by the accumulation and the solving tasks, and it is used as a template on top of which information as the input raw files, the input constants or input list of `AlignmentTFiles` is added automatically by the tasks. The information added by the tasks varies from iteration to iteration and between LB groups. Once completed, the resulting file defines the `Athena` alignment job that is launched to run the alignment. The X in the name stands for a variable called 'Step' that identifies the job and allows to select between different alignConfig files.

When one Tier-0 task ends, it has to produce an output map, that reports in which conditions the job ended. The most important variables that the map includes are two. The first one, `exitCode`, determines if the job succeeded (0) or not (any other value). In case of failure, the task is repeated up to a maximum number of attempts. The other important variable is `exitAcronym`, that will be shown in the Tier-0 tasklister, a web site that allows to monitor and operate jobs running at Tier-0. The `exitAcronym` allows a fast detection of the error if used correctly. As the output map has to be produced in any case, the three alignment scripts have been written with a `python try/except` structure covering all possible scenarios: From a problem accessing the list of files to run, to an error when importing the configuration files, or an error coming from the alignment `Athena` job. Further details about the Tier-0 alignment machinery can be found here [69]

Another peculiarity of the Tier-0 batch system is that name uniqueness of the jobs has to be guaranteed. An alignment job at Tier-0 is identified by the run number, the stream used and the iteration and step numbers. An example of one of these identifiers is `data17_13TeV.00334842.calibration_IDTracks.Step0.Iter0.c0`. An additional identifier, known as the `try` number, is used to allow repetitions of failed or miss configured jobs, corresponding to the number together to the `c` in the example. Step, iteration and try numbers run from 0 to 9. In order to avoid the submission of repeated tasks to the Tier-0 system, a macro that keeps a record of the used identifiers has been built, allowing the user only to submit tasks that have not been ran before.

Tasks at Tier-0 are submitted through the placement of a TOM (Tier-0 Management) message in a specific path, were a cron job digests the message and starts the task processing. When a new alignment job is submitted to Tier-0, an individual accumulation job is started for every raw data file of the selected run and stream. Once all jobs are done, the solving and the merging jobs are started. If the solving task ends successfully, it automatically places a new TOM message to sign out next alignment iteration. This process is continued until all the iterations configured by the user are completed.

Chapter 7

Determination of a baseline detector alignment

It is known that movements of large structures of the ID happen over time. Some of these subdetector displacements or deformations happen in a regular basis, as the pixel vertical displacement (chapter 4), and some others are caused by 'seismic events', as failures in the cooling system, what happens from time to time. The alignment performed at the calibration loop (chapter 6) is able to correct for all these displacements of large substructures of the ID.

In the other hand, it has not been observed that these movements affect the relative alignment between modules. The module level alignment, L3, shows a quite stable behaviour over time, meaning that the shape of the different subdetectors does not vary much. In order to deliver data of the best online quality, it is desirable for the CL alignment to start from a quite accurate detector description, such that the CL alignment has only to correct for the movements of large structures described above.

This chapter describes the procedure followed in the derivation of a detailed alignment baseline. Two examples are given. The first one is the derivation of 2017 first alignment baseline, on top of which the calibration loop corrections are computed. The second one follows the derivation of a set of weak mode free alignment constants for the end of the year reprocessing of 2017 data. Both alignments have been performed using the TZ-tool described in section 6.3.

7.1 Initial 2017 alignment

During 2017, the IBL operation temperature was changed from +5°C, the operating temperature in late 2016, to -20 °C, its nominal operation temperature. According to equation 5.2, such a temperature change implies a variation of the IBL bowing of 250 μm. Therefore, in order to provide a good set of alignment constants for the first 2017 *pp* collisions, a dedicated alignment baseline was needed. The starting point for the baseline were the last constants from 2016.

These were the constants used for the 2016 reprocessing, meaning that weak modes had already been removed. The IBL bowing was extrapolated to -20 °C. They were tested using cosmic-ray data of the 2017 commissioning period. With these data it was observed that the gross effect of the IBL temperature dependent bowing was correctly accounted.

Once the starting point was set, a full chain of alignment was performed using collision data from the first LHC fills of 2017: starting with L1 alignment to correct for any possible big structures movements occurred between the end of 2016 and the start of 2017 collisions, and continuing with alignment levels of increasing complexity until a module level alignment (L3) was reached. Two different runs were used to deliver the baseline. Run 324320, one of the first runs of 2017, was used to start with the baseline alignment derivation. After that, the derivation was continued and finished with run 325713, a longer run that provided larger statistics and tracks of higher quality.

In order to avoid the introduction of biases on the impact parameters or alignment weak modes (section 3.9), several constrains were used during the alignment derivation:

- **Beam spot constrain**: The beam spot position can be used as a constraint of the alignment (section 3.9.2), forcing the alignment corrections to conserve the beam spot position. It sets a strong constrain to the transverse impact parameter, d_0.
- **Null map constrain**: The alignment code of ATLAS allow the use of maps forcing the impact parameter to change by a certain amount (section 3.9.1). These maps are usually used in order to correct for alignment weak modes. An example of this is given in section 7.2. Alternatively, a map filled with null corrections can be used in order to fix the input values of the impact parameters, such that they are left unaltered by the alignment. Null map for charge over momentum q/p_{T} was used during the baseline alignment derivation.
- **Soft mode cut**: Sets a penalty term to the alignment corrections in order to avoid large non-physical ones arising from lack of statistics (section 3.10). Usually, it is only used for module level alignment.

The details about the alignment configuration of each of the steps followed during the derivation of the baseline are given in table 7.1. Figure 7.1 show the improvement achieved on the local-x residual distributions of the IBL (left) and the first layer of the Pixel (right) with the alignment performed using run 324320. As said before, the alignment was further improved using run 325713, reaching individual module alignment of the IBL, Pixel and SCT (L3), and a module level alignment of the TRT (L2). Figures 7.2 and 7.3 show the local-x mean residual distributions as a function of the modules η- and ϕ-identifiers for the Pixel and SCT barrels, at different stages of the alignment. The local-x mean residual distributions as a function of the module ϕ-identifier are also shown for the Pixel and SCT end caps in figures 7.4 and 7.5. It can be seen that, after the L3 alignment of the silicon detector, all distributions are flat below the micron level.

Run 324320

Level	IBL	Pixel	SCT	TRT	Constrains	p_{T} cut
L11	all	all	barrel: fixed EC: all but T_z	barrel: all but T_z EC: all but T_z	none	4 GeV
L3	all	fixed	fixed	fixed	beam spot	2.5 GeV
L2	all	barrel: all EC: T_x, T_y, R_z	L11	L11	beam spot q/p_{T} null map	2.5 GeV

Run 325713

Level	IBL	Pixel	SCT	TRT	Constrains	p_{T} cut
L11	all	all	barrel: fixed EC: all but T_z	barrel: all but T_z EC: all but T_z	beam spot	5 GeV
L2	fixed	barrel: fixed EC: all but T_z	all but T_z	L11	beam spot q/p_{T} null map	5 GeV
L27	all	barrel: all EC: L2 config	L11	L11	beam spot q/p_{T} null map	5 GeV
L3 Pixel	all	all	L11	L11	beam spot q/p_{T} null map soft mode cut	5 GeV
L3 SCT	L11	L11	all	L11	beam spot q/p_{T} null map soft mode cut	5 GeV
L2 TRT	L11	L11	L11	barrel: all but T_z EC: T_x, T_y, R_z	beam spot q/p_{T} null map	5 GeV

Table 7.1: Step by step alignment configuration followed during the derivation the first alignment baseline of 2017. ATLAS runs 324320 and 325713 were used.

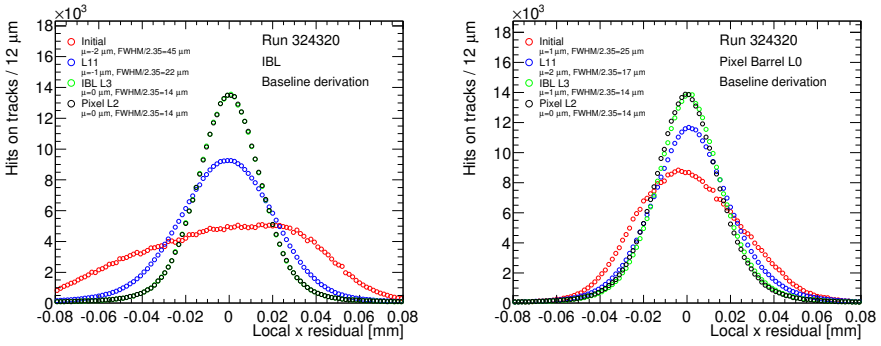

(a) (b)

Figure 7.1: IBL (a) and Pixel first layer (b) local-x residual distributions for four different alignment constants: from last 2016 alignment constants, after the IBL bowing was extrapolated to -20 °C (in red); after a L11 alignment (in blue); after a L3 alignment of the IBL (in green); and after a L2 alignment of the Pixel (in black).

The performance of the new ID baseline alignment was evaluated with a 82 pb^{-1} sample of $Z \to \mu^+\mu^-$ events. The track selection consists of two opposite sign muons with $p_{\mathrm{T}} > 15$ GeV and an invariant mass between 60 and 120 GeV. In figure 7.6, the 2017 detector residuals obtained using the 2017 alignment baseline are compared to the ones obtained with 0.6 fb^{-1} of 2016 reprocessed data. They are also compared with the performance obtained from simulated

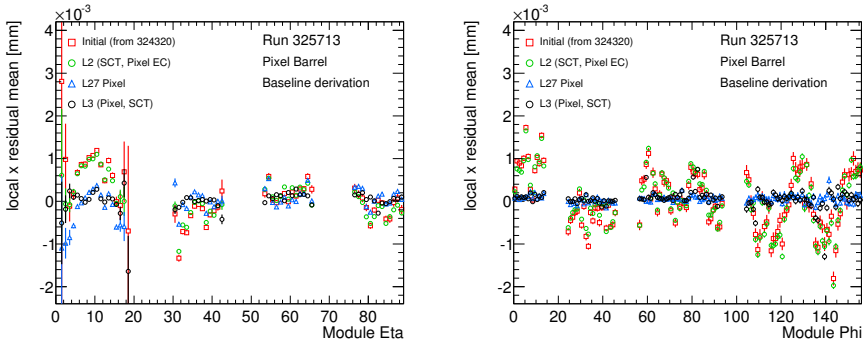

(a) (b)

Figure 7.2: Mean local-x residual of IBL and Pixel as a function of the η (a) and ϕ (b) identifiers of the modules for different alignment constants. Details about each constants are given in table 7.1.

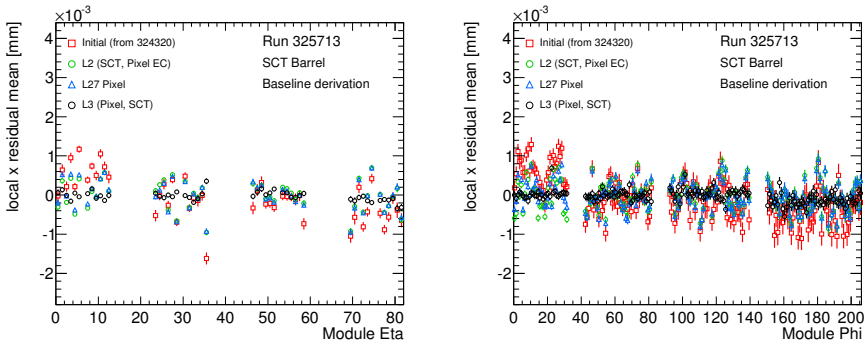

(a) (b)

Figure 7.3: Mean local-x residual of SCT as a function of the η (a) and ϕ (b) identifiers of the modules for different alignment constants. Details about each constants are given in table 7.1.

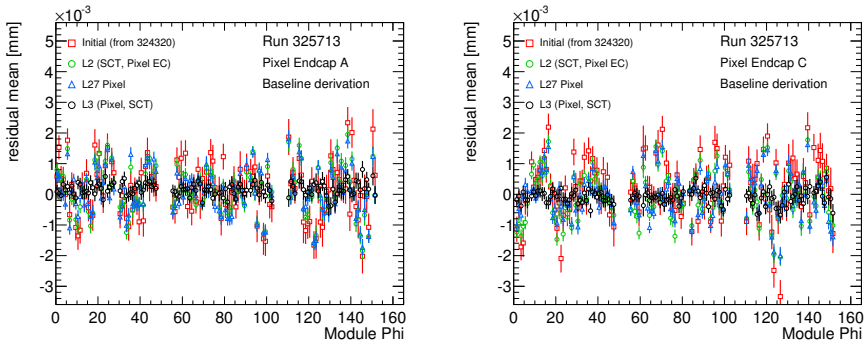

(a) (b)

Figure 7.4: Mean local-x residual of Pixel end cap A (a) and C (b) as a function of the ϕ identifier of the modules for different alignment constants. Details about each constants are given in table 7.1.

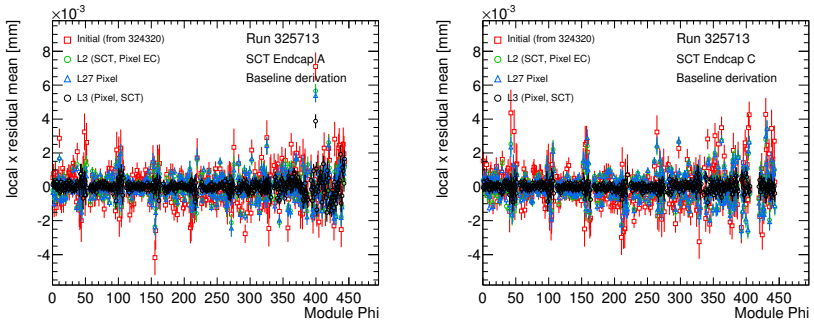

(a) (b)

Figure 7.5: Mean local-x residual of SCT end cap A (a) and C (b) as a function of the ϕ identifier of the modules for different alignment constants. Details about each constants are given in table 7.1.

$Z \to \mu^+\mu^-$ events with a perfect geometry. Despite being delivered few weeks after the start of 2017 data taking, the new ID alignment baseline provides a similar performance to the one of the final 2016 alignment [70].

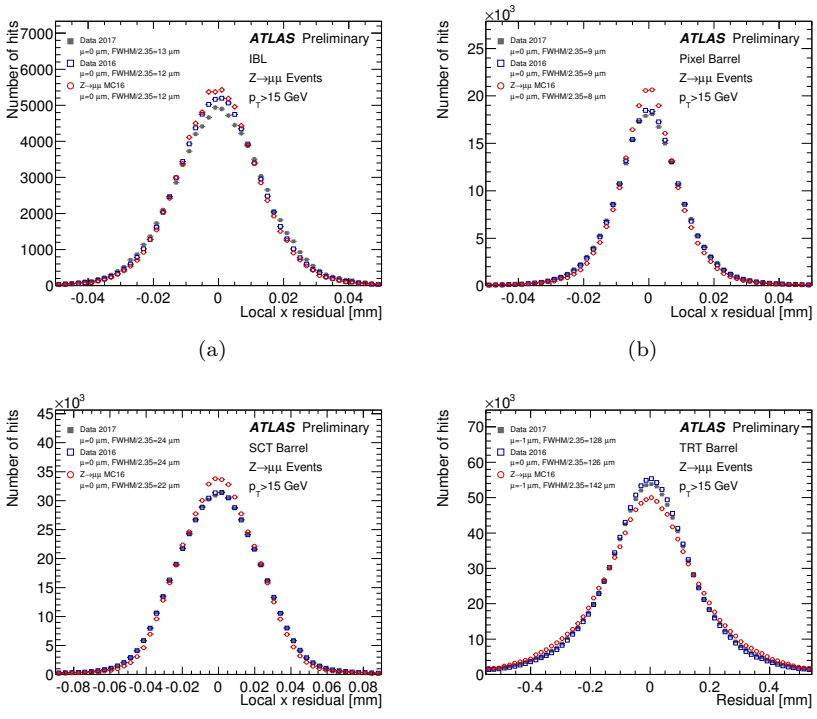

(a) (b) (c) (d)

Figure 7.6: Mean local-x residual of IBL (a) and Pixel (b), SCT (c) and TRT (d) barrels for early 2017 data compared to a run from 2016 and to simulated $Z \to \mu^+\mu^-$ events. 2017 data is shown in grey full squares, 2016 data in blue open squares and the Monte Carlo in red open circles.

7.2 2017 data reprocessing alignment

Usually, at the end of each year's data taking period of the LHC, ATLAS data are reprocessed to include the best available knowledge of the detector calibration in order to provide data of the highest possible quality. For the reprocessing campaign, the alignment team prepares a set of alignment constants for which any bias due to weak modes is removed or reduced as much as possible. These alignment constants will become the baseline on top of which time-dependent constants are delivered for every recorded run, following the same configuration than for the online calibration loop alignment (sec. 6.2).

A baseline derivation is performed for every identified stable period: it can be defined as a period in which the shape of every ID subdetector is constant. The presence of movements between subdetectors is not a problem, as they can be corrected with the usual CL time-dependent alignment. In 2017, two stable periods were identified:

- First period goes from the start of the collisions until mid September-
- Second one goes from that date until the end of the 2017 data taking period.

Around mid September, the ATLAS magnet was turned off and on, resulting in movements of the ID sensors and causing subdetector shape deformations. [1] The presence of subdetector shape misalignments between the two different periods made necessary to create two separated alignment baselines for the data reprocessing. Results shown on this section are from the second period, but the same procedure and similar results were achieved for the first one.

For the derivation of 2017 second period baseline, three consecutive runs were selected in order to derive the $\delta_{sagitta}$, d_0 and z_0 correction maps using the $Z \to \mu^+\mu^-$ method (section 3.9.3). The three selected runs were recorded in September 2017 and sum up to 1.4 fb^{-1} of stable beams luminosity. These maps are used as input for the alignment, forcing the impact parameters to change, and obtaining alignment constants in which the biases are reduced. The derivation of the baseline follows an iterative procedure in which the output alignment constants of an iteration are used to recalculate the correction maps, which are used as input for the next iteration of the alignment.

Figures 7.7, 7.8 and 7.9 show the $\delta_{sagitta}$, d_0 and z_0 correction maps derived before (left) and (after) the completion of the weak mode free baseline. Alignment constants available before the reprocessing baseline were the ones obtained with the online alignment performed at the calibration loop. The d_0 corrections were already small before the alignment campaign. Shown values in both maps are compatible with the statistical fluctuations of the $Z \to \mu^+\mu^-$ method. A clear reduction on the $\delta_{sagitta}$ and z_0 maps is seen after the alignment derivation. The biases are present mostly for large values of η, what correspond to the far end-cap region.

[1] The magnet was turned off as a prevention due to a fire incident in the ATLAS cavern that needed the fire brigade intervention.

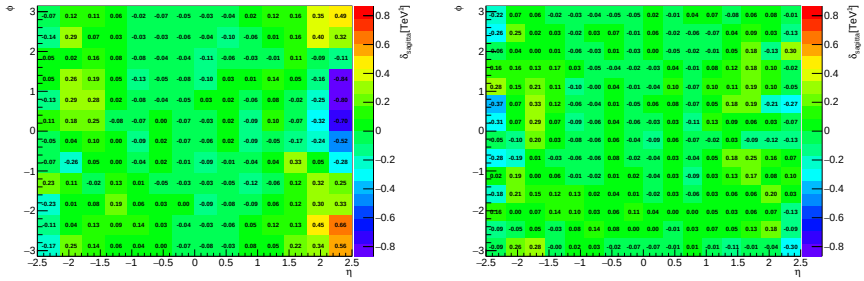

(a) (b)

Figure 7.7: Average $\delta_{sagitta}$ correction to compensate the bias as a function of ϕ and η before (a) and after (b) the derivation of a weak mode free baseline for the reprocessing campaign. These maps are derived with 1.4 fb^{-1} of pp collision at 13 TeV.

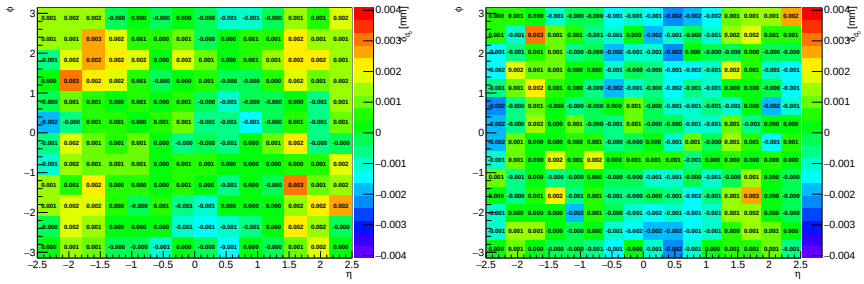

(a) (b)

Figure 7.8: Average d_0 correction to compensate the bias as a function of ϕ and η before (a) and after (b) the derivation of a weak mode free baseline for the reprocessing campaign. These maps are derived with 1.4 fb^{-1} of pp collision at 13 TeV.

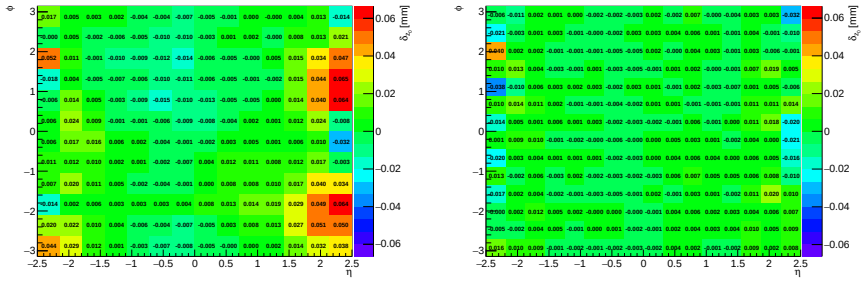

(a) (b)

Figure 7.9: Average z_0 correction to compensate the bias as a function of ϕ and η before (a) and after (b) the derivation of a weak mode free baseline for the reprocessing campaign. These maps are derived with 1.4 fb^{-1} of pp collision at 13 TeV.

Biases before the alignment were already relatively small if compared to the level seen in previous years at the pre-reproccesing stage. The main reason for this is the way the initial 2017 baseline alignment was derived (section 7.1). The derivation was started from the final alignment constants of 2016, for which the biases coming from weak modes were removed with the reprocessing. The use of alignment constraints as the beam spot position or the null maps prevented the introduction of new biases.

The alignment derivation was done with one of the three runs used to produce the correction maps, run 336852. All alignment jobs were done using the TZ-tool. Although the original plan was to use the whole run and to deliver the alignment baseline on top of the CL corrections, making use of the time-dependent corrections, due to technical problems this idea had to be abandoned. Instead, it was necessary to start from a fixed geometry for the whole run. In order to reduce the impact that the Pixel drift could have in the alignment derivation, only the last 500 LB of the run were used. As it can be seen in figure 4.10, the change in the vertical position of the Pixel is smaller at the end of the run, so an averaged position could be used for the last ∼500 minutes of the run. The measured change in Pixel T_y during these 500 LB was of 2.2 μm.

The alignment procedure for the reprocessing baseline was similar to the one described in previous sections. Alignment was performed in different steps, progressively increasing the level of the alignment until a module level alignment (L3) of IBL, Pixel and SCT was performed. Nevertheless, there are two main differences in this case:

- **Correction maps**: The alignment framework allows the use of $\delta_{sagitta}$, d_0 and z_0 correction maps. When maps are used, the track parameters are changed in the reconstruction, what affects the track-to-hit residual and forces the alignment algorithm to find a new geometry in which the track parameter bias are reduced.

- **Maps recalculation**: Once a map has been used in an alignment iteration, it can not be used again, as the values of the impact parameter biases are modified by the alignment. Therefore maps have to be recalculated after each iteration, slowing down the whole process. Order of 10 iterations are usually needed for reaching convergence, and in 2017 an average of one iteration per day was achieved.

Part III

Top quark physics

Chapter 8

Data and simulated samples

This chapter describes the data and MC simulation samples used in the analysis. All the samples used in this work are official samples produced by the ATLAS single top quark working group. Details about their production can be found in appendix A.

8.1 Data samples

This analysis is performed using data of the proton-proton (pp) collisions delivered by the LHC in 2012 at a centre-of-mass-energy of $\sqrt{s} = 8$ TeV and collected by the ATLAS detector. The full ATLAS 2012 data set is used, after detector and data-quality requirements: data are filtered using a good runs list (GRL) that requires LHC stable beams and data quality for all detectors and trigger sub-components. The amount of data used corresponds to an integrated luminosity of 20.2 fb^{-1}, with an uncertainty of the $\pm 1.9\%$ [71]. The events are required to pass either single-electron or single-muons triggers. The triggers already impose a threshold of 24 GeV on the transverse momentum (p_{T}) and isolation requirements. In order to recover sensitivity for high-p_{T} leptons, those triggers are completed with triggers without isolation requirements but with higher p_{T} thresholds: 60 GeV for electrons and 36 GeV for muons.

8.2 Simulated baseline samples

This section presents the baseline samples used to model the signal and background processes of this analysis. A summary of all signal and background baseline samples is presented in table 8.1. Additional samples have been produced in order to study and determine various sources of systematic uncertainties, but these ones are presented in appendix A.

For this analysis, two MC samples are produced for the signal t-channel single top quark process. The first one is used as the main baseline sample to determine the expected event yields and template distributions. It is generated

Process	Generator	Parton shower	Normalisation	PDF	tune	Detector
t-channel	POWHEG-BOX (r2556)	PYTHIA (v6.426)	NNLO+NNLL	CT10f4	P2011C	FullSim
t-channel	LO PROTOS (v2.2)	PYTHIA (v6.426)	NNLO+NNLL	CTEQ6L1	P2011C	ATLFAST-II
Wt-channel	POWHEG-BOX (r2819)	PYTHIA (v6.426)	NNLO	CT10	P2011C	FullSim
s-channel	POWHEG-BOX (r2819)	PYTHIA (v6.426)	NNLO	CT10	P2011C	FullSim
$t\bar{t}$	POWHEG-BOX (r3026)	PYTHIA (v6.427)	NNLO+NNLL	CT10	P2011C	FullSim
WW, WZ, ZZ	LO SHERPA (v2.14)	SHERPA	NLO	CT10	-	ATLFAST-II
W/Z+jets	LO SHERPA (v1.41)	SHERPA	NNLO	CT10	-	ATLFAST-II

Table 8.1: Summary table of the baseline simulated samples used in the analysis.

with the next-to-leading-order (NLO) generator POWHEG-BOX [72], which uses the four-flavour scheme (2→3 process, figure 1.4(b)) for the matrix element calculations [73]. The events are generated with the fixed four-flavour CT104f [74] parton distribution functions (PDFs). The renormalisation scale μ_{R} and the factorisation scale μ_{F} are set to the recommendation given in [73], and calculated event-by-event with:

$$\mu_R = \mu_F = 4\sqrt{m_b^2 + p_{\mathrm{T},\ b}^2} \tag{8.1}$$

where m_b and $p_{\mathrm{T},\ b}$ are the mass and the transverse momentum of the b-quark from the initial gluon splitting, respectively. The top quarks are decayed using MADSPIN preserving all spin correlations.

The second set of samples is used to compute the parton-level unfolding corrections and to check the reliability of the unfolding method. The leading-order (LO) generator PROTOS (v2.2) [75], together with the CTEQ6L1 PDFs [76, 77], is used to generate t-channel single-top samples implementing the SM Wtb couplings as well as various configurations of anomalous couplings. The baseline POWHEG-BOX sample can not be used to calculate the unfolding corrections due to the fact that there are ambiguities when defining the final-state spectator quark at parton level from a NLO generator, and that is necessary to define the top quark and W boson polarisation axes, as explained in chapter 11. The computation of the t-channel process in PROTOS incorporates just the 2→3 process. Anomalous couplings are enabled in both the production and decay Wtb vertices by varying simultaneously the real part of V_{L} together with either the imaginary or the real part of g_{R}. For each non-standard configuration, the two couplings are varied such that the total top quark decay width Γ_t is kept invariant. The factorisation scale is set to $\mu_{\mathrm{F}}^2 = -p_W^2$ for the initial-state light-quark, and to $\mu_{\mathrm{F}}^2 = p_{b\bar{b}}^2 + m_b^2$ for the gluon, where p_W is the momentum of the exchanged W boson and $p_{b\bar{b}}$ the momentum of the $b\bar{b}$ system coming from the gluon splitting.

The other two single top quark processes, the s-channel and the associated Wt production, as well as the $t\bar{t}$ production, are simulated using the NLO generator POWHEG-BOX (r2819, r3026) implementing the CT10 PDF sets. The t- and s-channel processes do not interfere even at NLO in QCD and are thus well defined with that precision [14]. In the simulation of the Wt process, the diagram removal scheme is used to eliminate overlaps between this process and

the $t\bar{t}$ production at NLO. For the baseline $t\bar{t}$ sample generation, the parameter h_{damp}, which effectively regulates the high-p_{T} gluon radiation, has been set to the top quark mass, m_t, as suggested by studies presented in [78]. The resummation damping factor, h_{damp}, is one of the parameters controlling the matrix element/parton showering matching in POWHEG and effectively regulates the high-p_{T} radiation. This setting was found to improve the modelling of the distribution of the transverse momentum of the $t\bar{t}$ system with respect to the default parameterization ($h_{\mathrm{damp}} = \infty$).

The parton shower (PS) and the underlying event (UE) are simulated with PYTHIA (v6.426) [79] using the PERUGIA 2011C tune [80] with the CTEQ6L1 PDF sets for all the POWHEG-BOX samples (t-, s- and Wt-channels and $t\bar{t}$) and the t-channel PROTOS samples. All these processes were simulated assuming a top quark mass of 172.5 GeV, and the decay of the top quark was assumed to proceed exclusively through $t \to Wb$. The baseline POWHEG-BOX samples are passed through the GEANT4-based full simulation of the ATLAS detector, while the PROTOS samples and all the samples used to estimate the various modelling uncertainties are processed with the `ATLFAST-II` simulation of the detector.

Other important backgrounds for the analysis of t-channel signal events are the production of a vector boson, W or Z, in association with jets (W/Z+jets). In this analysis, the multileg SHERPA (v1.4.1) [81] generator, with its own tune and the CT10 PDF sets, is used to produce the baseline single-boson samples. SHERPA uses the CKKW method [82] to remove overlaps between the n and $n+1$ parton samples. Double counting between the inclusive $W/Z + n$ parton samples and samples with associated heavy-quark pair production is done consistently by using massive c- and b-quarks in the shower. Filtered and vetoed W+jets and Z+jets samples are thus produced in order to get separate sets for production of a W/Z boson in association with light-quark jets (W/Z+LF) or heavy-quark jets (W/Z+HF divided in W/Z+bb and W/Z+cc samples). SHERPA is not only used to generate the hard process, but also for the complete event generation including the modelling of the underlying event.

The other electroweak processes which constitute a non-negligible background for t-channel signal events are the diboson (VV) productions (WW, WZ and ZZ). The diboson samples are produced using SHERPA (v.2.14) and contain up to three additional partons. The samples are filtered for leptons with a transverse momentum greater than 5 GeV and a dilepton invariant mass above 0.1 GeV for the Z/γ^*.

Finally the last contributing background process is the QCD-produced multijet production, which in hadronic collisions is characterised by a cross section of several orders of magnitude above top quark and vector-boson productions. Both the normalisation and the modelling are estimated from data using the matrix method [83], using control data samples enriched in multijets events. More details about the method used are presented in section 10.1.

Chapter 9

Event selection

In this analysis, the signal sought is that of the single top quarks produced in the t-channel with a leptonic decay. It is important to identify a clear signature of the signal events in order to select them among all ATLAS data. The main production channel of single top quarks at the LHC is the $q+g \to q'+t+\bar{b}$ channel as shown in figure 1.4(b). Due to its heavy mass, the top quarks decays immediately to a W boson and a b-quark. Only the events in which the W boson decays leptonically are considered for the analysis. Therefore, the signal signature is composed by:

- Two jets, one of them being b-tagged, a lepton and a neutrino, that appears as $E_{\mathrm{T}}^{\mathrm{miss}}$.
- The second jet corresponds to the spectator quark, that is usually a light-quark, and hence, a non-b-tagged jet.
- The $\bar{b}$-quark from the splitting gluon is typically almost collinear with the beam, leaving the detector undetected. Thus, no additional b-jet matching the $\bar{b}$-quark is requested.
- The lepton mentioned before can be either a electron, a muon or a τ-lepton. Events in which the W boson decays into a τ-lepton are only considered in the analysis if the τ-lepton subsequently decays to a electron or a muon (35% branching fraction [84]).
- The leptonic decay of the τ-lepton produces two additional neutrinos, what implies a less precise measurement of the W boson kinematics, due to the inherent difficulties of the neutrino reconstruction.

Events from other sources than the single-top t-channel production can mimic the signal signature. The two main background sources are $t\bar{t}$-production and the production of a W boson in association with jets. Events from $t\bar{t}$-production can easily be interpreted as signal as there are real top quark involved, of which, one can decay leptonically, while the other one could fake the spectator quark. W+jets production can also fake the t-channel signal if a b-tagged jet is present in the final state or if a non-b-jet is wrongly mistagged.

Multijet production contributes to the background if, together with two jets, an additional jet is misidentified as a fake lepton. Other minor but important background sources are the single top quark s- and Wt-channel production, that once again can fake the signal as there are real top quarks in the final state; the diboson production, that can consist of either WW, WZ or ZZ; and the Z+jets production.

The design of a proper event selection has to be such that it enhances the probability of rightly selecting a genuine candidate event, while diminishing the probability of accepting a background one as signal. Other important factor to consider is the efficiency of the signal selection, as it has to be always as high as possible in order not to compromise data statistics.

The event selection used in this analysis follows a two-step procedure, respectively named *preselection* and *selection*. In the *preselection*, candidate events are selected based on the expected signal topology at the level of the basic physics objects defined in section 2.3. In the final state, an isolated electron or muon is required, together with significant $E_{\mathrm{T}}^{\mathrm{miss}}$, and two jets, one of them being b-tagged. Additional cuts are applied in *selection*, to further isolate the t-channel signal events from background contamination.

Candidate events must:

- Fire the appropriate single-lepton trigger.
- Pass the the quality criteria defined in the good-runs-lists.
- Pass generic event quality requirements used to remove mis-reconstructed events and to reject non-collision background events.
- Contain at least one good primary vertex candidate reconstructed from at least five associated tracks with $p_{\mathrm{T}} > 400$ MeV.
- Contain no jets with $p_{\mathrm{T}} > 20$ GeV affected by noise burst in the EM calorimeter.

In addition, alternative specific event selections are used to define samples allowing to determine background contributions via data-driven methods, and to control the good modelling of the data by the MC simulations. Two of the control samples are also used to constrain the normalisation of the two main background contributions in the selected signal region, the $t\bar{t}$ and the W+jets productions. The normalisation procedure is described in section 10.2.

9.1 Signal preselection

The definitions of the objects used in the analysis, including electrons, muons, jets, b-tagged jets and $E_{\mathrm{T}}^{\mathrm{miss}}$, as well as the basic event selection are chosen to match those used for the t-channel cross-section measurements reported in [85]. Preselected signal events are required to:

- Contain exactly one isolated lepton candidate (electron or muon).

- Contain exactly two selected jets, one of them being b-tagged with the MV1c b-tagging algorithm.
- Have a missing transverse momentum $E_{\mathrm{T}}^{\mathrm{miss}} > 30$ GeV.
- Pass the energy/momentum thresholds and pseudorapidity acceptances described in section 2.3.
- The selected lepton must match within $\Delta R < 0.15$ to the appropriate trigger object.

To reduce the contribution from mismeasured multijet events, two additional cuts are applied. The first cut is applied on the transverse mass of the lepton–$E_{\mathrm{T}}^{\mathrm{miss}}$ system: $m_{\mathrm{T}}(W) > 50$ GeV. This transverse mass, referred to as the W boson transverse mass, is defined as follows:

$$m_{\mathrm{T}}(W) = \sqrt{2p_{\mathrm{T}}(\ell)E_{\mathrm{T}}^{\mathrm{miss}}\left(1 - \cos\Delta\phi(\ell, E_{\mathrm{T}}^{\mathrm{miss}})\right)} \ , \tag{9.1}$$

where $\Delta\phi(\ell, E_{\mathrm{T}}^{\mathrm{miss}})$ is the difference in azimuthal angle between the lepton transverse momentum and the missing transverse momentum.

The second cut further reduces the multijet events by applying an additional isolation cut to low-p_{T} leptons on events in which the lepton is back-to-back to the leading jet. This is done through the following condition:

$$p_{\mathrm{T}}(\ell) / \left(1 - \frac{\pi - |\Delta\phi(\ell, \mathrm{jet}_1)|}{\pi - 1}\right) > 40 \text{ GeV} \tag{9.2}$$

where $\Delta\phi(\ell, \mathrm{jet}_1)$ is the difference in azimuthal angle between the lepton and the leading jet momentum components on the transverse plane. When $\Delta\phi(\ell, \mathrm{jet}_1)$ is close to π, as would happen for back-to-back lepton and jet, the term $\pi - |\Delta\phi(\ell, \mathrm{jet}_1)|$ is close to zero and, therefore, the denominator is approximately one, so only leptons with transverse momentum above ∼40 GeV pass the cut. The momentum threshold linearly decreases together with $|\Delta\phi(\ell,\ \mathrm{jet}_1)|$ until $|\Delta\phi| = 1$. From this point, the cut is not longer applied, as the denominator changes sign, implying that every event would be rejected independently of the lepton p_{T}. For low $|\Delta\phi(\ell, \mathrm{jet}_1)|$ events, just the regular 25 GeV threshold in the lepton transverse momentum is applied.

This set of preselection requirements define the so-called *preselected* signal region.

9.2 W boson and top quark reconstruction

The selection of the signal events require to reconstruct the kinematics of the W boson and of the top quark. They are reconstructed from the identified and selected objects: lepton, b-tagged jet and missing transverse momentum. The kinematics of the W boson and of the top quark are also needed for the definition of the various angular observables measured in this analysis. Their reconstruction is presented in this section.

The lepton and neutrino four-momenta are used to reconstruct the W boson. Since the neutrino escapes undetected, the x- and y-components of the missing transverse momentum are assumed to correspond to the transverse momentum of the neutrino, as the total transverse momentum of the collision products has to be null, by conservation of the two colliding protons transverse momentum. In the other hand, the z-component can not be directly measured. The unmeasured longitudinal component of the neutrino momentum is computed by imposing a W boson mass constraint on the lepton-neutrino system.

$$\begin{aligned} W \to l\nu \quad &\longrightarrow \quad p^W = p^l + p^\nu \\ (p^W)^2 = (p^l + p^\nu)^2 \quad &\longrightarrow \quad M_W^2 = m_l^2 + 2(E^l E^\nu - \mathbf{p}^l \cdot \mathbf{p}^\nu) \end{aligned} \tag{9.3}$$

where the mass of the neutrino m_ν has already been neglected. As was said before, it is assumed that the missing transverse momentum matches the neutrino transverse momentum, so its total energy and its three-momentum are given by

$$\begin{aligned} E_\nu &= \sqrt{(E_T^{\text{miss}})^2 + (p_z^\nu)^2} \\ \mathbf{p}^\nu &= (E_T^{\text{miss}} \cos\phi_{E_T^{\text{miss}}},\ E_T^{\text{miss}} \sin\phi_{E_T^{\text{miss}}},\ p_z^\nu) \end{aligned} \tag{9.4}$$

Therefore, equation 9.3 can be written as

$$M_W^2 = m_l^2 + 2\left[E^l\sqrt{(E_T^{\text{miss}})^2 + (p_z^\nu)^2} - (p_x^l p_x^\nu + p_y^l p_y^\nu + p_z^l p_z^\nu)\right] \tag{9.5}$$

where all the terms are known except from p_z^ν. If equation 9.5 is squared, it can be rewritten as quadratic equation, leading to two possible solutions for p_z^ν:

$$p_z^\nu = \frac{p_z^l R \pm E_l\sqrt{R^2 - 4(E_T^{\text{miss}})^2(E_l^2 - (p_z^l)^2)}}{2(E_l^2 - (p_z^l)^2)} \tag{9.6}$$

where

$$R = M_W^2 - m_l^2 + 2(p_x^l p_x^\nu + p_y^l p_y^\nu) \tag{9.7}$$

has been defined in order to have a more compact notation.

Equation 9.6 returns two solution for the neutrino longitudinal momentum. Additionally, if the radicand becomes negative, both solutions become complex. When two possible real solutions are found, the solution giving the smallest magnitude of the longitudinal neutrino momentum is taken. In case of obtaining complex solutions, the magnitude of the measured E_T^{miss} is reduced until the radicand becomes null in order to obtain a physical solution. These complex solutions appear because of the assumption $E_T^{\text{miss}} = p_{\text{T}}^\nu$, as there can be other contributions to E_T^{miss} such as extra neutrinos from b-hadrons or τ decays. The non-perfect calibration and resolution of the E_T^{miss} measurement can also induce these complex solutions. Further details about the neutrino reconstruction can be found here [86].

The kinematics of the top quark candidate is reconstructed by combining the four-momentum of the reconstructed W boson with the four-momentum of the selected b-tagged jet. Events with exactly two jets are selected, one of them being b-tagged, therefore there is no ambiguity in the association of jets to quarks.

9.3 Signal selection

In addition to the basic single top t-channel event *preselection* (section 9.1), additional requirements are applied to further separate the signal from the background contributions.

An important source of background comes from $t\bar{t}$ events, in particular dileptonic events in which only one of the leptons passes the object selections required for signal candidates. In order to reduce this contribution, a dilepton veto is used: electrons and muons with $p_{\mathrm{T}} > 10$ GeV and fulfilling the loosened object requirements described in sections 2.3.1 and 2.3.2 are selected as *loosened leptons*. Loosened leptons overlapping with any of the signal lepton or jet candidates ($\Delta R < 0.4$) are removed from the selection. Events containing one or more loose leptons are rejected. This dilepton veto, was initially developed for the search for single top s-channel events [87]. With the dilepton veto, the loss of signal events is less than 1%, whereas an important rejection of the $t\bar{t}$ (18%), single top (11%) and Z+jets (24%) background events is obtained. The rejection factors are very low for all other backgrounds (W+jets, diboson and multijet).

To finally select the signal events, the following four selection cuts are applied (ordered according to their separation power against the main backgrounds):

- The pseudorapidity of the non b-tagged jet must satisfy $|\eta(\text{non } b\text{-jet})| > 2.0$, since the spectator jet tends to be forward in the t-channel process.
- The difference in pseudorapidity between the two jets, $|\Delta\eta(b\text{-jet,non } b\text{-jet})|$, must be larger than 1.5, to reduce the contribution from $t\bar{t}$ background events.
- The mass of the reconstructed top quark is required to be within 130 GeV and 200 GeV. As explained in section 9.2, the top quark is reconstructed from the lepton-neutrino-b-jet system, and therefore, when concerning the selection cut it will be referred to as $m(l\nu b)$.
- The sum of the transverse momentum of all selected objects, H_T(lepton, $E_{\mathrm{T}}^{\mathrm{miss}}$, jets), must be larger than 195 GeV, to further reduce the background events, in particular the W+jets contribution.

The choice of the above four selection variables is based on the studies performed for the 7 TeV cut-based t-channel analysis published in [88] and they were used again in the studies carried out for the 8 TeV cross-section measurement based on neural networks [85]. These final cuts define the signal region. Table 9.1 shows the event yields of the signal and background processes passing the final selection cuts and filling the signal region. No normalisation scale factors are applied at this stage. Electron and muon channels have been combined. The t-channel events represent the 56% of the signal region event yields. The two main backgrounds are the $t\bar{t}$ and the W+jets productions, representing the 18% and the 17% of the total events in the signal region, respectively. A signal to background ratio of 1.3 is achieved at this stage. Figure 9.1 shows the combined electron plus muon selected events in the preselection as a function of the

four variables that are used for the final cuts. Individual plots for electrons or muons only are presented in appendix C. The dilepton veto is already applied when making the plots. The regions indicated by the arrows and the vertical lines show the portion of events that pass each of the four final cuts. At this stage a good overall agreement is seen between the data and the theoretical predictions. The t-channel, W+jets and top-background processes contributions are scaled with the constrained normalisation factors presented in section 10.2.

	Signal	$t\bar{t}$ CR	Anti-signal CR	W+jets VR
t-channel	5980 ± 22	1922 ± 13	13632 ± 33	10559 ± 29
$t\bar{t}$	1894 ± 11	59589 ± 62	41165 ± 51	20291 ± 36
Wt, s-channel	262 ± 12	3018 ± 46	6808 ± 64	3932 ± 51
W+jets	1854 ± 47	6370 ± 67	44510 ± 220	250460 ± 730
Z+jets, Diboson	190 ± 9	1121 ± 34	4915 ± 57	17770 ± 17
Multijet	420 ± 290	880 ± 620	9300 ± 6500	21000 ± 15000
Total Expected	10600 ± 300	72900 ± 630	120000 ± 6500	324000 ± 15000
ATLAS data	10527	74121	124467	372847
S/B	1.30 ± 0.08	0.0264 ± 0.003	0.113 ± 0.006	0.0326 ± 0.0015

Table 9.1: Predicted and observed event yields in the signal region, the $t\bar{t}$ and anti-signal control regions, and in the W+jets validation region. The electron and muon channels are combined. For the simulated samples, the uncertainties corresponds to the errors due to the limited size of the MC samples. For the multijet background case, which is obtained from a data-driven technique, an uncertainty of the 70% is assigned to the normalisation.

9.4 Control regions selection

Two specific background-enriched control regions are defined in order to estimate the contributions of the most important background processes in the t-channel signal region by computing scale factors for the overall normalisation. This is discussed in detail in section 10.2. In addition to these two control regions a validation region is used to further control the modelling of the W+jets processes. These three specific background-enriched regions are:

- A control region enriched in $t\bar{t}$ events: This region is defined by considering preselected events containing two additional non b-tagged jets (i.e. four jets are required in total, being just one of b-tagged). The threshold value applied to the MV1c algorithm is the same one than the used for the signal (section 2.3.4). The expected contribution of the signal process in this $t\bar{t}$ control region is about 3%. The $t\bar{t}$ contribution is expected to represent 82% of the total. Figure 9.2 shows the distribution in the $t\bar{t}$ control region of the four variables used for the final signal selection cuts for electrons and muons combined. Individual plots for electrons or muons only are presented in appendix C. The t-channel, W+jets and

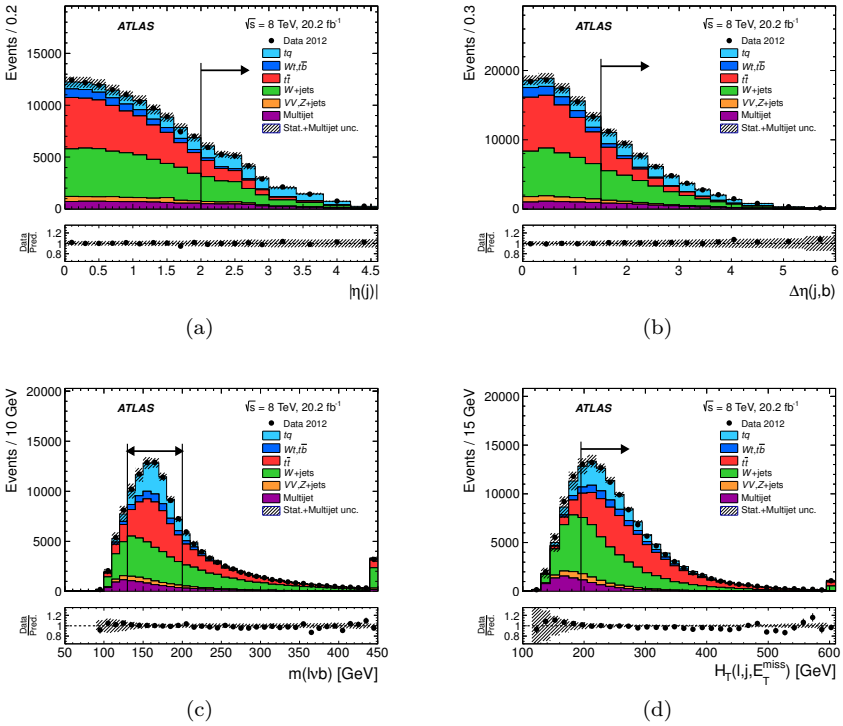

Figure 9.1: Distributions of the variables used to select the signal sample from the preselected events (the dilepton veto is applied) (a) non b-tagged jet pseudorapidity, (b) difference in pseudorapidity between the b-tagged jet and the non b-tagged jet, (c) reconstructed top quark mass, and (d) sum of the transverse momentum of all selected objects. The vertical lines and the arrows represent the selected signal region. The predicted distributions are re-scaled using the values given in table 10.1 (section 10.2). The uncertainty bands correspond to the errors due to the limited size of the MC samples added in quadrature with the data-driven normalisation uncertainty estimated for the multijet contribution and with the normalisation factors uncertainties. The last bin of the histogram includes the overflows. The lower panel shows the ratio of data to MC prediction.

top-background processes contributions are scaled with the constrained normalisation factors presented in section 10.2.

- An enriched control region in W+jets events: This region is defined in order to control the modelling of the W+jets background. It is constructed with the events passing the *preselection* requirements (section 9.1) but failing any of the four cuts used in the *selection* (section 9.3). This definition provides events with a close W+jets flavour composition to the signal region one. Together with the $t\bar{t}$ control region, this one is used to constrain the normalisation of the W+jets and $t\bar{t}$ background contributions in the signal region. The expected contribution of the signal process in this control region is about 11%. The W+jets and $t\bar{t}$ contributions are expected to represent around 37% and 34% of the total number of events. This control region is labelled as anti-signal control region. Figure 9.3 shows the distribution of the four variables used for the final signal selection cuts for electrons plus muons entering the anti-signal control region. Individual plots for electrons or muons only are presented in appendix C. The t-channel, W+jets and top-background processes contributions are scaled with the constrained normalisation factors presented in section 10.2.

- In order to further validate the modelling of the W+jets background, a third region enriched in W+jets events is defined as a validation region. This region is filled by events that satisfy the *preselection* cuts (section 9.1), but with a softer b-tagging cut. To avoid any overlap with the signal region, all events passing the signal preselection are not included here. The working b-tagging point corresponds to a b-tagging efficiency of 80% for $t\bar{t}$ events. The signal fraction in this so-called W+jets validation region is expected to be of the order of 3%. This region has much larger enrichment in W+jets events (77%) than the anti-signal region, but the flavour composition is totally different to the signal region, and therefore it is not used to constrain the W+jets normalisation at the signal region. Figure 9.4 shows the distribution in the W+jets validation region of the four variables used for the final signal selection cuts. The distributions are normalised in order to match the observed event yields.

The electron and muon channels combined event yields of the two control regions and the W+jets validation region are shown in table 9.1. No normalisation scale factors are applied to the event yields shown in the table.

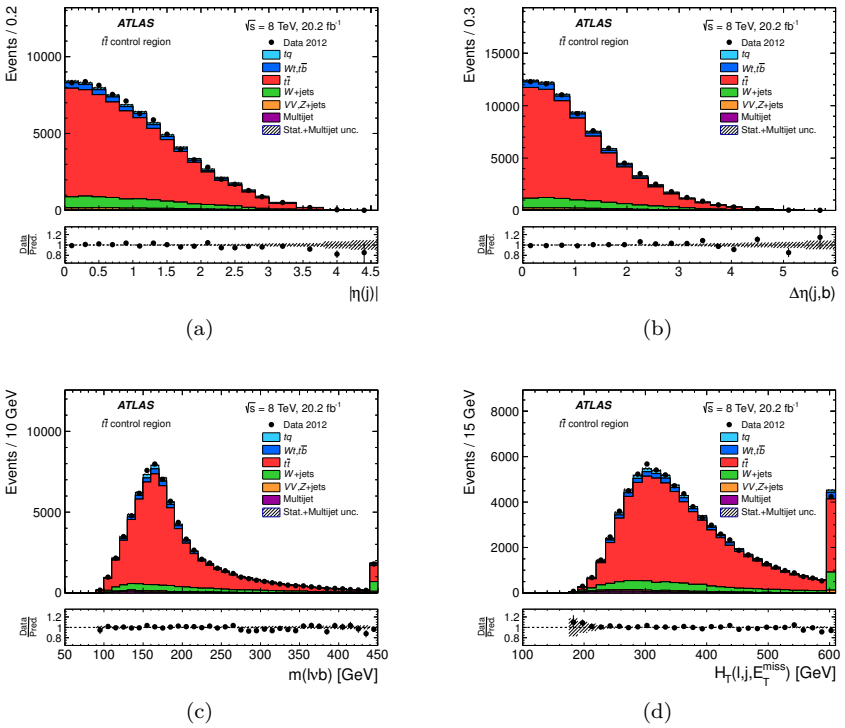

Figure 9.2: Distributions of the selection variables in the $t\bar{t}$ control region: (a) non b-tagged jet pseudorapidity, (b) difference in pseudorapidity between the b-tagged jet and the non b-tagged jet, (c) reconstructed top quark mass, and (d) sum of the transverse momentum of all selected objects. The predicted distributions are re-scaled using the values given in Table 10.1 (Section 10.2). The uncertainty bands correspond to the errors due to the limited size of the simulation samples added in quadrature with the data-driven normalisation uncertainty estimated for the multijet contribution and with the normalisation factors uncertainties. The last bin of the histogram includes the overflows. The lower panel shows the ratio of data to MC prediction.

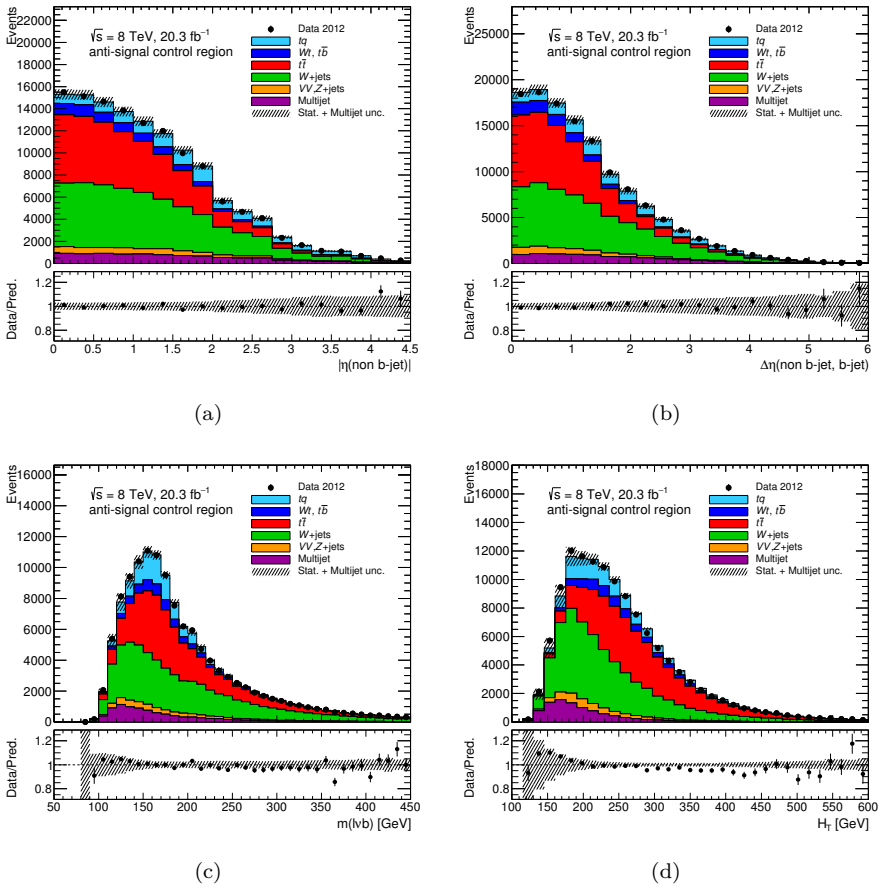

Figure 9.3: Distributions of the selection variables in the anti-signal control region: (a) non b-tagged jet pseudorapidity, (b) difference in pseudorapidity between the b-tagged jet and the non b-tagged jet, (c) reconstructed top quark mass, and (d) sum of the transverse momentum of all selected objects. The predicted distributions are re-scaled using the values given in Table 10.1 (Section 10.2). The uncertainty bands correspond to the errors due to the limited size of the simulation samples added in quadrature with the data-driven normalisation uncertainty estimated for the multijet contribution and with the normalisation factors uncertainties. The lower panel shows the ratio of data to MC prediction.

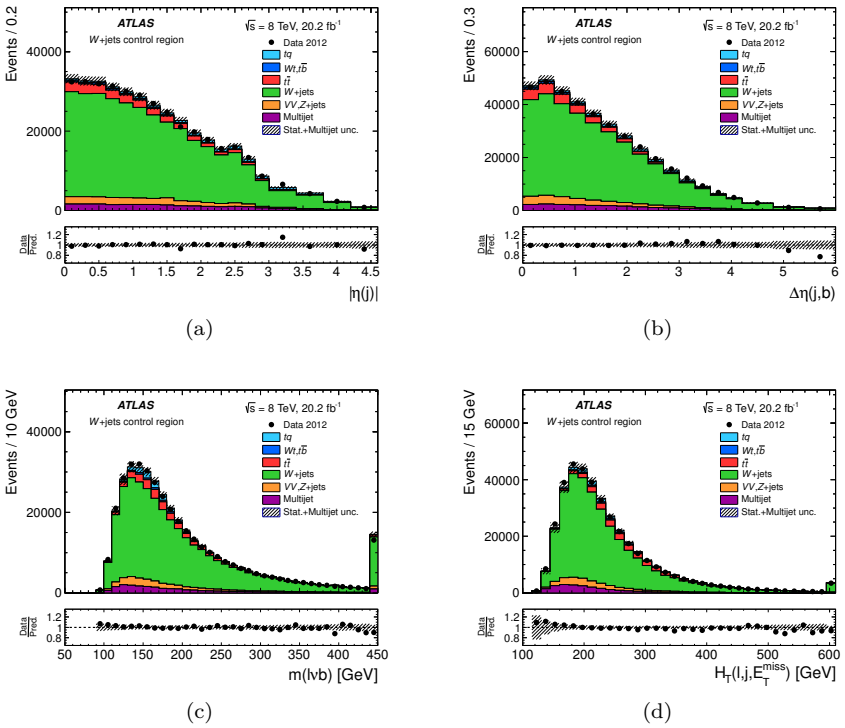

Figure 9.4: Distributions of the selection variables in the W+jets validation region: (a) non b-tagged jet pseudorapidity, (b) difference in pseudorapidity between the b-tagged jet and the non b-tagged jet, (c) reconstructed top quark mass, and (d) sum of the transverse momentum of all selected objects. The predicted distributions are normalised to match the observed number of events, as explained in section 10.2. The uncertainty bands correspond to the errors due to the limited size of the simulation samples added in quadrature with the data-driven normalisation uncertainty estimated for the multijet contribution and with the normalisation factors uncertainties. The last bin of the histogram includes the overflows. The lower panel shows the ratio of data to MC prediction.

Chapter 10

Samples normalisation and modelling

For all processes, signal and backgrounds except the multijet production, the normalisation is initially determined by scaling the simulated MC samples described in section 8.2 to their cross-section predictions. The event distribution modelling is taken from the simulated samples.

Single-top processes:

- The simulated t-channel single-top events are normalised to the cross-section calculated at NLO in QCD, through NNLL resummation. The predicted t-channel production cross-section at $\sqrt{s} = 8$ TeV is $87.7^{+3.4}_{-1.9}$ pb [89].
- The associated Wt-channel events are normalised with the predicted NNLO production cross-section of 22.4 ± 1.5 pb [90].
- The s-channel production to the predicted NNLO cross-section of 5.61 ± 0.22 pb [91].
- All three single top quark cross-sections assume a top quark mass of 172.5 GeV and use the MSTW2008 NNLO set [92] of PDFs.
- The quoted uncertainties include the QCD scale uncertainty and the correlated PDF–α_s uncertainty.

$t\bar{t}$ production:

- The $t\bar{t}$ events are normalised with the $t\bar{t}$ production cross-section calculated at NNLO in QCD including resummation of NNLL soft gluon terms with TOP++2.0 [93–98]. Its predicted value is 253^{+13}_{-15} pb calculated according to [98].
- The quoted uncertainty, evaluated according to the PDF4LHC prescription [99], corresponds to the sum in quadrature of the α_S uncertainty and the PDF uncertainty, calculated from the envelope of the uncertainties at

68% CL of the MSTW2008 NNLO, CT10 NNLO [100] and NNPDF2.3 5F FFN [101] PDF sets.

Vector-boson production:

- The inclusive cross-sections of vector-boson production are calculated to NNLO with the FEWZ program [102] and the MSTW2008 NNLO PDF set.
- The diboson samples are normalised to the NLO cross-sections predictions calculated using the MCFM program [103].
- A normalisation uncertainty of the 20% is assigned to the W+jets background. This uncertainty is assigned from parameter variations of the SHERPA generator covering the measured W+jets cross-sections [104].
- A normalisation uncertainty of 20% is also assumed for Z+jets and diboson processes.

Multijet background:

- The normalisation as well as the event modelling of the multijet background is extracted from data with the matrix method, which is described in the next section.

10.1 Multijet modelling and normalisation

Multijet events pass the signal selection in two cases. An extra jet is misidentified as an isolated lepton. A non-prompt lepton appears to be isolated. Both are referred to as fake leptons. In the muon channel, the non-prompt muons come mostly from the decay of heavy flavour hadrons. On the other hand, non-prompt electrons also arise from photon conversions into electron-positron pairs inside a jet and from jets with electromagnetic fractions.

The multijet contributions in the electron and muon channels are estimated with the data-driven matrix method [83, 105]. In this approach, a set of equations is solved, which relates the observed sample composition in terms of selected leptons of two different categories, loose and tight, to its true composition in terms of prompt (coming from a W boson decay) and fake leptons. The tight category corresponds to the signal selection described in sections 2.3.1 and 2.3.2. To define the loose category, the isolation requirements are removed. In the electron case, a loosened identification quality is also used. The idea behind the matrix method is that both tight and loose categories are composed of prompt and fake leptons, being the tight lepton sample a sub-sample of the loose one:

$$\begin{aligned} N^{\text{loose}} &= N^{\text{loose}}_{\text{prompt}} + N^{\text{loose}}_{\text{fake}} \quad , \\ N^{\text{tight}} &= N^{\text{tight}}_{\text{prompt}} + N^{\text{tight}}_{\text{fake}} \quad , \end{aligned} \tag{10.1}$$

where $N^{\text{loose}}_{\text{prompt}}$ is the number of prompt leptons passing passing the loose criteria and $N^{\text{loose}}_{\text{fake}}$ is the number of fake leptons entering in the loose category. Similar definitions are applied in the tight case. As the tight category is a subset of the loose one, the ratio between the tight and loose prompt components can be expressed as an efficiency, ϵ_{prompt}, that measures the probability of a prompt loose lepton of being selected as a tight lepton. The fake efficiency, ϵ_{fake}, is defined in the same way. According to that, equation 10.1 can be rewritten as

$$N^{\text{tight}} = \epsilon_{\text{prompt}} N^{\text{loose}}_{\text{prompt}} + \epsilon_{\text{fake}} N^{\text{loose}}_{\text{fake}} \quad . \tag{10.2}$$

Combining equations 10.1 and 10.2, the number of fake leptons passing the tight selection requirements can be expressed as:

$$N^{\text{tight}}_{\text{fake}} = \frac{\epsilon_{\text{fake}}}{\epsilon_{\text{prompt}} - \epsilon_{\text{fake}}} \left(\epsilon_{\text{prompt}} N^{\text{loose}} - N^{\text{tight}} \right) \quad , \tag{10.3}$$

These efficiencies are determined using dedicated event samples enriched in prompt and fake leptons and containing at least two jets in order to match the signal signature. The prompt efficiency ϵ_{prompt} can be measured in data applying a selection where the contamination of fake leptons is small and counting the fraction of loose events that also pass the tight selection. Such a sample is constructed with events coming from the leptonic decay of a Z-boson. A tag-and-probe method is used to extract the prompt efficiencies. Strict selection criteria is applied on one of the two decay leptons, the 'tag' one, and the second lepton candidate, 'probe', is used for the efficiency measurements. In order not to bias the probe sample, each valid combination is used: A certain lepton of a pair could be used as tag in one case an as probe in the other.

The fake efficiencies ϵ_{fake} in the electron channel are estimated from samples defined by requiring a low $m_{\text{T}}(W)$ value ($m_{\text{T}}(W) < 20$ GeV) on events containing a single loose electron. An additional inverted triangular cut is also applied to further enrich this selection in multijet events ($E_{\text{T}}^{\text{miss}} + m_{\text{T}}(W) < 60$ GeV).

The fake muon background is dominated by heavy flavour quark decays which tend to have a large impact parameter. In the muon channel, the fake efficiencies are measured from events containing exactly one loose muon having a high significance of the transverse impact parameter relative to the primary vertex ($d_0^{sig} > 5$).

Usually, both ϵ_{prompt} and ϵ_{fake} depend strongly on the lepton and jets properties such as the lepton η and p_{T}, or the distance between the lepton and the closest jet, ΔR_{min}. Therefore, not only the number of fake lepton has to predicted but also of the shape of the most relevant kinematic distributions in order to achieve a proper modelling of the multijet background. The prompt efficiencies of electrons and muons are extracted as a function of the three properties mentioned above. The electron fake efficiency is parameterised according to the electron pseudorapidity, the transverse momentum of the leading jet, and the ratio of the leading jet p_{T} to ΔR_{min}. For the muon channel, the fake efficiency is derived as a function of the muon pseudorapidity and transverse momentum, the distance ΔR_{min}, and the significance of the d_0 parameter.

The multijet contributions in the electron and muon channels can also be estimated using the mixed data-simulation jet-electron and purely data-driven

anti-muon models, respectively [106]. These alternative multijet estimates lead to significant differences on the predicted event yields with respect to the matrix method results. On the other hand, a good overall modelling of the data is found with the angular distributions provided by the jet-electron and anti-muon methods, although notable differences in shape are found for these distributions with respect to the matrix method.

From these various studies, an overall normalisation uncertainty of 70% is assigned on the estimate of the multijet background contribution. In addition, a systematic uncertainty is considered in the analysis to take into account the differences in multijet shape modelling found between the matrix method and the jet-electron/anti-muon models (section 14.3).

10.2 Constrained normalisation factors

The overall normalisation factors of the two main background processes are derived with a data-driven method, based on a maximum-likelihood fit, together with the overall normalisation of the t-channel contribution. The event yields in the signal region and the $t\bar{t}$ and anti-signal control regions are simultaneously fitted in other to extract three normalisation factors:

- The W+jets normalisation, for which the light and heavy flavour contributions have been merged.
- The top quark background normalisation, that includes $t\bar{t}$, single top Wt and s-channel contributions.
- The overall t-channel normalisation.
- The two sets of backgrounds have been merged in order to reduce the statistical fluctuations.
- The t-channel normalisation is included in order to constrain the low, but non-negligible contribution of t-channel events in the two control regions.

In the fitting procedure, the scale factors associated with the predicted W+jets and top quark background event yields are considered as constrained parameters of the fit, while all other background contributions (Z+jets, diboson and multijet productions), which have lower contributions, are fixed to their simulated or data-driven predictions.

The likelihood function used in the fit is given by the product of the Poisson distributions of the individual signal and background rates per selection (signal, anti-signal and $t\bar{t}$), multiplied by Gaussian priors that constrain the background rates:

$$L(\beta^s;\beta^b_j) = \prod_{i=1}^{N_{selections}} \frac{e^{-\mu_i}\cdot\mu_i^{n_i}}{n_i!} \cdot \prod_{j=1}^{N_{backgrounds}} G\left(\beta^b_j;1,\Delta_j\right) \tag{10.4}$$

$$\text{with} \quad \mu_i = \mu_i^s + \sum_{j=1}^{N_{backgrounds}} \mu^b_{ij} \quad , \quad \mu^s_i = \beta^s\cdot\tilde{\nu}^s_i \;\; and \;\; \mu^b_{ij} = \beta^b_j\cdot\tilde{\nu}^b_{ij} \tag{10.5}$$

This likelihood function includes for each selection (signal, anti-signal and $t\bar{t}$) a Poisson term in the observed number of events (n_i) with the expectation value (μ_i) defined as the sum of the expected contributions from signal (μ_i^s) and all simulated or data-driven backgrounds (μ_{ij}^b). The index j runs over the background processes. For a given process, the expectation value in each selection is given by the product combining the predicted number of events ($\tilde{\nu}_i^s$ for signal or $\tilde{\nu}_{ij}^b$ for backgrounds) in the considered sample and a scale factor (β^s or β_j^b).

The Gaussian constraints Δ_j used in the likelihood fit for the top quark and W+jets background normalisation factors are set to the theoretical cross section uncertainties, which have been discussed at the beginning of this section. For the merged top quark background processes, a constraint value of 6%, combining the cross section uncertainties in proportion to the contribution of each individual process, is applied; for the W+jets contribution, a constraint of 20% is considered. The overall normalisation of the signal is completely left free in the fit. The t-channel overall normalisation could in principle be used to determine the t-channel cross section, but the level of precision achieved is lower than that of the dedicated ATLAS analysis. For the Z+jets, diboson and data-driven multijet backgrounds, which are not allowed to vary, the constraint values are set to 0.

The scale factors extracted for the W+jets and top quark backgrounds and the t-channel signal contribution are reported in table 10.1 for the electron and muon channels and for the two lepton flavours merged.

Process	e-channel	μ-channel	e+μ-channels
t-channel	0.952±0.028	0.952±0.026	0.952±0.019
W+jets	1.062±0.019	1.130±0.016	1.101±0.012
$t\bar{t}$,Wt,s-channel	1.015±0.007	1.008±0.007	1.011±0.005

Table 10.1: Scale factors extracted for the t-channel signal contribution, and for the W+jets and top quark background processes from the simultaneous maximum-likelihood fit of the numbers of data events observed in the signal region and in the $t\bar{t}$ and anti-signal control regions. The uncertainties come from the likelihood fit. They are related to the Poissonian and Gaussian terms of the likelihood function (equation 10.4).

Values very close to 1 are found for the merged top quark background processes, which are dominated by $t\bar{t}$ production. Therefore, the evaluated data-driven normalisation factors are consistent with the NNLO cross section calculations, which central values are used to normalise the corresponding simulations samples, and which theoretical uncertainties are used to constrain the fit.

For the scale factors fitted for the W+jets contribution, a significant difference is found between the electron and muon channels ($\Delta\beta_{\mu/e}^{W+jets} = \beta_{\mu}^{W+jets} - \beta_{e}^{W+jets} = 0.068 \pm 0.025$). The uncertainty on the normalisation of the multijet events can account for such a difference: When the multijet event yields are varied up and down by considering a normalisation uncertainty of ±70%, varia-

tions of ±0.157 and ±0.146 are obtained on the W+jets scale factors fitted for the electron and muon channels. These variations largely cover the difference found between the two channels when using the nominal multijet event yields. It should be noted that the impact on the scale factors associated with the top quark backgrounds is much less important. Variations of ±0.004 and ±0.006 are obtained for the electron and muon channels.

It has been found that the extracted scale factors are not sensitive to the fit constraints applied on the merged top quark background. Exactly the same values than those reported in table 10.1 are extracted when the top quark background normalisation constrain is changed from 6% to 100%. Identical result is found with the single and diboson background normalisation constrain. The same set of scale factors is also found when the multijet contribution is not kept fixed but allowed to float within a 70% normalisation constraint, showing that there is also no significant sensitivity of the likelihood fit results to the multijet contribution. The W+jets scale factors are only changed by a few per cent.

The normalisation correction factors given in table 10.1 are used to control the good modelling of the kinematic and angular variable distributions in the $t\bar{t}$ control region, and in the preselection and anti-signal regions. The kinematic distributions shown in figures 9.1, 9.2 and 9.3 include the normalisation factors derived with the combined electron-muon channels. Appendix C shows the same kinematic distributions for the individual cases of electron and muons only. These plots include the individual normalisation factors.

For the polarisation measurement, which is carried out with the unfolding method presented in chapter 13, the W+jets and top quark backgrounds are re-normalised using the scale factors reported in table 10.1. The re-normalisation is applied before subtracting the predicted background contributions to the observed angular distributions.

Chapter 11

Polarisation observables and angular asymmetries

In this chapter, the relationship between the top quark and W boson polarisations and the angular distributions of their decay products with respect to spin directions are discussed. The angular asymmetries from which the top quark and W boson polarisation observables are measured are also presented, as their sensitivity to anomalous Wtb couplings.

The top quark polarisation is determined from the angular distributions of its decay products reconstructed in the top quark rest frame, while the W boson spin observables are determined from angular distributions reconstructed in the W boson rest frame.

11.1 Top quark polarisation

In the top quark rest frame, the angular distribution of any decay product X of the top quark is given by:

$$\frac{1}{\Gamma}\frac{d\Gamma}{d(\cos\theta_X)} = \frac{1}{2}\left(1 + \alpha_X P \cos\theta_X\right) \tag{11.1}$$

where θ_X is the angle between the chosen top quark spin axis and the direction of motion of the chosen decay product in the top quark rest frame, Γ the total decay width of the top quark, α_X the spin analysing power associated with the decay child X, and P the degree of polarisation with respect to the top quark spin axis.

In top quark decay, with the top decaying almost exclusively to a W boson and a b-quark, the charged lepton is the most sensitive spin analyser. Within the SM, the LO value for the spin analysing power of the charged lepton is exactly 1, while the values -0.41 and $+0.41$ are calculated for the b-quark and the boson W^+, respectively (assuming a top quark mass of 175 GeV [18, 19]). The QCD NLO corrections to the spin analysing power of the charged lepton

are at the per mill level: $\alpha_\ell = 0.998$ is found for ℓ^+ assuming a top quark mass of 175 GeV [107] ($\alpha_\ell = -0.998$ for ℓ^-).

In the other hand, for t-channel single top quark production, the most sensitive spin analyser is the d-quark [15, 16, 108]. As shown in section 1.3.1, the d-quark usually corresponds to the spectator quark in the case of top quark production (figure 11.1(a)). This defines the so-called spectator basis, in which the top quark spin direction is taken along the spectator quark, boosted to the top quark rest frame. The overall fraction of spin-up top quarks in the spectator basis at 8 TeV is predicted to be 0.91 [16].

For antitop quark production (figure 11.1(b)), the d-quark comes most times from one of the incoming protons, corresponding the spectator jet with the scattered light-quark. But as the transference of momentum between the incoming light quark and the spectator quark is small, the spector basis gives a high degree of polarization: -0.86 at 8 TeV calculated at NLO for top-antiquark production [16]. Another benefit of using the spectator basis is that it defines a single basis that works both for top and antitop quark production, what simplifies much the analysis.

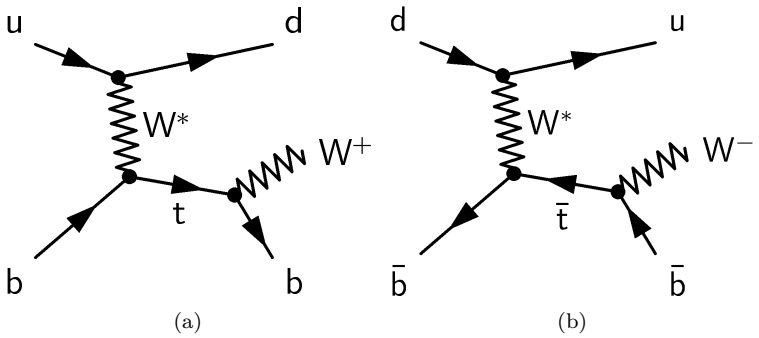

Figure 11.1: Representative leading-order Feynman diagrams of single-top quark production via the t-channel exchange of a virtual W boson ($W*$), including the decay of the top quark. These diagrams show the 2→2 processes, but a 3→2 process is also possible (figure 1.4), in which the initial $b/\bar{b}$ quark comes from the split of a gluon.

As discussed in section 1.3.1, other basis that can be defined in addition to the spectator basis is the beam line basis, in which the antitop quark spin is taken along the direction of the beam that is providing the initial down-quark. The spectator quark can be used to choose among the two beams, giving the correct answer 98% for $dg \to q't\bar{b}$ [17].

For the measurements reported on this work, the helicity basis is used to define the top quark spin axis . Additionally, the beam line basis is used in order to define additional directions on the top quark production frame, as shown on figure 11.2. The top quark spin direction $\hat{s}_t$, taken along the spectator-quark momentum in the top quark rest frame, defines the $\hat{z}$ axis, $\hat{y}$ is taken orthogonal to $\hat{s}_t$ and to the initial quark three-momentum $\vec{p}_q$, and $\hat{x}$ is determined requiring that the coordinate system is right-handed. That is,

$$\hat{z} = \frac{\hat{s}_t}{|\hat{s}_t|}, \quad \hat{y} = \frac{\hat{s}_t \times \vec{p}_q}{|\hat{s}_t \times \vec{p}_q|}, \quad \hat{x} = \hat{y} \times \hat{z}. \tag{11.2}$$

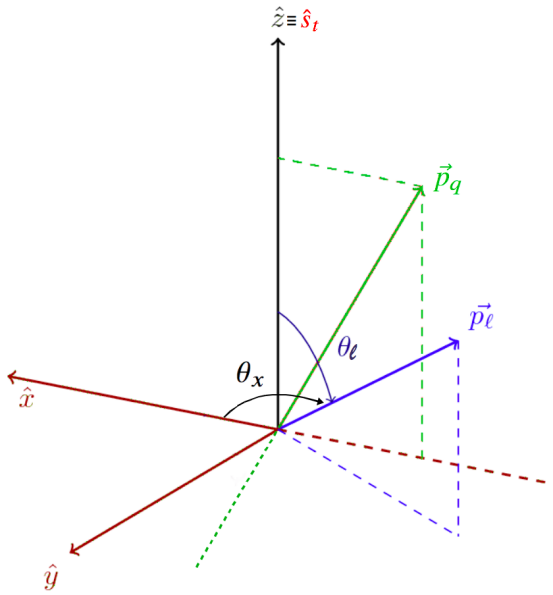

Figure 11.2: Right-handed coordinate system and angles used to define the top quark production system and their related angular asymmetries in the production and decay of polarised top quarks. The top quark spin direction $\hat{s}_t$, taken along the spectator-quark momentum in the top quark rest frame, defines the $\hat{z}$ axis. $\hat{y}$ is taken orthogonal to $\hat{s}_t$ and the initial quark three-momentum $\vec{p}_q$ (in green), and $\hat{x}$ is determined requiring that the coordinate system is right-handed. The diagram also shows the charged lepton momentum $\vec{p}_\ell$ in the top quark rest frame (in blue) that is used to measure the top quark polarisation in the decay. The polar angle of the charged lepton momentum $\vec{p}_\ell$ in the top quark rest frame is labelled θ_ℓ. The polar angles between the charged lepton momentum and the $\hat{x}$ and $\hat{y}$ axis are labelled θ_x and θ_y (not shown) respectively and are used to construct forward-backward asymmetries.

Using the PROTOS generator [75], together with the CTEQ6L1 parton distribution functions [77], the SM values in the $2 \to 3$ process $qg \to q't\bar{b}$ for the polarisation in the three axis are $\vec{P}_t = (0, 0, 0.90)$ and $\vec{P}_{\bar{t}} = (-0.14, 0, -0.86)$ for top and antitop quarks production respectively [17]. The top quark polarisation along the $\hat{z}$-axis, which will be directly denominated as the top quark polarisation (P hereafter) agrees very well with the NLO values [16]: $P = 0.91$ and $P = -0.86$ for quarks and antiquarks respectively. In the $\hat{x}$-axis, the polarisation P_x is not null for antitop quarks due to the spectator quark not being the d-quark in the leading production process $ug \to dt\bar{b}$, as discussed before.

As said before, using the spectator quark direction to choose among both beams gives the correct answer 97% of the times for $ug \to dt\bar{b}$ and 98% of the times for $dg \to ut\bar{b}$, which are the two main production channels for single top and antitop quarks. In the remaining production channels, the estimation success rate decreases. This implies that the measured or 'observed' polarisations $\bar{P}_x$ and $\bar{P}_y$ are slightly smaller than if the initial quark direction were certainly known. The relations between $P_{x,y}$ and $\bar{P}_{x,y}$ have been calculated with a MC [17], resulting in a linear dependency, independent of the anomalous couplings (section 11.4):

$$\begin{aligned} \bar{P}_{x,y} &= 0.89 P_{x,y} \quad (t), \\ \bar{P}_{x,y} &= 0.81 P_{x,y} \quad (\bar{t}). \end{aligned} \tag{11.3}$$

11.2 W boson spin observables

In the framework of a completely general formalism developed in ref. [21], the spin density matrix elements for the W boson helicity components 0, ± 1 resulting from the decay of polarised top quarks can be parameterised in terms of the expected values of six independent spin observables: $\langle S_1 \rangle$, $\langle S_2 \rangle$, $\langle S_3 \rangle$, $\langle A_1 \rangle$, $\langle A_2 \rangle$ and $\langle T_0 \rangle$. Being $(\theta^*_\ell, \phi^*_\ell)$ the polar and azimuthal angles of the charged lepton momentum in the W boson rest frame, the fully differential decay width of a W^+ boson can be written as:

$$\begin{aligned} \frac{1}{\Gamma}\frac{d\Gamma}{d(\cos\theta^*_\ell)d\phi^*_\ell} &= \frac{3}{8\pi}\left[\frac{2}{3} - \frac{1}{\sqrt{6}}\langle T_0 \rangle \left(1 - 3\cos^2\theta^*_\ell\right) + \langle S_3 \rangle \cos\theta^*_\ell\right] \\ &+ \frac{3}{8\pi}\left[\langle S_1 \rangle \cos\phi^*_\ell \sin\theta^*_\ell + \langle S_2 \rangle \sin\phi^*_\ell \sin\theta^*_\ell\right] \\ &- \frac{3}{8\pi}\left[\langle A_1 \rangle \cos\phi^*_\ell \sin 2\theta^*_\ell + \langle A_2 \rangle \sin\phi^*_\ell \sin 2\theta^*_\ell\right] \end{aligned} \tag{11.4}$$

In this formalism, the W boson spin axis is taken along the direction of the W boson momentum in the top quark rest frame. It is equivalent to consider the reverse b-quark momentum in the W boson rest frame. The used right-handed coordinate system and the various decay angles defined for the charged lepton in the W boson rest frame are depicted in Figure 11.3. In this coordinate system, the W boson momentum defines the $\hat{z}$ axis and the top quark spin direction $\hat{s}_t$, which is taken along the spectator-quark momentum in the top quark rest frame, is set in the $\hat{x} - \hat{z}$ plane.

The angular distribution expressed by Equation 11.4 implies an integration over all the possible directions of the top quark spin with respect to the W boson helicity axis. The polarisation P associated with the chosen top quark spin basis is propagated to the off-diagonal spin observables $\langle S_1 \rangle$, $\langle S_2 \rangle$, $\langle A_1 \rangle$ and $\langle A_2 \rangle$, which depend in a proportional way on the value of P. Therefore, in the spectator basis, the values of $\langle S_1 \rangle$, $\langle S_2 \rangle$, $\langle A_1 \rangle$ and $\langle A_2 \rangle$ are expected not to be exactly the same for top quark and top-antiquark productions. The two diagonal spin observables $\langle S_3 \rangle$ and $\langle T_0 \rangle$ do not depend on P, and are related to the W boson helicity fractions F_R, F_L and F_0 according to:

$$\langle S_3 \rangle = F_\mathrm{R} - F_\mathrm{L} \tag{11.5}$$

$$\langle T_0 \rangle = \frac{1}{\sqrt{6}}\left(1 - 3F_0\right) \tag{11.6}$$

From the values of the helicity fractions predicted by the SM at NNLO in QCD assuming a top quark mass of 172.8 GeV and a b-quark mass of 4.8 GeV [109], one obtains $\langle S_3 \rangle = -0.309$ and $\langle T_0 \rangle = -0.433$. Combining the predicted degrees of polarisation $P_t = 0.91$ and $P_{\bar{t}} = -0.86$ with the t-channel single-top cross-sections $\sigma_t = 54.9$ pb and $\sigma_{\bar{t}} = 29.7$ pb calculated at NLO in QCD for top quark and top-antiquark productions [110], the SM predictions for $\langle S_1 \rangle$, $\langle S_2 \rangle$, $\langle A_1 \rangle$ and $\langle A_2 \rangle$ are: $\langle S_1 \rangle = 0.456$, $\langle A_1 \rangle = 0.228$ and $\langle S_2 \rangle = \langle A_2 \rangle = 0$. These values are calculated at the tree level assuming a top quark mass of 172.5 GeV from the expressions of the density matrix elements given in [20, 21].

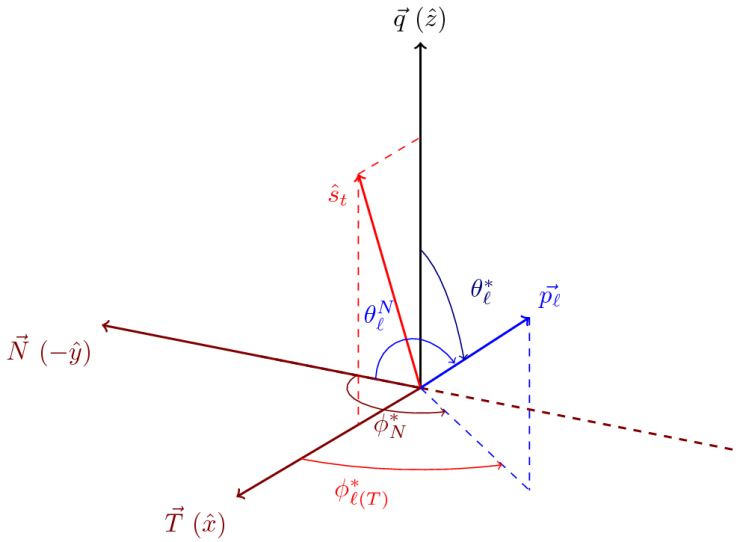

Figure 11.3: Right-handed coordinate system and angles used to define the W boson spin observables and their related angular asymmetries in the decay of polarised top quarks. The W boson momentum $\vec{q}$ in the top quark rest frame defines the $\hat{z}$ axis. The top quark spin direction $\hat{s}_t$, taken along the spectator-quark momentum in the top quark rest frame, is set in the $\hat{x} - \hat{z}$ plane. The polar and azimuthal angles of the charged lepton momentum $\vec{p}_\ell$ in the W boson rest frame are labelled θ^*_ℓ and ϕ^*_ℓ. The normal and transverse axes are defined with respect to $\vec{q}$ and $\hat{s}_t$ according to $\vec{N} = \hat{s}_t \times \vec{q}$ and $\vec{T} = \vec{q} \times \vec{N}$, matching the $\hat{x}$ and $-\hat{y}$ axes of the coordinate system.

11.3 Angular asymmetries

The top quark polarisation and the W boson spin observables can be determined by integrating the angular distributions expressed by equations 11.1 and 11.4. As it will be explained below, all the polarisation values can be extracted from the measurement of asymmetries based on single or combined angular observables. Two different types of asymmetries are used in this study. The most used is the forward-backward asymmetry, that can be constructed generically as

$$A_{\text{FB}} = \frac{N(\cos\theta > 0) - N(\cos\theta < 0)}{N(\cos\theta > 0) + N(\cos\theta < 0)} \tag{11.7}$$

where $\cos\theta$ is a given angular observable. The forward-backward asymmetry measures the ratio of events contained in the forward region versus the ones contained in the backward region.

The second asymmetry used in the study is the edge-central asymmetry, that measures the ratio between events contained in the central region versus the ones that take place in the outer ones:

$$A_{\text{EC}} = \frac{N(|\cos\theta| > \frac{1}{2}) - N(|\cos\theta| < \frac{1}{2})}{N(|\cos\theta| > \frac{1}{2}) + N(|\cos\theta| < \frac{1}{2})}. \tag{11.8}$$

Table 11.1 summarises all the relations between the proposed asymmetries and the top quark and W boson spin observables.

Asymmetry	Angular observable	Polarisation observable	SM prediction
A_{FB}^{ℓ}	$\cos\theta_l$	$\frac{1}{2}\alpha_l P$	0.45
A_{FB}^{X}	$\cos\theta_x$	$\frac{1}{2}\alpha_l \bar{P}_x$	0.02
A_{FB}^{Y}	$\cos\theta_y$	$\frac{1}{2}\alpha_l \bar{P}_y$	0
A_{FB}^{tW}	$\cos\theta_W \cos\theta_l^*$	$\frac{3}{8}P(F_R + F_L)$	0.10
A_{FB}	$\cos\theta_l^*$	$\frac{3}{4}\langle S_3\rangle = \frac{3}{4}(F_R + F_L)$	-0.23
A_{EC}	$\cos\theta_l^*$	$\frac{3}{8}\sqrt{\frac{3}{2}}\langle T_0\rangle = \frac{3}{16}(1 - 3F_0)$	-0.20
A_{FB}^{T}	$\cos\theta_l^T$	$\frac{3}{4}\langle S_1\rangle$	0.34
A_{FB}^{N}	$\cos\theta_l^N$	$-\frac{3}{4}\langle S_2\rangle$	0
$A_{\mathrm{FB}}^{T,\phi}$	$\cos\theta_l^* \cos\phi_T^*$	$-\frac{2}{\pi}\langle A_1\rangle$	-0.14
$A_{\mathrm{FB}}^{N,\phi}$	$\cos\theta_l^* \cos\phi_N^*$	$\frac{2}{\pi}\langle A_2\rangle$	0

Table 11.1: Asymmetries with their associated observables and their relation to the top quark polarisations and W boson spin observables. The values predicted by the SM are also given. They are calculated using the predictions at NLO in QCD for P, $\bar{P}_x$, $\bar{P}_y$ and α_l, the predictions at NNLO for the helicity fractions F_R, F_L and F_0, and the predictions at LO for $\langle S_1\rangle$, $\langle S_2\rangle$, $\langle A_1\rangle$ and $\langle A_2\rangle$. The uncertainties in these values are lower than 0.01. They are estimated from the uncertainties in the top quark, b-quark and W boson masses, added in quadrature, including the uncertainty in α_s and an estimate of the higher-order effects for the asymmetries related to the W boson spin observables [17, 20, 21].

The product of the top quark polarisation P and the spin analysing power of the charged lepton α_ℓ can be extracted from the forward-backward asymmetry A_{FB}^{ℓ} of the $\cos\theta_\ell$ angular distribution.

The polarisation of the top quark can also be extracted from another asymmetry, A_{FB}^{tW}, in a more direct way, as there is no need to make an assumption on the value of the spin analysing power of the electron α_ℓ, which can not be measured independently. The forward-backward asymmetry A_{FB}^{tW} is directly proportional to the product of the top quark polarisation P and the sum of the two transverse helicity fractions of the W boson, $F_{\mathrm{R}}$and F_{L}. A_{FB}^{tW} is defined with respect to the combined angular observable $\cos\theta_W \cos\theta_\ell^*$.

Two more observables can be defined in the top quark production reference system (figure 11.2) using the momentum of the incoming quark. From the $\cos\theta_x$ and $\cos\theta_y$ angular distributions, the A_{FB}^{X} and A_{FB}^{Y} forward-backward asymmetries are defined respectively, and their are directly proportional to $\alpha_\ell \bar{P}_x$ and $\alpha_\ell \bar{P}_y$.

The W boson spin observables are also extracted from asymmetries. After integrating Equation 11.4 over the azimuthal angle ϕ_ℓ^* (figure 11.2), the W boson spin observables $\langle S_3\rangle$ and $\langle T_0\rangle$ can be derived from the forward-backward asymmetry A_{FB} and from the edge-central asymmetry A_{EC} of the angular distribution in $\cos\theta_\ell^*$, the same angle involved in A_{FB}^{tW}.

The spin observables $\langle S_1\rangle$ and $\langle S_2\rangle$ can be determined using the definitions of

the normal axis $\vec{N} = \hat{s}_t \times \vec{q}$ and of the transverse axis $\vec{T} = \vec{q} \times \vec{N}$ proposed in [20] (Figure 11.3). The two observables are proportional to the forward-backward asymmetries A_{FB}^{T} and A_{FB}^{N} in the angular observables $\cos\theta_\ell^T$ and $\cos\theta_\ell^N$.

The last two spin observables $\langle A_1 \rangle$ and $\langle A_2 \rangle$ can be determined from the forward-backward asymmetries calculated with respect to the combined angular observables $\cos\theta_\ell^* \cos\phi_\ell^*$ and $\cos\theta_\ell^* \sin\phi_\ell^*$, respectively. This is also equivalent to extract them from the forward-backward asymmetries $A_{\mathrm{FB}}^{T,\phi}$ and $A_{\mathrm{FB}}^{N,\phi}$ involving the combination of $\cos\theta_\ell^*$ with the cosine of the azimuthal angles ϕ_T^* and ϕ_N^*.

All the asymmetry definitions given in this section can be used indifferently of the sign of the lepton charge. The corresponding differential distribution for W^- bosons, which are originated from the decay of an antitop quark, are obtained from Equation 11.4 by changing the signs associated with the terms in $\cos\theta_\ell^*$ and in $\sin\theta_\ell^*$. This leads to an extra minus sign in all the derived relations between asymmetries and observables, except for the equation giving A_{EC}. However, in practice, these relations remain the same because the helicity fractions are interchanged, and the polarisations P_t and $P_{\bar{t}}$ have opposite signs. Therefore, top and antitop quarks can be combined without problems for the final mesaurement of all asymmetries.

11.4 Wtb anomalous couplings measurements

As it is shown in section 1.3.2, the SM Lagrangian of the Wtb vertex (equation 1.4) can be generalised using effective field operator formalism in order to include deviations from the SM. The most general Lagrangian (equation 1.5) includes a right-handed vector operator V_{R} and left- and right-handed tensor operators g_{L} and g_{R}, which are all null in the SM.

The asymmetries proposed in previous section can be used to measure and constrain the values of the different anomalous couplings. Figures 11.4 and 11.5 display the dependences of the asymmetries on the real and imaginary parts of the couplings g_{R}, g_{L} and V_{R}. They are calculated assuming a top quark mass of 172.5 GeV and a b-quark mass of 4.8 GeV. The top quark and top-antiquark productions are combined using the predicted polarisation values P_t and $P_{\bar{t}}$ and the t-channel cross-sections σ_t and $\sigma_{\bar{t}}$ are calculated at NLO in QCD. The calculations are based on the TopFit code [111], in which the analytic expressions of the W boson spin observables, of the top quark polarisation and of the spin analysing powers are implemented as a function of the Wtb coupling values.

The asymmetry A_{FB}^{ℓ} exhibits a quadratic dependence on the real and imaginary parts of g_{R} and V_{R}. The asymmetry A_{FB}^{tW} is only slightly sensitive $\mathrm{Re}\, g_{\mathrm{R}}$, while it has no sensitivity $\mathrm{Im}\, g_{\mathrm{R}}$. The W boson helicity asymmetries A_{FB}, A_{EC}, as well as the transverse asymmetry A_{FB}^{T}, are mainly sensitive to $\mathrm{Re}\, g_{\mathrm{R}}$ (their sensitivity to $\mathrm{Im}\, g_{\mathrm{R}}$ is very poor). The combined transverse asymmetry $A_{\mathrm{FB}}^{T,\phi}$ exhibits also a preferential sensitivity to $\mathrm{Re}\, g_{\mathrm{R}}$. The W boson normal asymmetries A_{FB}^{N} and $A_{\mathrm{FB}}^{N,\phi}$ are only sensitive to $\mathrm{Im}\, g_{\mathrm{R}}$. The A_{FB}^{X} and A_{FB}^{Y} asymmetries constructed from the top quark P_x and P_y polarisations are only sensitive to $\mathrm{Re}\, g_{\mathrm{R}}$ and $\mathrm{Im}\, g_{\mathrm{R}}$ respectively. The impact that the incoming quark selection

has on P_x and P_y has been included on the A_{FB}^{X} and A_{FB}^{Y} predictions.

Of particular interest is the measurement of $\mathrm{Im}\, g_{\mathrm{R}}$, which is only accessible through single top quark production. In the SM, values exactly equal to zero are predicted at the tree level for A_{FB}^{N}, $A_{\mathrm{FB}}^{N,\phi}$ and A_{FB}^{Y}. Therefore, measuring values different from zero for these three asymmetries, which are related to the W boson spin observables $\langle S_2 \rangle$ and $\langle A_2 \rangle$ and the top quark P_y polarisation, would unambiguously sign the presence of a complex phase in the Wtb vertex. Their dependence on $\mathrm{Im}\, g_{\mathrm{R}}$ is compared in figure 11.6, together with their dependence on $\mathrm{Re}\, g_{\mathrm{R}}$, which is null for the three asymmetries. It can be seen that the most sensitive asymmetry to $\mathrm{Im}\, g_{\mathrm{R}}$ is A_{FB}^{Y}, followed by A_{FB}^{N}, being $A_{\mathrm{FB}}^{N,\phi}$ the one with less sensitivity. In this analysis, both A_{FB}^{N} and A_{FB}^{Y} are used to extract limits on $\mathrm{Im}\, g_{\mathrm{R}}$, firstly because when this analysis was started, neither A_{FB}^{X} and A_{FB}^{Y} had been proposed yet to be measured [17], meaning that by that time, A_{FB}^{N} was the most sensitive observable to $\mathrm{Im}\, g_{\mathrm{R}}$. Additionally, better constrains on $\mathrm{Im}\, g_{\mathrm{R}}$ can be set by combining both asymmetries results.

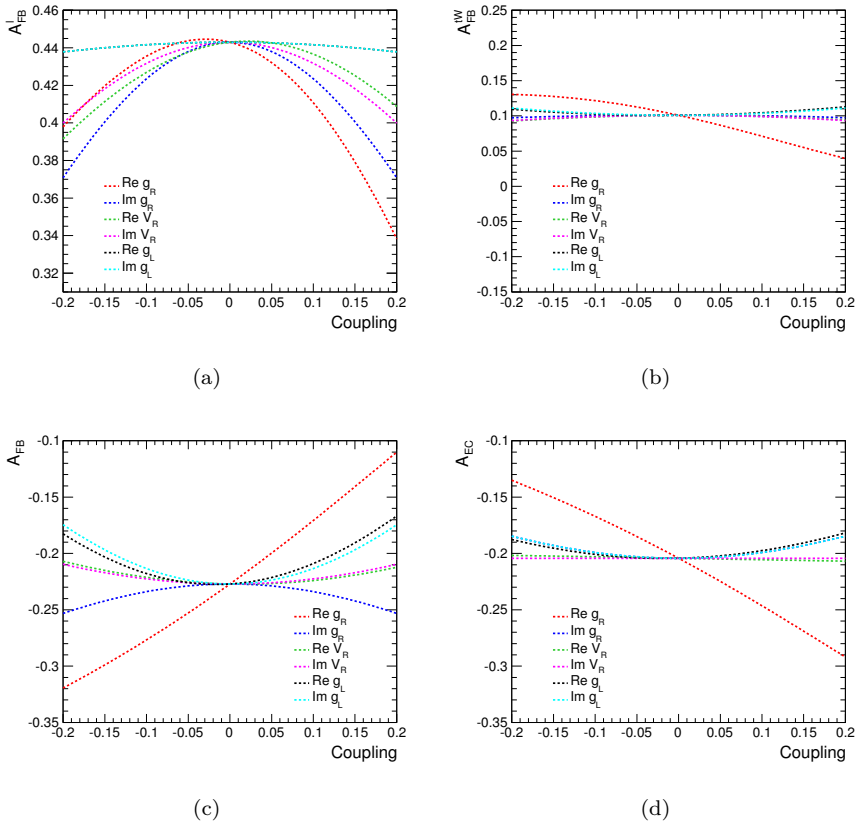

Figure 11.4: Dependence on the real and imaginary parts of the anomalous couplings g_{R}, g_{L} and V_{R}, taking $V_{\mathrm{L}} = 1$, for the asymmetries (a) A_{FB}^{ℓ}, (a) A_{FB}^{tW}, (c) A_{FB}, and (d) A_{EC}. The calculations are based on the relations given in [20, 112], and implemented in the TopFit code [111].

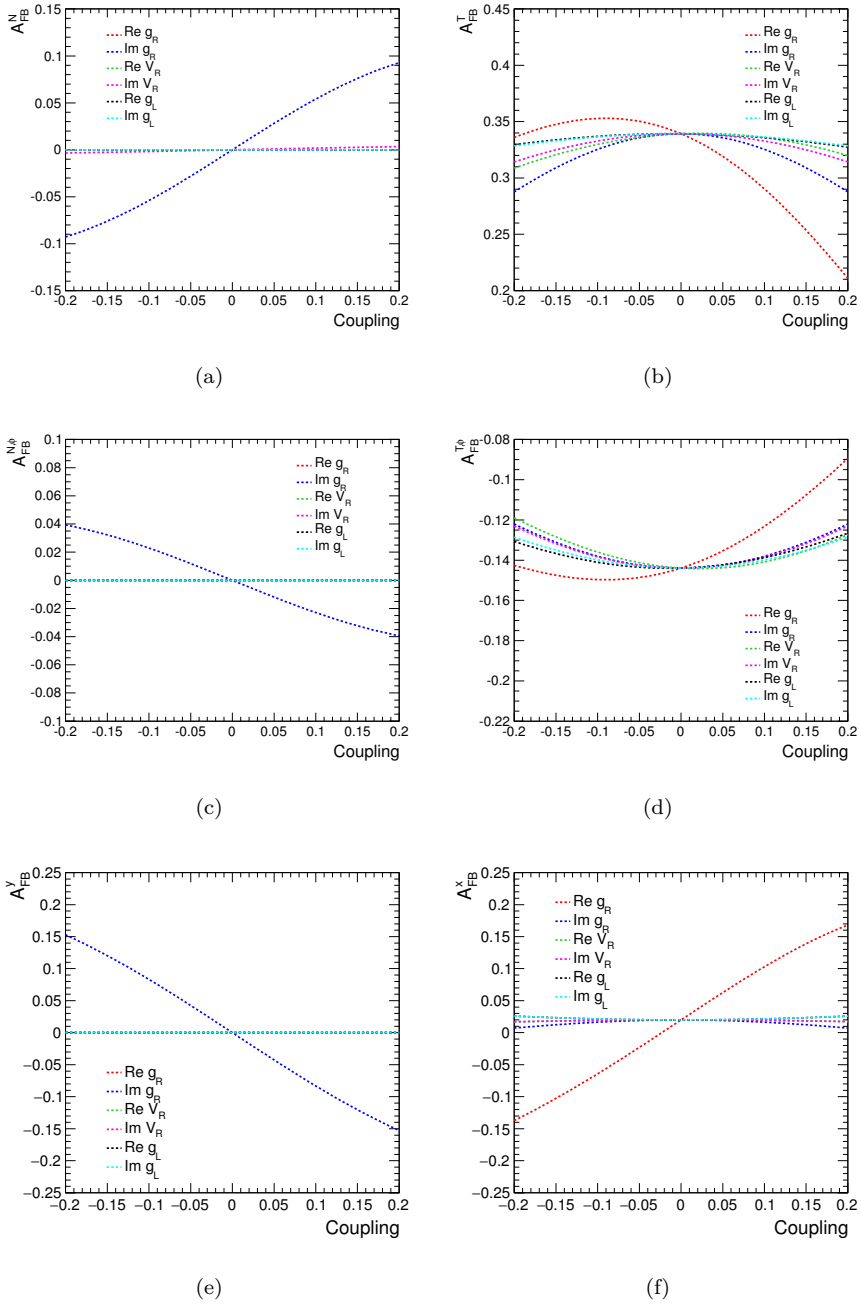

Figure 11.5: Dependence on the real and imaginary parts of the anomalous couplings g_{R}, g_{L} and V_{R}, taking $V_{\mathrm{L}} = 1$, for the asymmetries (a) A_{FB}^{N}, (b) A_{FB}^{T}, (c) $A_{\mathrm{FB}}^{N,\phi}$, (d) $A_{\mathrm{FB}}^{T,\phi}$, (e) A_{FB}^{Y} and (f) A_{FB}^{X}. The calculations are based on the relations given in [17, 20, 112], and implemented in the TopFit code [111].

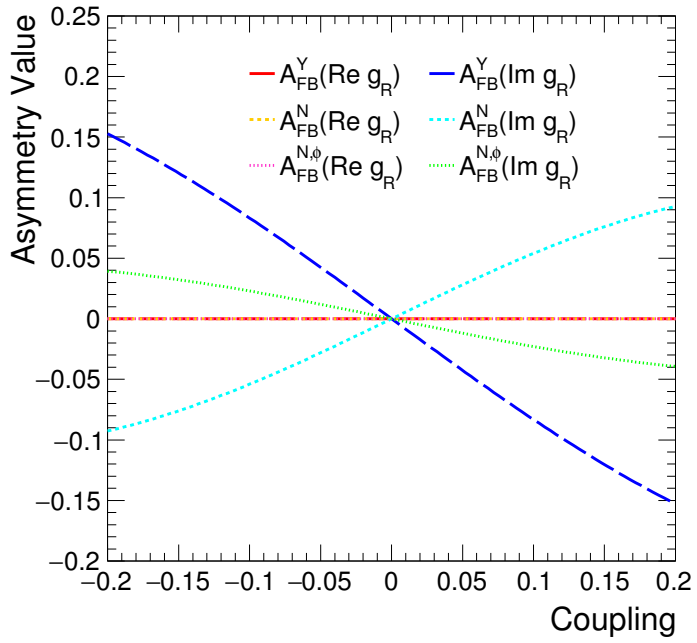

Figure 11.6: Dependence on the real and imaginary parts of the anomalous coupling g_{R} taking $V_{\mathrm{L}} = 1$, for the asymmetries A_{FB}^{N}, $A_{\mathrm{FB}}^{N,\phi}$ and A_{FB}^{Y}, The calculations are based on the relations given in [17, 20, 112], and implemented in the TopFit code [111].

Chapter 12

Angular distributions

This chapter presents the angular distributions at reconstruction level from which the different asymmetries discussed in section 11.3 are extracted. The definition of the angular distributions follows the two coordinate systems presented in sections 11.1 and 11.2. The momentum of the charged lepton is computed in either the top quark or the W boson rest frames, and its angle is calculated with respect to various top quark and W boson spin axes. The two rest frames and the polarisation axes are determined from the various reconstructed objects: the charged lepton, the spectator jet, the b-tagged jet and the $E_{\mathrm{T}}^{\mathrm{miss}}$.

Three asymmetries are defined with the coordinate system of figure 11.2, as explained in section 11.3. A_{FB}^{ℓ} is defined from $\cos\theta_{\ell}$. Similarly, A_{FB}^{X} and A_{FB}^{Y} are defined from $\cos\theta_{x}$ and $\cos\theta_{y}$ respectively.

For the measurement of the asymmetries A_{FB} and A_{EC} related to the W boson helicity, the coordinate system described in figure 11.3 is used. The corresponding angular observable is $\cos\theta_{\ell}^{*}$.

Same coordinate system is used to extract A_{FB}^{N} and A_{FB}^{T} related to the W boson normal and transverse polarisations. The corresponding angular observables are $\cos\theta_{\ell}^{N}$ and $\cos\theta_{\ell}^{T}$.

$A_{\mathrm{FB}}^{N,\phi}$ and $A_{\mathrm{FB}}^{T,\phi}$ are extracted from the distributions of the angular observables combining $\cos\theta_{\ell}^{*}$ with $\cos\phi_{N}^{*}$ and $\cos\phi_{T}^{*}$, where ϕ_{N}^{*} and ϕ_{T}^{*} are the azimuthal angles of the charged lepton defined in the W boson rest frame with respect to the normal and transverse axes, respectively. The corresponding angular observables are thus $\cos\theta_{\ell}^{*}\cos\phi_{N}^{*}$ and $\cos\theta_{\ell}^{*}\cos\phi_{T}^{*}$.

A_{FB}^{tW}, which is related to a combination of the top quark polarisation and of W boson helicity fractions, is measured from the distribution of the product of the angular observables $\cos\theta_{W}$ and $\cos\theta_{\ell}^{*}$, where $\cos\theta_{W}$ is the angle in the top quark rest frame of the reconstructed W boson with respect to the non b-tagged jet momentum. The corresponding angular observable is $\cos\theta_{W}\cos\theta_{\ell}^{*}$.

The angular distributions measured in the signal region using these various axis definitions are presented in figures 12.1 and 12.2, together with their comparison with the predicted signal-plus-background distributions given by the

MC simulations and the data-driven estimates. The angular distributions are presented for the combination of the electron and muon channels. Apart from the $\cos\theta^*_\ell$ distribution, that is also defined using 4 bins, needed to define A_{EC}, all remaining angular distributions are defined using only 2 same-sized bins, as they are just used to extract forward-backward asymmetries. More details about the binning choice are given in section 13.1.

In all figures presented below, the predicted distributions are re-normalised with the constrained scale factors given in table 10.1. The plotted uncertainty bands correspond to the errors due to the limited size of the simulation samples added in quadrature with the data-driven normalisation uncertainty estimated for the multijet contribution and with the errors of the constrained scale factors.

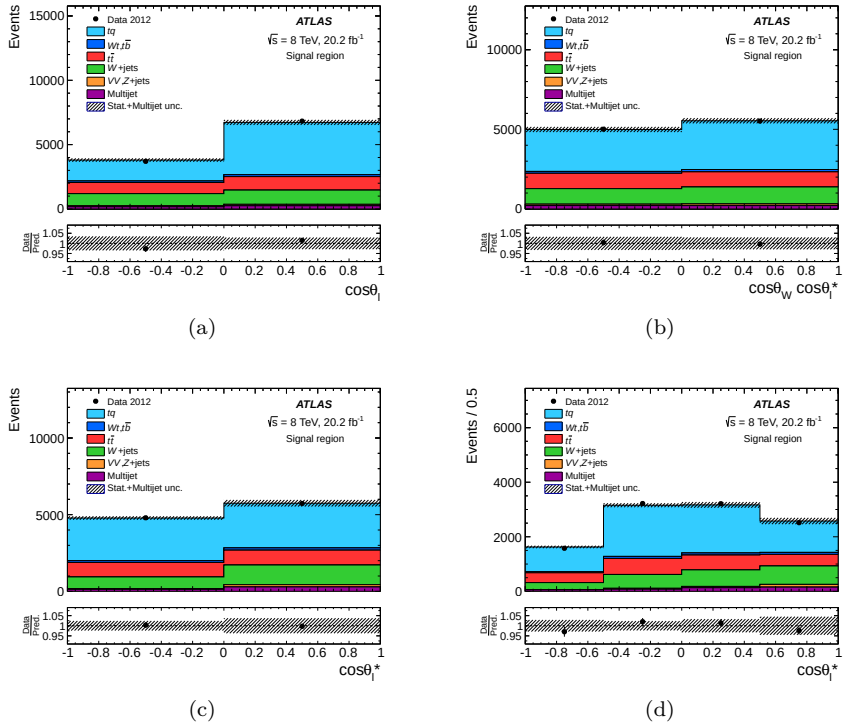

Figure 12.1: Angular distributions in the signal region for the combined electron and muon channels (a) $\cos\theta_\ell$, (b) $\cos\theta_W \cos\theta^*_\ell$, (c) $\cos\theta^*_\ell$ with 2 bins, and (d) $\cos\theta^*_\ell$ with 4 bins. The predicted distributions are re-scaled using the values given in table 10.1. The uncertainty bands correspond to the errors due to the limited size of the simulation samples added in quadrature with the data-driven normalisation uncertainty estimated for the multijet contribution.

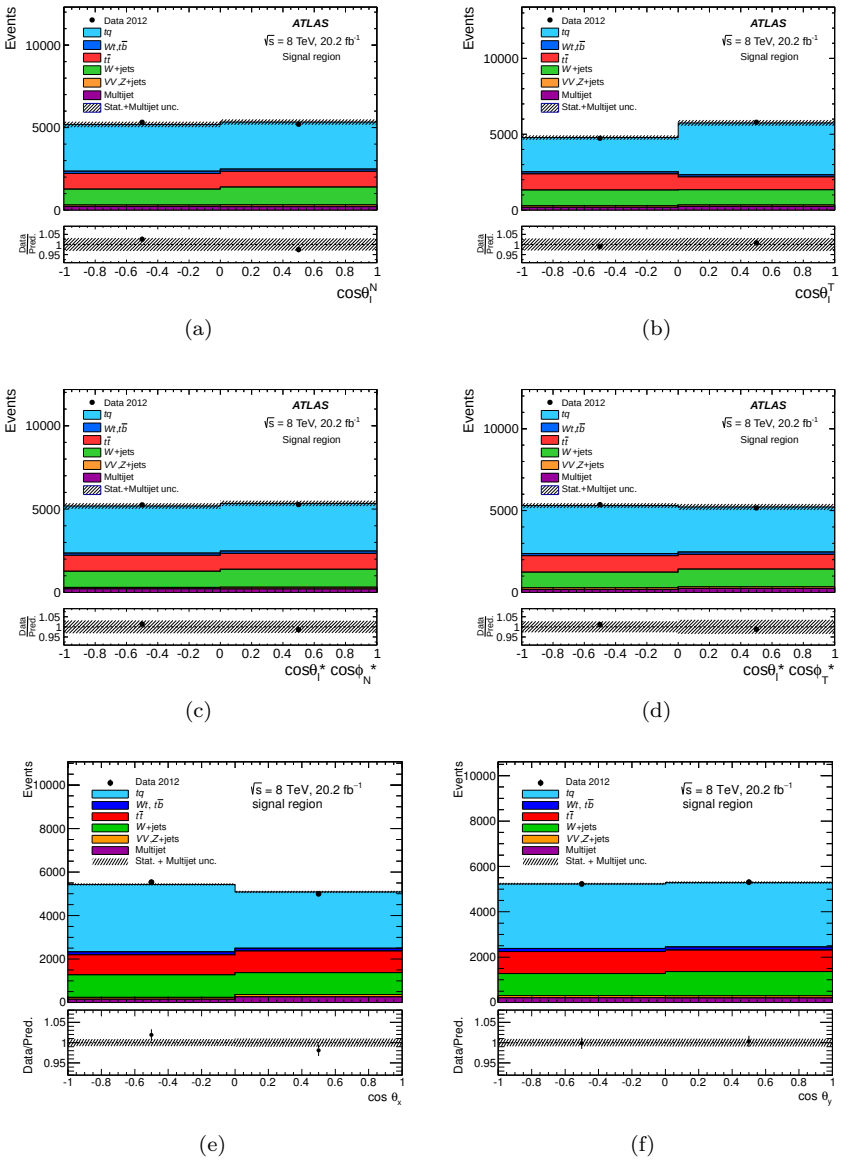

Figure 12.2: Angular distributions in the signal region for the combined electron and muon channels (a) $\cos\theta_\ell^N$, (b) $\cos\theta_\ell^T$, (c) $\cos\theta_\ell^* \cos\phi_N^*$, (d) $\cos\theta_\ell^* \cos\phi_T^*$, (e) $\cos\theta_x$ and (f) $\cos\theta_y$. The predicted distributions are re-scaled using the values given in table 10.1. The uncertainty bands correspond to the errors due to the limited size of the simulation samples added in quadrature with the data-driven normalisation uncertainty estimated for the multijet contribution.

Chapter 13

Unfolding procedure

Before extracting asymmetries from the various measured angular distributions, the angular distribution are unfolded at parton level, so the asymmetries can be directly compared to the theoretical calculations. Partons are defined from the matrix-element hard process and immediate decays, such that jets can be identified with their corresponding quarks.

The unfolding procedure correct the signal distributions from distortions due to finite resolution of the detector as well from the triggering, reconstruction and selection efficiencies. The effects due to hadronization and parton showering are also included. In order to illustrate the impact that the reconstruction and the selection has in the angular distributions, figure 13.1 shows the $\cos\theta_l$ distribution at parton level, also referred to as truth level (left), and after the signal reconstruction and selection, referred to as reco level (right). It can be seen that the signal acceptance towards values of $\cos\theta_l \sim 1$ drops drastically. Values of $\cos\theta_l \sim 1$ correspond to events in which the lepton and the spectator jet are produced in almost the same direction, what is incompatible with the isolation requirements for the leptons described in section 2.3 and chapter 9, implying that this kind of events are removed from the final selection.

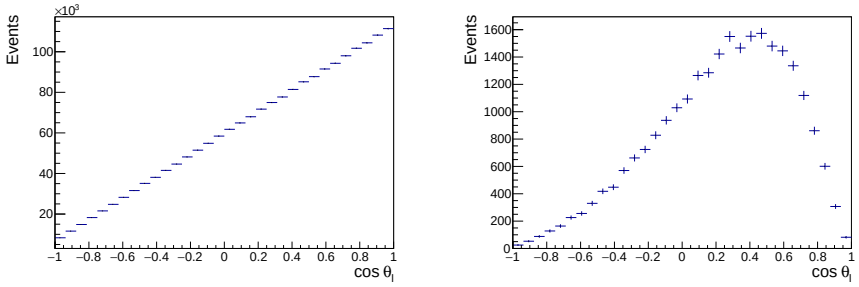

(a) (b)

Figure 13.1: Distribution of $\cos\theta_l$ at (a) parton (truth) level and at (b) reconstruction level. The impact that the event selection has in the signal acceptance is clearly visible at $\cos\theta_l \sim 1$, where the acceptance drastically drops.

The unfolding corrections are calculated from simulated events of the signal process through the separate generation of a migration matrix and of an efficiency curve. A couple of migration matrix and efficiency values is computed for each angular observable. An example of those migration matrices and efficiency curves is shown in figure 13.2 where the migration matrix and efficiency curve are shown for the $\cos\theta_l$ distribution. Both the migration matrices and selection efficiencies are computed from samples of t-channel single top quark events simulated with the PROTOS generator (section 8.2 for details).

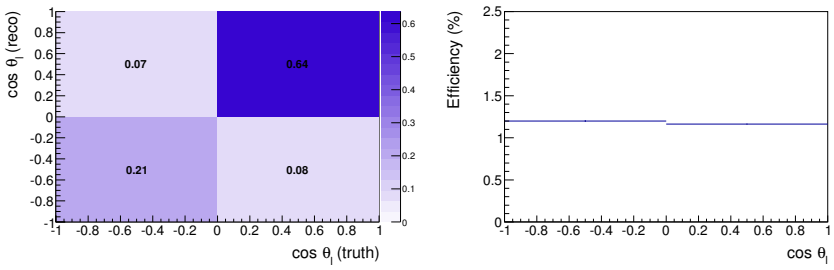

(a) (b)

Figure 13.2: (a) Migration matrix and (b) efficiency curve for the $\cos\theta_l$ distribution.

The unfolding procedure is applied to the angular distributions after subtracting the background contributions, determined with the templates presented in chapter 12. Unfolding a distribution needs an inversion of the migration matrix M, which transforms the reconstructed angles into their parton level values. However, in most of the cases, there is no exact inverse matrix M^{-1} such as $M \cdot M^{-1} = I$, where I is the unity matrix. Hence, approximations are needed to perform the matrix inversion to acceptable accuracy. After inversion of the migration matrix M, the distribution of the true angular observable is corrected for the selection efficiencies ϵ to get the distribution at parton level from which the polarisation measurement is carried out.

The number of unfolded signal events N_j^{unfolded} in each bin j of the parton-level distribution is obtained from the background-subtracted yields N_i^{measured} measured in all bins i of the reconstructed distribution, according to

$$N_j^{\text{unfolded}} = \frac{\Sigma_i M_{ji}^{-1} N_i^{\text{measured}}}{\epsilon_j} \tag{13.1}$$

where M_{ji} is the migration matrix element that relates the parton-level bin j with the reconstructed value bin i of the considered angular variable, and ϵ_j is the event selection efficiency.

The unfolded results presented in this note are obtained using the Bayes unfolding algorithm [113] implemented in the RooUnfold package [114]. It is a widely used method to invert the resolution matrix based in the iterative application of the Bayes theorem. In this approach, the simulated angular distribution of the t-channel events obtained after having applied all the selection requirements is taken as initial prior and the posterior probability density function, which is taken from the currently unfolded observed distribution, is used

as prior for the next iteration step. The regularisation parameter of this method is just the number of iterations.

13.1 Angular binning

The number of bins was chosen taking account the migration matrix associated with the angular variable, the precision expected for the measured asymmetry, and the results of the convergence studies presented in the next section, together with the size of the expected systematic uncertainties (section 14.5).

It was seen that choosing the smallest possible number of bins for the angular asymmetries led to better measurement precision. For example, for a forward-backward asymmetry the minimum number of bins needed is 2. In general, for the asymmetries measured in this work, smaller total expected uncertainties were obtained if only 2 bins were used in the definition of the angular distributions, instead of using 4 or 8. Only for the measurement of the asymmetry A_{FB}, a better precision was found using 4 bins. However, a better convergence behaviour was obtained with 2 bins and, finally, the 2 bins configuration was chosen. For the edge-central asymmetry case, the minimum number of bins needed is 3, but 4 were chosen in order to have same size bins.

Historically, the studies leading to the publication of this analysis in [115] were started with a larger number of bins for the measured asymmetries, for which performing the unfolding with a direct matrix inversion was not always possible. All the analysis was developed using the most general approach of the iterative Bayesian unfolding. Although in the case of using 2 bins asymmetries, as it was finally chosen, the direct matrix inversion gives the same results than the ones obtained with the iterative Bayesian unfolding, the last method was maintained as all the analysis code was made with it. Additionally, the interpolation method described in section 13.5 was developed also to work based on the Bayesian unfolding.

Two bins of same width are thus considered when extracting the forward-backward asymmetries A_{FB}^{ℓ}, A_{FB}^{tW}, A_{FB} A_{FB}^{X}, A_{FB}^{Y}, A_{FB}^{N}, A_{FB}^{T}, $A_{\mathrm{FB}}^{N,\phi}$ and $A_{\mathrm{FB}}^{T,\phi}$, whereas 4 bins of same width are defined for the extraction of the asymmetry A_{EC}. For all measured asymmetries, the Bayes unfolding algorithm is used for the signal unfolding.

13.2 Number of iterations

To define the optimal number of iterations of the bayesian unfolding algorithm, convergence tests are performed. The convergence studies presented in this section are performed using the baseline PROTOS+PYTHIA sample, which has been generated with the SM couplings and has been interfaced to the `ATLFAST-II` detector simulation, and various POWHEG-BOX+PYTHIA samples: two samples with the P2011C tune and processed both through the full and `ATLFAST-II` simulations and a sample with the P2012 tune and the `ATLFAST-II` simulation. The predicted angular distributions associated with these samples are unfolded

with the resolution and efficiency corrections calculated with the baseline SM PROTOS simulation.

Figures 13.3 and 13.4 show the evolution, as a function of the number of bayesian iterations, of the asymmetries extracted from the unfolded angular distributions. The number of iterations used for the final measurement extraction is selected with the following convergence criterion: for a given asymmetry, the unfolding procedure is considered to have converged when the absolute change between two successive steps becomes lower than 0.0005. It is also required that a stable convergent value is reached, meaning that no further divergences are present.

For all asymmetries, the convergence of the unfolded PROTOS distributions happens at the first iteration. This is due to the fact that the same sample is used to build the unfolded angular distributions and to compute the resolution and efficiencies corrections. When unfolding the distributions reconstructed from the various POWHEG-BOX samples, the convergence for the extracted asymmetry values is slower. Four to ten iterations are needed for most asymmetries. Only the asymmetry $A_{\mathrm{FB}}^{T,\phi}$ requires additional iterations to reach convergence: 25 in total.

The numbers of iterations chosen for the various measured asymmetries are summarised in table 13.1. They correspond to the values from which the convergence is reached for at least two of the three tested POWHEG-BOX samples.

Asymmetry	Number of iterations
A_{FB}^{ℓ}	6
A_{FB}^{X}	4
A_{FB}^{Y}	3
A_{FB}^{tW}	8
A_{FB}	6
A_{EC}	6
A_{FB}^{N}	4
A_{FB}^{T}	10
$A_{\mathrm{FB}}^{N,\phi}$	10
$A_{\mathrm{FB}}^{T,\phi}$	25

Table 13.1: Numbers of the bayesian unfolding algorithm iterations chosen for the measured asymmetries.

The results displayed in figures 13.3 and 13.4 also show, in most of the cases, important shifts of the convergence curves around the PROTOS response. A grey band is displayed around the PROTOS sample unfolded points to indicate the uncertainty due to the limited size of the PROTOS sample. These statistical uncertainties are estimated through the generation of pseudo-experiments, as explained in section 14.4. In most of the cases, the statistical uncertainties are enough to cover the observed differences.

The only two exceptions are the A_{FB}^{X} asymmetry, for which, only the POWHEG-BOX passed through the full ATLAS simulation falls outside the grey band, and the A_{FB} asymmetry, for which that happens to both POWHEG-BOX+P2011C tune samples. This means that the unfolding response is sensitive to the event modelling, *i.e.* to the generator modelling (LO *vs* NLO), to the parton shower tune (P2011C *vs* P2012), and to the detector simulation (full *vs* fast). To take into account the differences in the unfolding response, a systematic uncertainty evaluated from the comparison of the measurement results obtained when unfolding the PROTOS and POWHEG-BOX angular distributions is considered. The largest uncertainty between the three POWHEG-BOX samples is taken as systematic uncertainty (chapter 14).

In order to test the goodness of the bayesian unfolding, the results of the bayesian unfolding are compared to the ones achieved by an alternative unfolding method. The last bin of figures 13.3 and 13.4 show the result of unfolding the signal with a simple inversion of the migration matrix. A perfect concordance between both methods is achieved once the bayesian unfolding has converged. From this result and the results of the closure test presented in next section, no additional systematic uncertainties are considered for the unfolding procedure.

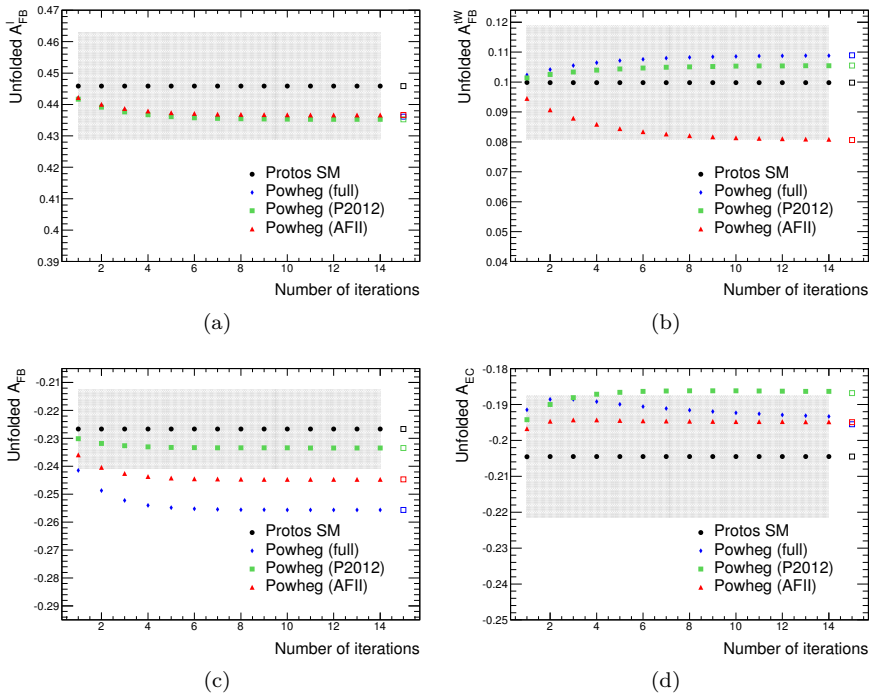

Figure 13.3: Unfolded values of the asymmetries as a function of the number of iterations of the bayesian unfolding algorithm: (a) A_{FB}^{ℓ}, (b) A_{FB}^{tW}, (c) A_{FB}, and (d) A_{EC}. The SM PROTOS (black points), the nominal POWHEG-BOX (blue diamonds), the POWHEG-BOX with the P2012 tune (green boxes), and the `ATLFAST-II` POWHEG-BOX (red triangles) event samples are used. A grey band around the PROTOS sample points is drawn with a width equal to the statistical uncertainty due to the limited size of the simulated sample. The results given by a simple inversion of the migration matrix are also shown for comparison (empty squares at the last bin).

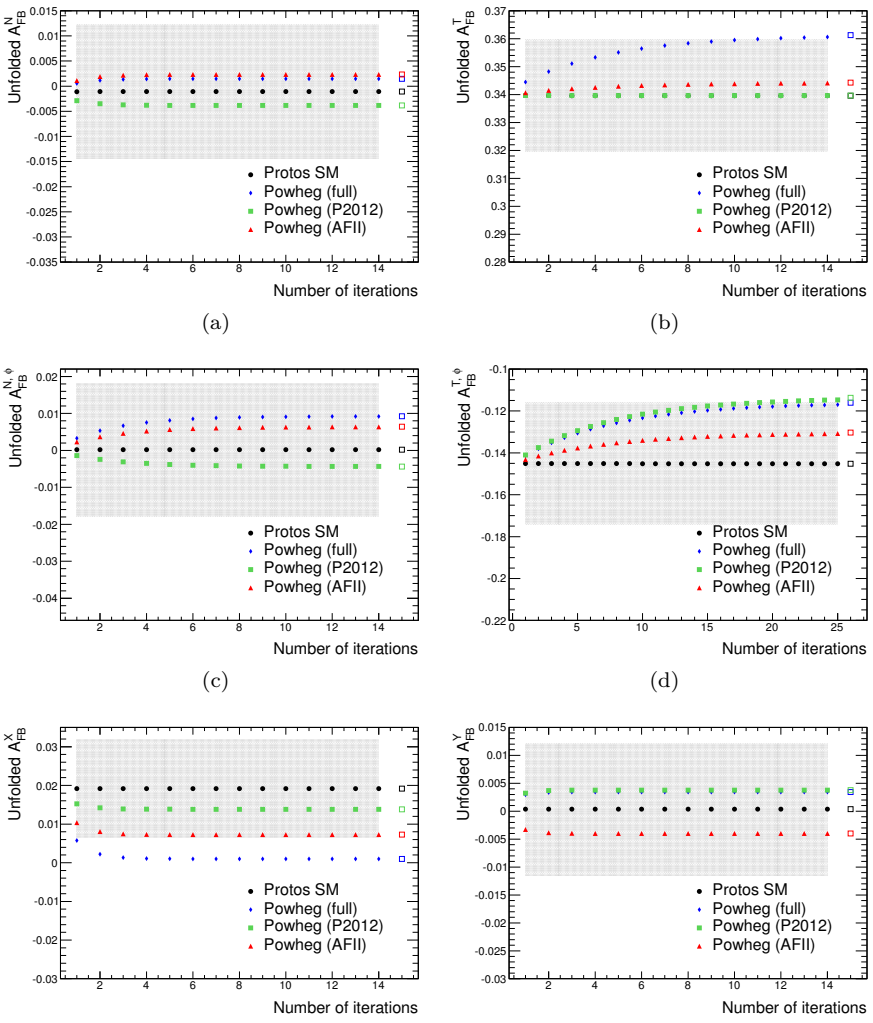

Figure 13.4: Unfolded values of the asymmetries as a function of the number of iterations of the bayesian unfolding algorithm: (a) A_{FB}^{N}, (b) A_{FB}^{T}, (c) $A_{\mathrm{FB}}^{N,\phi}$, (d) $A_{\mathrm{FB}}^{T,\phi}$, (e) A_{FB}^{X}, (f) A_{FB}^{Y}. The SM PROTOS (black points), the nominal POWHEG-BOX (blue diamonds), the POWHEG-BOX with the P2012 tune (green boxes), and the `ATLFAST-II` POWHEG-BOX (red triangles) event samples are used. A grey band around the PROTOS sample points is drawn with a width equal to the statistical uncertainty due to the limited size of the simulated sample. The results given by a simple inversion of the migration matrix are also shown for comparison (empty squares at the last bin).

13.3 Closure test

A closure test is performed to check the accuracy of the unfolding algorithm using statistically independent event samples for the unfolded angular distributions and for the resolution and efficiency corrections. To that end, the baseline PROTOS sample is split randomly into two sub-sets of same size. The first sub-set is used to determine the unfolding corrections: migration matrix and efficiency curve of every angular distributions. The second sub-set is used to built the angular distributions, which are later unfolded using the corrections of the first sub-set. The measurement results are then compared to the parton-level (or truth) values taking into account the expected statistical uncertainties related to the limited size of the MC simulation samples.

The results of the closure test obtained for the different asymmetries are displayed in figure 13.5. For each measured asymmetry, the relative difference between the unfolded and parton-level values is shown with the statistical uncertainty associated with the limited sizes of the split PROTOS event samples. Within the expected statistical uncertainties, all the measurement results are compatible with the true parton-level values, which are represented by the horizontal dashed line in the plot. Therefore, no bias will be considered in the measurement of all asymmetries.

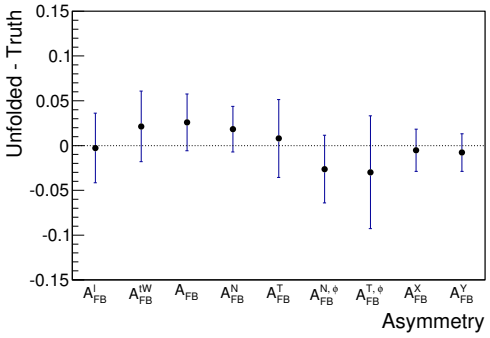

Figure 13.5: Absolute differences between the asymmetry values derived from the unfolded and parton-level angular distributions. The PROTOS event sample with the SM couplings is divided into two sub-sets, from which the unfolding corrections and the unfolded distributions are defined. The distributions are unfolded using the bayesian unfolding algorithm. The error bars represent the statistical uncertainties due to the limited sizes of the two t-channel simulation sub-samples. The horizontal dashed line corresponds to the closure.

13.4 Linearity

The PROTOS sample used to calculate the baseline unfolding corrections is generated with the SM values of the Wtb couplings: $V_{\mathrm{L}} = 1$, $V_{\mathrm{R}} = g_{\mathrm{L}} = g_{\mathrm{R}} = 0$. Additionally, PROTOS samples implementing non-standard values for the imaginary and real parts of g_{R} have been also generated: the covered range in Im g_{R} is ± 0.23, while from 0.18 to -0.26 is covered in Re g_{R}. These values are chosen as

they widely cover the ranges allowed by previous measurements [22, 116–118].

In order to provide measurements completely independent of any "a priori" assumption on the anomalous couplings, the linearity of the unfolding method has to be ensured. That means that the true value of the asymmetry is recovered with the unfolding for all the covered range of anomalous couplings, independently of its true value. The first test to be done is if the unfolding corrections derived with the SM couplings provides already a good linearity. Figures 13.6 and 13.7 show the results of this test for all the asymmetries measured in this work. All the PROTOS samples with anomalous values of $\mathrm{Im}\, g_\mathrm{R}$ and $\mathrm{Re}\, g_\mathrm{R}$ are unfolded to parton level using the unfolding corrections derived from the SM PROTOS sample. Samples with anomalous values of $\mathrm{Im}\, g_\mathrm{R}$ are plotted in blue, while the red colour is used for the samples with anomalous values of $\mathrm{Re}\, g_\mathrm{R}$. The SM PROTOS sample is also unfolded using the SM unfolding corrections, and it is plotted in black. A dotted line representing the case of a perfect linearity is painted too: the value of the asymmetry at reconstructed and truth level match.

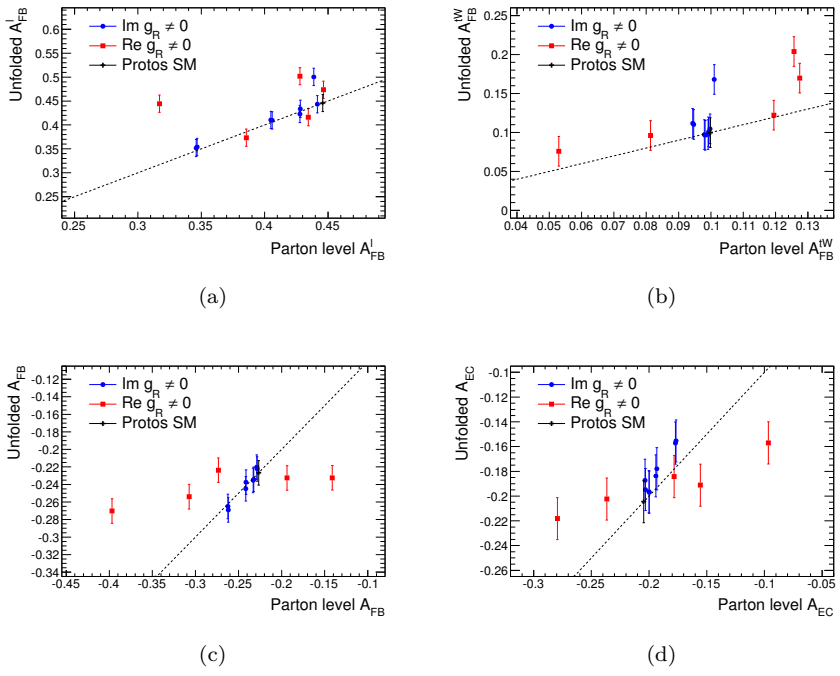

Figure 13.6: Linearity tests of the asymmetries (a) A_FB^{ℓ}, (b) A_FB^{tW}, (c) A_FB and (d) A_EC. The PROTOS samples with anomalous $\mathrm{Im}\, g_\mathrm{R}$ (blue) and $\mathrm{Re}\, g_\mathrm{R}$ (red) couplings are unfolded using the SM PROTOS unfolding corrections. The dashed lines represents the case of perfect linearity, in which the reconstructed and unfolded asymmetry match.

As it can be seen, in general, the SM unfolding corrections does not recover linearity. Most of the asymmetries have low sensitivity to the values of $\mathrm{Im}\, g_\mathrm{R}$ and $\mathrm{Re}\, g_\mathrm{R}$, taking into account the statistical uncertainty of the simulation. Of particular interest are the asymmetries A_FB^{N} and A_FB^{Y} (figures 13.7(a) and

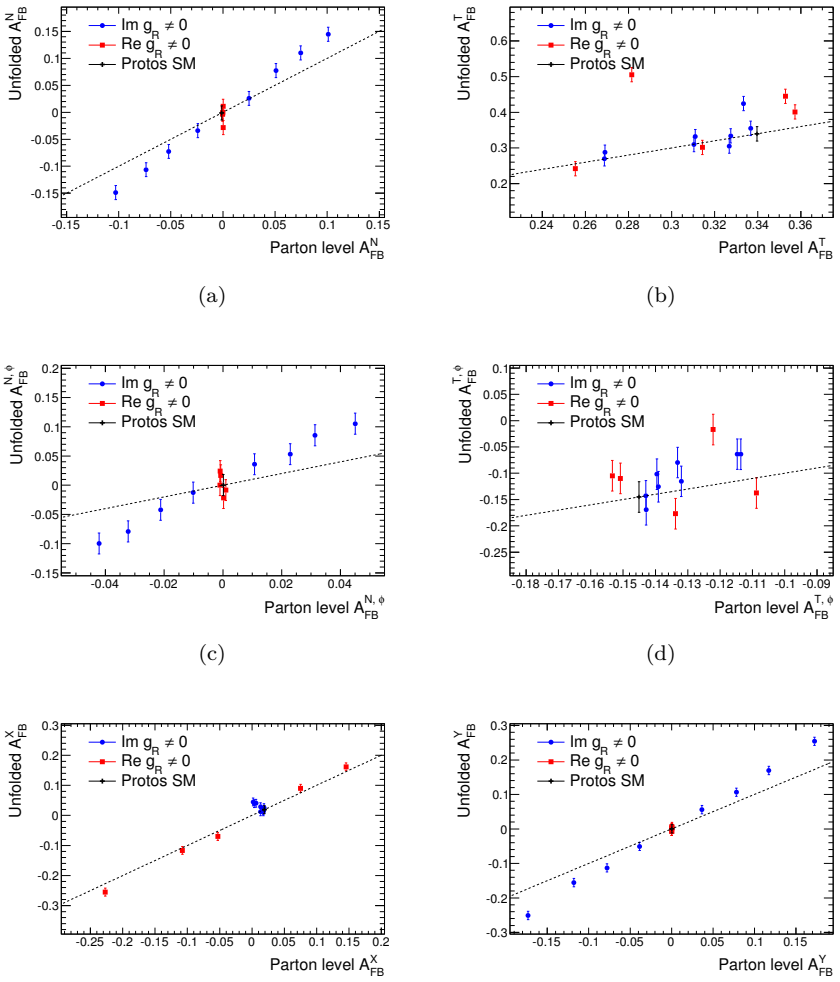

Figure 13.7: Linearity tests of the asymmetries (a) A_{FB}^{N}, (a) A_{FB}^{T}, (c) $A_{\mathrm{FB}}^{N,\phi}$, (d) $A_{\mathrm{FB}}^{T,\phi}$, (e) A_{FB}^{X} and (f) A_{FB}^{Y}. The PROTOS samples with anomalous $\mathrm{Im}\, g_{\mathrm{R}}$ (blue) and $\mathrm{Re}\, g_{\mathrm{R}}$ (red) couplings are unfolded using the SM PROTOS unfolding corrections. The dashed lines represents the case of perfect linearity, in which the reconstructed and unfolded asymmetry match.

13.7(f)), which are quite sensitive to the value of the $\mathrm{Im}\, g_\mathrm{R}$, and A_FB^X (figure 13.7(e)), sensitive to the value of the $\mathrm{Re}\, g_\mathrm{R}$. As one of the objectives of this analysis is the extraction of limits for $\mathrm{Im}\, g_\mathrm{R}$ and $\mathrm{Re}\, g_\mathrm{R}$, a method that recovers linearity for this three asymmetries has been developed and it is presented in section 13.5.

For all other asymmetries, the final measurement on real data will be performed using the SM unfolding corrections as they are not sensitive to anomalous values of $\mathrm{Im}\, g_\mathrm{R}$ and $\mathrm{Re}\, g_\mathrm{R}$. Therefore, their measurements will be presented as a cross-check of the SM value. The asymmetry A_FB^ℓ is also used in the limit extraction. It can be seen already the low sensitivity of A_FB^ℓ with both $\mathrm{Im}\, g_\mathrm{R}$ and $\mathrm{Re}\, g_\mathrm{R}$, as the size of simulation statistical errors already makes difficult to discern between the different values of the anomalous couplings. Once all the statistical and systematic uncertainties errors are taken into account (chapter 14), it results that the measurement of A_FB^ℓ is completely independent of the true values of the anomalous couplings, so it can be used in the limit extraction without compromising it.

13.5 Unfolding interpolation

It was found that unfolding samples generated with anomalous Wtb vertex couplings using the corrections derived with the SM PROTOS sample does not recover the simulated value for different angular asymmetries due to the presence of non linearities. The non linear response of the unfolding is due to the fact that the efficiency and the migration corrections between true and reconstructed levels are not independent of the anomalous Wtb vertex couplings values. These are modified because the kinematics of the t-channel single top production and decay change as the Wtb vertex couplings change.

As the main objective of this analysis is to constrain the values of the anomalous couplings through the measurement of a series of angular asymmetries, these non linearities have to be removed, as they would bias the measurements.

On this section a method of unfolding that remove the non linearities on $\mathrm{Re}\, g_\mathrm{R}$ and $\mathrm{Im}\, g_\mathrm{R}$ is described. It will be used to measure the normal forward-backward asymmetry, A_FB^N and the A_FB^Y asymmetry which are both predicted to have a high sensitivity to $\mathrm{Im}\, g_\mathrm{R}$, while being independent of $\mathrm{Re}\, g_\mathrm{R}$. Due to the fact that the unfolding method presented here recovers a good linearity, the measured values of A_FB^N and A_FB^Y are thus independent of any assumptions on $\mathrm{Re}\, g_\mathrm{R}$ and $\mathrm{Im}\, g_\mathrm{R}$, as the parton-level is recovered.

This method will be also used to measure the A_FB^X asymmetry, which is predicted to be sensitive to $\mathrm{Re}\, g_\mathrm{R}$ while being insensitive to $\mathrm{Im}\, g_\mathrm{R}$. Although the unfolding of this asymmetry presented an acceptable linearity already with the unfolding corrections of the SM PROTOS sample itself, the method presented here is proven to be very stable and reliable. Therefore it is preferred to follow the same procedure than with the A_FB^N and A_FB^Y measurements.

For the three asymmetries just mentioned, apart from $\mathrm{Im}\, g_\mathrm{R}$ ($\mathrm{Re}\, g_\mathrm{R}$), the SM values are assumed for all the other anomalous couplings.

13.5.1 Method

The method builds a new set of unfolding corrections by combining the migration and efficiency corrections provided by some PROTOS samples for which either $\mathrm{Im}\, g_{\mathrm{R}}$ or $\mathrm{Re}\, g_{\mathrm{R}}$ has been varied. For a given non-standard scenario, the method iteratively varies the weights of the different sample's corrections until convergence is reached in the measured asymmetry.

For both A_{FB}^{N} and A_{FB}^{Y}, five PROTOS samples with different simulated values of $\mathrm{Im}\, g_{\mathrm{R}}$ are used to construct the final unfolding correction. $\mathrm{Re}\, g_{\mathrm{R}}$ is null for all the samples. In the case of the A_{FB}^{X} measurement, six samples with different values of $\mathrm{Re}\, g_{\mathrm{R}}$ are used in the final unfolding correction building. In both cases, one of the used samples is the SM one, with null values of $\mathrm{Re}\, g_{\mathrm{R}}$ and $\mathrm{Im}\, g_{\mathrm{R}}$.

The combination of the different samples is made following a linear interpolation based on Lagrange polynomials. For example, for a certain value x of the forward-backward normal asymmetry A_{FB}^{N} of a sample (data or simulation), the unfolding correction is given by:

$$L(x) = f_1 \cdot p_1(x) + f_2 \cdot p_2(x) + f_3 \cdot p_3(x) + f_4 \cdot p_4(x) + f_5 \cdot p_5(x) \qquad (13.2)$$

with the weights $p_i(x)$ defined as:

$$\begin{aligned}
p_1(x) &= \frac{(x-x_2)(x-x_3)(x-x_4)(x-x_5)}{(x_1-x_2)(x_1-x_3)(x_1-x_4)(x_1-x_5)},\\
p_2(x) &= \frac{(x-x_1)(x-x_3)(x-x_4)(x-x_5)}{(x_2-x_1)(x_2-x_3)(x_2-x_4)(x_2-x_5)},\\
p_3(x) &= \frac{(x-x_1)(x-x_2)(x-x_4)(x-x_5)}{(x_3-x_1)(x_3-x_2)(x_3-x_4)(x_3-x_5)},\\
p_4(x) &= \frac{(x-x_1)(x-x_2)(x-x_3)(x-x_5)}{(x_4-x_1)(x_4-x_2)(x_4-x_3)(x_4-x_5)},\\
p_5(x) &= \frac{(x-x_1)(x-x_2)(x-x_3)(x-x_4)}{(x_5-x_1)(x_5-x_2)(x_5-x_3)(x_5-x_4)}
\end{aligned}$$

being f_i the sets of migration and efficiency corrections, and x_i the values of A_{FB}^{N} at parton level corresponding to the five samples i with different $\mathrm{Im}\, g_{\mathrm{R}}$ values.

The unfolding correction for A_{FB}^{Y} is constructed using the same formula. In the case of the A_{FB}^{X} measurement, a similar one is used, with the only difference that a total of six PROTOS samples are combined, including the SM PROTOS sample too.

The weights $p_i(x)$ are obtained with an iterative procedure that works as follows:

- For the first iteration, all weights but the SM sample one are set to zero. The built combination is therefore the SM one, which is used to unfold the signal.

- Once the signal has been unfolded to true parton-level, the asymmetry is measured obtaining a value x.
- The obtained value of the asymmetry, x, is then used to define a new set of weights using the set of equations 13.5.1.
- The sets of migration and efficiency corrections of the different samples are combined using equation 13.2 and the resulting combination is used to unfold again the signal, obtaining a new value of the asymmetry.
- The procedure is repeated until the convergence of the extracted asymmetry is reached.
- The criteria of convergence has been set to the difference between the extracted value of the asymmetry and the one extracted in the previous iteration being smaller than 0.0001.

The interpolation method is expected to work whenever the value x of the measured asymmetry is within the range of the simulated samples. The method is expected to fail outside this range as the interpolation would no longer be valid. Therefore, the initial seed, the value of the asymmetry extracted at the first iteration using the SM correction, is forced to be within this range. In case that after the iterations, the measured asymmetry x ends up to be outside this range, the unfolding correction provided by the new physics PROTOS sample with the truth value of the asymmetry closest to x is used. However, the simulated samples for this analysis cover a range wide enough for both $\mathrm{Re}\, g_{\mathrm{R}}$ and $\mathrm{Im}\, g_{\mathrm{R}}$ according to the current limits on both [22, 116–118].

13.5.2 Number of bayesian unfolding iterations

As explained in section 13.1, the unfolding of the signal is performed with a bayesian unfolded technique [113] implemented in RooUnfold [114]. The regularisation parameter of the bayesian unfolding is the number of bayesian unfolding iterations, which has not to be confused with the number of iterations of the iterative interpolation method explained on previous lines. This section focus on the number of bayesian iterations.

The first step at the iterative interpolation method is to extract the seeding value of the measured asymmetry by unfolding the signal with only the SM corrections. For this first unfolding, the number of bayesian iterations is determined from the convergence test presented in section 13.2. The convergence tests have also been performed with all the anomalous PROTOS samples, using the ones with anomalous values of $\mathrm{Im}\, g_{\mathrm{R}}$ for A_{FB}^{N} and A_{FB}^{Y} and the ones with anomalous values of $\mathrm{Re}\, g_{\mathrm{R}}$ in the case of A_{FB}^{X}. The results of these convergence tests are shown in figures 13.8(a), 13.8(c) and 13.9(a). Same number of iterations of the bayesian unfolding are needed to reach the convergence than with the POWHEG-BOX samples: 4 iterations for A_{FB}^{N} and A_{FB}^{X} and 3 for A_{FB}^{Y}.

Once the seeding value is obtained, the iterative interpolation method unfolds the signal with the built migration and efficiency corrections until the convergence of the measured asymmetry is reached. It has been checked that

using a different number of bayesian iterations inside the interpolation method does not vary the final calculated weights, neither the measured value of the asymmetry. Figures 13.8(b), 13.8(d) and 13.9(b) show that the final result of the measured asymmetries (A_{FB}^{N}, A_{FB}^{X} and A_{FB}^{Y}) is independent of the number of performed unfolding iterations at each step of the iterative interpolation unfolding. However, it has been observed that the total number of iterations that the interpolation method needs to achieve the convergence of the asymmetry increase with the number of used bayesian iterations. Additionally, it has been found that in some rare cases, RooUnfold fails to find a smooth convergence, returning a completely wrong unfolded distribution. The slightest variation on the RooUnfold inputs (*e.g.* removing one event out of ten millions on the truth distribution) was able to recover a good convergence of the method. Although the reasons behind these feature of RooUnfold were not understood, it was found that they were more frequent as the used number of bayesian iterations increased. For these reasons, just one bayesian iteration is performed for each of the unfolds inside the iterative method.

As a summary, the number of bayesian iterations used in each step are the following: When deriving the seed for the iterative interpolation method, a total of 4 iterations are performed (3 for A_{FB}^{Y}). Inside the loop of the interpolation method, each of the unfolds is performed in just 1 iteration. Once the method has converged and the final weights are determined, a last unfolding of the signal is performed with 4 total bayesian iterations (3 for A_{FB}^{Y}).

The interpolation method has been also tested with the different POWHEG-BOX samples: the baseline POWHEG-BOX sample (P2011C tune and passed through the full detector simulation), the one passed through the `ATLFAST2` simulation (P2011C tune) and the one with the P2012 tune and passed through the `ATLFAST2` simulation. Figure 13.10 shows the results of the test. The extracted value for each sample is independent of the number of bayesian unfolding iterations performed.

13.5.3 Closure tests

A closure test of the interpolation method has been performed with the available PROTOS samples. In the case of the A_{FB}^{N} and the A_{FB}^{Y} asymmetries, the test uses the samples with anomalous $\mathrm{Im}\, g_{\mathrm{R}}$ couplings, while the samples with anomalous $\mathrm{Re}\, g_{\mathrm{R}}$ couplings have been used in the A_{FB}^{X} asymmetry closure test. Additionally, the sample with SM couplings has been used in all closure tests. Results of the tests are shown in figure 13.11, where the difference between the unfolded and parton-level values of the asymmetry are plotted as a function of the respective anomalous couplings value of the sample. An independent set of weights is derived using the iterative interpolation method for each tested sample, building with them a set of unfolding corrections that is used to unfold the angular distribution of each sample and to extract the value of the asymmetry.

As explained above, in the case of A_{FB}^{N} and A_{FB}^{Y}, a total of five samples are used by the interpolation method: four samples with anomalous $\mathrm{Im}\, g_{\mathrm{R}}$ couplings plus the one with the SM couplings. Four additional samples with anomalous $\mathrm{Im}\, g_{\mathrm{R}}$ couplings have been produced in order to perform closure and linearity

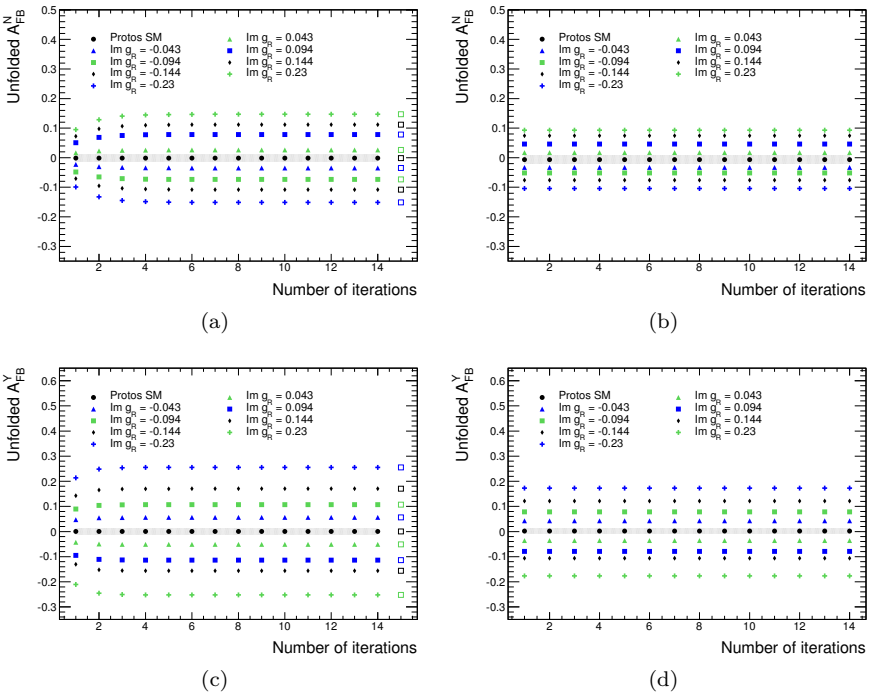

Figure 13.8: Unfolded values of the asymmetry A_{FB}^{N} (top) and A_{FB}^{Y} (bottom) as a function of the number of iterations of the Bayes algorithm obtained with the SM based unfolding (left) and with the iterative Lagrange interpolation unfolding (right). The PROTOS samples with anomalous $\mathrm{Im}\, g_{\mathrm{R}}$ couplings are used. The interpolation method is applied to each of these PROTOS samples. A grey band around the SM PROTOS sample points is drawn with a width equal to the statistical uncertainty due to the limited size of the simulated sample. The results given by a simple inversion of the migration matrix are also shown for comparison (open squares at the last bin).

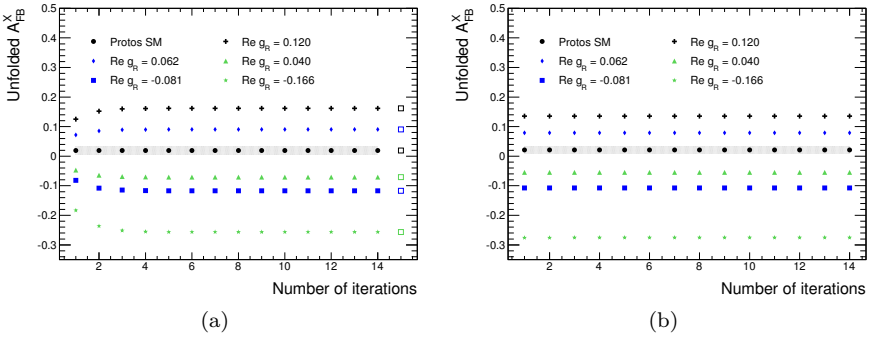

Figure 13.9: Unfolded values of the asymmetry A_{FB}^{X} as a function of the number of iterations of the Bayes algorithm obtained with the SM based unfolding (a) and with the iterative Lagrange interpolation unfolding (b). The PROTOS samples with anomalous $\mathrm{Im}\, g_{\mathrm{R}}$ couplings are used. The interpolation method is applied to each of these PROTOS samples. A grey band around the SM PROTOS sample points is drawn with a width equal to the statistical uncertainty due to the limited size of the simulated sample. The results given by a simple inversion of the migration matrix are also shown for comparison (open squares at the last bin).

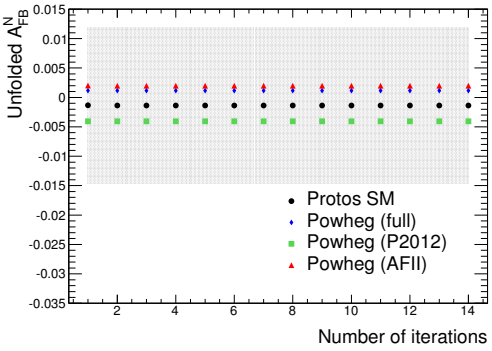

(a)

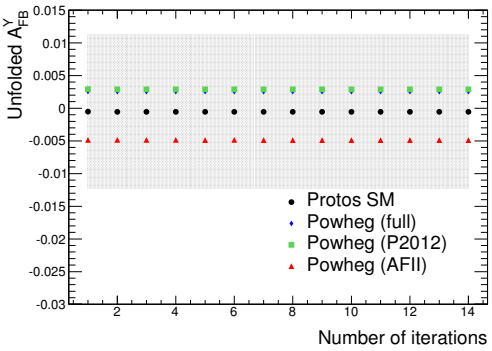

(b)

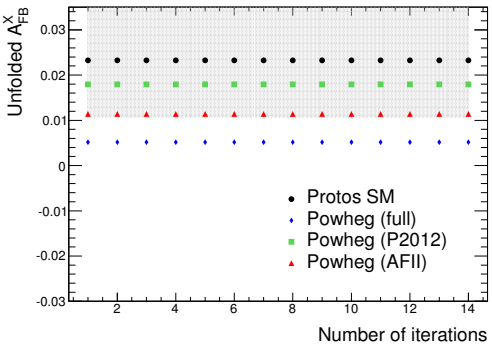

(c)

Figure 13.10: Unfolded values of the asymmetry A_{FB}^{N} (a), A_{FB}^{Y} (b) and A_{FB}^{X} (c) as a function of the number of iterations of the Bayes algorithm for the following samples: the SM PROTOS (black points), the nominal POWHEG-BOX (blue diamonds), the POWHEG-BOX with the P2012 tune (green boxes), and the `ATLFAST-II` POWHEG-BOX (red triangles). A grey band around the SM PROTOS sample points is drawn with a width equal to the statistical uncertainty due to the limited size of the simulated sample.

tests. These samples are not used by the interpolation method at any point. In the cases in which the closure test is performed over a sample that is used in the interpolation method, the sample is split into two statistically independent sub-sets of the same size. One of the sub-sets replace the original sample in the interpolation method to build the interpolated unfolding corrections, while the other sub-set is used to perform the closure test. For the A_{FB}^{X} asymmetry, apart from the samples used by the interpolation method (*i.e.* five samples with anomalous $\mathrm{Re}\, g_{\mathrm{R}}$ couplings plus the one with the SM couplings) no additional sample with anomalous $\mathrm{Re}\, g_{\mathrm{R}}$ couplings were available. The closure test is performed only with split samples.

All asymmetries show good results on the closure test. It can be seen in figure 13.11 that an overall agreement between the values of the asymmetries extracted from the unfolded and parton-level distributions is achieved. Most points are below the one sigma region around the perfect closure, represented by the horizontal dashed line, and the few points that remains outside this region are below the two sigma region.

13.5.4 Linearity tests

The iterative interpolation unfolding method was derived in order to remove the non linearities obtained when the unfolding is done using only the SM PROTOS unfolding corrections. Therefore, it has been tested that this method actually recovers a good linearity: that the unfolded value of the asymmetry matches the parton-level value for any value that is within the covered range of anomalous couplings.

The results of the test are shown in figure 13.12. The unfolded value of the asymmetry is shown as a function of the parton-level value of the asymmetry. Results can be compared with those obtained performing the unfolding only with the SM corrections. Green squares represent the extracted values of the asymmetries following the interpolation method, while the ones obtained from the SM correction are displayed with blue dots. The asymmetry extracted from the SM sample applying the SM corrections is shown with a black dot. It can be seen that a good linearity is recovered for both A_{FB}^{N} and A_{FB}^{Y} for samples with anomalous $\mathrm{Im}\, g_{\mathrm{R}}$ couplings, including the four additional samples that are not used in the interpolation step. Similar performance is seen for A_{FB}^{X} for samples with anomalous $\mathrm{Re}\, g_{\mathrm{R}}$ couplings, although all six samples are used for the interpolation in this case. Contrary to the closure test, the full PROTOS samples are considered here.

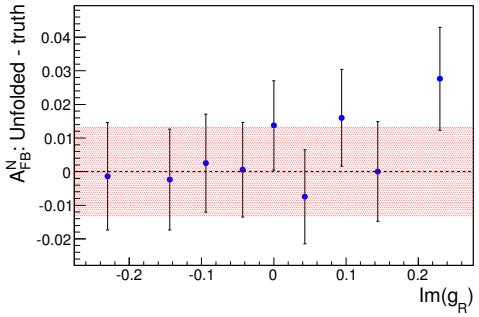

(a)

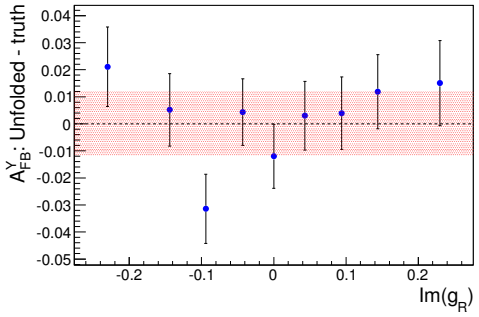

(b)

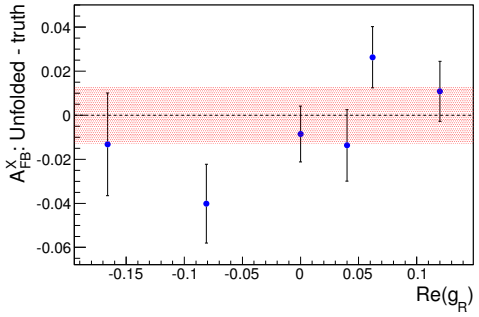

(c)

Figure 13.11: Differences between the values derived from the unfolded and parton-level angular distributions of the normal forward-backward asymmetry $A^N_{\rm FB}$ (a) and of the forward-backward asymmetries $A^Y_{\rm FB}$ (b) and $A^X_{\rm FB}$ (c). The distributions are unfolded with the Bayes algorithm using the corrections computed through the interpolation method. The various PROTOS samples with anomalous Im $g_{\rm R}$ couplings are tested for $A^N_{\rm FB}$ and $A^Y_{\rm FB}$, while the ones with anomalous Re $g_{\rm R}$ couplings are tested for $A^X_{\rm FB}$. Additionally, the PROTOS sample with the SM couplings, is tested for all asymmetries. The error bars represent the statistical uncertainties due to the limited sizes of the samples. The horizontal dashed line corresponds to the closure. A red band around the closure line is painted with a semi-width equal to the SM PROTOS sample statistical uncertainty.

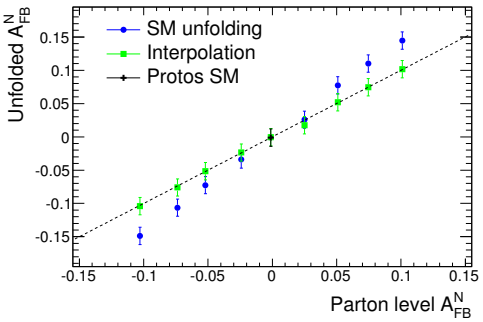

(a)

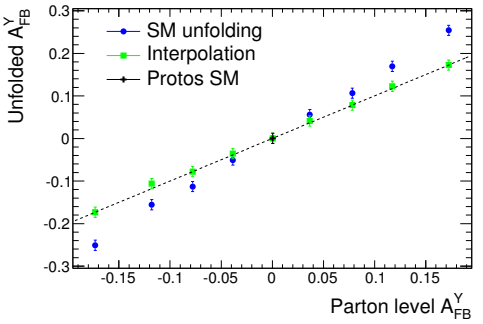

(b)

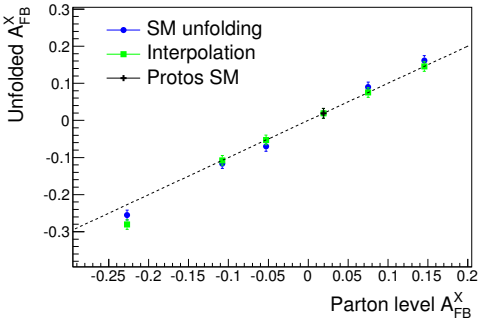

(c)

Figure 13.12: Unfolded value of the (a) normal forward-backward asymmetry A_{FB}^{N} and of the forward-backward asymmetries A_{FB}^{Y} (b) and A_{FB}^{X} (c) as a function of the parton level truth value. The PROTOS samples with the SM couplings, as well as those with anomalous $\mathrm{Im}\, g_{\mathrm{R}}$ couplings, are used for A_{FB}^{N} and A_{FB}^{Y}, while those with anomalous $\mathrm{Re}\, g_{\mathrm{R}}$ couplings are used for for A_{FB}^{X}. The results obtained with the interpolated unfolding corrections (green squares) are compared to those provided by the SM based unfolding (blue dots). The unfolding of the SM sample using the SM corrections is also shown (black dot). The error bars represent the uncertainties due to the limited statistics of the unfolded event distributions. The dashed line corresponds to the perfect linearity case.

Chapter 14

Systematic uncertainties

Various sources of systematic uncertainty are considered in the analysis reported in this work. The signal and all background processes have systematic uncertainties which have an impact both on the rate of the individual contributions and on the shape of their associated angular distributions. Signal systematic uncertainties also affect the migration matrices and efficiency corrections used to unfold the signal distributions.

The sources of systematic uncertainties are grouped into three categories: background normalisation uncertainties, detector modelling uncertainties, and signal and background modelling uncertainties. The effects due to the limited size of the data and simulated event samples are also taken into account when evaluating the measurement uncertainty. Each type of systematic or statistical uncertainty is estimated separately. Finally, all uncertainties are added in quadrature to get the total uncertainty.

In order to estimate the impact that the various sources of uncertainties have on the measurement, the variations are propagated in a correlated way to the rates and shapes. As the signal and background processes normalisation factors are extracted with a maximum-likelihood fit involving two additional control regions (section 10.2), the variations are also propagated to the control regions. For each source of systematic or statistical variation, a new set of normalisation factors is extracted once the variations have been propagated. As the shape of the signal and background processes in the control region does not have any impact on the fit result, only rate variations are propagated to the control regions. With this method, the impact of the systematic uncertainties on the control regions is correctly propagated to the measured asymmetries.

14.1 Background normalisation uncertainties

The impact of the normalisation uncertainties associated with the various background contributions are evaluated by varying their total rates before subtraction to the data. No shape variations are considered for this type of uncertainties. The differences between the measurements performed from the nominal

and varied rates give the systematic normalisation uncertainties.

- **Theoretical cross sections:** The event yields associated with the simulated $t\bar{t}$, single top, Z+jets and diboson processes are evaluated using the selection acceptances and the theoretically predicted cross sections reported in chapter 10: theoretical relative uncertainties of $\pm 6\%$, $\pm 7\%$ and $\pm 4\%$ are assigned to the $t\bar{t}$, Wt and s-channel background processes, respectively. For the Z+jets process, a cross section uncertainty of $\pm 20\%$ is considered as well as for the diboson contribution. For background processes that are merged in the analysis, the theoretical cross section uncertainties are combined in proportion to the contribution of each individual process in the selected event samples: a relative uncertainty of $\pm 6\%$ is thus considered for the merged $t\bar{t}$, Wt and s-channel background contributions, and a relative uncertainty of $\pm 20\%$ is applied for the merged Z+jets and diboson backgrounds. For the W+jets normalisation, a relative uncertainty of $\pm 20\%$ is considered. This uncertainty is evaluated from studies carried out with SHERPA samples generated with various configurations, and reported in [85].

  By default, the method for extracting the normalisation factors of signal and background processes explained in section 10.2 already includes the cross section theoretical uncertainties of each process as a constrain of the fit.

- **Multijet normalisation:** The multijet background is normalised through the data-driven analysis based on the matrix method, as described in section 10.1. A relative systematic uncertainty of $\pm 70\%$ is assigned to the overall normalisation. It is evaluated from the comparison with the results obtained using alternative procedures to estimate the multijet contribution.

- **Luminosity:** The normalisation of the simulated background contributions is also affected by the uncertainty on the integrated luminosity. This uncertainty is $\pm 1.9\%$ [71]. Its impact is estimated by varying accordingly the overall normalisation factors of the background MC samples.

14.2 Detector modelling uncertainties

The detector modelling uncertainties are evaluated by varying in a correlated way the rates and the distribution shapes predicted by the MC simulations for the signal and background processes. The differences between the measurements performed from the nominal and varied rates and shapes give the systematic uncertainties. No instrumental systematic uncertainties are considered in the analysis for the data-driven multijet contribution.

Most of the systematic uncertainties listed below includes each various sources of uncertainties, which are calculated individually an added in quadrature.

- **Lepton reconstruction:** Includes the impact of the energy/momentum scale and resolution of the lepton, and the lepton trigger and identifi-

cation efficiency. The impact of the lepton energy scale and resolution uncertainties are evaluated by scaling or smearing up and down the lepton transverse energy/momentum by 1σ and re-applying the object and event selections to the simulated samples. Scale factors are applied to the MC lepton trigger and identification efficiencies in order to reproduce the efficiencies measured in the data and the predicted event yields are re-computed using the efficiency scale factors shifted up and down by 1σ.

- **Jet energy scale:** Calibrates the measured calorimeter-level jet energy to the particle-level, taking into account the calibration method, pile-up effects, the calorimeter response, the detector simulation and other sources. It is derived using information from test-beam, collision and simulation data. A parametrisation with 26 uncorrelated components is considered, each of which depends on the p_{T} and η of the reconstructed jet. For each of these contributions, the energy of each simulated jet is re-scaled up and down by the corresponding 1σ before re-applying the object and event selections.

- **Jet reconstruction:** Includes uncertainties from the jet energy resolution and reconstruction efficiency, together with the uncertainties due to the jet vertex fraction. The uncertainty due to the energy resolution is extracted by smearing the energy of the jets and re-applying the object and event selections. The jet reconstruction efficiency is derived by matching jets reconstructed from tracks to the calorimeter based jets. Its uncertainty is evaluated by randomly dropping jets from MC and determining the induced production rate and shape variations. The JVF measures the ratio of the p_{T} of tracks coming from the primary vertex versus the p_{T} all tracks contained in a jet. As it is used as a cut in the selection, the uncertainty is evaluated by changing the nominal JVF requirements value.

- **Jet flavour tagging:** The corrections that account for differences in the b-tagging efficiency and c-jet and light-jet mistagging rates are varied within their uncertainties, which have been measured in data. The three sources are calculated separately and later added together. The c-tagging efficiency also includes the τ-tagging efficiency.

- **Missing transverse momentum:** the $E_{\mathrm{T}}^{\mathrm{miss}}$ is reconstructed from the lepton and the jets in the event. Energy scale and resolution uncertainties from these objects are propagated to the missing transverse momentum through the re-computation of the corresponding terms. Other contributions as the cell out terms (soft energy depositions not included in the reconstruction) are also included.

14.3 Signal/background modelling uncertainties

The systematic uncertainties associated with the modelling of the signal and background processes are evaluated by comparing different MC simulated samples, for which either specific parameters or the whole event generator is changed.

Most of the samples implementing the modelling variations are generated with the ATLFAST2 simulation of the detector. In that case, if the nominal sample production is based on the full detector simulation, relative systematic uncertainties are estimated from the comparison with a sample equivalent to the nominal one but passed through ATLFAST2. The relative uncertainty is then propagated to the nominal result to get the corresponding measurement uncertainties.

- **MC generator and parton shower modelling:** The nominal samples described in section 2.2 are compared with the ones listed in appendix A.1, which have been derived using alternative MC generators and parton shower modelling. In each case, the full differences in the measured asymmetries between the two compared MC samples are taken as up and down systematic uncertainties.

- **Scales and initial/final-state radiation:** The uncertainty due to the choice of the factorisation and normalisation scales is evaluated for the three single top processes by comparing POWHEG+PYTHIA samples, produced with varied re-normalisation and factorisation scales, to the nominal samples. These samples are also generated with more or less parton shower radiation (ISR/FSR). For the $t\bar{t}$ process, it is measured with two dedicated POWHEG-BOX+PYTHIA event samples generated with more and less parton shower radiation. In all cases, the combination giving the largest difference with respect to the nominal measurement is used to define the up and down systematic uncertainties. Details about the samples used are given in appendix A.1.

- **Parton distribution functions:** To estimate the systematic uncertainties related to the parton distribution functions (PDFs), the signal and all background simulated samples are re-weighted according to each of the PDF uncertainty eigenvectors. The uncertainty is estimated, following the PDF4LHC prescription [99], by calculating the envelope of the uncertainties at 68% confidence level of the CT10 [74], MSTW2008nlo68 [92] and NNPDF2.3 [101] sets with normalisation to the nominal cross section. The largest up and down variations are then taken as systematic uncertainties.

- **W+jets modelling:** it includes the uncertainties due to the W+jets shape modelling and flavour composition. The impact of the heavy flavour composition on the shapes of the W+jets angular distributions is determined by varying the ratio between the W+bb and W+cc contributions by a factor $\pm 50\%$. The contribution from W+light jets is very small in the signal region and no systematic uncertainty is taken into account.

  For certain kinematic variables, the simulated W+jets samples do not describe very well the data. By introducing event re-weighting as a function of some kinematics, a good modelling can be recovered. This technique was already used in the search of FCNC in single top quark at 8 TeV [119]. While the W+jets events are not re-weighted for the analysis, the W+jets mis-modelling is taken into account through an additional systematic uncertainty. It is estimated conservatively by comparing the results given by the shape re-weightings based on the W's p_{T} and m_{T} and ΔR(b-jet,non b-jet) distributions. For all measured asymmetries, the re-weighting derived

from the distribution of the W boson transverse mass gives the largest differences with respect to the nominal case. The full differences in the measured asymmetries are taken as up and down systematic uncertainties

- **Multijet shape modelling:** A systematic uncertainty associated with the data-driven shape modelling of the multijet events is evaluated by comparing the shapes provided by the baseline estimate with the matrix method and the alternative modelling given by the jet-electron and anti-muon models. For this comparison, the jet-electron/anti-muon distributions are normalised using the nominal event yields. The full differences in the measured asymmetries are taken as up and down systematic uncertainties.

14.4 Statistical uncertainties

The uncertainties due to the limited sizes of the MC samples are evaluated using pseudo-experiments.

The nominal background samples are varied in shape and rate in the signal region. A bin-per-bin gaussian smearing is done for every process, using the nominal bin value and its statistical error as the mean and the width of the gaussian distribution. The sum over the varied bins gives the variation in rate for each background. In the control regions, only rate variations are considered, as the shape does not have any impact on the extraction of the normalisation factors.

No variations are performed for the multijet component as its contribution is obtained with data-driven methods. As explained in section 14.1, the impact of the multijet normalisation is measured through an specific systematic.

The impact of the size of the simulated signal samples is measured by varying the unfolding migration matrices bin-per-bin. A gaussian smearing with a width equal to the statistical error of each bin is performed in the migration matrix. The integration over the truth angles of the fluctuated matrix gives the fluctuated reconstructed signal. Additionally, the integration over the reconstructed angles is used to calculate the efficiency variations in the truth distributions. As the number of generated truth events is much larger, statistical variations of the truth distributions are discarded.

Another way of calculating the uncertainties due to the signal samples size is to treat the signal as all the other backgrounds, making general rate variations in the two control regions and bin-per-bin rate and shape variations in the signal region, according to the statistical errors. It has been checked that this method leads to the same results.

The uncertainties due to the limited size of the data sample are evaluated through pseudo-experiments too. Poissonian fluctuations on the expected signal and backgrounds angular distributions are performed for each process except the data-driven multijet contribution. As it is done in the simulation statistics case, each process is varied in shape and rate in the signal region but only in rate in the two control regions. The fluctuated event yields are used to calculate a set

of normalisation factors for every pseudo-experiment.

For both data and simulation statistical uncertainty, 10k pseudo-experiments are run. The standard deviation associated with the distribution of the measured asymmetry provided by an ensemble of pseudo-experiments is taken as the corresponding statistical uncertainty.

14.5 Expected uncertainties

The expected uncertainties are estimated using the signal acceptances, the background rates and the angular distribution shapes given by the simulated or data-driven samples. These samples are normalised with the theoretical cross sections presented in section 10. The multijet process normalisation is obtained with the data-driven method discussed in section 10.1.

For each systematic uncertainty, which can either be an *up* or *down* variation of a systematic source or a pseudo-experiment of a statistical one, the variations due to the uncertainty source are propagated in the signal and control regions. This defines the so called *pseudo-data*. For each pseudo-data, a set of normalisation factors is extracted from the varied event yields following the method described in 10.2. The nominal background contributions, scaled with the normalisation factors just mentioned, are then subtracted from the pseudo-data distributions in the signal region. What remains compose the *pseudo-signal*, which is subsequently unfolded using the nominal migration matrices and efficiency corrections. The difference between the nominal value of an asymmetry and the asymmetry extracted from the unfolded pseudo-signal is taken as the uncertainty due to that specific systematic source.

The only different case is the calculation of the uncertainty due to the signal simulated statistics. In that case, the signal variations are performed directly to the migration matrices and efficiency corrections, which are later used to perform the signal unfolding.

14.6 Observed uncertainties

To estimate the observed systematic uncertainties, the nominal signal and background processes event yields given by the MC are re-scaled in order to reproduce the observed data event yields, both in the signal and in the two control regions. In order to do that, using the method described in section 10.2, a set of normalisation factors for the signal and the top and W+jets backgrounds are extracted. The measured signal is obtained by subtracting all background processes from the events in the signal region, after the normalisation factors just mentioned above have been applied. The remaining events compose the measured signal. As the shape of the measured signal and the simulated t-channel will not generally coincide, a bin-per-bin scaling of the MC t-channel is done such that it properly reproduces the observed data shape.

Once the data-to-simulation scale factors have been calculated, these are

used to normalise the nominal signal and background processes and the uncertainty extraction follows the same procedure than for the expected uncertainties. Once the pseudo-signal is obtained, it is re-weighted using the bin-per-bin scaling factors described in previous paragraph, before performing the unfolding. Once again, the difference between the asymmetry extracted from the pseudo-signal and the measured asymmetry is taken as the observed uncertainty.

The uncertainties presented below are the observed uncertainties.

14.7 Uncertainty breakdowns

Tables 14.1 to 14.3 give the breakdowns of the contributions to the observed statistical and systematic uncertainties on the measurement of the asymmetries related to the top quark polarisation observables and to the W boson spin observables. Individual systematic uncertainties in which only the *up* or the *down* contribution has an impact on the measurement have been symmetrised in order to give a more conservative total uncertainty. After performing this symmetrisation, the systematic contributions are merged according to the type of reconstructed object for the detector-related uncertainties and to the type of process for the normalisation and modelling uncertainties, following the categories described in sections 14.1, 14.2 and 14.3. The contributions merged in a common category are added quadratically. The tables with the breakdown of the expected statistical and systematic uncertainties are shown in appendix B.

For most asymmetries, the main uncertainty contribution comes from the limited size of the data sample, but others are dominated by systematics. The most important sources of systematic uncertainties are the modelling of the t-channel and $t\bar{t}$ processes, and the jet energy scale and reconstruction. The limited sizes of the simulation samples are in general the fourth contribution to the measurement uncertainties. It is interesting to remark that the largest contribution to the total uncertainty of both A_{FB}^{N} and A_{FB}^{Y}, the two asymmetries used to set limits in Im g_{R} is the statistical uncertainty.

Focusing in the two new asymmetries proposed in [17], A_{FB}^{X} and A_{FB}^{Y}, it can be seen that despite having quite similar data and simulation statistical errors, A_{FB}^{X} ends having a much larger total systematic uncertainty than A_{FB}^{Y}. The jet reconstruction and energy scale systematics are its main source of uncertainty, followed by the $t-$channel generator scales. The data statistics is only the fourth main source. The background normalisation, the $t-$channel LO-NLO generator, the $t\bar{t}$ generator and the $W+$jets, multijet modelling are other important contributions to the total systematic uncertainty.

Uncertainty source	$\Delta A_{\mathrm{FB}}^{l} \times 10^2$	$\Delta A_{\mathrm{FB}}^{tW} \times 10^2$	$\Delta A_{\mathrm{FB}} \times 10^2$	$\Delta A_{\mathrm{EC}} \times 10^2$
Statistical uncertainty	± 2.6	± 3.1	± 2.3	± 2.8
Simulation statistics	± 1.7	± 1.9	± 1.4	± 1.7
Luminosity	< 0.1	< 0.1	< 0.1	< 0.1
Background normalisation	± 0.5	± 0.5	± 0.9	± 0.7
E_T^{miss} reconstruction	$^{+0.9}_{-0.1}$	$^{+0.4}_{-0.7}$	$^{+1.1}_{-0.7}$	$^{+0.8}_{-0.2}$
Lepton reconstruction	$^{+1.0}_{-0.4}$	$^{+0.1}_{-1.3}$	± 1.4	$^{+0.6}_{-0.3}$
Jet reconstruction	± 2.1	± 2.5	± 1.2	± 1.8
Jet energy scale	$^{+1.3}_{-1.2}$	$^{+2.0}_{-1.6}$	$^{+3.4}_{-2.7}$	$^{+2.0}_{-0.7}$
Jet flavour tagging	± 0.9	± 0.3	± 0.6	± 0.4
PDF	± 0.2	< 0.1	< 0.1	± 0.2
$t\bar{t}$ generator	± 2.3	± 1.0	± 0.2	± 1.2
$t\bar{t}$ parton shower	± 0.6	± 0.5	± 2.7	± 0.3
$t\bar{t}$ scales	± 0.2	± 0.4	± 1.2	± 0.3
Wt,$s-$channel generator	± 1.0	± 1.1	± 0.4	± 0.3
Wt,$s-$channel scales	± 0.9	± 0.3	± 0.3	± 0.3
$t-$channel NLO generator	± 1.4	± 0.6	± 0.6	± 2.7
$t-$channel LO-NLO generator	± 1.5	± 2.0	± 2.6	± 1.8
$t-$channel parton shower	± 0.5	± 1.0	± 3.5	± 0.2
$t-$channel scales	± 1.1	± 2.0	± 0.6	± 1.6
W+jets, multijet modelling	$^{+1.9}_{-2.4}$	$^{+0.9}_{-1.0}$	$^{+2.2}_{-2.1}$	$^{+1.3}_{-1.2}$
Systematic uncertainty	± 5.4	$^{+5.2}_{-5.3}$	$^{+7.3}_{-6.9}$	$^{+5.3}_{-4.8}$

Table 14.1: Breakdown of the contributions to the observed statistical and systematic uncertainties on the A_{FB}^{l}, A_{FB}^{tW} and A_{FB} forward-backward asymmetries, extracted from the distributions in $\cos\theta_l$, $\cos\theta_W \cos\theta_l^*$ and $\cos\theta_l^*$ respectively. The breakdown for the edge-central asymmetry A_{EC} of the distribution $\cos\theta_l^*$ is also shown. For better readability the uncertainties are scaled by 10^2.

Uncertainty source	$\Delta A_{\mathrm{FB}}^{N} \times 10^2$	$\Delta A_{\mathrm{FB}}^{T} \times 10^2$	$\Delta A_{\mathrm{FB}}^{N,\phi} \times 10^2$	$\Delta A_{\mathrm{FB}}^{T,\phi} \times 10^2$
Statistical uncertainty	± 2.2	± 3.1	± 3.0	± 4.6
Simulation statistics	± 1.3	± 2.0	± 1.8	± 2.9
Luminosity	< 0.1	< 0.1	< 0.1	< 0.1
Background normalisation	± 0.4	± 1.1	± 0.6	± 1.1
E_T^{miss} reconstruction	$^{+0.3}_{-0.4}$	$^{+0.5}_{-0.3}$	$^{+0.5}_{-0.8}$	$^{+0.4}_{-1.3}$
Lepton reconstruction	$^{+0.1}_{-0.2}$	$^{+1.3}_{-1.5}$	$^{+0.6}_{-0.5}$	$^{+1.6}_{-0.6}$
Jet reconstruction	± 0.8	± 0.5	± 1.6	± 1.3
Jet energy scale	$^{+0.9}_{-0.8}$	$^{+3.9}_{-4.6}$	$^{+0.6}_{-2.5}$	$^{+4.5}_{-2.5}$
Jet flavour tagging	± 0.2	± 0.6	± 0.3	± 0.6
PDF	± 0.1	± 0.1	± 0.1	± 0.4
$t\bar{t}$ generator	± 0.2	± 3.5	± 1.7	± 1.3
$t\bar{t}$ parton shower	± 1.5	± 1.0	± 0.9	± 1.6
$t\bar{t}$ scales	± 0.3	± 0.8	± 0.3	± 1.3
Wt,$s-$channel generator	± 0.2	± 0.8	± 0.3	± 1.4
Wt,$s-$channel scales	± 0.6	± 0.5	± 0.4	± 0.9
$t-$channel NLO generator	± 0.3	± 4.5	± 2.6	± 7.2
$t-$channel LO-NLO generator	± 0.5	± 1.9	± 1.3	± 3.2
$t-$channel parton shower	± 0.7	± 0.9	< 0.1	± 1.1
$t-$channel scales	± 0.9	± 2.2	± 1.4	± 2.6
W+jets, multijet modelling	$^{+0.7}_{-0.6}$	$^{+1.3}_{-1.7}$	± 0.6	$^{+2.3}_{-1.7}$
Systematic uncertainty	± 2.9	$^{+8.3}_{-8.8}$	$^{+4.8}_{-5.4}$	$^{+10.9}_{-10.1}$

Table 14.2: Breakdown of the contributions to the observed statistical and systematic uncertainties on the A_{FB}^{N}, A_{FB}^{T}, $A_{\mathrm{FB}}^{N,\phi}$ and $A_{\mathrm{FB}}^{T,\phi}$ forward-backward asymmetries, extracted from the distributions in $\cos\theta_l^N$, $\cos\theta_l^T$, $\cos\theta_l^* \cos\phi_N^*$ and $\cos\theta_l^* \cos\phi_T^*$, respectively. For better readability the uncertainties are scaled by 10^2.

Uncertainty source	$\Delta A_{\mathrm{FB}}^{Y} \times 10^2$	$\Delta A_{\mathrm{FB}}^{X} \times 10^2$
Statistical uncertainty	± 1.9	± 2.0
Simulation statistics	± 1.2	± 1.3
Luminosity	< 0.1	< 0.1
Background normalisation	± 0.3	$^{+1.6}_{-1.7}$
E_T^{miss} reconstruction	± 0.2	± 0.2
Lepton reconstruction	$^{+0.4}_{-0.3}$	± 0.2
Jet reconstruction	± 1.1	± 2.8
Jet energy scale	$^{+0.5}_{-0.4}$	$^{+2.8}_{-2.2}$
Jet flavour tagging	± 0.1	± 0.3
PDF	< 0.1	± 0.4
$t\bar{t}$ generator	± 0.3	± 1.3
$t\bar{t}$ parton shower	± 0.4	± 0.5
$t\bar{t}$ scales	± 0.3	± 0.6
Wt,$s-$channel generator	± 0.2	± 0.3
Wt,$s-$channel scales	± 0.4	± 0.3
$t-$channel NLO generator	± 0.5	± 0.1
$t-$channel LO-NLO generator	± 0.4	± 1.5
$t-$channel parton shower	± 1.0	± 0.2
$t-$channel scales	± 1.0	± 2.2
W+jets, multijet modelling	$^{+0.2}_{-0.3}$	$^{+1.5}_{-0.9}$
Systematic uncertainty	± 2.5	$^{+5.7}_{-5.3}$

Table 14.3: Breakdown of the contributions to the observed statistical and systematic uncertainties on the A_{FB}^{Y} and A_{FB}^{X} forward-backward asymmetries of the distributions in $\cos\theta_y$ and $\cos\theta_x$ respectively. For better readability the uncertainties are scaled by 10^2.

Chapter 15

Results

This chapter presents the results of the measurement of the various asymmetries and of their related top quark and W boson polarisation observables. Limits on the anomalous couplings $\mathrm{Im}\, g_\mathrm{R}$ and $\mathrm{Re}\, g_\mathrm{R}$ are set from various of the measured asymmetries. The asymmetries A_FB^N and A_FB^Y have been used to extract limits on $\mathrm{Im}\, g_\mathrm{R}$. A_FB^X is used to set limits on $\mathrm{Re}\, g_\mathrm{R}$. In all cases, A_FB^ℓ, which was found to be insensitive to both anomalous couplings is used in the limit extraction in order to constrain the value of the spin analysing power of the leptons, α_ℓ.

As explained previously, before unfolding the signal to parton-level, the background contributions are first subtracted to the measured angular distributions. The anti-signal and $t\bar{t}$ control regions are used to constrain the background normalisation factors in the signal region, which are extracted from a maximum-likelihood fit, as explained in section 10.2.

For most asymmetries, the unfolding corrections (resolution matrices and efficiency curves) are determined from the t-channel PROTOS+PYTHIA simulation implementing the SM values of the Wtb couplings. For the measurement of A_FB^N, A_FB^X and A_FB^Y, the unfolding corrections computed through the interpolation method presented in section 13.5 are used. This method allows to measure A_FB^N and A_FB^Y independently of any assumption on the value of the anomalous coupling $\mathrm{Im}\, g_\mathrm{R}$ and A_FB^X independently of any assumptions on $\mathrm{Re}\, g_\mathrm{R}$.

The systematic and statistical uncertainties associated with the measured asymmetries are evaluated through the procedures explained in chapter 14 considering the various sources of systematic uncertainty described in that section. Tables with the breakdown of the observed uncertainties for all measured asymmetries are presented in section 14.7.

The measurement results presented here are extracted from angular distributions combining both the electron and muon channels. The top quark and top-antiquark productions are also merged. The angular distributions are defined using 2 or 4 bins, as explained in section 13.1, and are unfolded using the Bayes algorithm with the numbers of iterations summarised in table 13.1.

15.1 Asymmetries and spin observables

The values measured for the asymmetries related to the top quark polarisation observables and to the W boson spin observables are presented in table 15.1.

	Value	Stat.	Syst.	Final value	SM pred.
A_{FB}^{ℓ}	0.49	0.03	0.05	0.49 ± 0.06	0.45
A_{FB}^{X}	-0.03	0.02	$^{+0.06}_{-0.05}$	-0.03 ± 0.06	0.02
A_{FB}^{Y}	0.01	0.02	0.03	0.01 ± 0.03	0
A_{FB}^{tW}	0.10	0.03	0.05	0.10 ± 0.06	0.10
A_{FB}	-0.26	0.02	0.07	-0.26 ± 0.08	-0.23
A_{EC}	-0.25	0.03	0.05	-0.25 ± 0.06	-0.20
A_{FB}^{T}	0.39	0.03	0.09	0.39 ± 0.09	0.34
A_{FB}^{N}	-0.04	0.02	0.03	-0.04 ± 0.04	0
$A_{\mathrm{FB}}^{T,\phi}$	-0.17	0.05	$^{+0.11}_{-0.10}$	$-0.17 \pm ^{+0.12}_{-0.11}$	-0.14
$A_{\mathrm{FB}}^{N,\phi}$	-0.03	0.03	0.05	-0.03 ± 0.06	0

Table 15.1: Summary of the measured asymmetries results. The uncertainties due to the limited statistics of the ATLAS data are shown independently under the column *Stat.* The squared sum of all other sources of uncertainty is given on the column labelled as *Syst.* The final measured values, together with their total uncertainty are shown on the second to last column, which can be compared with their respective SM predictions, shown on the last column.

The values for the top quark polarisation P combined to the spin analysing power α_ℓ and to the sum of the W boson helicity fractions F_{R} and F_{L}, derived using equations of table 11.1, are presented in table 15.2.

	Value	Stat.	Syst.	Final value	SM pred.
$\alpha_\ell P$	0.97	0.05	0.11	0.97 ± 0.12	0.90
$\alpha_\ell \bar{P}_x$	-0.05	0.04	0.11	-0.05 ± 0.12	0.04
$\alpha_\ell \bar{P}_y$	0.01	0.04	0.05	0.01 ± 0.06	0
$P(F_{\mathrm{R}} + F_{\mathrm{L}})$	0.25	0.08	0.14	0.25 ± 0.16	0.27

Table 15.2: Summary of the measured top quark polarisations and W boson helicity fractions. The uncertainties due to the limited statistics of the ATLAS data are shown independently under the column *Stat.* The squared sum of all other sources of uncertainty is given on the column labelled as *Syst.* The final measured values, together with their total uncertainty are shown on the second to last column, which can be compared with their respective SM predictions, shown on the last column.

Finally, the values for the W boson spin observables derived from the corresponding asymmetries, using once again the equations shown in table 11.1, are listed in table 15.3

	Value	Stat.	Syst.	Final value	SM pred.
$\langle T_0 \rangle$	-0.55	0.06	0.12	-0.55 ± 0.13	-0.433
$\langle A_1 \rangle$	0.27	0.07	$^{+0.16}_{-0.17}$	$0.27 \pm ^{+0.17}_{-0.19}$	0.228
$\langle A_2 \rangle$	-0.05	0.05	0.09	-0.05 ± 0.10	0
$\langle S_1 \rangle$	0.52	0.04	0.12	0.52 ± 0.12	0.456
$\langle S_2 \rangle$	0.06	0.03	0.04	0.06 ± 0.05	0
$\langle S_3 \rangle$	-0.35	0.03	0.10	-0.35 ± 0.10	-0.309

Table 15.3: Summary of the measured W boson spin observables results. The uncertainties due to the limited statistics of the ATLAS data are shown independently under the column *Stat.* The squared sum of all other sources of uncertainty is given on the column labelled as *Syst.* The final measured values, together with their total uncertainty are shown on the second to last column, which can be compared with their respective SM predictions, shown on the last column.

Figure 15.1(a) show the measured and predicted values of all asymmetries except for A_{FB}^{X} and A_{FB}^{Y}, that were not included in the official ATLAS analysis published in [115]. The derived values for the six W boson observables are compared to their predicted values in figure 15.1(b). A good compatibility between the measurements and the SM predictions is observed. The measured values for A_{FB}^{X} and A_{FB}^{Y} are also compatible with their respective SM predictions, as can be seen in table 15.1. The extracted top quark polarizations $\bar{P}_x$ and $\bar{P}_y$ do also match the SM predictions.

15.2 Limits

This section presents the limits set for the anomalous couplings $\mathrm{Im}\, g_{\mathrm{R}}$ and $\mathrm{Re}\, g_{\mathrm{R}}$. The limits on $\mathrm{Im}\, g_{\mathrm{R}}$ are extracted from the measured value of A_{FB}^{N} and A_{FB}^{Y}, which depends on top quark degree of polarisations P and $\bar{P}_y$, respectively, and on the spin analysing power α_ℓ. As A_{FB}^{N} and A_{FB}^{Y} depend on α_ℓ, their measurement is combined with the measured value of A_{FB}^{ℓ}, which depends on P and on α_ℓ, to constrain it. As discussed in section 13.5, the asymmetries A_{FB}^{N} and A_{FB}^{Y} are measured independently of any assumption on $\mathrm{Im}\, g_{\mathrm{R}}$ in the unfolding step. This last point, together with the fact that A_{FB}^{ℓ} is completely independent of the $\mathrm{Im}\, g_{\mathrm{R}}$ value, makes possible a limit setting on this coupling. In the other hand, for the same reasons, limits on $\mathrm{Re}\, g_{\mathrm{R}}$ are extracted from the measured value of A_{FB}^{X} and A_{FB}^{ℓ}. Although the signal unfolding has been made independently of any assumptions on $\mathrm{Im}\, g_{\mathrm{R}}$ ($\mathrm{Re}\, g_{\mathrm{R}}$), the SM couplings have been assumed for the subtracted top quark backgrounds. However, for the main $t\bar{t}$ background a negligible dependence on $\mathrm{Im}\, g_{\mathrm{R}}$ ($\mathrm{Re}\, g_{\mathrm{R}}$) is expected.

The limit extraction is based on the TopFit code [111]. By taking into account the analytic expressions introduced in [17, 20, 21] for the dependence on the Wtb couplings of the W boson spin observable $\langle S_2 \rangle$, of the top quark polarisations P, P_x and P_y, and of the charged lepton spin analysing power

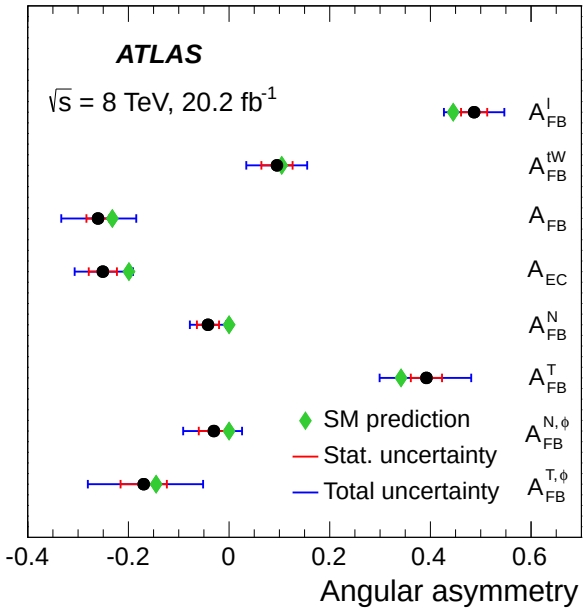

(a)

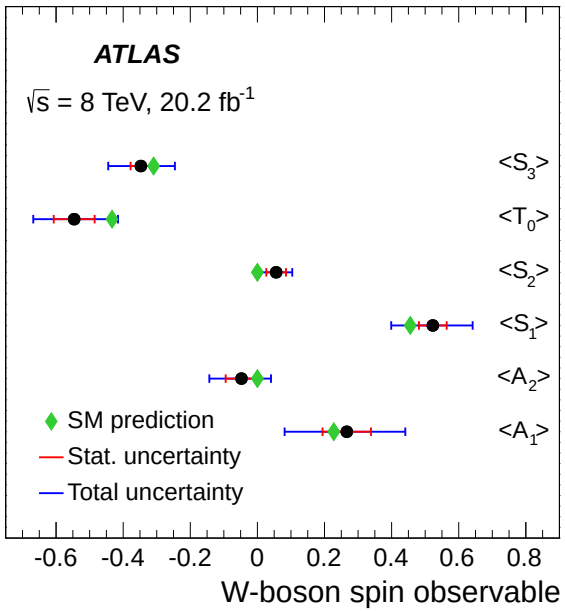

(b)

Figure 15.1: Summary of the (a) measured asymmetries and of the (b) measured values of the W boson spin observables, plus the comparison with the SM predictions.

α_ℓ, it is possible to determine the allowed region for the anomalous couplings $\mathrm{Im}\, g_\mathrm{R}$ and $\mathrm{Re}\, g_\mathrm{R}$ from the measured values of the asymmetries A_FB^N, A_FB^Y, A_FB^X and A_FB^ℓ. In the calculation, the top quark and top-antiquark productions are combined, as explained in section 11.4, using the cross-sections calculated at NLO in QCD (chapter 10). The calculation of the observables as a function of $\mathrm{Im}\, g_\mathrm{R}$ ($\mathrm{Re}\, g_\mathrm{R}$) is performed assuming a top quark mass of 172.5 GeV, a W boson mass of 80.4 GeV and a b-quark mass of 4.8 GeV. In the TopFit code, the parametrisation of the top quark polarisation P as a function of the Wtb couplings is derived from event samples generated with the protos simulation [20]. The parametrisation of the top quark polarisation P_x and P_y as a function of the Wtb couplings was not originally included in the TopFit code, but they were including following the same method than for the polarisation P, according to the parametrisation given in [17]

The limit setting is based on the construction of a χ^2 function, with the test statistic computed according to:

$$\chi^2 = \sum_{i,j} (M_\mathrm{FB}^i - T_\mathrm{FB}^i)(M_\mathrm{FB}^j - T_\mathrm{FB}^j)\ Cov(i,j)^{-1} \tag{15.1}$$

where M_FB^i is the measured central value of the asymmetry A_FB^i (i stands for ℓ, N, X or Y), and T_FB^i its predicted value for a given coupling $\mathrm{Im}\, g_\mathrm{R}$ ($\mathrm{Re}\, g_\mathrm{R}$). The term $Cov(i,j)^{-1}$ stands for the elements of the inverse of the covariance matrix. The overall covariance matrix is computed from the sum of the covariance matrices associated with the various sources of statistical and systematic uncertainty. The theoretical uncertainties, which are negligible compared to the measurement uncertainties, are not taken into account in the χ^2 calculation.

The covariance between two asymmetries is calculated from the uncertainty breakdown tables, before individual components are combined in the categories described in chapter 14, and before performing any symmetrisation of the uncertainties, such that the correlation between the different components are not lost. The idea behind this method is that the correlation between two asymmetries is extracted from the correlations between their different uncertainty sources.

For a certain systematic uncertainty source, the individual *up* contributions of both asymmetries are compared and a correlation factor is given to that specific contribution according to the following rules:

- If they have the same sign, a correlation factor $\rho_k = 1$ is assigned.
- If they have opposite signs, a correlation factor $\rho_k =$ -1 is given.
- If any of the contributions is null, a correlation factor $\rho_k = 0$ is assigned.

This procedure is repeated with the *down* contributions and for every source of systematic uncertainty.

The statistical correlations between two asymmetries are evaluated from the generation of pseudo-experiments using the so-called bootstrapping method [120]. Bootstrapped event samples are constructed from the data sample by assigning each event a weight pulled from a poissonian distribution with unit

mean. The angular distributions are then reconstructed using the weighted events. The procedure is repeated with statistically independent weights and 50k ensembles of pseudo-experiments are generated. The correlation coefficient between the two asymmetries is finally determined from the ensemble of pseudo-experiments. Figure 15.2 shows an example of the histogram constructed from the set of pseudo experiments from which the statistical correlation is extracted.

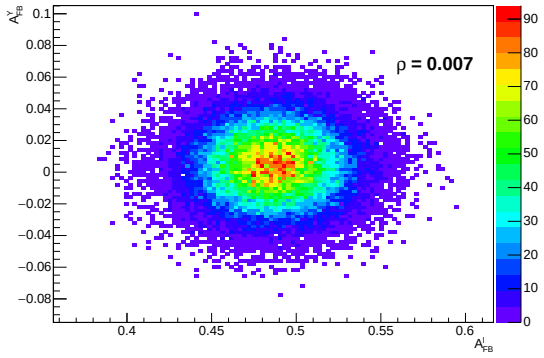

Figure 15.2: Statistical correlation between the measured asymmetries $A^Y_{\rm FB}$ and $A^\ell_{\rm FB}$ evaluated from data using the bootstrapping method. The derived correlation coefficient, computed from the ratio between the covariance of the two asymmetries and the product of their standard deviations, is quoted.

Once a correlation factor ρ_k has been assigned for every source of statistical or systematic source of uncertainty, the total correlation matrix is calculated from

$$Cov(i,j) = \begin{pmatrix} \sigma^2(A^i_{\rm FB}) & \sum\limits_k \rho_k \sigma_k(A^i_{\rm FB})\sigma_k(A^j_{\rm FB}) \\ \sum\limits_k \rho_k \sigma_k(A^i_{\rm FB})\sigma_k(A^j_{\rm FB}) & \sigma^2(A^j_{\rm FB}) \end{pmatrix} \tag{15.2}$$

where the index k runs over all sources of statistical and systematic uncertainties. The overall correlation coefficient is computed as

$$\rho = \frac{\sum\limits_k \rho_k \sigma_k(A^i_{\rm FB})\sigma_k(A^j_{\rm FB})}{\sigma(A^i_{\rm FB})\sigma(A^j_{\rm FB})} \tag{15.3}$$

Table 15.4 shows the obtained results for the statistical and overall correlations between the different asymmetries that are used for setting limits on the anomalous couplings $\mathrm{Im}\, g_{\rm R}$ and $\mathrm{Re}\, g_{\rm R}$.

Once that all terms entering in equation 15.1 have been calculated, the extraction of limits on the anomalous couplings can be performed. For the case $\mathrm{Im}\, g_{\rm R}$, the limit extraction assumes that $V_{\rm L} = 1$ and that all anomalous couplings other than $\mathrm{Im}\, g_{\rm R}$ vanish ($V_{\rm R} = g_{\rm L} = 0$ and $\mathrm{Re}\, g_{\rm R} = 0$). Using the asymmetries $A^\ell_{\rm FB}$ and $A^N_{\rm FB}$, the limits at the 95% confidence level (CL) obtained on $\mathrm{Im}\, g_{\rm R}$ are

$$\mathrm{Im}\, g_{\rm R} \in [-0.18, 0.06]$$

Asymmetry A	Asymmetry B	Stat. correl.	Overall correl.
$A^{\ell}_{\rm FB}$	$A^{N}_{\rm FB}$	0.006	0.152
$A^{\ell}_{\rm FB}$	$A^{Y}_{\rm FB}$	0.007	0.090
$A^{\ell}_{\rm FB}$	$A^{X}_{\rm FB}$	-0.231	0.057
$A^{N}_{\rm FB}$	$A^{Y}_{\rm FB}$	0.050	0.412
$A^{N}_{\rm FB}$	$A^{X}_{\rm FB}$	0.007	0.293
$A^{Y}_{\rm FB}$	$A^{X}_{\rm FB}$	0.015	0.333

Table 15.4: Summary of the measured statistical and overall correlations between the asymmetries used in the limit extraction: $A^{\ell}_{\rm FB}$, $A^{N}_{\rm FB}$, $A^{Y}_{\rm FB}$ and $A^{X}_{\rm FB}$.

If $A^{\ell}_{\rm FB}$ and $A^{Y}_{\rm FB}$ are used instead, the limits at the 95% CL obtained on $\mathrm{Im}\, g_{\rm R}$ are

$$\mathrm{Im}\, g_{\rm R} \in [-0.07, 0.07]$$

The width of the allowed region is reduced by a factor 1.7 using $A^{Y}_{\rm FB}$ instead of $A^{N}_{\rm FB}$ in the limit extraction. Finally, equation 15.1 can be easily generalised in order to use more than two asymmetries. With the same assumptions than in the previous cases, when the measurements of $A^{\ell}_{\rm FB}$, $A^{N}_{\rm FB}$ and $A^{Y}_{\rm FB}$ are combined, the obtained limits at the 95% CL are

$$\mathrm{Im}\, g_{\rm R} \in [-0.07, 0.02]$$

The combined extraction further reduces the region of allowed values for $\mathrm{Im}\, g_{\rm R}$ by a factor 2.6 with respect the results obtained only with $A^{N}_{\rm FB}$ and by a factor 1.5 with respect the results obtained only with $A^{Y}_{\rm FB}$.

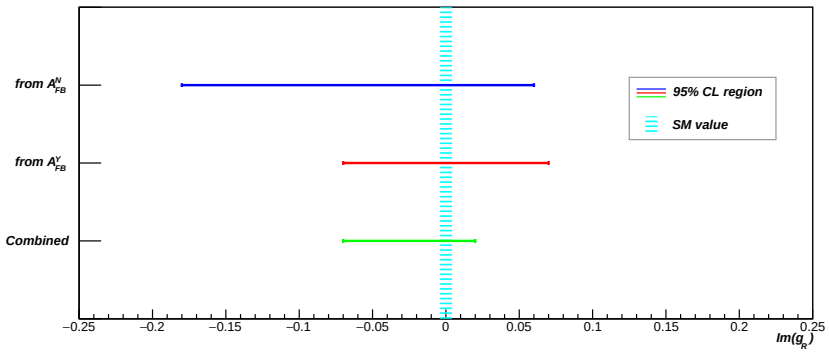

Figure 15.3: Intervals of allowed values of the imaginary part of $g_{\rm R}$ at the 95% CL extracted from $A^{N}_{\rm FB}$ (in blue), from $A^{Y}_{\rm FB}$ (in red) and from the combination of both (in green). In all cases, $A^{\ell}_{\rm FB}$ is also used in the limit extraction in order to constrain the value α_{ℓ}. The vertical dashed light blue line at $\mathrm{Im}\, g_{\rm R} = 0$ is drawn to illustrate the SM value of $\mathrm{Im}\, g_{\rm R}$. The three obtained intervals are compatible with the SM prediction.

The obtained limits are shown in Figure 15.3. The blue line shows the 95% CL region obtained with A_{FB}^{N}, the red line corresponds with the limits obtained using A_{FB}^{Y}, and finally, with a green line it is shown the limits obtained with their combination. A vertical dashed light blue line is placed at $\mathrm{Im}\, g_{\mathrm{R}} = 0$, that is the SM value for $\mathrm{Im}\, g_{\mathrm{R}}$.

The measured interval of allowed values for the imaginary part of g_{R} measured with A_{FB}^{N} and published in [115] already improved slightly the limits set at 7 TeV by the ATLAS collaboration from the measurement of double differential angular decay rates in t-channel single-top production [22]. The extracted constraints were $\mathrm{Im}\, g_{\mathrm{R}} \in [-0.17, 0.23]$ at the 95% CL, assuming $V_{\mathrm{L}} = 1$. It also improved significantly the limits extracted from the combination of the LHC (8 TeV) and Tevatron results on the W boson helicity fractions and single top quark production cross sections [116]. The one-dimensional limits extracted from this combination were $\mathrm{Im}\, g_{\mathrm{R}} \in [-0.27, 0.27]$ at the 95% CL. But the use of the new observable A_{FB}^{Y}, together with A_{FB}^{N} and A_{FB}^{ℓ}, largely improves the obtained limits on the $\mathrm{Im}\, g_{\mathrm{R}}$, reducing them in a factor 2.6, using the same data and techniques.

Finally, the obtained limits can be compared with a recently published ATLAS analysis which is also able to set limits on $\mathrm{Im}\, g_{\mathrm{R}}$ [121]. This is a more complex analysis than the one presented in this thesis, what allows to extract the limits without performing assumptions for the rest of the anomalous couplings. The extracted constrains in this analysis are $\mathrm{Im}(g_{\mathrm{R}}/V_{\mathrm{L}}) \in [-0.07, 0.06]$, a similar value to the one extracted from A_{FB}^{Y} and wider than the one extracted from the combination of A_{FB}^{Y} and A_{FB}^{N}. But it has to be remarked here that the assumptions made in both analysis are different, being the ones made in this work much more restrictive.

Limits on $\mathrm{Re}\, g_{\mathrm{R}}$ can be extracted from the combination of A_{FB}^{X} and A_{FB}^{ℓ}, where as in the case of the limits on $\mathrm{Im}\, g_{\mathrm{R}}$, A_{FB}^{ℓ} is used to constrain the value of the charged lepton spin analysing power α_{ℓ}. Following the same approach, the obtained limits at the 95% CL are

$$\mathrm{Re}\, g_{\mathrm{R}} \in [-0.22, 0.10]$$

In this case, the extracted limits for $\mathrm{Re}\, g_{\mathrm{R}}$ are not as precise as other measurements. The best constraints on $\mathrm{Re}\, g_{\mathrm{R}}$ derive from measurements of the W boson helicity fractions in top quark pair decays, with $\mathrm{Re}\, g_{\mathrm{R}} \in [-0.02, 0.06]$ and $\mathrm{Re}\, g_{\mathrm{R}} \in [-0.05, 0.05]$, both at the 95% CL, from ATLAS at $\sqrt{s} = 8$ TeV [117] and from CMS at $\sqrt{s} = 7$ and 8 TeV [118]. The ATLAS analysis mentioned before [121] also extracts limits for $\mathrm{Re}\, g_{\mathrm{R}}$ but without making assumptions in the values of other anomalous couplings, obtaining $\mathrm{Re}(g_{\mathrm{R}}/V_{\mathrm{L}}) \in [-0.12, 0.17]$.

The paper proposing the new observables A_{FB}^{Y} and A_{FB}^{X} [17] predicted that the size of the limits achieved in the real and imaginary parts of g_{R}, with both asymmetries would be similar, but the larger uncertainty on A_{FB}^{X} leads to a much larger interval in the real part of g_{R}. It has been checked that, even if A_{FB}^{X} had been measured with the same uncertainty than A_{FB}^{Y}, the limits in $\mathrm{Re}\, g_{\mathrm{R}}$ would be wider than the ones for $\mathrm{Im}\, g_{\mathrm{R}}$.

Chapter 16

Summary and conclusions

This thesis can be divided in two well sepparated parts: the first part refers to the alignment of the ATLAS Inner Detector, and the second one to angular measurements in the production and decay of single t-channel top quarks.

Inner Detector alignment

The techniques used to align the ATLAS ID and the upgrades implemented in the alignment framework during LHC Run-II have been discussed in this work. Dynamic displacements and deformations of ID subdetectors take place during the data taking, compromising the quality of the recorded data. The two more relevant movements or deformations of the ID are a vertical displacement of the Pixel and the bowing of the IBL.

It has been observed that the Pixel suffers a fast vertical displacement when switched on (first hour of data taking). A slower but longer displacement in the opposite direction has become significant since 2016, due to the increase in the LHC luminosity.

The shape of the IBL staves, was found to vary with the IBL temperature, introducing a bowing of $\sim$300 μm at the centre of the staves when the IBL is cooled down from room temperature to the operational temperature ($\Delta T=$ 35°C). A time-dependent IBL bowing appeared due to higher radiation levels in the IBL modules since September 2015. The alignment framework has been upgraded to correct the IBL bowing in a time-dependent basis.

Time-dependent corrections have been implemented in the automatic alignment performed at the Calibration Loop each time a new run is recorded. These dynamic corrections are able to correct both the vertical displacement of the Pixel and the IBL bowing variations during the run, removing the impact that these time-dependent misalignments have in the data. Despite of the harsher conditions of the ID during LHC Run-II, thanks to the upgrades performed in the alignment framework, a similar alignment performance to the one of Run-I has been achieved.

Finally, in order to profit the computing resources of Tier-0, a new alignment

machinery has been developed allowing the sending of aligment jobs to the Tier-0 system. This tool has been extensively used during 2017 for the derivation of the alignment baselines for the CL alignment.

Single top quark physics

Several polarization observables have been measured on t-channel single top quark events using 20.2 fb^{-1} of data collected with the ATLAS detector at the LHC in 2012 at $\sqrt{s} = 8$ TeV. The selected events contain one isolated electron or muon, large missing transverse momentum and exactly two jets, of which one is tagged as a b-jet. A cut-based analysis has been developed in order to discriminate the signal events from the background contributions.

The polarization observables are measured from asymmetries of various angular distributions unfolded at parton level. Most of the angular distributions have been unfolded with unfolding correction based on Standard Model simulations. In the other hand, for the extraction of three asymmetries, model-independent corrections derived through an interpolation method developed for this analysis have been used. These asymmetries have been used to set limits on the values of Wtb anomalous couplings.

All the measured asymmetries and polarization observables are in good agreement with the predictions of the Standard Model. This thesis extends the analysis published in [115], including two new asymmetries defined in the single top quark production frame. These new observables, proposed in [17], are predicted to have a large sensitivity to the real and imaginary parts of g_{R}.

Limits on the real and imaginary part of the anomalous coupling g_{R} have been set, using several measured asymmetries. The extracted limits on the imaginary part of g_{R} improve the most recently published limits. In the other hand, the extracted limit in the real part of g_{R} is not as precise as other published measurements. In both cases, the limtis set are compatible with the Standard Model preditions for the real and imaginary part of g_{R}.

Part IV

Resumen/Resum

Capítulo 17

Resumen en español

El quark top es el quark más masivo que se conoce. Debido a su gran masa, el quark top se desintegra mediante la interacción electrodébil antes de que llegue a hadronizar. Esta propiedad hace que no se pierda su polaridad debido a las interacciones de QCD que afectan a la hadronización de todos los demás quarks. El quark top es el único caso en el que se puede estudiar un quark en un estado casi libre.

El quark top puede ser producido por dos mecanismos: producción por pares a través de la interacción fuerte o producción en solitario a través de la interacción débil. Aunque la producción mayoritaria en un colisionador de protones como el LHC es la producción por pares, la producción en solitario es interesante ya que permite estudiar en detalle la estructura del vértice Wtb, al mediar dicho vértice tanto la producción como la desintegración del quark top. Los quarks top en solitario son producidos en tres canales diferentes: los canales t, s y Wt. Estos tres canales presentan una topología final distinta, como muestran los diagramas de Feynman mostrados en la figura 17.1.

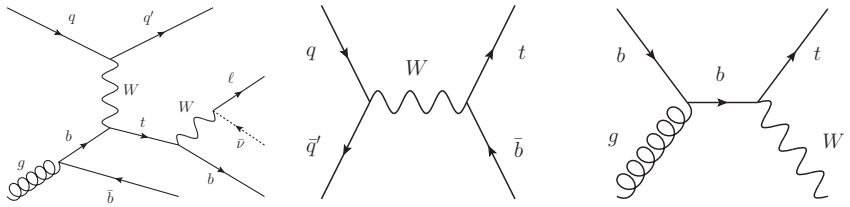

(a) (b) (c)

Figura 17.1: Diagramas de Feynman a LO para la producción de quarks top en solitario a través de los canales t ((a)), s ((b)) y Wt ((c)). Para el caso del canal t, se muestra también la desintegración leptónica del bosón W.

En este análisis se estudian diversos observables angulares en el canal t, ya que los quarks top producidos en este canal presentan un alto grado de polarización. El lagrangiano del modelo estándar (SM) que media la producción

y la desintegración de quarks top en solitario a través del vértice Wtb es

$$\mathcal{L}_{Wtb} = -\frac{g}{2\sqrt{2}} \left\{ W_\mu^\dagger \bar{t} \gamma^\mu (1-\gamma_5) V_{tb} b + \text{h.c.} \right\} \tag{17.1}$$

Este lagrangiano puede extenderse utilizando teoría efectiva de campos para incluir acoplamientos anómalos. El lagrangiano mas general que puede escribirse viene dado por

$$\mathcal{L}_{Wtb} = -\frac{g}{\sqrt{2}} \bar{b} \gamma^\mu \left(V_{\text{L}} P_L + V_{\text{R}} P_R \right) t W_\mu^- - \frac{g}{\sqrt{2}} \bar{b} \frac{i\sigma^{\mu\nu}}{M_W} q_\nu \left(g_{\text{L}} P_L + g_{\text{R}} P_R \right) t W_\mu^- + \text{h.c.} \tag{17.2}$$

donde $V_{\text{L,R}}$ parametrizan los acoplamientos vectoriales y $g_{\text{L,R}}$ los matriciales. Todos los acoplamientos pueden tomar valores complejos. En el SM, todos los acoplamientos son nulos salvo V_{L}, que coincide con el término V_{tb} de la matriz de CKM. De especial interés es la parte imaginaria de g_{R}, ya que un valor no nulo de la misma implicaría la presencia de una componente que viola CP en el sector del quark top. Utilizando quarks top producidos a través del canal t se pueden medir diversos observables angulares sensibles a los acoplamientos anómalos. En concreto, la parte imaginaria de g_{R} solo es accesible a través de este tipo de eventos.

17.1 ATLAS y el LHC

El LHC, con sus 27 km de circunferencia, es el mayor y más potente acelerador de partículas jamás construido. El LHC puede acelerar protones hasta una energía nominal de centro de masas de 14 TeV. Durante el Run-I, el LHC funcionó a 7 y 8 TeV, mientras que ha estado funcionando a 13 TeV en el Run-II. Para alcanzar estas energías tan altas, se necesitan campos magnéticos enormes. El LHC fue construido utilizando dipolos magnéticos superconductores que llegan a generar un campo magnético de 8 T. Para que actúen como superconductores, los dipolos han de ser enfriados a una temperatura de 1.9 K usando helio líquido superfluido. Cavidades de radio-frecuencia para acelerar los protones, cuadrupolos magnéticos para enfocar los haces y otros sistemas complejos de imanes completan el LHC. Aparte de las altas energías alcanzadas por el LHC, este es capaz de proporcionar un gran número de colisiones por segundo, lo que se denomina luminosidad. La luminosidad nominal del LHC es de $L = 10^{34}$ $\text{cm}^{-2}\text{s}^{-1}$, aunque esa cantidad ya ha sido sobrepasada durante el Run-II.

En el LHC se sitúan cuatro grandes experimentos, situado cada uno en uno de los puntos de colisión de los haces: ATLAS, CMS, LHCb y ALICE. El trabajo presentado en esta tesis se engloba dentro del experimento ATLAS, una colaboración internacional en la que participan alrededor de 3000 científicos de alrededor de 40 países distintos. El detector ATLAS es un detector multipropósito, diseñado para estudiar un amplio espectro de procesos: desde medidas de precisión del SM, a la búsqueda de nuevas partículas. ATLAS se compone de diferentes subdetectores, especializado cada uno en la detección y medida de diferentes partículas (figura 17.2).

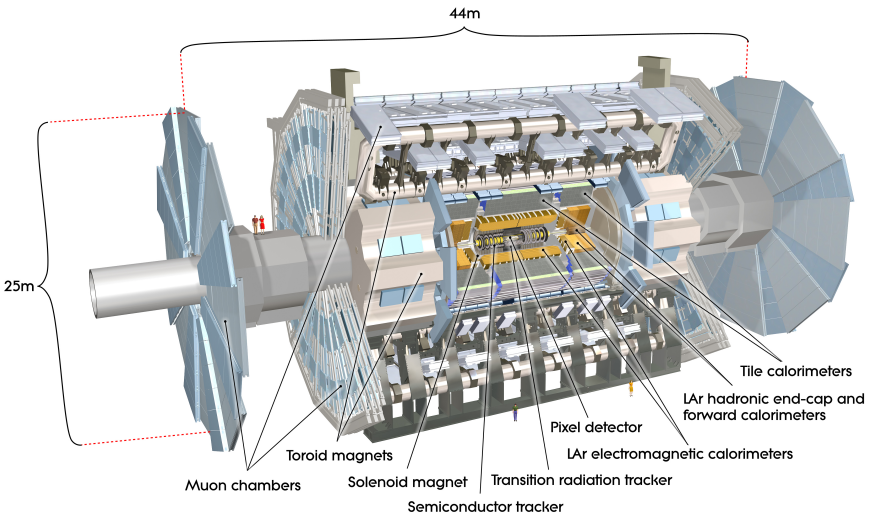

Figura 17.2: Vista cortada del detector ATLAS, mostrando sus componentes principales: Las cámaras de muones, los calorímetros electromagnético y hadrónico, el Detector Interno y los sistemas de imanes: el toroide y el solenoide [29].

En las capas más externas del detector ATLAS se sitúan las cámaras de muones. Estos detectores se especializan en la detección y en la medida de la trayectoria de muones, la única partícula, a excepción del neutrino, capaz de atravesar el detector ATLAS. Tras las cámaras de muones encontramos los calorímetros de ATLAS. Un calorímetro es un detector diseñado para parar las partículas que lo atraviesan y medir su energía. ATLAS cuenta con dos tipos distintos de calorímetros: el calorímetro electromagnético, diseñado para medir la energía de partículas que interactúan elctromagnéticamente, como electrones y fotones, y el calorímetro hadrónico, diseñado para medir la energía de los jets. Los jets son conos estrechos de hadrones y otras partículas producidas a partir de la hadronización de un quark o de un gluón. Por último, en la capa más interna de ATLAS, se encuentra el Detector Interno (ID), especializado en la medida y reconstrucción de las trayectorias de las partículas cargadas que lo atraviesan, también conocidas como trazas. Además de estos detectores, ATLAS cuenta con dos sistemas de imanes. El primero es un solenoide que rodea el ID y proporciona un campo magnético uniforme de 2 T en el interior del mismo. Este campo curva la trayectoria de las partículas cargadas que atraviesan el ID, lo que permite medir su momento. El segundo sistema de imanes es el toroide, situado junto a las cámaras de muones. El toroide proporciona un campo magnético que curva los muones para determinar su momento.

El ID está formado a su vez de distintos detectores, basados en diferentes tecnologías. En general, tiene la geometría de un barril, formado por capas cilíndricas que rodean el haz y discos que actúan como tapas de barril en cada extremo del detector (figura 17.3). El detector más cercano al punto de colisión es el Pixel, basado en tecnología de píxeles. Está compuesto de tres capas de barril y tres discos a cada lado del mismo. Para el Run-II, se añadió el IBL, una nueva capa de barril situada más cerca del punto de colisión. Mecánicamente es

independiente del Pixel. Tras el Pixel se sitúa el SCT, basado en tecnología de detectores de tiras de silicio. Está formado por cuatro capas de barril y nueve discos a cada lado. Por último, encontramos el TRT, un detector de radiación de transición distribuido así mismo en barril y dos tapas.

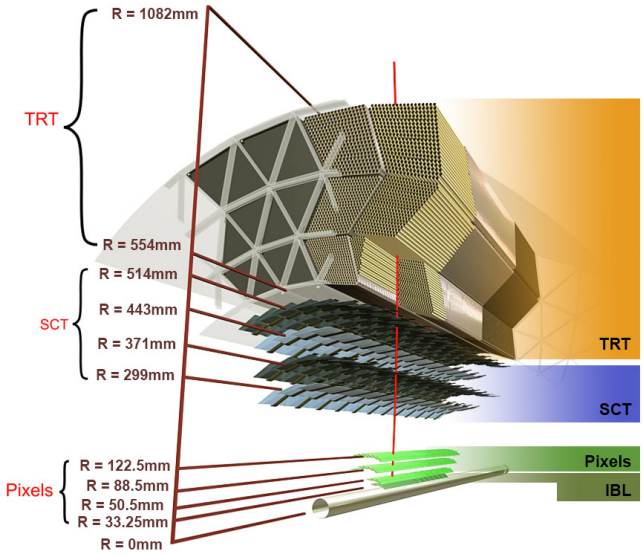

Figura 17.3: Visualización de la estructura del barril del ID. En la figura se muestran el tubo del haz, el IBL, el Pixel, el SCT y el TRT [31].

17.2 Alineamiento del Detector Interno

El Detector Interno de ATLAS contiene su sistema de reconstrucción de trazas, el cual se usa para reconstruir las trayectorias de las partículas cargadas que lo atraviesan. La precisión de la reconstrucción depende de varios factores: la resolución intrínseca de los módulos del detector, la cantidad de material en el mismo y la precisión del alineamiento. Desalineamientos del detector pueden introducir sesgos sistemáticos en las trayectorias medidas y una degradación de la resolución de los parámetros de las trazas medidas. Por lo tanto, conocer con exactitud y precisión la posición de los elementos del detector es crucial para un buen funcionamiento del ID.

17.2.1 Algoritmo de alineamiento

El ID no es accesible mientras ATLAS se encuentra en operación, por lo que el alineamiento del mismo ha de hacerse de forma indirecta. En ATLAS se utilizan las propias trazas reconstruidas por el detector para su alineamiento. El método utilizado consiste en la minimización de una función de χ^2 construida a partir de los residuos traza-señal.

Un residuo se define como la distancia que hay entre la señal de determinado detector (o hit) y la intersección predicha de la traza reconstruida con dicho

detector. Matemáticamente, puede expresarse como $\mathbf{r} = (\mathbf{m} - \mathbf{e}(\boldsymbol{\tau}, \mathbf{a}))$, donde m son las medidas del detector y $\mathbf{e}(\boldsymbol{\tau}, \mathbf{a})$ es el vector a la traza predicha. La traza depende tanto de los parámetros de la traza, $\boldsymbol{\tau}$, como de los parámetros de alineamiento, $\mathbf{a}$. La función de χ^2 se define mediante

$$\chi^2 = \sum_t \mathbf{r}(\boldsymbol{\tau}, \mathbf{a})^T V^{-1} \mathbf{r}(\boldsymbol{\tau}, \mathbf{a}) \tag{17.3}$$

donde $\mathbf{r}(\boldsymbol{\tau}, \mathbf{a})$ es un vector con todos los residuos que el sistema puede proporcionar, y V es la matriz de covariancia, una matriz que contiene las incertidumbres en las medidas del detector. En general, V no será una matriz diagonal, ya que las múltiples colisiones de coulomb introducen correlaciones entre los distintos módulos que componen el ID. El alineamiento del ID se lleva a cabo minimizando la función de χ^2 respecto a los parámetros de alineamiento.

$$\frac{d\chi^2}{d\mathbf{a}} = 0 \rightarrow 2 \sum_t \left(\frac{d\mathbf{r}}{d\mathbf{a}} \right)^T V^{-1} \mathbf{r} = 0 \tag{17.4}$$

Como los residuos dependen tanto de los parámetros de alineamiento como los parámetros de las trazas, es necesario hallar primeramente como varían los residuos al cambiar los parámetros de las trazas. Se reconstruyen las trazas para la colección de hits disponible y se calculan las derivadas de los residuos respecto a los parámetros de las trazas. Seguidamente, para esas mismas trazas, se calculan las derivadas respecto a los parámetros de alineamiento. Una vez calculadas las derivadas, se puede resolver la ecuación 17.4, con lo que se obtienen las correcciones de alineamiento. El nuevo conjunto de parámetros de alineamiento viene dado por

$$\mathbf{a} = \mathbf{a_0} - \mathcal{M}^{-1} \mathbf{v} \tag{17.5}$$

donde $\mathbf{a_0}$ es el conjunto inicial de parámetros de alineamiento, $\mathcal{M}$ es una matriz a la que se le da el nombre de 'big matrix' y $\mathbf{v}$ un vector conocido como el 'big vector'. Para llegar a la ecuación 17.5 se hace la aproximación de que los parámetros originales de alineamiento están próximos a la solución que minimiza la función χ^2. Como normalmente, los parámetros originales están lejos de los finales, la aproximación deja de ser válida, y es necesario iterar para alcanzar la convergencia de las correcciones.

17.2.2 Movimiento vertical del Pixel

Entre el Run-I y el Run-II del LHC, se descubrió que el Pixel sufre un desplazamiento vertical durante la primera hora de toma de datos, justo cuando el detector pasa de modo reposo a encendido. Este comportamiento fue descubierto mientras se estudiaba el extraño comportamiento que sufría el haz al principio de cada run [1]. El haz mostraba siempre una rápido descenso durante la primera hora de toma de datos. Los estudios llevados a cabo desde el grupo de alineamiento determinaron que era el Pixel el que se movía hacia arriba al principio de cada run y no el haz. La figura 17.4 muestra ambos desplazamientos

[1] Se define un run como el periodo en el que ATLAS toma datos de forma continua.

para su comparación. Puede verse que ambos coinciden en tiempo, aunque el movimiento del haz es mayor y muestra una componente mas lenta a lo largo de todo el run que no es debida a movimientos relativos del ID.

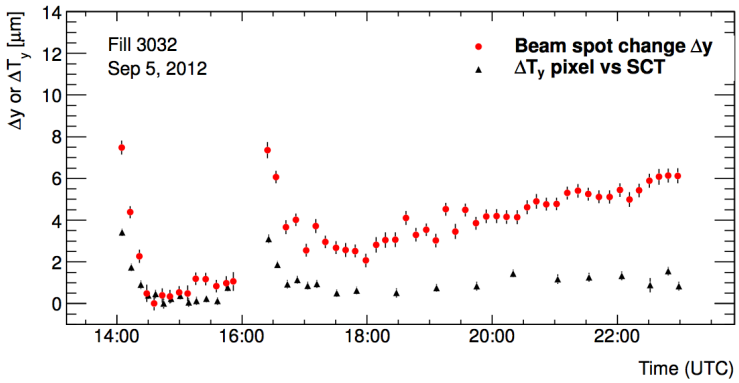

Figura 17.4: Comparación del cambio en posición vertical del haz Δy (en rojo) con el cambio en las correcciones de alineamiento del Pixel respecto al barril del SCT ΔT_y (en negro). Ambas cantidades están normalizadas, con lo que pueden compararse directamente [56].

Durante el Run-II del LHC, a medida que las colisiones aumentaban en luminosidad, se vio que el Pixel comenzaba a mostrar un desplazamiento en la dirección contraria durante el resto de run. Esta nueva componente es mas lenta pero tiene lugar durante todo el run. Se ha visto que existe una gran correlación entre la posición del Pixel y la luminosidad instantánea del run, tal y como se muestra en la figura 17.5.

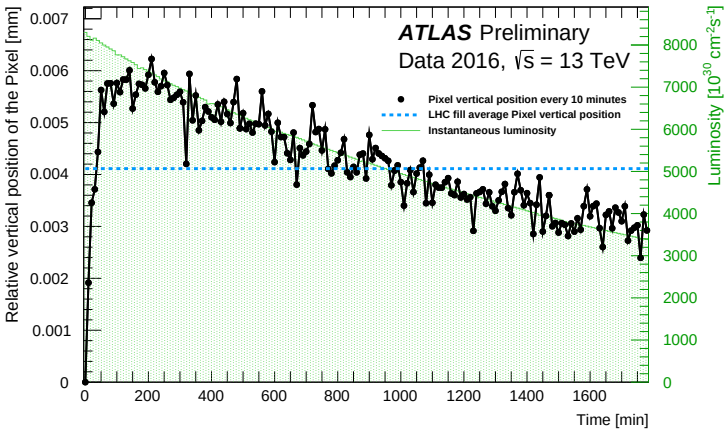

Figura 17.5: Movimientos del Pixel durante un run del LHC. Existen dos componentes diferentes: durante la primera hora de toma de datos, el Pixel se eleva rápidamente varias micras. Tras este primer desplazamiento, el Pixel desciende lentamente durante el resto del run. La velocidad de la segunda componente muestra una alta correlación con la luminosidad instantánea del run [59].

17.2.3 Combado del IBL

El IBL fue instalado en ATLAS tras el Run-I del LHC y se probó por primera vez utilizando rayos cósmicos durante la puesta en marcha de ATLAS como preparación para el Run-II del LHC. Durante este periodo de pruebas se descubrió que el IBL se deformaba dependiendo de la temperatura de operación del mismo. Las duelas del IBL se comban por el centro cuando se enfrían. La figura 17.6 muestra los residuos del IBL a lo largo de la duela para distintas temperaturas en las que se tomaron datos con el IBL. Para todas las temperaturas, las trazas han sido reconstruidas utilizando las constantes de alineamiento obtenidas con los datos recogidos con el IBL a T = -20°C, la temperatura de operación nominal del IBL. Puede observarse claramente el cambio en la forma de las duelas del IBL (figura 17.7). Cuando el IBL es enfriado de +15°C a -20°C las duelas se comban unas 300 μm por el centro de las mismas.

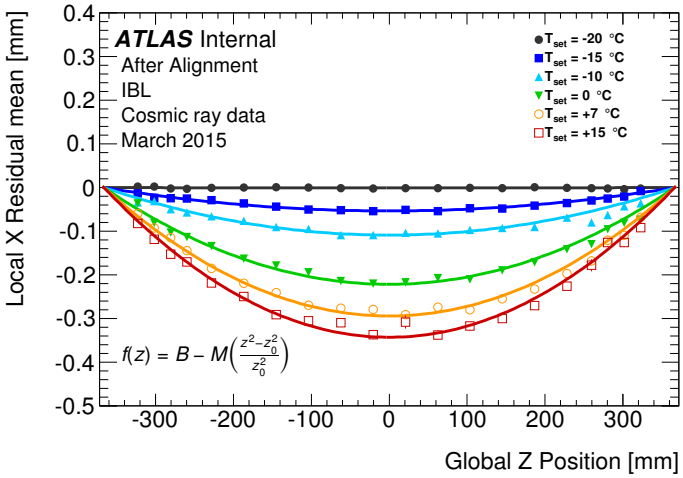

Figura 17.6: La media de los residuos traza-señal en función de la posición de los detectores a lo largo de la duela del IBL. Para cada posición, se hace la media de las catorce duelas que componen el IBL. Se ha realizado un ajuste a cada distribución utilizando una función parabólica [61].

Se ha utilizado una ecuación polinomial de segundo orden para ajustar cada una de las temperaturas medidas, ya que se ha visto que dicha función describe bien el combado del IBL. La función de ajuste viene dada por

$$f(z) = B - M\left(\frac{z^2 - z_0^2}{z_0^2}\right) \tag{17.6}$$

donde z es la posición del módulo a lo largo de la duela, z_0 = 366.5 mm se corresponde con los puntos de sujeción en cada extremo de la duela, B es la base que describe una traslación global de la duela en su conjunto y M es la magnitud del combado. Para cada temperatura medida, se ha extraído la correspondiente magnitud del combado M, tras lo cual se ha llevado a cabo un ajuste lineal del conjunto. De la pendiente de dicho ajuste se extrae que

$$\frac{\mathrm{d}M}{\mathrm{d}T} = -10{,}6 \pm 0{,}7 \ [\mu\mathrm{m/K}] \tag{17.7}$$

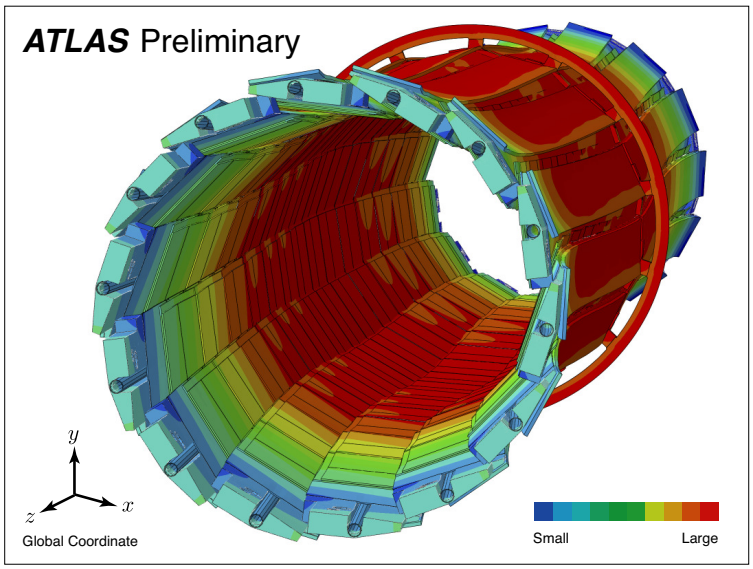

Figura 17.7: Simulación mediante análisis de elementos finitos del IBL. Los resultados de la simulación coinciden con el combado del IBL observado a través del alineamiento del detector. [61]

Cuando la intensidad de las colisiones del LHC aumentó a finales de 2015, se observó que el combado del IBL, que hasta ese momento había mostrado un valor estable, comenzaba a sufrir variaciones durante la toma de datos. Debido a esta nueva componente dinámica, fue necesario actualizar el software del alineamiento para permitir correcciones que dependiesen del tiempo. La figura 17.8 muestra que una vez introducido el alineamiento dinámico, el efecto del combado del IBL en los datos es corregido.

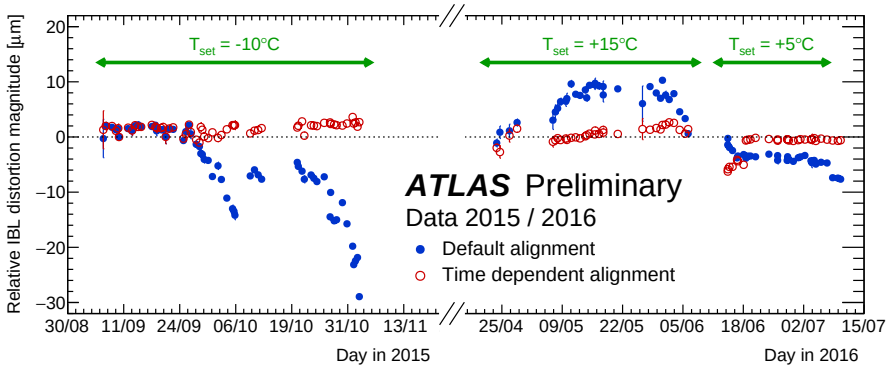

Figura 17.8: Evolución de la magnitud del combado del IBL durante 2015 y 2016 para dos conjuntos de geometrías: el alineamiento de base para cada periodo (puntos azules) y después del alineamiento en el Calibration Loop (círculos rojos). Cada periodo tiene un alineamiento de base diferente, ya que la temperatura del IBL es diferente en cada periodo y su geometría depende de la misma [66].

17.2.4 Alineamiento en el Calibration loop

Cada vez que un nuevo run es grabado en ATLAS, se realiza un calibrado exprés de los datos recogidos durante las 48 horas siguientes a la toma de datos. El objetivo de dicho calibrado es proporcionar rápido acceso a datos de alta calidad para los análisis de física. Este proceso es conocido como el Calibration Loop (CL) y el alineamiento es una de las tareas incluidas en el mismo.

Ya en el Run-I del LHC se introdujo un alineamiento automático de cada nuevo run grabado en ATLAS. Durante aquel periodo, el ID mostraba un comportamiento bastante estable, por lo que no era necesario actualizar la geometría del detector durante largos periodos de tiempo. Los resultados del alineamiento eran comprobados manualmente y, únicamente si se observaban movimientos en el detector, se actualizaba la descripción del ID.

En el Run-II se ha mantenido el alineamiento en el CL, pero la presencia de movimientos dinámicos como el desplazamiento vertical del Pixel o el combado del IBL han hecho necesario automatizar todo el proceso de alineamiento y actualización de la base de datos que describe la geometría del ID. La figura 18.9 muestra las correcciones de alineamiento en función del tiempo obtenidas en el CL para un run de 2016. Debido a las dos componentes del movimiento vertical del Pixel, el código de alineamiento se ha preparado para poder correr a dos velocidades. Actualmente, durante la primera hora de toma de datos, el ID se alinea cada 20 minutos. El resto del run, el periodo se aumenta hasta los 100 minutos. Puede observarse que con dicha configuración, se consigue corregir el movimiento del Pixel (en negro).

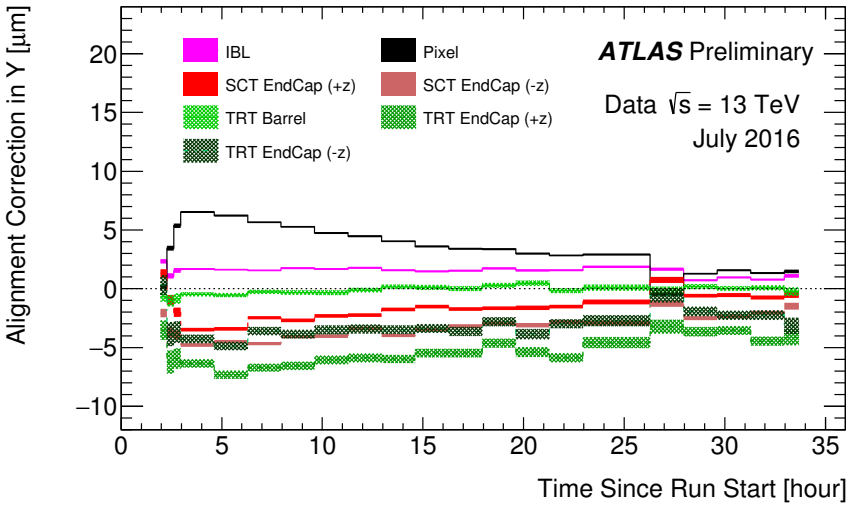

Figura 17.9: Correcciones a la posición vertical de los componentes del ID en función del tiempo. El barril del SCT se mantiene fijo como referencia. Las bandas indican la incertidumbre estadística [58].

17.3 Física del quark top

Esta sección resume el análisis realizado utilizando 20.2 fb^{-1} de datos de colisiones protón-protón con una energía de centro de masas de 8 TeV, proporcionadas por el LHC en 2012 y grabadas con el detector ATLAS. El análisis se han estudiado diversas distribuciones angulares en la producción y desintegración de quarks top producidos en solitario a través del canal t. Mediante asimetrías en estas distribuciones angulares, pueden establecerse límites a los valores de los acoplamientos anómalos en el el vértice Wtb (ecuación 17.2). Se ha estudiado también la polarización del quark top y del bosón W en este tipo de eventos.

17.3.1 Selección de la señal

En un colisionador de protones como el LHC se producen gran variedad de sucesos, entre los que hay que seleccionar la señal de interés. Como se mencionó anteriormente, en este análisis se busca la desintegración leptónica de un quark top producido en solitario a través del canal t (figura 17.1(a)). Por lo tanto, la señal buscada se compone de:

- Dos jets, uno de ellos etiquetado como b-jet y el otro como jet ligero. Los jets se identifican con los quarks iniciales, que hadronizan instantáneamente.
- Un electrón o un muón. Si el bosón W se desintegra a través de un τ, solo se considerará como señal si seguidamente el τ se desintegra leptónicamente.
- Un neutrino, que se identifica a través de la energía perdida en el plano transverso.

En este análisis se usa un proceso de selección basado en cortes, aplicados en dos pasos diferentes llamados preselección y selección. En la preselección, se requiere la presencia de los componentes mencionados anteriormente con unas características de energía y calidad genéricos., Por su parte, la selección consiste en cuatro cortes, en conjunto con un veto a la presencia de un segundo leptón. La figura 17.10 muestra la región de señal antes de aplicar los cuatro cortes de selección para electrones y muones combinados.

Aparte de la región de señal, se han definido dos regiones adicionales de control, denominadas región $t\bar{t}$ y anti-señal, que se usan para extraer factores de normalización para el fondo. En concreto, la región $t\bar{t}$ se usa para constreñir la contribución de eventos provenientes de producción por pares de quarks top, y la región anti-señal se usa para extraer la normalización de eventos provenientes de W+jets. Por último, se ha definido una región de validación llamada región W+jets para comprobar el modelado de este fondo. La tabla 17.1 muestra el número de eventos en la región de señal y en cada una de las regiones de control. La figura 17.11 muestra la distribución de la masa reconstruida del quark top en las dos regiones de control.

Para todos los procesos, señal y fondo, la normalización se extrae de las predicciones de su sección eficaz y se modelan utilizando muestras simuladas con

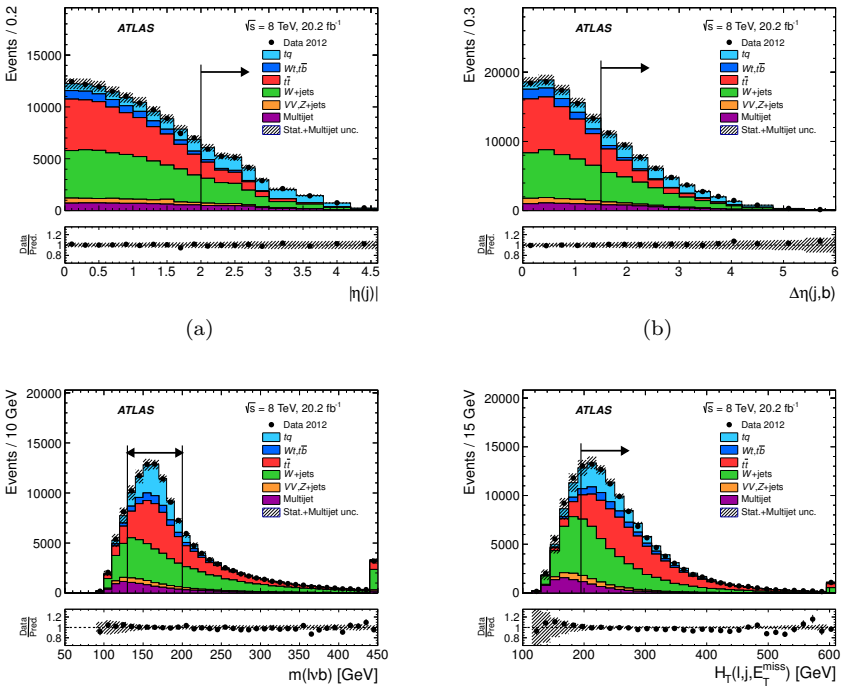

Figura 17.10: Distribuciones de las variables usadas para seleccionar la señal a partir de los eventos preseleccionados (el veto al segundo leptón ya está aplicado). Las líneas verticales delimitan la señal seleccionada para la región de señal. (a) pseudorapidez del quark espectador, (b) diferencia en pseudorapidez de ambos jets, (c) masa reconstruida del quark top, y (d) suma de la masa transversa de todos los objetos reconstruidos.

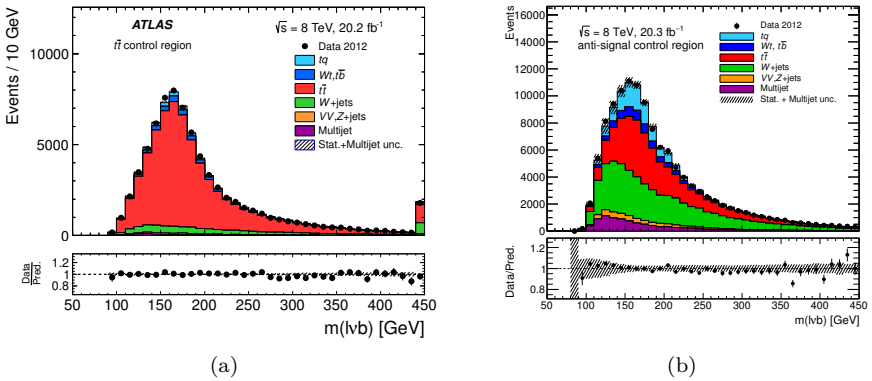

Figura 17.11: Distribución de la masa reconstruida del quark top en las regiones de control $t\bar{t}$ (a) y anti-señal (b) para electrones y muones combinados.

	Señal	$t\bar{t}$	Anti-señal	W+jets
canal t	5980 ± 22	1922 ± 13	13632 ± 33	10559 ± 29
$t\bar{t}$	1894 ± 11	59589 ± 62	41165 ± 51	20291 ± 36
canales Wt, s	262 ± 12	3018 ± 46	6808 ± 64	3932 ± 51
W+jets	1854 ± 47	6370 ± 67	44510 ± 220	250460 ± 730
Z+jets, Dibosón	190 ± 9	1121 ± 34	4915 ± 57	17770 ± 17
Multijet	420 ± 290	880 ± 620	9300 ± 6500	21000 ± 15000
Total Esperado	10600 ± 300	72900 ± 630	120000 ± 6500	324000 ± 15000
Datos de ATLAS	10527	74121	124467	372847
S/F	1.30 ± 0.08	0.0264 ± 0.003	0.113 ± 0.006	0.0326 ± 0.0015

Cuadro 17.1: número de eventos predicho y observado en las regiones de señal, de control y de validación. Electrones y muones han sido combinados.

Monte Carlo. La única excepción es el fondo de multijet, cuya normalización y modelado se ha extraído utilizando un método empírico llamado el método de matriz.

Además, utilizando las dos regiones de control, se extraen factores de normalización adicionales para los dos principales fondos: fondos de quark top y fondos de W+jets. Estos factores de escala se extraen realizando un ajuste múltiple a las regiones de señal y de control, donde los parámetros libres son la normalización de los dos fondos y la de la señal. La función de ajuste utiliza distribuciones poisonianas para las tasas de eventos en las distintas regiones, y distribuciones gausianas para constreñir la contribución de cada fondo.

Antes de realizar las medida de la asimetrías, se sustraen los fondos predichos de la región de señal, después de escalarlos con los factores de normalización empíricos. Lo que queda en la región de señal tras la substracción es por tanto nuestra señal.

17.3.2 Observables de polarización y asimetrías angulares

Una vez seleccionada la señal, se reconstruye el evento en su totalidad: El bosón W es reconstruido a partir del leptón y del neutrino, y el quark top a partir del bosón W y del b-jet. A partir de los momentos del quark top, del quark espectador, del bosón W, del leptón y del quark ligero inicial se pueden definir diferentes direcciones angulares relacionadas con las polarizaciones del quark top y del bosón W. Estas direcciones angulares (figura 17.12) se utilizan para definir una serie de asimetrías angulares que pueden usarse para comprobar las predicciones del SM. Este tipo de asimetrías, se construyen según

$$A_{\mathrm{FB}} = \frac{N(\cos\theta > 0) - N(\cos\theta < 0)}{N(\cos\theta > 0) + N(\cos\theta < 0)} \tag{17.8}$$

y evalúan la diferencia en el número de sucesos que aparecen hacia delante frente a los que aparecen hacia atrás. De particular interés son las asimetrías en los

ángulos θ_y y θ_l^N, ya que ambas tienen una gran sensibilidad a valores anómalos del vértice Wtb, en concreto a la componente imaginaria de g_{R} (Im g_{R}). La tabla 17.2 muestra todas las asimetrías medidas en este trabajo. Seis de las distribuciones angulares medidas se muestran en la figura 17.13.

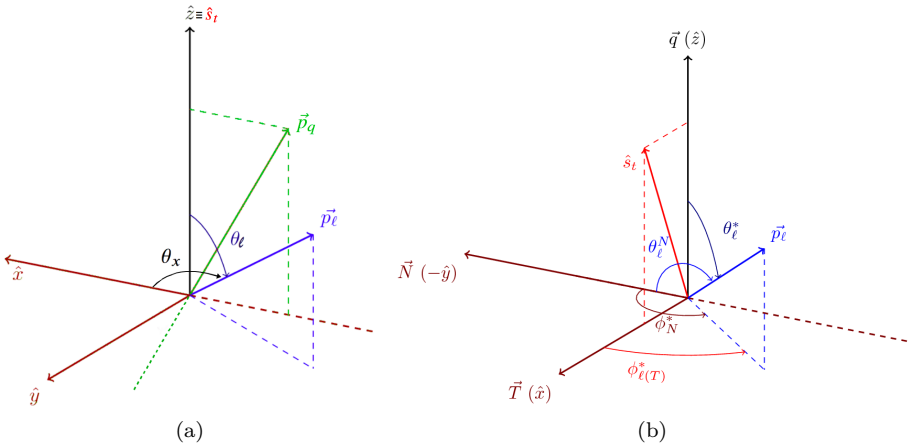

Figura 17.12: Los dos sistemas de referencia usados para definir las distribuciones angulares tanto en la producción 17.12(a) como en la desintegración 17.12(b) del quark top. En el pueden verse los momentos del quark espectador, $\hat{s}_t$, del leptón, $\vec{p}_\ell$, del quark inicial ligero $\vec{p}_q$ y del bosón W, $\vec{q}$, todos ellos respecto al centro de masas del quark top.

Asimetría	Observable angular	Observable de polarización	Predicción del SM
A_{FB}^{ℓ}	$\cos\theta_l$	$\frac{1}{2}\alpha_l P$	0.45
A_{FB}^{X}	$\cos\theta_x$	$\frac{1}{2}\alpha_l \bar{P}_x$	0.02
A_{FB}^{Y}	$\cos\theta_y$	$\frac{1}{2}\alpha_l \bar{P}_y$	0
A_{FB}^{tW}	$\cos\theta_W \cos\theta_l^*$	$\frac{3}{8}P(F_R + F_L)$	0.10
A_{FB}	$\cos\theta_l^*$	$\frac{3}{4}\langle S_3\rangle = \frac{3}{4}(F_R + F_L)$	-0.23
A_{EC}	$\cos\theta_l^*$	$\frac{3}{8}\sqrt{\frac{3}{2}}\langle T_0\rangle = \frac{3}{16}(1 - 3F_0)$	-0.20
A_{FB}^{T}	$\cos\theta_l^T$	$\frac{3}{4}\langle S_1\rangle$	0.34
A_{FB}^{N}	$\cos\theta_l^N$	$-\frac{3}{4}\langle S_2\rangle$	0
$A_{\mathrm{FB}}^{T,\phi}$	$\cos\theta_l^* \cos\phi_T^*$	$-\frac{2}{\pi}\langle A_1\rangle$	-0.14
$A_{\mathrm{FB}}^{N,\phi}$	$\cos\theta_l^* \cos\phi_N^*$	$\frac{2}{\pi}\langle A_2\rangle$	0

Cuadro 17.2: Asimetrías medidas en este análisis con sus observables angulares asociados y su relación con los observables de polarización del quark top y del bosón W. Se muestran también las predicciones del SM para dichas asimetrías [17, 20, 21].

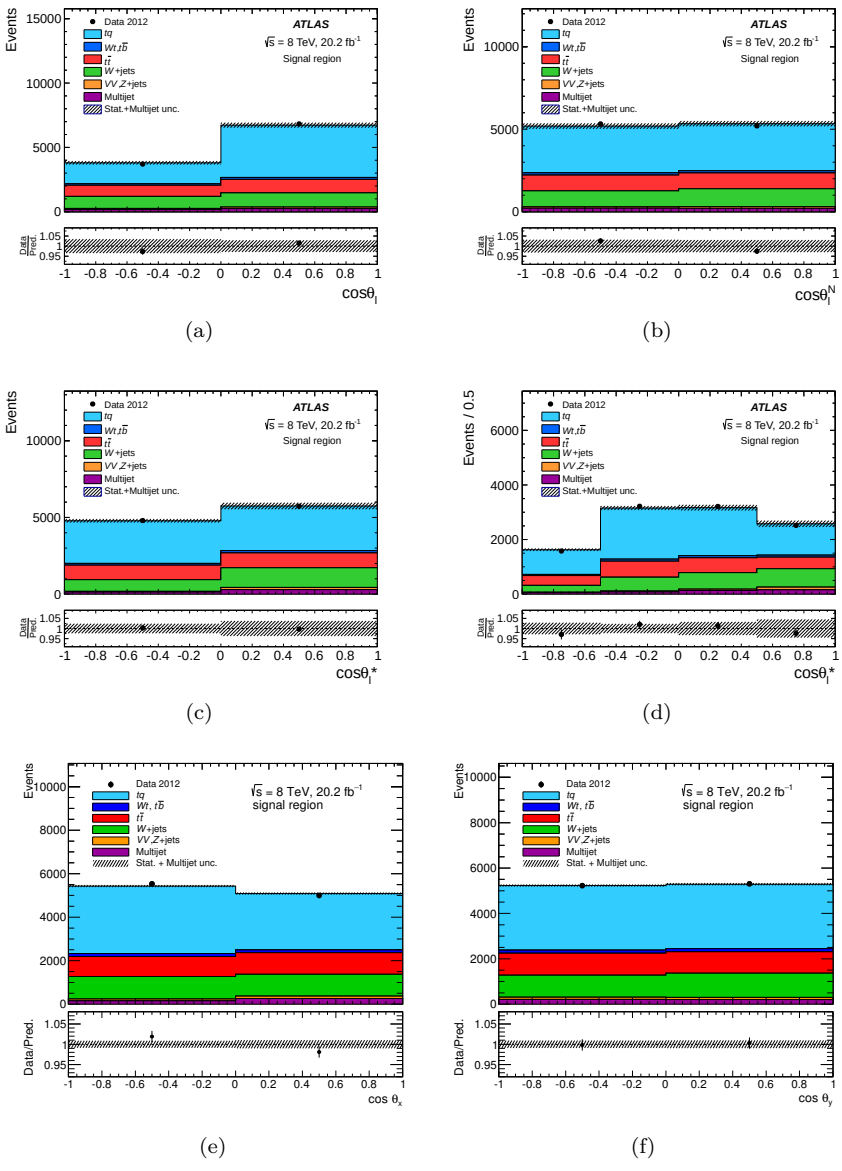

Figura 17.13: Distribuciones angulares en la región de señal (a) $\cos\theta_\ell$, (b) $\cos\theta_\ell^N$, (c) $\cos\theta_\ell^*$ con 2 bines y (d) $\cos\theta_\ell^*$ con 4 bines, (e) $\cos\theta_x$ y (f) $\cos\theta_y$. Electrones y muones han sido combinados.

17.3.3 Deconvolución de las distribuciones angulares

Antes de extraer las asimetrías de las distribuciones angulares, es necesario deconvolucionarlas de nivel reconstruido a nivel de generador, de forma que las medidas puedan ser comparadas directamente con las predicciones teóricas. Además, es necesario corregir el impacto que tienen en las distribuciones la resolución finita del detector y las eficiencias de reconstrucción y selección. Las correcciones de deconvolución se obtienen a partir de simulaciones de Monte Carlo de la señal. Para cada distribución se calcula una matriz de migración M y una curva de eficiencia ϵ, las cuales relacionan el número de eventos reconstruidos en un bin i con el número de eventos generados en otro bin j según

$$N_j^{\text{generado}} = \frac{\Sigma_i M_{ji}^{-1} N_i^{\text{reconstruido}}}{\epsilon_j} \tag{17.9}$$

La mayoría de las distribuciones angulares se han deconvolucionado usando las correcciones obtenidas de una muestra de generada con PROTOS, en la que se han implementado los valores del SM del vértice Wtb. Sin embargo, para la medida de tres asimetrías (A_{FB}^N, A_{FB}^Y y A_{FB}^X) se ha desarrollado un método de deconvolución que interpola las correcciones SM con correcciones que implementan acoplamientos anómalos. De esta forma, se consigue que la medida final de estas asimetrías se lleve a cabo sin realizar ninguna suposición sobre el valor de los valores de estos acoplamientos anómalos. Esto es interesante porque se predice que estas asimetrías tienen una alta sensibilidad a valores anómalos de los acoplamientos. En particular, A_{FB}^N, A_{FB}^Y son sensibles a Im g_{R} y A_{FB}^X a Re g_{R}. La figura 17.14 muestra como el método de interpolación desarrollado es capaz de extraer el valor correcto de las asimetrías (se muestran A_{FB}^N y A_{FB}^Y) en todo el rango simulado, mientras que las correcciones obtenidas a partir del SM muestran problemas de linealidad.

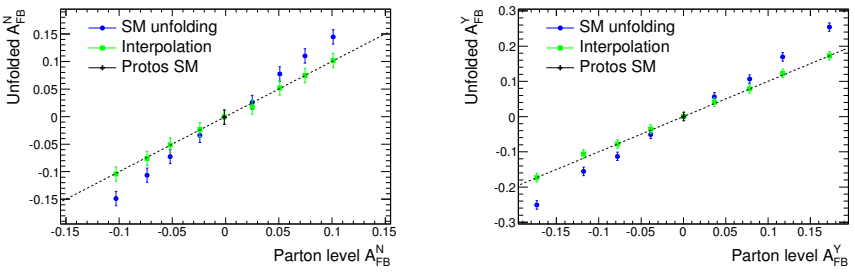

(a) (b)

Figura 17.14: Valor deconvolucionado de (a) A_{FB}^N y (b) A_{FB}^Y en función del valor generado de la asimetría. La deconvolución se ha hecho directamente con las correcciones obtenidas de la muestra SM (puntos azules) o con el método de interpolación (cuadros verdes). Los errores representan la incertidumbre debida a la estadística limitada de las muestras. La línea de puntos muestra el caso de linealidad perfecta.

17.3.4 Resultados

Varias y diversas fuentes dan lugar a una incertidumbre en la medida final de las asimetrías. Ejemplos de estas contribuciones son: la resolución en la reconstrucción de jets, la normalización de los fondos, la incertidumbre en la luminosidad o el modelado de la señal o de los fondos. Las diferentes contribuciones de incertidumbres sistemáticas han sido evaluadas individualmente, y el valor total de la incertidumbre es igual a la suma cuadrática de todas las contribuciones. Todas las incertidumbres, tanto estadísticas como sistemáticas han sido extraídas mediante la realización de pseudo-experimentos, en las que variaciones de las diferentes fuentes de incertidumbre se propagan hasta la medida final.

La tabla 17.3 muestra el resultado de las distintas asimetrías medidas en este análisis. En general, se observa un buen acuerdo entre el valor medido y la predicción del SM. A partir de estas asimetrías, usando las ecuaciones mostradas en la tabla 17.2, pueden calcularse los observables de polarización del quark top y del bosón W. Los resultados se muestran en la tabla 17.4.

	Valor	Stad.	Sist.	Valor final	Pred. SM
A_{FB}^{ℓ}	0,49	0,03	0,05	$0,49 \pm 0,06$	0,45
A_{FB}^{X}	−0,03	0,02	$^{+0,06}_{-0,05}$	$-0,03 \pm 0,06$	0,02
A_{FB}^{Y}	0,01	0,02	0,03	$0,01 \pm 0,03$	0
A_{FB}^{tW}	0,10	0,03	0,05	$0,10 \pm 0,06$	0,10
A_{FB}	−0,26	0,02	0,07	$-0,26 \pm 0,08$	−0,23
A_{EC}	−0,25	0,03	0,05	$-0,25 \pm 0,06$	−0,20
A_{FB}^{T}	0,39	0,03	0,09	$0,39 \pm 0,09$	0,34
A_{FB}^{N}	−0,04	0,02	0,03	$-0,04 \pm 0,04$	0
$A_{\mathrm{FB}}^{T,\phi}$	−0,17	0,05	$^{+0,11}_{-0,10}$	$-0,17^{+0,12}_{-0,11}$	−0,14
$A_{\mathrm{FB}}^{N,\phi}$	−0,03	0,03	0,05	$-0,03 \pm 0,06$	0

Cuadro 17.3: Resumen de las asimetrías medidas. Se muestran por separado las incertidumbres debidas a la estadística limitada de los datos de ATLAS y la suma cuadrática del resto de incertidumbres sistemáticas. Se muestran asimismo los valores finales de las asimetrías junto a su error total, los cuales pueden compararse con las predicciones del SM.

Por último pueden establecerse límites a las componentes real e imaginaria del acoplamiento anómalo g_{R}. Para ello se utilizan las asimetrías A_{FB}^{N}, A_{FB}^{Y} y A_{FB}^{X}, las cuales se han medido utilizando el método de deconvolución interpolado. Gracias a este método, las medidas de A_{FB}^{N} y A_{FB}^{Y} se han realizado sin realizar ninguna suposición del valor de Im g_{R} (la medida de A_{FB}^{X} se ha realizado sin suposiciones en Re g_{R}). En ambos casos, para el resto de acoplamientos anómalos se han asumido los valores predichos por el SM.

Los límites se extraen a partir de una función de χ^2 en la que se comparan los valores medidos de las asimetrías con sus valores predichos en función de los acoplamientos anómalos. La función de χ^2 también tiene en cuenta las

	Valor	Stad.	Sist.	Valor final	Pred. SM
$\alpha_\ell P$	0,97	0,05	0,11	$0{,}97 \pm 0{,}12$	0,90
$\alpha_\ell \bar{P}_x$	$-0{,}05$	0,04	0,11	$-0{,}05 \pm 0{,}12$	0,04
$\alpha_\ell \bar{P}_y$	0,01	0,04	0,05	$0{,}01 \pm 0{,}06$	0
$P(F_\mathrm{R} + F_\mathrm{L})$	0,25	0,08	0,14	$0{,}25 \pm 0{,}16$	0,27
$\langle T_0 \rangle$	$-0{,}55$	0,06	0,12	$-0{,}55 \pm 0{,}13$	$-0{,}433$
$\langle A_1 \rangle$	0,27	0,07	$^{+0,16}_{-0,17}$	$0{,}27^{+0,17}_{-0,19}$	0,228
$\langle A_2 \rangle$	$-0{,}05$	0,05	0,09	$-0{,}05 \pm 0{,}10$	0
$\langle S_1 \rangle$	0,52	0,04	0,12	$0{,}52 \pm 0{,}12$	0,456
$\langle S_2 \rangle$	0,06	0,03	0,04	$0{,}06 \pm 0{,}05$	0
$\langle S_3 \rangle$	$-0{,}35$	0,03	0,10	$-0{,}35 \pm 0{,}10$	$-0{,}309$

Cuadro 17.4: Resumen de los observables de polarización del top quark y del bosón W medidos. Se muestran por separado las incertidumbres debidas a la estadística limitada de los datos de ATLAS y la suma cuadrática del resto de incertidumbres sistemáticas. Se muestran asimismo los valores finales de las asimetrías junto a su error total, los cuales pueden compararse con las predicciones del SM.

correlaciones entre las distintas asimetrías, las cuales se calculan a partir de las correlaciones existentes entre las distintas fuentes de incertidumbre. Para cada par de asimetrías, se comparan una a una las distintas fuentes de incertidumbre. Si van en el mismo sentido, se le asigna un peso $\rho = 1$. Si tienen signo contrario se les asigna el peso $\rho = -1$. La correlación total viene dada por la media ponderada de estos pesos. Para calcular la correlación estadística se ha utilizado el método 'bootstrap'. La tabla 17.5 muestra las correlaciones medidas entre las diferentes asimetrías. En la tabla también se muestra la asimetría A^ℓ_FB, ya que esta se usa en la extracción de los límites para constreñir el valor de α_l. Se ha comprobado que la medida de A^ℓ_FB es completamente independiente de los valores de Re y Im g_R.

Asimetría A	Asimetría B	Correl. Stad.	Correl. total
A^ℓ_FB	A^N_FB	0,006	0,152
A^ℓ_FB	A^Y_FB	0,007	0,090
A^ℓ_FB	A^X_FB	-0,231	0,057
A^N_FB	A^Y_FB	0,050	0,412
A^N_FB	A^X_FB	0,007	0,293
A^Y_FB	A^X_FB	0,015	0,333

Cuadro 17.5: Resumen de las correlaciones estadísticas y totales medidas entre las distintas asimetrías que se usan en la extracción de límites: A^ℓ_FB, A^N_FB, A^Y_FB y A^X_FB.

La figura 17.15 muestra los límites obtenidos en Im g_R, utilizando A^N_FB y A^Y_FB

individualmente, o la combinación de ambas, aunque siempre conjuntamente con A_{FB}^{ℓ}. El límite obtenido a partir de la combinación de las tres asimetrías es $\mathrm{Im}\, g_{\mathrm{R}} \in [-0{,}07, 0{,}02]$, siendo este el más restrictivo de los tres y mejorando la precisión de medidas anteriores de Im g_{R}.

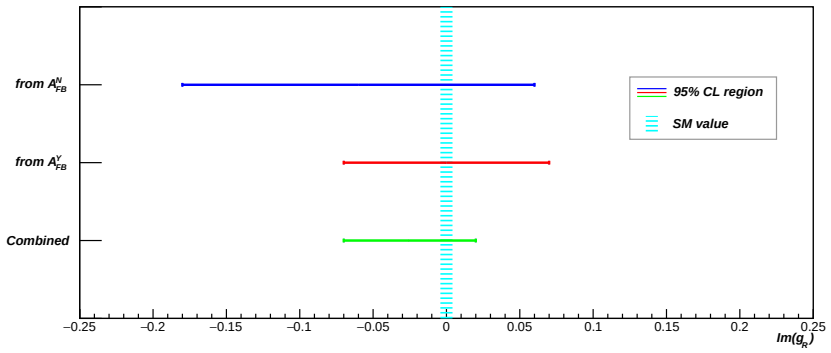

Figura 17.15: Intervalos permitidos para la parte imaginaria de g_{R}al 95 % de nivel de confianza extraídos de las asimetrías A_{FB}^{N}, A_{FB}^{Y} y A_{FB}^{ℓ}. La línea vertical azul en $\mathrm{Im}\, g_{\mathrm{R}} = 0$ muestra el valor predicho por el SM.

A partir de la asimetría A_{FB}^{X}, combinada asimismo con A_{FB}^{ℓ}, pueden establecerse límites a los valores permitidos de la parte real de g_{R}. En este caso, el límite obtenido es $\mathrm{Re}\, g_{\mathrm{R}} \in [-0{,}22, 0{,}10]$, menos restrictivo que el límite en la parte imaginaria. Esto es debido a que la incertidumbre sistemática de la medida de A_{FB}^{X} es mayor que las de A_{FB}^{N} y A_{FB}^{Y}, con lo que el límite extraído es más amplio. El límite obtenido en Re g_{R} es menos preciso que otros límites extraídos a partir de medidas de las fracciones de helicidad del bosón W.

Capítol 18

Resum en valencià

El quark top és, de tots els quarks, el més massiu. És degut a la seua gran massa, que el quark top es desintegra abans d'hadronitzar i ho fa mitjançant la interacció electrofeble. Esta propietat fa que si fora produït amb certa polarització, esta no es perga degut a les interaccions de la cromodinàmica quàntica (QCD). Cosa que si ocorre als altres quarks. Per tant, el quark top és l'únic que ens permet estudiar un quark en un estat quasi lliure.

La producció del quark top pot ocòrrer per dos mecanismes: o bé en producció a parelles (mitjançant la interacció forta) o bé en producció en solitari (on la interacció feble n'és la mediadora). Encara que en les col·lisions de protons, com les que ocorren al LHC, la producció majoritària és a parelles, la producció en solitari és un fenòmen interessant. Cert, la producció de quarks top en solitari ens permet estudiar en detall l'estructura del vèrtex Wtb. Això és gràcies a que eixe vèrtex apareix tant en la producció com en la desintegració del quark top. Nominalment, els quarks top en solitari es produïxen en tres canals diferents: t, s i Wt. Cadascun d'estos tres canals presenten una signatura final distinta, tal i com mostren els diagrames de Feynman de la figura 18.1.

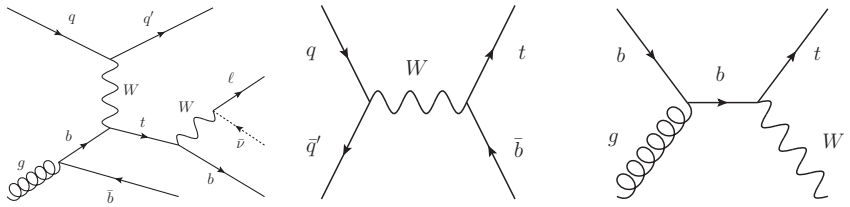

(a) (b) (c)

Figura 18.1: Diagrames de Feynman a LO per la producció de quarks top en solitari a través dels canals t ((a)), s ((b)) y Wt ((c)). En el cas del canal t, també es mostra la desintegració leptònica del bosó W.

En este treball s'ha estudiat diversos observables angulars del canal t, ja que els quarks top produïts en este canal presenten un grau alt de polarització. La lagrangiana del model estàndard (SM) que media en la producció i desintegragió

dels quarks top en solitari a través del vèrtex Wtb és

$$\mathcal{L}_{Wtb} = -\frac{g}{2\sqrt{2}} \left\{ W_\mu^\dagger \bar{t} \gamma^\mu (1-\gamma_5) V_{tb} b + \text{h.c.} \right\} \tag{18.1}$$

Esta lagrangiana pot extendre's utilizant la teoria efectiva de camps per tal d'incloure acoblaments anòmals. D'esta manera, la lagrangiana més general que pot escriure's ve donada per

$$\mathcal{L}_{Wtb} = -\frac{g}{\sqrt{2}} \bar{b} \gamma^\mu \left(V_{\text{L}} P_L + V_{\text{R}} P_R \right) t W_\mu^- - \frac{g}{\sqrt{2}} \bar{b} \frac{i\sigma^{\mu\nu}}{M_W} q_\nu \left(g_{\text{L}} P_L + g_{\text{R}} P_R \right) t W_\mu^- + \text{h.c.} \tag{18.2}$$

on $V_{\text{L,R}}$ parametritzen els acoblaments vectorials, metres que les $g_{\text{L,R}}$ ho fan amb els matricials. En el cas més genèric, tots els acoblaments poden prendre valors complexes. Però segons els SM, tots els citats acoblaments són nuls llevat de V_{L}, el qual coincidix just amb el terme V_{tb} de la matriu CKM. D'especial interés és la part imaginària de g_{R}, ja que si esta prenguera un valor no nul, això implicaria la presència d'una component que viola CP en el sector del quark top. Per fi, utilitzant quarks top en solitari produïts a través del canal t, es poden medir diversos observables angulars, alguns d'ells sensibles als acoblaments anòmals. Concretament, la part imaginària de g_{R} sols és accesible a través d'este tipus d'esdeveniments.

18.1 ATLAS i l'LHC

El gran col·lisionador d'hadrons (LHC) fa més de 27 km de circumferència. És també el major i més potent accelerador de partícules mai construït. L'LHC pot accelerar protons i fer-los col·lidir fins una energia nominal en centre de mases de 14 TeV. Durant el Run-I, l'LHC va funcionar a 7 i 8 TeV, mentres que per al Run-II, funciona a 13 TeV. Per assolir estes energies tan altes, es necessiten camps magnètics enormes. L'LHC empra dipols magnètics superconductors que arriben a generar un camp magnètic dipolar de 8 T. Ara bé, per que els dipols arriben a ser superconductors, han de ser refredats fins la temperatura de 1.9 K usant heli líquid superfluït. Altres sistemes que completen l'LHC són les cavitats de radio-freqüència per accelerar els protons, quadrupols magnèticos per enfocar els feixos i també altres sistemas complexos d'imants. Apart de les altes energies abastides pel LHC, este també és capaç de proporcionar un gran número de col·lisions per segon (definit com lluminositat). La lluminositat nominal del LHC és de $L = 10^{34}$ cm^{-2}s^{-1}. Tot siga dit que esta quantitat ja ha sigut sobrepassada durant el Run-II.

Al LHC hi operen quatre grans experiments. Cadascun d'ells es situa en un punt de col·lisió dels feixos. Els grans experiments són ATLAS, CMS, LHCb i ALICE. El treball presentat en esta tesi s'engloba dins de l'experiment ATLAS. Esta és una colaboració internacional en la que participen al voltant de 3000 científics d'uns 40 països distints. ATLAS també és un detector de propòsit general, disenyat per estudiar un espectre ample de processos: des de mesures de precisió del SM fins la recerca de noves partícules i fenòmens físics. ATLAS es

compossa de diferents subdetectores. Cadascun està especialitzat en la detecció i mesura de diferents partículas i/o de les seues propietats (figura 18.2).

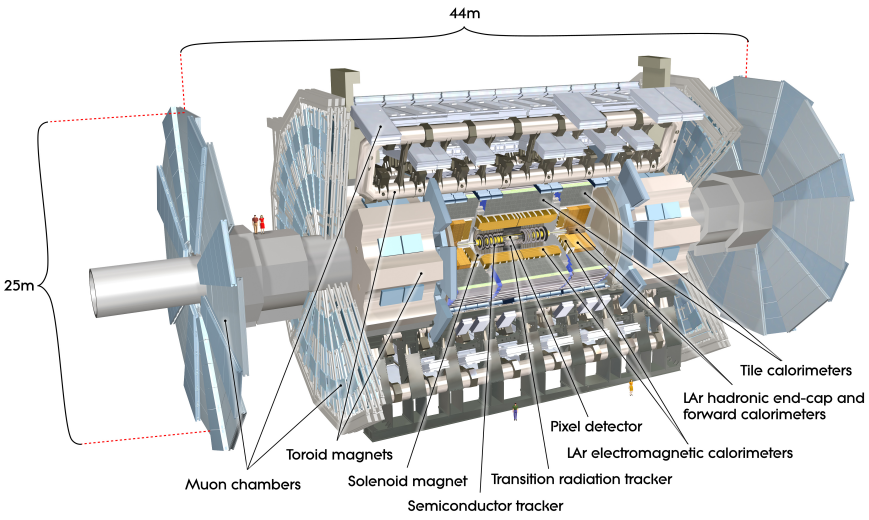

Figura 18.2: Vista axial del detector ATLAS, mostrant els seus principals components: les cambres de muons, els calorímetres electromagnétic i hadrónic, el Detector Intern i els sistemes d'imants: toroide i solenoide [29].

Les capes exteriors del detector ATLAS estan ocupades per les cambres de muons. Com el seu non indica, este tipus de cambres estan especialitzades en detectar la presència de muons i en reconstruir la seua trajectòria. Els muó és l'únic tipus de particula (a excepcció del neutrino) capaç de travesar tot el detector ATLAS sencer. Abans de les cambres de muons, trobem els calorímetres. Un calorímetre és un tipus de detector que preten aturar les partícules que li arriben i mesurar amb precisió la seua energia. Segons la naturalesa de les seues interaccions, les partícules s'aturen en un tipus de calorímetre o un altre. Ja sabem que ni els muons ni els neutrinos s'aturen amb un calorímetre convencional. El calorímetre electromagnètic atura i mesura l'energia de partícules que interactuen electromagnéticament, com ara electrons i fotons. Per altra banda, el calorímetre hadrònic, atura i mesura l'energia de partícules que interacionen fortament, com ara els hadrons. Lo únic és que els hadrons que sorgixen de les col·lisions de protons venen agrupats en forma de jets. Un jet és una aglomeració col·limada de partícules (principalment hadrons, però pot tindre electrons i muons també) que viatgen en una direcció comuna i que solen ser produïdes durant l'hadronització d'un quark o un gluó. En la part més interna d'ATLAS, es troba el Detector Intern (ID). Este és un detector especialitzat en la reconstrucció de las trajectòries de las partícules carregades que el travessen, deixant senyals com una rastra de punts. A més de tots estos detectores, ATLAS també compta amb dos sistemes d'imants. El primer és un solenoide que envolta l'ID i proporciona un camp magnètic axial uniforme de 2 T al seu interior. Este camp corba la trajectòria de las partícules carregades, cosa que permet mesurar el seu moment. El segon sistema d'imants ésta format per 8 toroides i està situat junt amb les cambres de muons. Els toroides proporcionen un campo magnètic que

corba les trajectòries dels muons per determinar el seu moment.

L'ID està format per tres sub-detectors, emprant cadascun una tecnologia diferent. En general, l'ID té la geometria d'un barril, format per capes cilíndriques que rodejan l'eix del feix i uns discs que actuen com a tapes del barril en cada extrem (figura 18.3). El detector més proper al punt de col·lisió és el Pixel, el qual esta compost per 1744 moduls de píxels planars distribuïts en tres capes de barril i tres discs en cada extrem. Per el Run-II, al Pixel se li va afegir l'IBL. Este és una una nova capa del barril situada més pròxima al punt de col·lisió. Encara que mecánicament, l'IBL és independient del Pixel. L'IBL utilitza tant sensors de píxels planar com 3D. Després del Pixel es situa l'SCT. Este detector empra moduls de micro-bandes de silici planar. L'SCT està format per quatre capes de barril i nou discs en cada extrem. Finalment, es troba el TRT, format per miliers de tubs de deriva, els quals detecten la radiació de transició. El TRT també està distribuït en una part central en forma de barril, i dues tapes formades per discs.

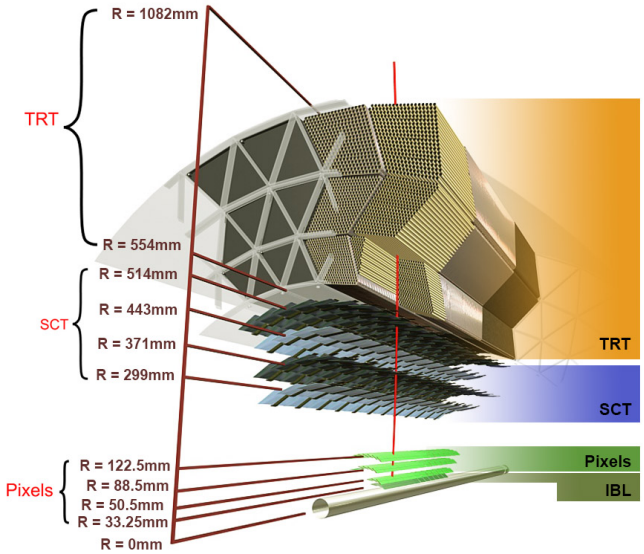

Figura 18.3: Visualització de l'estructura del barril de l'ID. En la figura es mostra el tub del feix, IBL, Pixel, SCT i TRT [31].

18.2 Alineament del Detector Intern

El Detector Intern d'ATLAS conté el seu sistema de reconstrucció de traces, el qual s'usa per reconstruir les trajectòries de les partícules carregades que el travessen. La precisió de la reconstrucció depèn de diversos factors com ara: la resolució intrínseca dels mòduls del detector, la quantitat de material que travessen les partícules i la precisió amb la que es coneix la posició dels mòduls (alineament). Un desalineament del detector (és a dir: utilitzar en la reconstrucció una posició dels mòduls que no es correspon amb la real) pot introduir: primer una degradació de la resolució dels paràmetres de les traces

reconstruïdes i també (i lo qual és quasi pijor) esbiaixos sistemàtics en els valors dels paràmetres. Per tant, conèixer amb exactitud i precisió la posició dels elements del detector és crucial per conseguir unes bones prestacions de l'ID.

18.2.1 Algoritm d'alineament

Cal tindre en compte que l'ID no és accesible mentres ATLAS es troba en mode operació. Per tant l'alineament del detector s'ha de fer de forma indirecta. En ATLAS s'utilitzen les pròpies traces reconstruïdes pel detector per tal d'alinear-lo. El mètode utilitzat consisteix en la minimització d'una funció χ^2 construïda a partir dels residus traça-senyal.

Un residu es definix com la distància entre la posició del senyal (hit) registrat per un sensor i l'extrapolació de la traça reconstruïda a dit sensor. Matemàticament, els residus poden expresar-se com un vector $\mathbf{r} = (\mathbf{m} - \mathbf{e}(\boldsymbol{\tau}, \mathbf{a}))$, on $\mathbf{m}$ són les mesures en cada mòdul i $\mathbf{e}(\boldsymbol{\tau}, \mathbf{a})$ són les extrapolacions, les quals depenen dels paràmetres de les traces ($\boldsymbol{\tau}$) i la posició dels sensors ($\mathbf{a}$). La funció χ^2 es defineix mitjançant

$$\chi^2 = \sum_t \mathbf{r}(\boldsymbol{\tau}, \mathbf{a})^T V^{-1} \mathbf{r}(\boldsymbol{\tau}, \mathbf{a}) \tag{18.3}$$

on $\mathbf{r}(\boldsymbol{\tau}, \mathbf{a})$ és el vector genèric de residus. És a dir, conté tots els residus que el sistema pot proporcionar. V és la matriu de covariança que conté les incertesses en les mesures (hits) del detector. En principi V és diagonal, però en general, V no ho és degut a que la dispersió multiple coulombiana introdueix correlaciones entre els diferents mòduls que participen en la reconstrucció de la traça. L'alineament del ID es du a terme minimitzant la funció χ^2 (equació 18.3) respecte dels paràmetros d'alineament. És a dir, amb:

$$\frac{d\chi^2}{d\mathbf{a}} = 0 \rightarrow 2 \sum_t \left(\frac{d\mathbf{r}}{d\mathbf{a}} \right)^T V^{-1} \mathbf{r} = 0 \tag{18.4}$$

Com que els residus depenen tant dels paràmetres d'alineament com dels paràmetres de les traces, hi ha una dependència imbricada, ja que les traces es reconstruixen amb una geometria inicial donada (descrita amb un conjunt inicial de paràmetres $\mathbf{a_0}$). Cadascuna de les traces es reconstruix partint de la col·lició de hits que la formen i amb una minimització de residus. Per tal d'obtindre els seus paràmetres es fa la corresponent minimització respecte dels paràmetres de les traces. Seguidamente, amb la col·lecció de traces ajustades, es calculen les derivades respecte dels paràmetres d'alineament. Una vegada calculades les derivades, el que obtenin és un sistema lineal d'equacions, de forma que en resoldre'l, s'obtenen les correccions als paràmetres d'alineamet inicials. El nou conjunt de paràmetres d'alineamiento ve donat per:

$$\mathbf{a} = \mathbf{a_0} - \mathcal{M}^{-1} \mathbf{v} \tag{18.5}$$

on $\mathcal{M}$ és una matriu (col·loquialment anomenada 'big matrix') del tamany de número de paràmetres a alinear, mentre que $\mathbf{v}$ és també un vector del mateix tamany (col·loquialment conegut per 'big vector'). Es necessari fer un comentari, per tal d'arribar a l'equació 18.5 hem fet un desenvolupament en sèrie i

quedat sols amb els primers termes. Açò és equivalent a fer la suposició que els parametres inicials estan pròxims als reals (aquells que minimitzen la funció χ^2). Si no fora eixe el cas, la metodologia coninua siguent igual de vàlida, sols que ara no és suficient en resoldre el sistema d'equacions una vegada. Hem de repetir-ho varies vegades (iteracions) fins que ens assegurem que el sistema ha convergit en una solució.

18.2.2 Movimient vertical del Pixel

Entre el Run-I y el Run-II del LHC, es va descobrir que el detector Pixel pateix un desplaçament vertical cada vegada que l'experiment mampren a prendre dades, just quan el detector pasa de mode repòs a activat. La durada d'eixe moviment és més o menys d'una hora. Este comportament fou descobert mentre s'estudiava les variacions sistemàtiques de la posició vertical del feix al principi de cada run[1]. En efecte, es veia que el run sempre baixava abruptament (aproximadament durant la primero hora prenent dades) i després s'estabilitzava. Els estudis duts a terme des del grup d'alineament van determinar que era el detector Pixel qui es movia cap amunt al principi de cada run i no el feix cap a vall. La figura 18.4 mostra el registre d'ambdós moviments junts per facilitar la comparativa. Pot veure's que tots dos coincidixen en el temps. Si bé el moviment que mostra la posició del feix és major, això s'entèn pel braç de palanca de l'extrapolació de la posició del detector fins la del feix. El moviment del feix també mostra una component més lenta, que en principi ja no és deguda a moviments del detector Pixel.

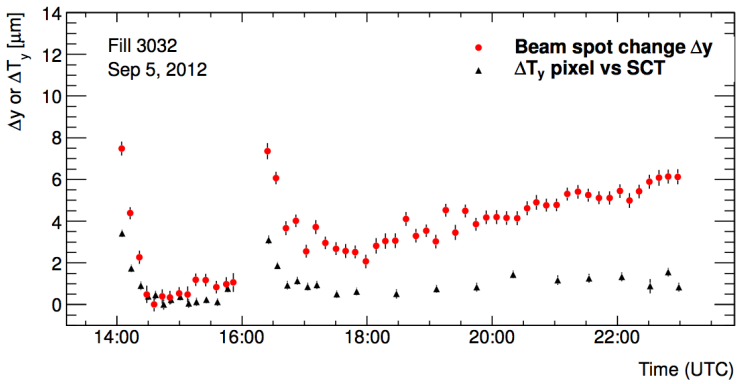

Figura 18.4: Comparació de canvi en la posició vertical del feix Δy (en roig) amb el canvi de les correccions d'alineament del Pixel repecte del barril del SCT ΔT_y (en negre). Ambdues quantitats estan escalades, per poder comparar-les directament [56].

Durant el Run-II del LHC, a mesura que la lluminositat dels feixos aumentava i aumentaven les col·lisions per creuament de feixos, es va observar un altre fenòmen. Ara el detector Pixel, després de pujar inicialment com ja s'ha descrit,

[1] Es defineix un run com un periode continu en el que el detector ATLAS està prenent dades i registrant-les.

el que feia era descendre lentament. Esta nova component és més lenta, però es dona mentre dura el run. S'ha vist que existix una gran correlació entre la velocitat de descens del Pixel i la lluminositat instantània del run, tal i com es mostra en la figura 18.5.

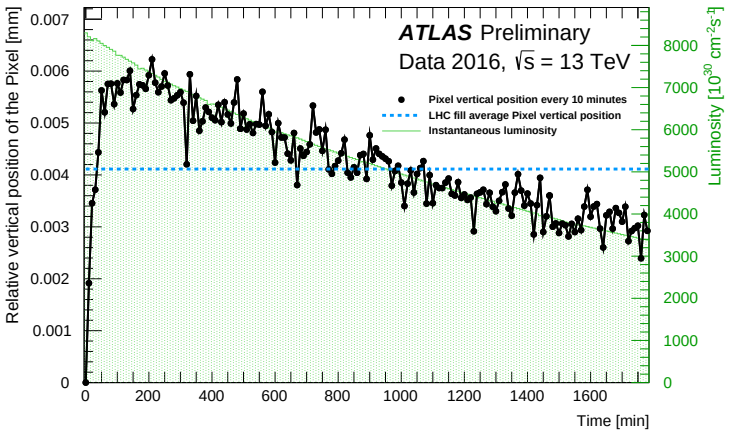

Figura 18.5: Moviments veritcals del dector Pixel durant un run d'ATLAS. Existixen dos components diferents: durant la primera hora prenent dades, el Pixel s'eleva ràpidament varies micres. Després d'este primer desplaçament, el Pixel descendix lentament durant la resta del run. La velocitat de la segona component mostra una alta correlació amb la lluminositat instantània del run [59].

18.2.3 Arquejat de les dogues del IBL

El detector IBL fou instalat en ATLAS just abans del Run-II del LHC. Va ser testejat inicialment amb runs de raigs còsmics, just durant el mateix periode que ATLAS feia proves preparant-se pel Run-II. Durant el periode inicial de proves, ja es va descobrir que l'IBL es deformava depenenet de la temperatura d'operació. La causa és que les dogues del IBL s'arquejen quan es refreden. La figura 18.6 mostra els residus dels raigs còsmics al IBL i al llarg de les dogues, tot per a distintes temperaturas d'operació. En eixe gràfic, totes les dades són reconstruïdes amb una geometria (alineament) comuna. S'ha emprat l'alineament del IBL a T = -20°C. L'elecció ve determinada perquè esta és la temperatura d'operació nominal del IBL. Al gràfic es pot observar clarament el canvi en la forma de les dogues del IBL (figura 18.7). S'ha estimat que quan l'IBL es refredat de +15°C a -20°C las dogues s'arquejen uns 300 μm del centre als extrems.

Per tal d'ajust ajustar la forma dels residus al llarg de la doga a diferents temperatures, s'ha utilitzat un polinomi de segon grau. ja que s'ha vist que dita funció descriu bé l'arquejat de les dogues del IBL. La funció d'ajust ve donada per:

$$f(z) = B - M\left(\frac{z^2 - z_0^2}{z_0^2}\right) \tag{18.6}$$

on z representa la posició del mòdul al llarg de la doga, $z_0 = 366.5$ mm correspon

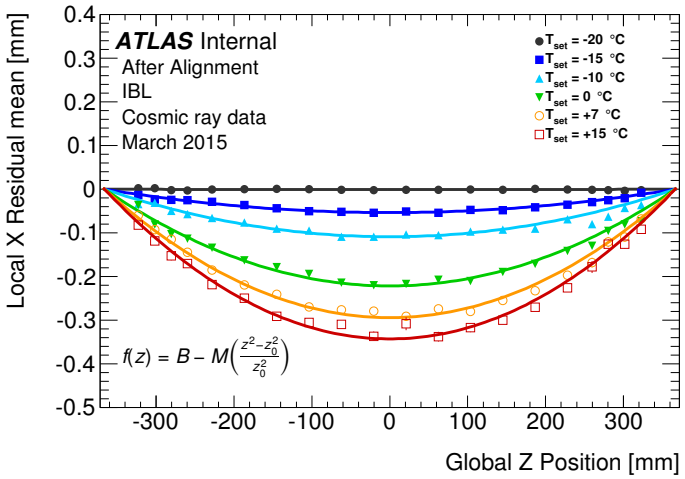

Figura 18.6: La mesura dels residus traça-senyal en funció de la posició dels mòduls al llarg de la doga del IBL. Cadascun dels punts representa la mitjana de las catorze dogues que componen l'IBL. Per quantificar l'artuqjament, la distribució a cada temperatura s'ha ajustat amb una funció parbólica [61].

amb els extrems de la doga. D'eixos extrems un està fixe i l'altre té una ranura. En l'equaciò, B és la base que descriu una traslació global de tota la doga conjuntament i M és la magnitut de l'arquejat. Per a cada temperatura d'operació, s'ha extret la seua corresponent magnitud d'arquejat M. Després d'això s'ha dut a terme un ajust lineal del conjunt de punts. De la pendent de dit ajust, hom extreu que la magnitud canvia uns 10 μm per grau de temperatura:

$$\frac{\mathrm{d}M}{\mathrm{d}T} = -10.6 \pm 0.7 \ [\mu\mathrm{m/K}] \tag{18.7}$$

A l'inici del Run-II, l'IBL mantenia una temperatura d'operació constant, amb lo qual, les dogues estaven estabilitzades. Però cap a finals de setembre de 2015, LHC va aumentar sensiblement la seua lluminositat. Això implica més partícules, més dades a reconstruir, major consum, major dany de radiació als sensors, en definitiva un petit canvi de temperatura. De manera immediata es va observar que l'IBL deixava de ser estable i començava a patir variacions run a run. Quan l'anàlisi es feu prou detallat, es va vore que els canvis es produien dins de cada run. Degut a este nou comportament dinàmic, fou necessari actualitzar el software de l'alineament per tal de permetre calcular i emprar correccions que depengueren del temps. La figura 18.8 mostra que una vegada introduït l'alineament dinàmic, l'efecte de l'arquejat de l'IBL dins de cada run és corregit.

18.2.4 Alineament en el bucle de calibratge

Cada vegada que ATLAS registra un nou run, és necesari realitzar un calibratge exprés de les dades d'eixe run. El procés de calibratge ha d'estar conclòs abans d'un màxim de 48 hores després de la presa de dades. L'objectiu del procés de calibratge és permetre que les dades reconstruïdes siguen d'alta qualitat i

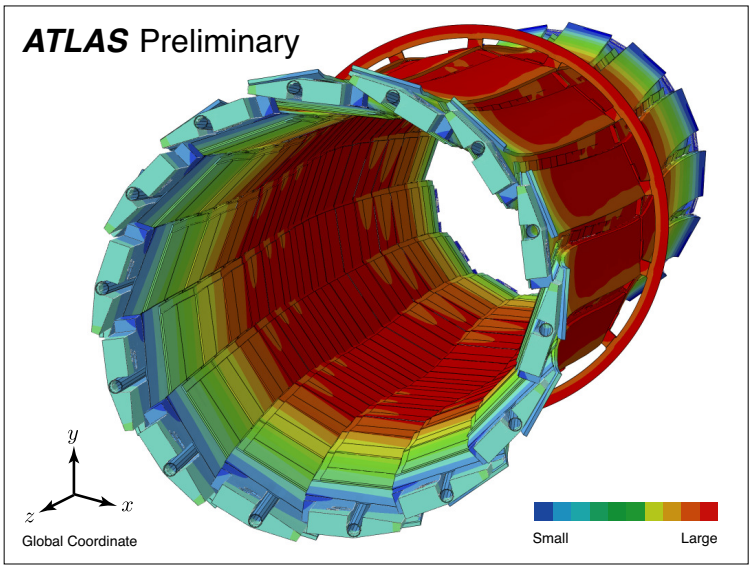

Figura 18.7: Simulació mijançant un anàlisi d'elements finits del IBL. Els resultats de la simulació coincidixen amb l'arquejanment de les dogues del IBL tal i com s'ha observat al alinear el detector real. [61]

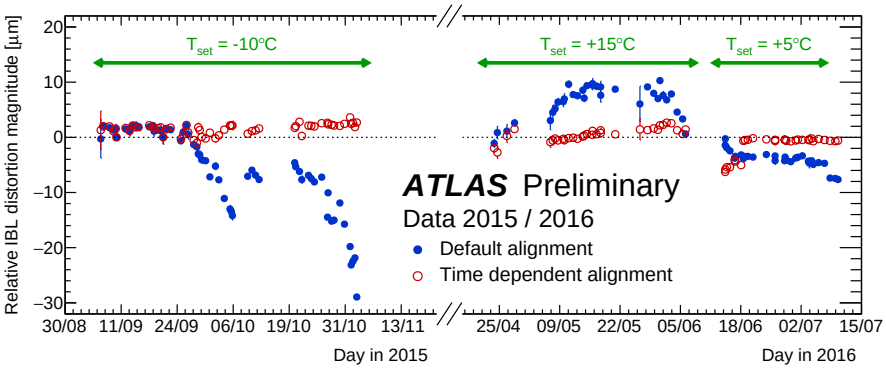

Figura 18.8: Evolució de la magnitut de l'arquejat del IBL durant 2015 i 2016 per a dos conjuts de geometries del detector: la primera amb l'alineament de base per a cada periode (punts blaus) i la segona després del bucle de calibratge (cercles rojos). Cada un dels periodes té un alineament de base distint perquè la temperatura d'operació del IBL és distinta. La geometria del IBL depén de la temperatura [66].

permeten anàlisis de física competitius. El procés en sí és conegut com a bucle de calibratge, i l'alineament del detector intern és una de les tasques incloses en el procés.

Cal recordar que durant el Run-I del LHC, ATLAS ja contava amb un alineament automàtic de cadascun dels runs enregistrats, dins del bucle de calibratge. Com durant en el Run-I, el comportament del ID era prou estable i durant períodes prou llargs, la geometria del detector (és a dir els paràmetres d'alineament) sols s'actulitzaven de quan en quan. Cal dir també que els resultats de l'alineament eren comprovats visualment run a run, i sols quan l'expert detectava/observava que els moviments eren significatius, aleshores s'actulitzaven els paràmetres d'alineament (és a dir, la descripció geométrica del ID).

El principi de funcionament del bucle de calibratge durant el Run-II és similar. Ara bé, la presència dels moviments dinàmics dins de cada run, com ara són: el moviment vertical del Pixel o l'arquejat de les dogues del IBL, ha requerit fer una automatització del procés. Esta automatització afecta tant l'execució dels treballs que calculen les noves constants d'alineament, com la seua validació i al seu registrament en la base de dades. La figura 18.9 mostra les correccions d'alineamient en funció del temps obtingudes en el bucle de calibratge per un run de l'any 2016. Degut a les dos components del movimient vertical del Pixel, el codi d'alineamient s'ha preparat per còrrer a dues velocitats. Durant la primera hora prenent dades, l'ID és alineat cada 20 minuts. Per la resta del run, el periode s'aumenta fins als 100 minuts. A la figura, pot observar-se que amb dita configuració del bucle de calibratge, es consiguix corregir el movimient del detector Pixel (en negre).

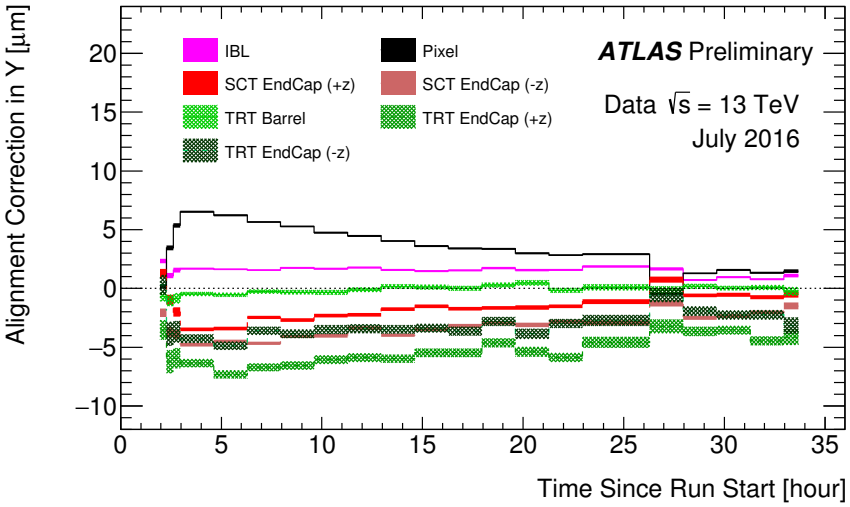

Figura 18.9: Correccions a la posició vertical en función del temps, de les estructures que componen l'ID. Mencionar que el barril del SCT defineix la referència i per tant es manté fixe. Les bandes que acompanyen les linies mostres la incertessa estadística [58].

18.3 Física del quark top

En esta secció es fa un resum de l'anàlisi realitzat amb 20.2 fb^{-1} de dades tretes de les col·lisions protó-protó proporcionades pel LHC durant 2012. Estes col·lisions es produeien a una energia en centre de mases de 8 TeV i foren registrades pel detector ATLAS. En l'anàlisi s'han estudiat diverses distribucions angulars de la producció (a través del canal t) i desintegració del quarks top en solitari. Estudiant les asimetries d'estes distribucions angulars, poden establir-se límits als valors dels acoblaments anòmals del vertex Wtb (equació 18.2). Cal dir que també s'ha estudiat la polarització amb la que emergen el quark top i el bosó W en este tipus d'esdeveniments.

18.3.1 Selecció del senyal

En una col·lisió de protons com les que ocòrren al LHC, es produeixen simultàniament una gran varietat d'esdeveniments. Entre tots eixos, cal seleccionar el senyal d'interés. En esta anàlisi es preten estudiar els esdeveniments on s'ha produït un quark top en solitari pel canal t, i este s'ha desintegrat pel canal leptònic del W (figura 18.1(a)). Per tant la topologia de l'esdeveniment es compon de:

- Dos jets, un d'ellos identificat com b-jet i l'altre com generat per un quark lleuger (o genèricament jet lleuger). Cal dir que el sabor dels jets es pren com aquell dels quarks que l'originen i que hadronitzen instantàniament.
- Un electró o un muó. Si el bosó W es desintegrarà mitjançant d'un τ, sols es considerarà como senyal si seguidament el τ es desintegra també leptónicament (e o μ).
- Un neutrino, la presència del qual es manisfesta com energia perduda en el plànol transvers.

La selecció d'esedeveniments d'esta anàlisi utilitza un procediment per talls de selecció. Si bé els talls s'apliquen en dos fases differerents. Primerament per fer una preseleció i després una selecció propiament dita. En la preselecció, el que es busca es que estiguen presents simultàniament tots els objectets mencionat abans, mentre que s'els requerix unes característiques d'energia i qualitat genèriques. D'esta manera es pot seleccionar tant el senyal com també altres esdeviniments amb una topologia semblant, amb els quals es permetrà fer tests de control. Per altra banda, la selecció consistix en talls més restrictius a més de vetar la presència d'un segon leptó. La figura 18.10 mostra les propietats en la regió del senyal abans d'aplicar els talls de selecció per electrons i muons combinats.

Apart de la regió de senyal, també s'han definit dos regions adicionals, que fem servir com a regions de control. Estes són denominades: regió $t\bar{t}$ i regió anti-senyal. Estes regions s'empren per extreure els factors de normalització del fons del SM a la producció de quarks top en solitari. Concretament, la regió $t\bar{t}$ es utilitzada per constrènyer la contribució d'esdeveniments provinents de producció de parelles de quarks top. Per altra banda, la regió anti-senyal

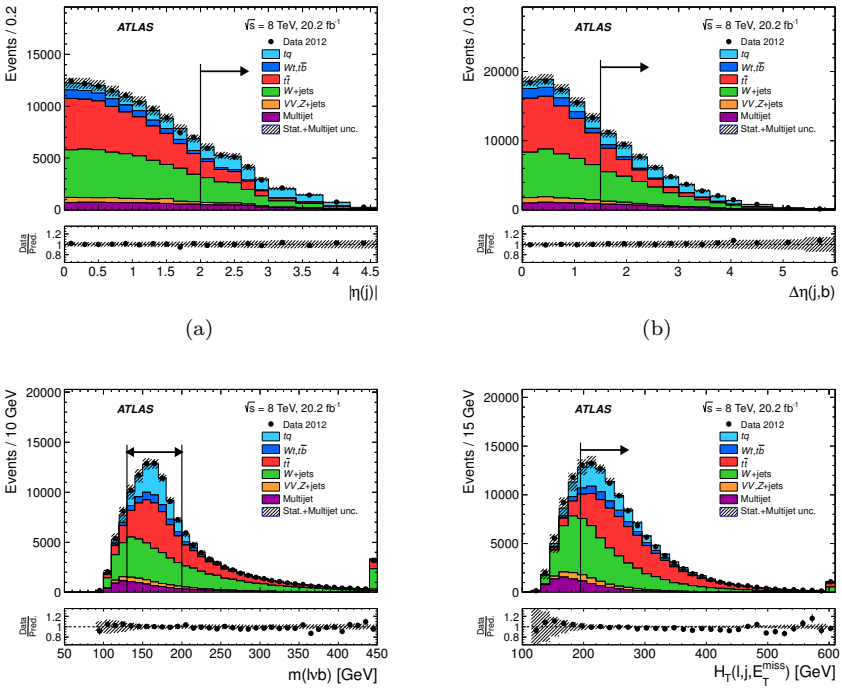

Figura 18.10: Distribucions dels observables emprats en la selecció del senyal partint dels esdeveniments preseleccionats (el veto al segon leptó ja està sent aplicat). Les línies verticals delimiten el tall per seleccionar el senyal. (a) pseudorapidesa del quark espectador, (b) diferència en pseudorapidesa de ambdós jets, (c) massa reconstruïda del quark top, i (d) suma de la massa transversa de tots els objectes reconstruïts.

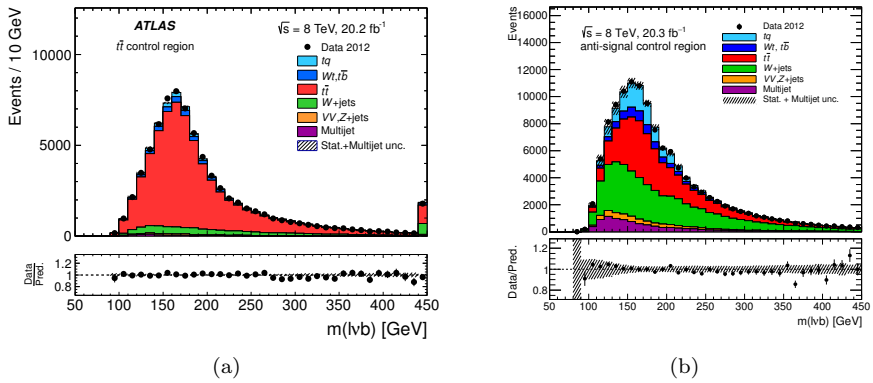

Figura 18.11: Distribució de la massa reconstruïda del quark top en les regions de control $t\bar{t}$ (a) i anti-senyal (b) per a electrons i muons combinats.

permet extreure el factor de normalització dels esdeveniments tipus W+jets. Finalment, també s'ha definit una regió de validació anomenada: W+jets amb l'objectiu de verificar si el fons està ben modelat. La taula 18.1 mostra el número d'esdeveniment en la regió del senyal i en cadascuna de les regions de control. La figura 18.11 presenta la distribució de la massa reconstruïda del quark top en les dos regions de control.

	Senyal	$t\bar{t}$	Anti-senyal	W+jets
canal t	5980 ± 22	1922 ± 13	13632 ± 33	10559 ± 29
$t\bar{t}$	1894 ± 11	59589 ± 62	41165 ± 51	20291 ± 36
canals Wt, s	262 ± 12	3018 ± 46	6808 ± 64	3932 ± 51
W+jets	1854 ± 47	6370 ± 67	44510 ± 220	250460 ± 730
Z+jets, Dibosó	190 ± 9	1121 ± 34	4915 ± 57	17770 ± 17
Multijet	420 ± 290	880 ± 620	9300 ± 6500	21000 ± 15000
Esperats	10600 ± 300	72900 ± 630	120000 ± 6500	324000 ± 15000
Dades ATLAS	10527	74121	124467	372847
S/F	1.30 ± 0.08	0.0264 ± 0.003	0.113 ± 0.006	0.0326 ± 0.0015

Taula 18.1: Número d'esdeveniments predit amb el SM i observat en les regiones de senyal, de control i de validació. Els esdeveniments amb electrons i muons s'han combinat.

La normalització de tots els procesos (tant de senyal com de fons) s'extreu de les prediccions de les seccions eficaces segons el SM i es modelen utilitzant mostres simulades amb Monte Carlo (MC). Si bé, els fons de multijet és una excepció a esta regla. La seua normalització es trau directament d'un subconjunt de dades real i amb un mètode empíric anomentat mètode de la matriu.

A més a més, utilitzant les dues regions de control, es poden calcular el factors de normalització adicionals per als dos tipus de fons principal: el fons de $t\bar{t}$ i el de W+jets. Estos factors de normalització s'obtenen fent un ajust multiple a les regions de senyal i de control. Els paràmetres lliures de l'ajust són precisament els factors de normalització del fons i del senyal. La funció d'ajust utilitza distribucions poisonianes per estimar la taxa d'esdeveniments en les distintes regions, amb priors gaussians per les contribucions de cada fons.

Amb tots eixos valors a la mà, per tal de realitzar la mesura de les asimetries, primer s'ha d'escalar els fons amb els factors de normalització empírics. Després sostreure els fons predits en la regió de senyal. Així ens queda el nostre senyal net.

18.3.2 Observables de polarització i asimetries angulars

Una vegada són seleccionats els esdeveniments de senyal amb tots els seus objectes, es pot fer la reconstrucció total de l'esdeveniment. El bosó W es reconstruït partint del leptó i del neutrino. Les propietats del quark top es treuen convinant les del bosó W i les del b-jet. Quan ja es coneixen els moments del quark

top, del quark espectador, del W, del leptó i del quark lleuger inicial, es poden definir diferents direccions i angles que estan relacionats amb la polarització del quark top i la del bosó W. Estos marcs de referència (figura 18.12) s'utilitcen per definir una sèrie d'asimetries angulars, els valors de les quals permeten fer comprovacions de les prediccions del SM. Este tipus d'asimetries, es construeix segons

$$A_{\mathrm{FB}} = \frac{N(\cos\theta > 0) - N(\cos\theta < 0)}{N(\cos\theta > 0) + N(\cos\theta < 0)} \tag{18.8}$$

i evaluen la diferència entre el número d'esdeveniments que apareixen en la direcció cap en davant i els que ho fan en la direcció cap en darrere. De particular interés són les asimetries en els angles θ_y i θ_l^N, ja que ambdues són altament sensibles a que els acoblaments del vèrtex Wtb prenguen valors anòmals. Més concretament, les asimetries en eixos angles són ben sensibles a la part imaginària de g_{R} (Im g_{R}). La taula 18.2 mostra totes les asimetries mesurades en este traball. Sis de les distribucions angulars que s'han mesurat es presenten en la figura 18.13.

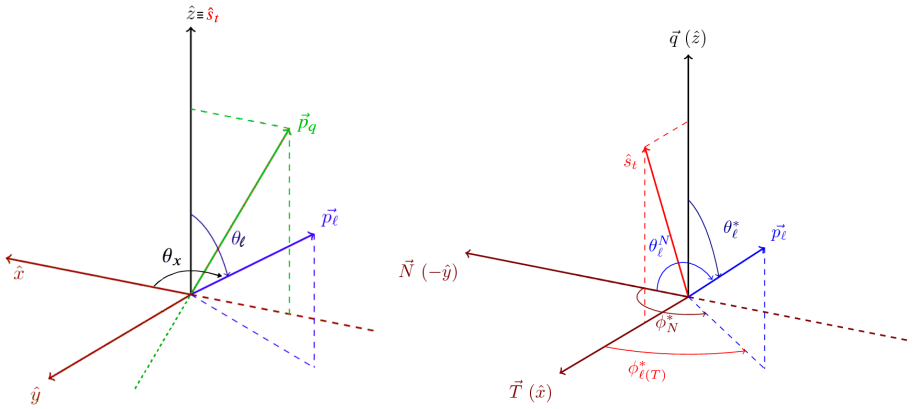

(a) (b)

Figura 18.12: Els dos sistemes de referència emprats en la definició de les distribucions angulars. Un és per la producció 18.12(a) i el segon per la desintegració 18.12(b) del quark top. Les direccions dels eixos venen definides per la direcció del moment del quark espectador, $\hat{s}_t$, del leptó, $\vec{p}_\ell$, del quark inicial lleuger $\vec{p}_q$ i del bosó W, $\vec{q}$, tots ells donats en el sistema en repos del quark top.

18.3.3 Deconvolució de les distribucions angulars

Les distribucions de les asimetries (i els seus valors) s'obtenen inicialment a nivell de la reconstrucció i selecció dels esdeveniments. Per tant, estos valors no es poden comparar directament amb les prediccions teòriques. Si volem poder fer eixa comparació, és necessari convertir els valors a nivell de reconstrucció en uns valors a nivell de partons (o nivell de generació). El procés de conversiò el que tracta és deconvolucionar (tornar en rere) els efectes del detector (per ejemple com afecta la resolució finita dels detectors i la seua eficàcia al hora de detectar les partícules), com també els efectes de la selecció del senyal (ja que per obtenir un senyal pot ser que hem introduït un biaix en el valor a testejar).

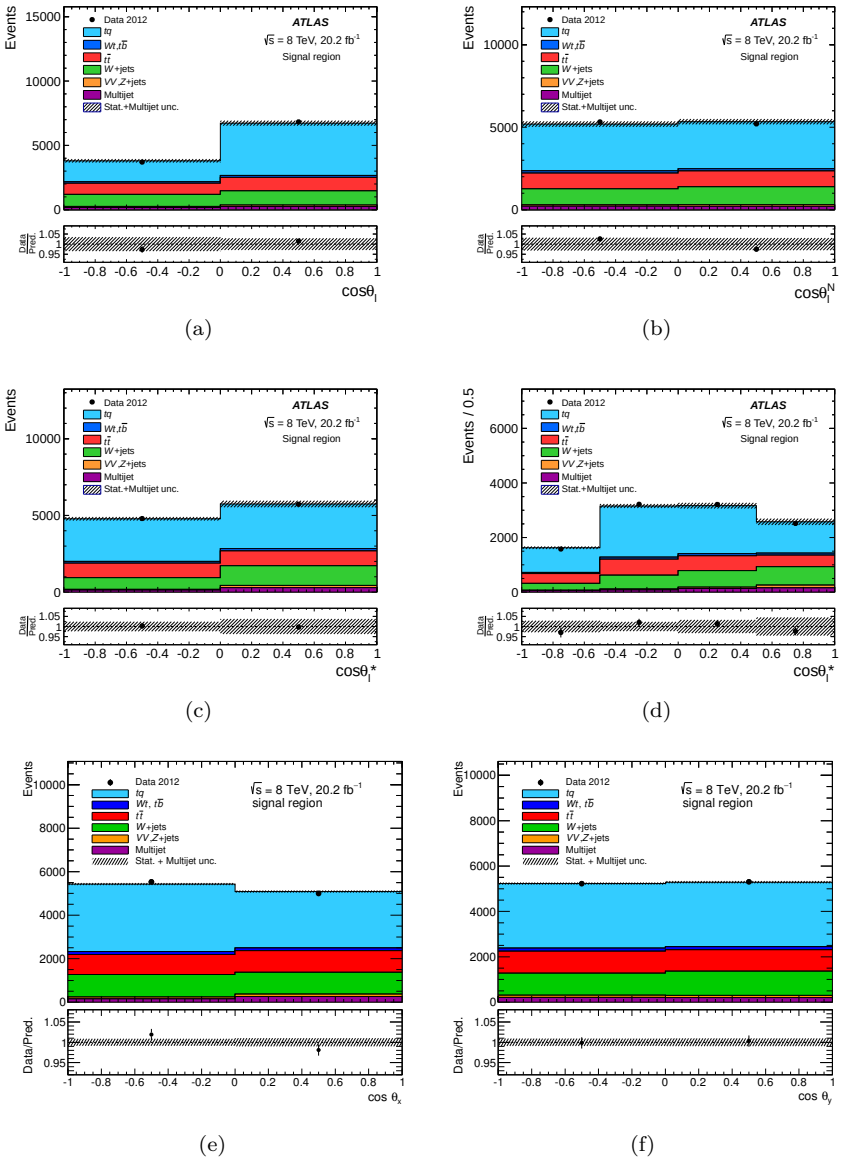

Figura 18.13: Distribucions angulars en la regió de senyal (a) $\cos\theta_\ell$, (b) $\cos\theta_\ell^N$, (c) $\cos\theta_\ell^*$ donades amb 2 (d) $\cos\theta_\ell^*$ i 4 canals, (e) $\cos\theta_x$ y (f) $\cos\theta_y$. Les distribucions combinen els esdeveniments selecionats en el canal d'electrons i de muons.

Asimetria	Observable angular	Observable de polarizatció	Predicció del SM
$A_{\rm FB}^{\ell}$	$\cos\theta_l$	$\frac{1}{2}\alpha_l P$	0.45
$A_{\rm FB}^{X}$	$\cos\theta_x$	$\frac{1}{2}\alpha_l \bar{P}_x$	0.02
$A_{\rm FB}^{Y}$	$\cos\theta_y$	$\frac{1}{2}\alpha_l \bar{P}_y$	0
$A_{\rm FB}^{tW}$	$\cos\theta_W \cos\theta_l^*$	$\frac{3}{8}P(F_R + F_L)$	0.10
$A_{\rm FB}$	$\cos\theta_l^*$	$\frac{3}{4}\langle S_3\rangle = \frac{3}{4}(F_R + F_L)$	-0.23
$A_{\rm EC}$	$\cos\theta_l^*$	$\frac{3}{8}\sqrt{\frac{3}{2}}\langle T_0\rangle = \frac{3}{16}(1 - 3F_0)$	-0.20
$A_{\rm FB}^{T}$	$\cos\theta_l^T$	$\frac{3}{4}\langle S_1\rangle$	0.34
$A_{\rm FB}^{N}$	$\cos\theta_l^N$	$-\frac{3}{4}\langle S_2\rangle$	0
$A_{\rm FB}^{T,\phi}$	$\cos\theta_l^* \cos\phi_T^*$	$-\frac{2}{\pi}\langle A_1\rangle$	-0.14
$A_{\rm FB}^{N,\phi}$	$\cos\theta_l^* \cos\phi_N^*$	$\frac{2}{\pi}\langle A_2\rangle$	0

Taula 18.2: Llistat de les asimetries mesurades en esta anàlis. Cada asimetria s'associa amb el seu observable angular i amb la seua relacció amb els observables de polarització del quark top i del bosó W. La llista es completa amb la predicció feta pel SM del valor de cada asimetria [17, 20, 21].

Les correccions de deconvolució s'obtenen partint de simulacions Monte Carlo d'esdeveniments de senyal. Per cadascuna de les distribucions es calcula una matriu de migracions M y una corba d'eficiència ϵ, les quals relaccionen el número d'esdeveniments reconstruïts en el canal i amb aquell de generats en el canal j, segons

$$N_j^{\rm generado} = \frac{\Sigma_i M_{ji}^{-1} N_i^{\rm reconstruido}}{\epsilon_j} \tag{18.9}$$

La majòria de les distribucions angulars s'han deconvolucionat emprant les correccions obtingudes de una mostra de MC generada amb PROTOS. En eixa mostra els valors dels acoblaments del vèrtex Wtb són els del SM. Ara bé, si la naturalessa haguera decidit que els acoblaments prenen valors que nosaltres diguem anòmals, les mostres reconstruïdes tindrien asimetries lleugerament distintes. Però no sols elles, sinó també les de partida, aquelles que volem mesurar. Per tant hem d'assegurar-nos que el métode de deconvolució no esbiaxe els valors mesurats de les asimetries. Es per tot això que s'ha desenvolupat un métode de deconvolució que combina la mostra del SM, amb mostres de MC generades amb acoplaments anòmals. De esta manera, es consiguix que la mesura final de les asimetries siga obtinnguda sense fer cap suposició a priori sobre el posible valor (siga SM o anòmal). Una derivada de tot este procés és que prediu quines de les asimetries angulars són més sensibles i quines són menys als valors anòmals de l'acoblament. En particular, $A_{\rm FB}^{N}$, $A_{\rm FB}^{Y}$ són sensibles a Im $g_{\rm R}$ mentres que $A_{\rm FB}^{X}$ és sensible a Re $g_{\rm R}$. La figura 18.14 mostra com el mètode de interpolació desenvolupat és capaç d'extreure el valor correcte de las asimetries (es presenta el cas d'$A_{\rm FB}^{N}$ i $A_{\rm FB}^{Y}$) en el tot el rang simulat amb valors anòmals del acoblament. Per contra, també es veu que si per la deconvolució es gastarà sols la mostra del SM, aleshores hi ha un problema de linearitat de la resposta.

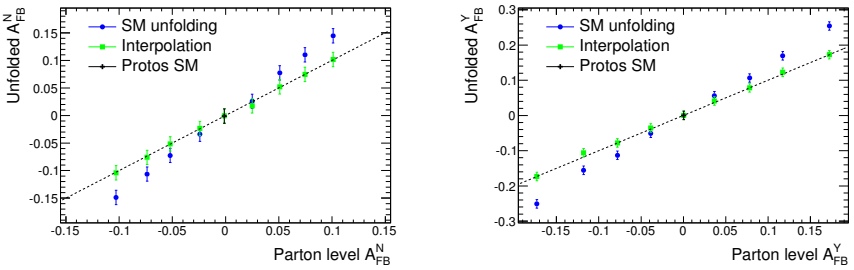

(a) (b)

Figura 18.14: Valor deconvolucionat d'(a) A_{FB}^{N} i (b) A_{FB}^{Y} en funció del valor generat per l'asimetria. La deconvolució se ha fet o bé directament amb les correcions del SM (puntos blaus) o amb el mètode d'interpolació (quadrats verds). Les barres d'error representen la incertesa deguda a la limitada estadística de les mostres. La línia puntejada està per indicar el cas de linealitat perfecta.

18.3.4 Resultats

El valor de la mesura s'ha d'acompanyar amb el de la seua incertesa. Són varies i diverses les fonts que intervenen en la incertesa final de les asimetries. Per exemple, tenim contribucions de: la resolución en la reconstrucció del jets, calibratge dels b-jets, la normalització dels fons, incertesa en la lluminositat o en el modelat tant del senyal com del fons. Totes estes son fonts d'incertesa sistemàtica i han estat evaluades individualment en esta anàlisi. El valor total de la incertesa és igual a la suma quadràtica de totes les contribucions. Per obtindre estes incerteses individuals, s'han dut a terme pseudo-experiments, en els que les variacions de las diferents fonts d'incertesa se propaguen fins la mesura final i el seu nou valor es compara amb el de referència.

La taula18.3 exhibix el resultat de cadascuna de les asimetries analitzades en este treball. En general, s'observa un bon acord entre el valor obtingut i el de la predicció feta pel SM. A partir dels valors de les asimetríes, i aplicant les ecuacions donades en la taula 18.2, es poden calcular els observables de polarització del quark top i del bosó W. Els resultats es presenten en la taula 18.4.

Finalment, podem establir limits als valors de les components real i imaginària de l'acoblament anòmal g_{R}. La determinació dels limits el que fa és emprar les asimetries A_{FB}^{N}, A_{FB}^{Y} y A_{FB}^{X}, ja que estes s'han obtingut amb el mètode de deconvolució interpolat. Recordem que gràcies a eixe mètode, les mesures d' A_{FB}^{N} i A_{FB}^{Y} s'han extret sense fer cap suposició inicial al valor de Im g_{R} (la mesura d' A_{FB}^{X} s'ha realizat sense suposicions en Re g_{R}). En ambdós casos, la resta d'acoblaments han pres el valor que prediu el SM.

Els limits s'extrauen a partir d'una funció χ^2 en la que es comparen els valors mesurats de les asimetries amb els seus valors predits en funció dels acoblaments anòmals. La funció χ^2 també té en compte les correlaciones entre les distintes asimetries, les quals es calculen de las correlacions existents entre les fonts d'incertesa considerades. Per a cada parella d'asimetries, es comparen una

	Valor	Esta.	Sist.	Valor final	Pred. SM
$A_{\rm FB}^{\ell}$	0.49	0.03	0.05	0.49 ± 0.06	0.45
$A_{\rm FB}^{X}$	-0.03	0.02	$^{+0.06}_{-0.05}$	-0.03 ± 0.06	0.02
$A_{\rm FB}^{Y}$	0.01	0.02	0.03	0.01 ± 0.03	0
$A_{\rm FB}^{tW}$	0.10	0.03	0.05	0.10 ± 0.06	0.10
$A_{\rm FB}$	-0.26	0.02	0.07	-0.26 ± 0.08	-0.23
$A_{\rm EC}$	-0.25	0.03	0.05	-0.25 ± 0.06	-0.20
$A_{\rm FB}^{T}$	0.39	0.03	0.09	0.39 ± 0.09	0.34
$A_{\rm FB}^{N}$	-0.04	0.02	0.03	-0.04 ± 0.04	0
$A_{\rm FB}^{T,\phi}$	-0.17	0.05	$^{+0.11}_{-0.10}$	$-0.17 \pm ^{+0.12}_{-0.11}$	-0.14
$A_{\rm FB}^{N,\phi}$	-0.03	0.03	0.05	-0.03 ± 0.06	0

Taula 18.3: Resum del valors mesurats per les asimetries angulars. Les incerteses es donen per separat. Una contribució és deguada l'estadística limitada de les dades recollides per ATLAS. L'altra presenta el valor total (suma quadràtica) de les inserteses sistemàtiques. També es donen els valors definitius de les asimetries, junt al seu error total. Estos poden comparar-se amb la predicció del SM.

	Valor	Esta.	Sist.	Valor final	Pred. SM
$\alpha_\ell P$	0.97	0.05	0.11	0.97 ± 0.12	0.90
$\alpha_\ell \bar{P}_x$	-0.05	0.04	0.11	-0.05 ± 0.12	0.04
$\alpha_\ell \bar{P}_y$	0.01	0.04	0.05	0.01 ± 0.06	0
$P(F_{\rm R} + F_{\rm L})$	0.25	0.08	0.14	0.25 ± 0.16	0.27
$\langle T_0 \rangle$	-0.55	0.06	0.12	-0.55 ± 0.13	-0.433
$\langle A_1 \rangle$	0.27	0.07	$^{+0.16}_{-0.17}$	$0.27 \pm ^{+0.17}_{-0.19}$	0.228
$\langle A_2 \rangle$	-0.05	0.05	0.09	-0.05 ± 0.10	0
$\langle S_1 \rangle$	0.52	0.04	0.12	0.52 ± 0.12	0.456
$\langle S_2 \rangle$	0.06	0.03	0.04	0.06 ± 0.05	0
$\langle S_3 \rangle$	-0.35	0.03	0.10	-0.35 ± 0.10	-0.309

Taula 18.4: Resum dels valors mesurats pels observables de polartització del quark top i del bosó W. Les incerteses es donen per separat. Una contribució és deguada l'estadística limitada de les dades recollides per ATLAS. L'altra presenta el valor total (suma quadràtica) de les inserteses sistemàtiques. També es donen els valors definitius dels observables de polarització, junt al seu error total. Estos poden comparar-se amb la predicció del SM.

a una com es comporten segons les distintes fonts d'incertesa sistemàtica. Si les asimetries canvien en el mateix sentit, s'els asigna una correlació $\rho = 1$. Mentre que si canvien en sentit contrari, s'els asigna una correlació $\rho = -1$. La correlació total ve donada per la mesura ponderada de totes les correlacions. Per tal de

calcular la correlació estadística s'ha emprat el mètodo 'bootstrap'. La taula 18.5 mostra les correlacions obtingudes entre les diferents asimetries. En eixa taula també es dona l'asimetria $A_{\rm FB}^{\ell}$, ja que és esta la que s'usa en l'extracció dels límits per a constrènyer el valor d' α_l. Evidentement, s'ha comprovat que la mesura de $A_{\rm FB}^{\ell}$ és completament independent dels valors de Re $g_{\rm R}$i Im $g_{\rm R}$.

Asimetria A	Asimetria B	Correl. Stad.	Correl. total
$A_{\rm FB}^{\ell}$	$A_{\rm FB}^{N}$	0.006	0.152
$A_{\rm FB}^{\ell}$	$A_{\rm FB}^{Y}$	0.007	0.090
$A_{\rm FB}^{\ell}$	$A_{\rm FB}^{X}$	-0.231	0.057
$A_{\rm FB}^{N}$	$A_{\rm FB}^{Y}$	0.050	0.412
$A_{\rm FB}^{N}$	$A_{\rm FB}^{X}$	0.007	0.293
$A_{\rm FB}^{Y}$	$A_{\rm FB}^{X}$	0.015	0.333

Taula 18.5: Resum de les correlacions estadística i total estimades per les distintes asimetries que es gasten en l'extracción de límits: $A_{\rm FB}^{\ell}$, $A_{\rm FB}^{N}$, $A_{\rm FB}^{Y}$ i $A_{\rm FB}^{X}$.

La figura 18.15 mostra els límits obtinguts en Im $g_{\rm R}$, utilitzant $A_{\rm FB}^{N}$ i $A_{\rm FB}^{Y}$ tant individualment o amb la combinació de les dues, si bé sempre s'ha usat conjuntament amb $A_{\rm FB}^{\ell}$. El límit obtingut a partir de la combinació de les tres asimetries és Im $g_{\rm R} \in [-0.07, 0.02]$, siguen este el més restrictiu dels tres, el qual millora la precisió dels límits anteriors a Im $g_{\rm R}$.

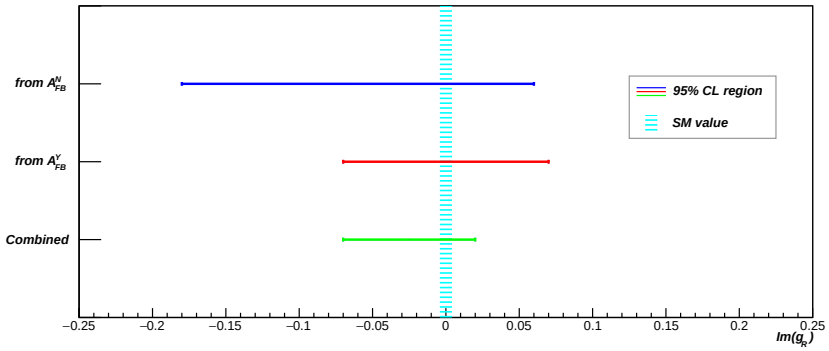

Figura 18.15: Intervals permesos per a la part imaginària de $g_{\rm R}$al 95% de nivell de confiança i extrets de les asimetries $A_{\rm FB}^{N}$, $A_{\rm FB}^{Y}$ y $A_{\rm FB}^{\ell}$. La línia vertical blava en Im $g_{\rm R} = 0$ mostra el valor predit pel SM.

A partir de l'asimetría $A_{\rm FB}^{X}$, combinada amb $A_{\rm FB}^{\ell}$, poden establir-se límits als valors permesos de la part real de $g_{\rm R}$. En este cas, el límite obtés és Re $g_{\rm R} \in [-0.22, 0.10]$, no tan restrictiu com el de la part imaginària. Açò està entés i és degut a que la incertesa sistemàtica d'$A_{\rm FB}^{X}$ és major que les d'$A_{\rm FB}^{N}$ i $A_{\rm FB}^{Y}$, per tant es pot constrènyer menys i el valor té un rang més ampli de valors. El límit obtingut en Re $g_{\rm R}$ és també menys precis que altres límits extrets a partir de les mesures de les fraccions d'helicitat del bosó W.

Appendices

Appendix A

Simulated samples

Baseline samples used in this work are described in section 8.2. This appendix describes the additional samples used for the various systematic uncertainties calculations. The process followed for the determination of the uncertainties is explained in chapter 14.

All the samples used in this work are official samples produced by the ATLAS single top quark working group. The common ntuples of the Single Top subgroup for lepton plus jets selection [122] are used. These ntuples are a slimmed and skimmed version of the centrally produced CommonD3PDs. They are produced with the SingleTopD3PDAnalysis package (`SingleTopD3PDAnalysis-00-18-01`) using the TopRootCore packages [123] (release `AnalysisTop-1.9.0` built from `TopRootCoreRelease-14-00-28`), which implements all the object calibrations and corrections provided by the combined performance groups, following the recommendations of the Top Reconstruction subgroup [40, 41, 124].

Additionally, summary tables listing of all the simulated samples used in the analysis are given in this appendix. Tables A.1 and A.2 give the list of the signal samples, while tables A.3, A.4, A.5 and A.6 give the list of the background samples. The signal and background top quark samples are normalised to the theoretical production cross-sections given in chapter 10, through the k-factors provided in the tables.

A.1 Additional samples

In order to estimate the impact than the modelling of the signal and the different background processes has in the measurements performed in this analysis, additional samples to the baseline ones have been produced.

For the evaluation of the uncertainty associated with the NLO generator, an additional t-channel sample is produced using the aMC@NLO event generator implemented in the MadGraph5 framework (v2.0) [125] interfaced to Herwig (v6.52) [126, 127] for parton showering and Jimmy (v4.31) [128] for the underlying-event modelling, with the ATLAS AUET2 tune [129] and the CT10f4

PDFs. The renormalisation and factorisation scales are set to be the same as implemented in POWHEG-BOX. The top quarks are decayed using MADSPIN. As for POWHEG-BOX, the aMC@NLO sample can not be used to compute the detector and physics corrections needed to unfold at parton-level.

To study the impact on the measurement of the parton shower modelling, a t-channel sample generated with POWHEG-BOX and coupled to HERWIG (v6.52) and JIMMY (v4.31) with the AUET2 tune is used.

Effects of the scales and of the initial- and final-state radiation (ISR/FSR) on the signal events are studied using a set of POWHEG-BOX samples (CT10 PDFs) generated with various choices of the renormalisation and factorisation scales. The hard-process generator is coupled to PYTHIA (v6.426) using the Perugia 2012 tune [80] with the CTEQ6L1 PDF sets. In these samples, the renormalisation and factorisation scales are increased or decreased by a factor two, and the parameter settings adjusted to have more or less parton shower radiation through the `radHi` and `radLo` parameterisations of the Perugia 2012 tune. A POWHEG-BOX sample produced with the baseline scales and the baseline Perugia 2012 tune is used as reference sample when evaluating the scale and radiation uncertainties.

For the evaluation of the uncertainty due to the generator and parton shower modelling, additional simulated samples for the s-channel, Wt and $t\bar{t}$ processes are produced using the MC@NLO generator (v4.03) [130–133] interfaced to HERWIG (v6.52) for parton showering and JIMMY (v4.31) for the underlying-event modelling with the ATLAS AUET2 tune and the CT10 PDFs. To study specifically the impact of the parton shower modelling from the main top quark background process, $t\bar{t}$ simulation samples generated using POWHEG-BOX, with CT10 PDFs and $h_{damp} = \infty$, interfaced to HERWIG (v6.52) with the AUET2 tune or to PYTHIA (v6.426) with the AUET2B tune, are used.

To estimate the uncertainty coming from the amount of initial-state and final-state radiation, two samples of $t\bar{t}$ events are produced with POWHEG-BOX (CT10 PDFs) interfaced to PYTHIA (v6.427) (CTEQ6L1 PDFs) with the Perugia 2012 tune, using parameter settings adjusted to vary the amount of ISR/FSR: one with $h_{damp} = m_t$ and a PYTHIA tune with less radiation (P2012 `radLo` tune), and one with $h_{damp} = 2m_t$ and a tune with more radiation (P2012 `radHi` tune). The uncertainty due to the amount of additional radiation is also investigated for the s-channel and Wt processes using samples generated with POWHEG-BOX (CT10 PDFs) coupled to PYTHIA (v6.426) with the Perugia 2012 tune (CTEQ6L1 PDFs). In these samples, the renormalisation and factorisation scales are increased or decreased by a factor two, and combined with the `radHi` and `radLo` parameterisations of the Perugia 2012 tune.

The POWHEG-BOX and MC@NLO samples, both for signal and background top-related processes, used for the generator, parton shower, radiation, scale and mass studies are processed using the `ATLFAST-II` simulation package of the ATLAS detector. As for the baseline samples, all the additional t-channel samples have been produced assuming a top quark mass of 172.5 GeV and the top quark decay being 100% through $t \to Wb$.

Sample	Data set ID	Generator	σ [pb]	k-factor	N_{MC}
t-channel (ℓ+jets, t)	110090	Powheg-Box+Pythia P2011C	17.5	1.05	5M
t-channel (ℓ+jets, t)	110090	Powheg-Box+Pythia P2011C	17.5	1.05	3M AFII
t-channel (ℓ+jets, $\bar{t}$)	110091	Powheg-Box+Pythia P2011C	9.4	1.06	5M
t-channel (ℓ+jets, $\bar{t}$)	110091	Powheg-Box+Pythia P2011C	9.4	1.06	2M AFII
t-channel (ℓ+jets, t)	110070	Powheg-Box+Pythia P2012	17.5	1.05	5M AFII
t-channel (ℓ+jets, $\bar{t}$)	110071	Powheg-Box+Pythia P2012	9.4	1.06	5M AFII
t-channel (ℓ+jets, t), μ_{F}=2.0, μ_{R}=2.0	110242	Powheg-Box+Pythia P2012radLo	15.9	1.16	2M AFII
t-channel (ℓ+jets, t), μ_{F}=2.0, μ_{R}=2.0	110243	Powheg-Box+Pythia P2012radHi	15.9	1.16	2M AFII
t-channel (ℓ+jets, t), μ_{F}=0.5, μ_{R}=0.5	110250	Powheg-Box+Pythia P2012radHi	17.9	1.03	2M AFII
t-channel (ℓ+jets, t), μ_{F}=0.5, μ_{R}=0.5	110251	Powheg-Box+Pythia P2012radLo	18.0	1.02	2M AFII
t-channel (ℓ+jets, $\bar{t}$), μ_{F}=2.0, μ_{R}=2.0	110052	Powheg-Box+Pythia P2012radLo	8.5	1.17	2M AFII
t-channel (ℓ+jets, $\bar{t}$), μ_{F}=2.0, μ_{R}=2.0	110053	Powheg-Box+Pythia P2012radHi	8.5	1.17	2M AFII
t-channel (ℓ+jets, $\bar{t}$), μ_{F}=0.5, μ_{R}=0.5	110060	Powheg-Box+Pythia P2012radHi	9.7	1.03	2M AFII
t-channel (ℓ+jets, $\bar{t}$), μ_{F}=0.5, μ_{R}=0.5	110061	Powheg-Box+Pythia P2012radLo	9.7	1.03	2M AFII
t-channel (ℓ+jets, t), m_t=175 GeV	110274	Powheg-Box+Pythia P2011C	17.5	1.05	3M AFII
t-channel (ℓ+jets, $\bar{t}$), m_t=175 GeV	110275	Powheg-Box+Pythia P2011C	9.4	1.06	2M AFII
t-channel (ℓ+jets, t)	110086	Powheg-Box+Herwig AUET2	17.5	1.05	5M AFII
t-channel (ℓ+jets, $\bar{t}$)	110087	Powheg-Box+Herwig AUET2	9.4	1.06	5M AFII
t-channel (ℓ+jets)	110121	aMC@NLO+Herwig AUET2	26.6	1.07	10M AFII

Table A.1: Signal MC samples used for the analysis. The cross-section column includes the branching ratio of the W boson leptonic decay channel (BR(ℓ)=0.324) but not the k-factor. ℓ stands for e, μ or τ. μ_{F} and μ_{R} are the factorisation and renormalisation scales, respectively. The radLo and radHi labels correspond to settings with less and more parton shower radiation with respect to the nominal parameterisation, respectively. The samples processed with the `ATLFAST2` detector simulation are labelled AFII in the last column.

Sample	Couplings	Data set ID	Generator	σ [pb]	k-factor	N_{MC}
	$\mathrm{Re}\,V_L$, $\mathrm{Im}\,g_R$, $\mathrm{Re}\,g_R$, $\mathrm{Re}\,V_R$					
t-channel (ℓ+jets)	1.0, 0.0, 0.0, 0.0	117788	Protos+Pythia P2011C	28.4	1.00	5M AFII
t-channel (ℓ+jets)	0.958, 0.23, 0.0, 0.0	117789	Protos+Pythia P2011C	28.4	1.00	3M AFII
t-channel (ℓ+jets)	0.958, −0.23, 0.0, 0.0	117790	Protos+Pythia P2011C	28.4	1.00	3M AFII
t-channel (ℓ+jets)	0.993, 0.094, 0.0, 0.0	117791	Protos+Pythia P2011C	28.4	1.00	3M AFII
t-channel (ℓ+jets)	0.993, −0.094, 0.0, 0.0	117792	Protos+Pythia P2011C	28.4	1.00	3M AFII
t-channel (ℓ+jets)	0.982, 0.144, 0.0, 0.0	110509	Protos+Pythia P2011C	28.4	1.00	3M AFII
t-channel (ℓ+jets)	0.992, 0.043, 0.0, 0.0	110510	Protos+Pythia P2011C	28.4	1.00	3M AFII
t-channel (ℓ+jets)	0.982, −0.144, 0.0, 0.0	110511	Protos+Pythia P2011C	28.4	1.00	3M AFII
t-channel (ℓ+jets)	0.992, −0.043, 0.0, 0.0	110512	Protos+Pythia P2011C	28.4	1.00	3M AFII
t-channel (ℓ+jets)	1.165, 0.0, 0.18, 0.0	110502	Protos+Pythia P2011C	28.4	1.00	3M AFII
t-channel (ℓ+jets)	1.065, 0.0, 0.07, 0.0	110503	Protos+Pythia P2011C	28.4	1.00	3M AFII
t-channel (ℓ+jets)	0.925, 0.0, −0.075, 0.0	110504	Protos+Pythia P2011C	28.4	1.00	3M AFII
t-channel (ℓ+jets)	0.867, 0.0, −0.131, 0.0	110505	Protos+Pythia P2011C	28.4	1.00	3M AFII
t-channel (ℓ+jets)	0.726, 0.0, −0.26, 0.0	110506	Protos+Pythia P2011C	28.4	1.00	3M AFII
t-channel (ℓ+jets)	0.866, 0.0, 0.0, 0.25	110507	Protos+Pythia P2011C	28.4	1.00	3M AFII
t-channel (ℓ+jets)	0.968, 0.0, 0.0, 0.50	110508	Protos+Pythia P2011C	28.4	1.00	3M AFII

Table A.2: Signal MC samples generated with Protos used in the analysis. The cross-section column includes the branching ratio of the W boson leptonic decay channel (BR(ℓ)=0.324) but not the k-factor. ℓ stands for e, μ or τ. The implemented values of the Wtb couplings are given. The samples processed with the `ATLFAST2` detector simulation are labelled AFII in the last column.

Sample	Data set ID	Generator	σ [pb]	k-factor	N_{MC}
s-channel (ℓ+jets)	110119	Powheg-Box+Pythia P2011C	1.64	1.11	6M
s-channel (ℓ+jets)	110119	Powheg-Box+Pythia P2011C	1.64	1.11	6M AFII
s-channel (ℓ+jets), μ_{F}=2.0, μ_{R}=2.0	110040	Powheg-Box+Pythia P2012radHi	1.69	1.07	1M AFII
s-channel (ℓ+jets), μ_{F}=2.0, μ_{R}=1.0	110041	Powheg-Box+Pythia P2012	1.70	1.07	1M AFII
s-channel (ℓ+jets), μ_{F}=1.0, μ_{R}=2.0	110042	Powheg-Box+Pythia P2012radHi	1.69	1.07	1M AFII
s-channel (ℓ+jets), μ_{F}=0.5, μ_{R}=1.0	110043	Powheg-Box+Pythia P2012	1.70	1.07	1M AFII
s-channel (ℓ+jets), μ_{F}=1.0, μ_{R}=0.5	110044	Powheg-Box+Pythia P2012radLo	1.70	1.07	1M AFII
s-channel (ℓ+jets), μ_{F}=0.5, μ_{R}=0.5	110045	Powheg-Box+Pythia P2012radLo	1.70	1.07	1M AFII
s-channel (ℓ+jets), m_t=175 GeV	110129	Powheg-Box+Pythia P2011C	1.80	1.07	0.5M AFII
s-channel (e+jets)	108343	MC@NLO+Herwig AUET2	0.56	1.07	1M AFII
s-channel (μ+jets)	108344	MC@NLO+Herwig AUET2	0.56	1.07	1M AFII
s-channel (τ+jets)	108345	MC@NLO+Herwig AUET2	0.56	1.07	1M AFII

Table A.3: s-channel single top quark background MC samples used for the analysis. The cross-section column includes the branching ratio but not the k-factor. ℓ indicates e, μ or τ. DS and DR stand for diagram removal and diagram subtraction schemes, respectively. SM BRs means the SM values of the branching ratios for top quark decay (BR($t \to Wb$) = 1). For the $t\bar{t}$ samples, the parameter h_{damp} is either set to the top quark mass m_t, to twice the top quark mass, or to infinity. The radLo and radHi labels correspond to settings with less and more parton shower radiation, respectively. The samples processed with the `ATLFAST2` detector simulation are labelled AFII in the last column.

Sample	Data set ID	Generator	σ [pb]	k-factor	N_{MC}
Wt (incl.), DR scheme	110140	Powheg-Box+Pythia P2011C	20.5	1.09	1M
Wt (incl.), DR scheme	110140	Powheg-Box+Pythia P2011C	20.5	1.09	20M AFII
Wt (incl.), DS scheme	110142	Powheg-Box+Pythia P2011C	18 1	1.23	1M
Wt (incl.), DR scheme, μ_F=2.0, μ_R=2.0	110046	Powheg-Box+Pythia P2012radHi	21.0	1.11	1M AFII
Wt (incl.), DR scheme, μ_F=2.0, μ_R=1.0	110047	Powheg-Box+Pythia P2012	21.1	1.06	1M AFII
Wt (incl.), DR scheme, μ_F=1.0, μ_R=2.0	110048	Powheg-Box+Pythia P2012radHi	20.0	1.14	1M AFII
Wt (incl.), DR scheme, μ_F=0.5, μ_R=1.0	110049	Powheg-Box+Pythia P2012	20.1	1.11	1M AFII
Wt (incl.), DR scheme, μ_F=1.0, μ_R=0.5	110050	Powheg-Box+Pythia P2012radLo	21.6	1.04	1M AFII
Wt (incl.), DR scheme, μ_F=0.5, μ_R=0.5	110051	Powheg-Box+Pythia P2012radLo	21.2	1.06	1M AFII
Wt (incl.), DR scheme, m_t=175 GeV	110130	Powheg-Box+Pythia P2011C	21 5	1.09	3M AFII
Wt (incl.)	108346	MC@NLO+Herwig AUET2	20.7	1.08	5M AFII

Table A.4: Wt-channel single top quark background MC samples used for the analysis. The cross-section column includes the branching ratio but not the k-factor. ℓ indicates e, μ or τ. DS and DR stand for diagram removal and diagram subtraction schemes, respectively. SM BRs means the SM values of the branching ratios for top quark decay (BR($t \to Wb$) = 1). For the $t\bar{t}$ samples, the parameter h_{damp} is either set to the top quark mass m_t, to twice the top quark mass, or to infinity. The radLo and radHi labels correspond to settings with less and more parton shower radiation, respectively. The samples processed with the `ATLFAST2` detector simulation are labelled AFII in the last column.

Sample	Data set ID	Generator	σ [pb]	k-factor	N_{MC}
$t\bar{t}$ (no all had.), h_{damp}=m_t	110404	POWHEG-BOX+PYTHIA P2011C	114	1.20	50M
$t\bar{t}$ (no all had.), h_{damp}=m_t	110404	POWHEG-BOX+PYTHIA P2011C	114	1.20	100M AFII
$t\bar{t}$ (no all had.), h_{damp}=∞	117050	POWHEG-BOX+PYTHIA P2011C	114	1.20	50M
$t\bar{t}$ (no all had.), h_{damp}=∞	105861	POWHEG-BOX+PYTHIA AUET2B	114	1.20	30M AFII
$t\bar{t}$ (no all had.), h_{damp}=∞	105860	POWHEG-BOX+HERWIG AUET2	116	1.19	30M AFII
$t\bar{t}$ (no all had.), h_{damp}=m_t	110407	POWHEG-BOX+PYTHIA P2012radLo	114	1.20	15M AFII
$t\bar{t}$ (no all had.), h_{damp}=$2m_t$	110408	POWHEG-BOX+PYTHIA P2012radHi	114	1.20	15M AFII
$t\bar{t}$ (no all had.), h_{damp}=∞, m_t=175 GeV	117842	POWHEG-BOX+PYTHIA P2011C	106	1.20	6M
$t\bar{t}$ (no all had.)	105200	MC@NLO+HERWIG AUET2	113	1.22	29M AFII

Table A.5: Top quark pair background MC samples used for the analysis. The cross-section column includes the branching ratio but not the k-factor. ℓ indicates e, μ or τ. DS and DR stand for diagram removal and diagram subtraction schemes, respectively. SM BRs means the SM values of the branching ratios for top quark decay ($\mathrm{BR}(t \to Wb) = 1$). For the $t\bar{t}$ samples, the parameter h_{damp} is either set to the top quark mass m_t, to twice the top quark mass, or to infinity. The radLo and radHi labels correspond to settings with less and more parton shower radiation, respectively. The samples processed with the `ATLFAST2` detector simulation are labelled AFII in the last column.

Sample	Data set ID	Generator	σ [pb]	k-factor	N_{MC}
$W \to e\nu$ b-filtered	167740	Sherpa	140	1.10	15M
$W \to e\nu$ c-filtered	167741	Sherpa	538	1.10	10M
$W \to e\nu$	167742	Sherpa	10295	1.10	50M
$W \to \mu\nu$ b-filtered	167743	Sherpa	140	1.10	15M
$W \to \mu\nu$ c-filtered	167744	Sherpa	466	1.10	10M
$W \to \mu\nu$	167745	Sherpa	10368	1.10	50M
$W \to \tau\nu$ b-filtered	167746	Sherpa	140	1.10	15M
$W \to \tau\nu$ c-filtered	167747	Sherpa	506	1.10	10M
$W \to \tau\nu$	167748	Sherpa	10327	1.10	50M
$Z \to e^+e^-$ b-filtered	167749	Sherpa	31.0	1.12	4M
$Z \to e^+e^-$ c-filtered	167750	Sherpa	314	1.12	3M
$Z \to e^+e^-$	167751	Sherpa	764	1.12	1M
$Z \to \mu^+\mu^-$ b-filtered	167752	Sherpa	31.0	1.12	4M
$Z \to \mu^+\mu^-$ c-filtered	167753	Sherpa	314	1.12	3M
$Z \to \mu^+\mu^-$	167754	Sherpa	764	1.12	1M
$Z \to \tau^+\tau^-$ b-filtered	167755	Sherpa	31.0	1.12	4M
$Z \to \tau^+\tau^-$ c-filtered	167756	Sherpa	314	1.12	3M
$Z \to \tau^+\tau^-$	167757	Sherpa	765	1.12	1M
$WW \to e\nu qq$	183734	Sherpa	7.3	1.06	3.2M
$WW \to \mu\nu qq$	183736	Sherpa	7.3	1.06	3.2M
$WW \to \tau\nu qq$	183738	Sherpa	7.3	1.06	3.2M
$ZZ \to e^+e^-qq$	183586	Sherpa	0.24	1.00	120k
$ZZ \to \mu^+\mu^-qq$	183588	Sherpa	0.24	1.00	120k
$WZ \to e\nu qq$	183735	Sherpa	1.91	1.05	840k
$WZ \to \mu\nu qq$	183737	Sherpa	1.91	1.05	840k
$WZ \to \tau\nu qq$	183739	Sherpa	1.91	1.05	840k
$ZW \to e^+e^-qq$	183585	Sherpa	1.46	1.05	700k
$ZW \to \mu^+\mu^-qq$	183587	Sherpa	1.46	1.05	700k

Table A.6: Baseline W+jets, Z+jets and diboson background MC samples used in the analysis. The cross-section column includes the branching ratio but not the k-factor. The samples processed with the `ATLFAST2` detector simulation are labelled AFII in the last column.

Appendix B

Expected uncertainties

Tables with the breakdown of the expected statistical and systematic uncertainties of all the measured asymmetries of the analysis. Systematic uncertainties with various components have been added in quadrature as explained in chapter 14. Uncertainties in which only the *up* or the *down* contribution has an impact on the measurement have been symmetrised in order to give a more conservative total uncertainty.

Uncertainty source	$\Delta A^{l}_{\mathrm{FB}} \times 10^2$	$\Delta A^{tW}_{\mathrm{FB}} \times 10^2$	$\Delta A_{\mathrm{FB}} \times 10^2$	$\Delta A_{\mathrm{EC}} \times 10^2$
Statistical uncertainty	± 2.5	± 3.0	± 2.3	± 2.7
Simulation statistics	± 1.7	± 1.6	± 1.3	± 1.6
Luminosity	< 0.1	< 0.1	< 0.1	< 0.1
Background normalisation	± 0.5	± 0.4	± 0.8	± 0.6
E_T^{miss} reconstruction	± 0.8	$^{+0.3}_{-0.7}$	$^{+0.9}_{-0.6}$	$^{+0.7}_{-0.2}$
Lepton reconstruction	$^{+1.0}_{-0.1}$	$^{+0.1}_{-1.2}$	± 1.3	$^{+0.5}_{-0.3}$
Jet reconstruction	± 2.1	± 2.2	± 1.1	± 1.5
Jet energy scale	$^{+1.6}_{-1.2}$	$^{+1.5}_{-1.6}$	$^{+3.0}_{-2.6}$	$^{+1.9}_{-0.6}$
Jet flavour tagging	± 0.8	± 0.3	± 0.6	± 0.3
PDF	< 0.1	± 0.1	< 0.1	< 0.1
$t\bar{t}$ generator	± 2.0	± 1.0	± 0.3	± 0.8
$t\bar{t}$ parton shower	± 0.6	± 0.4	± 2.6	± 0.1
$t\bar{t}$ scales	± 0.2	± 0.4	± 1.1	± 0.3
Wt,$s-$channel generator	± 0.9	± 0.8	± 0.3	± 0.2
Wt,$s-$channel scales	± 0.8	± 0.3	± 0.4	± 0.2
$t-$channel NLO generator	± 1.5	± 0.7	± 0.6	± 2.7
$t-$channel LO-NLO generator	± 1.8	± 2.4	± 3.0	± 1.5
$t-$channel parton shower	± 0.3	± 1.8	± 2.4	± 0.4
$t-$channel scales	± 1.2	± 2.1	± 0.6	± 1.6
W+jets, multijet modelling	$^{+1.5}_{-1.1}$	$^{+0.7}_{-0.4}$	$^{+0.7}_{-1.5}$	$^{+0.4}_{-1.2}$
Systematic uncertainty	$^{+5.2}_{-4.9}$	$^{+5.1}_{-5.3}$	$^{+6.3}_{-6.2}$	$^{+4.8}_{-4.5}$

Table B.1: Breakdown of the contributions to the expected statistical and systematic uncertainties on the A^{l}_{FB}, A^{tW}_{FB} and A_{FB} forward-backward asymmetries, extracted from the distributions in $\cos\theta_l$, $\cos\theta_W \cos\theta^*_l$ and $\cos\theta^*_l$ respectively. The breakdown for the edge-central asymmetry A_{EC} of the distribution $\cos\theta^*_l$ is also shown. For better readability the uncertainties are scaled by 10^2.

Uncertainty source	$\Delta A_{\mathrm{FB}}^{N} \times 10^2$	$\Delta A_{\mathrm{FB}}^{T} \times 10^2$	$\Delta A_{\mathrm{FB}}^{N,\phi} \times 10^2$	$\Delta A_{\mathrm{FB}}^{T,\phi} \times 10^2$
Statistical uncertainty	± 2.1	± 3.1	± 2.9	± 4.6
Simulation statistics	± 1.1	± 1.8	± 1.6	± 2.5
Luminosity	< 0.1	< 0.1	< 0.1	< 0.1
Background normalisation	± 0.4	± 1.1	± 0.5	± 1.0
E_T^{miss} reconstruction	± 0.3	$^{+0.4}_{-0.3}$	$^{+0.4}_{-0.8}$	$^{+0.2}_{-1.3}$
Lepton reconstruction	$^{+0.1}_{-0.2}$	$^{+1.3}_{-1.4}$	$^{+0.5}_{-0.4}$	$^{+1.3}_{-0.6}$
Jet reconstruction	± 0.8	$^{+0.5}_{-0.6}$	± 1.6	± 1.2
Jet energy scale	$^{+0.7}_{-1.3}$	$^{+3.8}_{-4.5}$	$^{+0.5}_{-2.3}$	$^{+4.0}_{-2.2}$
Jet flavour tagging	± 0.1	± 0.5	± 0.2	± 0.5
PDF	< 0.1	± 0.2	± 0.1	$^{+0.3}_{-0.4}$
$t\bar{t}$ generator	± 0.4	± 3.3	± 1.5	± 1.5
$t\bar{t}$ parton shower	± 1.5	± 1.0	± 0.8	± 1.5
$t\bar{t}$ scales	± 0.3	± 0.8	± 0.3	± 1.4
Wt,$s-$channel generator	± 0.2	± 0.7	± 0.3	± 1.2
Wt,$s-$channel scales	± 0.6	± 0.4	± 0.3	± 0.6
$t-$channel NLO generator	± 0.3	± 4.6	± 2.6	± 7.3
$t-$channel LO-NLO generator	± 0.3	± 1.9	± 1.2	± 3.5
$t-$channel parton shower	± 0.8	± 0.8	± 0.4	± 0.5
$t-$channel scales	± 0.9	± 2.2	± 1.5	± 2.6
W+jets, multijet modelling	$^{+0.1}_{-0.2}$	$^{+1.1}_{-0.6}$	$^{+0.2}_{-0.4}$	$^{+1.1}_{-1.3}$
Systematic uncertainty	$^{+2.7}_{-2.9}$	$^{+8.1}_{-8.4}$	$^{+4.5}_{-5.0}$	$^{+10.4}_{-9.9}$

Table B.2: Breakdown of the contributions to the expected statistical and systematic uncertainties on the A_{FB}^{N}, A_{FB}^{T}, $A_{\mathrm{FB}}^{N,\phi}$ and $A_{\mathrm{FB}}^{T,\phi}$ forward-backward asymmetries, extracted from the distributions in $\cos\theta_l^N$, $\cos\theta_l^T$, $\cos\theta_l^* \cos\phi_N^*$ and $\cos\theta_l^* \cos\phi_T^*$ respectively. For better readability the uncertainties are scaled by 10^2.

Uncertainty source	$\Delta A_{\mathrm{FB}}^{Y} \times 10^2$	$\Delta A_{\mathrm{FB}}^{X} \times 10^2$
Statistical uncertainty	± 1.9	± 2.0
Simulation statistics	± 0.9	± 1.0
Luminosity	< 0.1	< 0.1
Background normalisation	± 0.3	$^{+1.6}_{-1.7}$
E_T^{miss} reconstruction	± 0.2	± 0.2
Lepton reconstruction	$^{+0.4}_{-0.3}$	± 0.2
Jet reconstruction	± 1.1	± 2.8
Jet energy scale	$^{+0.5}_{-0.4}$	$^{+2.8}_{-2.2}$
Jet flavour tagging	± 0.1	± 0.3
PDF	< 0.1	± 0.4
$t\bar{t}$ generator	± 0.3	± 1.3
$t\bar{t}$ parton shower	± 0.4	± 0.5
$t\bar{t}$ scales	± 0.3	± 0.6
Wt,$s-$channel generator	± 0.2	± 0.2
Wt,$s-$channel scales	± 0.3	± 0.3
$t-$channel NLO generator	± 0.5	± 0.1
$t-$channel LO-NLO generator	± 0.4	± 1.5
$t-$channel parton shower	± 1.0	± 0.2
$t-$channel scales	± 1.0	± 2.2
W+jets, multijet modelling	$^{+0.2}_{-0.3}$	$^{+1.5}_{-0.9}$
Systematic uncertainty	± 2.3	$^{+5.6}_{-5.2}$

Table B.3: Breakdown of the contributions to the expected statistical and systematic uncertainties on the A_{FB}^{Y} and A_{FB}^{X} forward-backward asymmetries of the distributions in $\cos\theta_Y$ and $\cos\theta_X$ respectively. For better readability the uncertainties are scaled by 10^2.

Appendix C

Control plots for muons and electrons

In this appendix are shown the distributions of the four variables used for the final signal selection cuts (section 9.3) for muons and electrons individually. Plots are made for the signal region, for the two control regions, $t\bar{t}$ and anti-signal, and for the W+jets validation region. The t-channel, W+jets and top-background processes contributions are scaled with the constrained normalisation factors presented in section 10.2. These plots use the individual normalisation factors for electrons or muons only, not the combined normalisation factors.

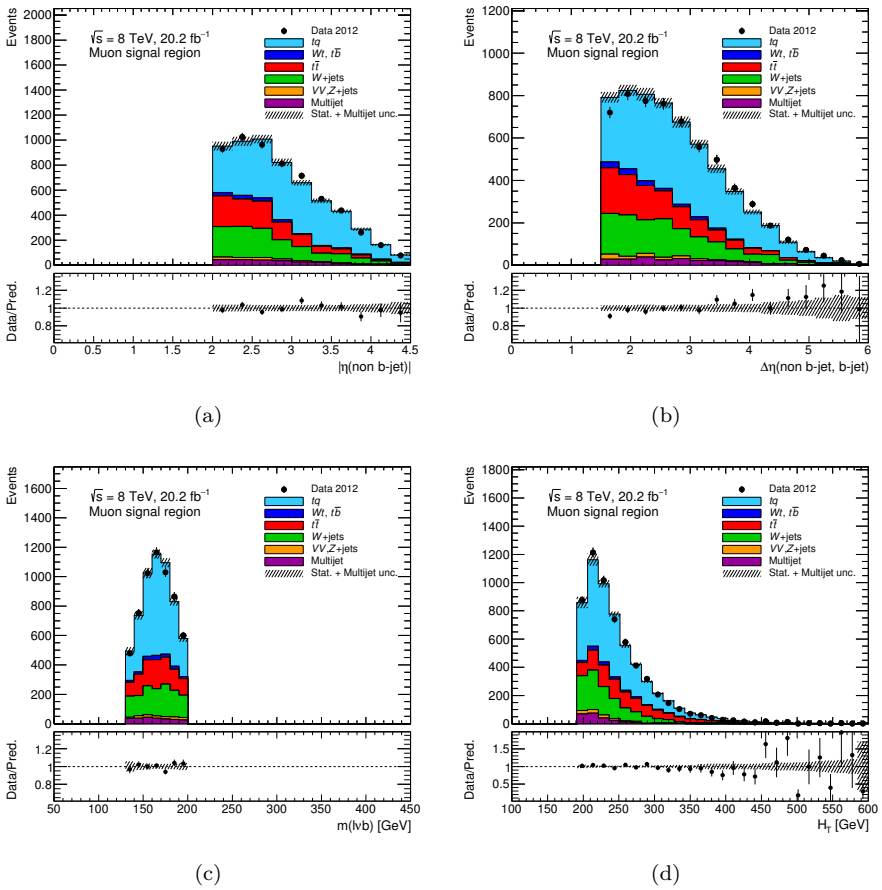

Figure C.1: Distributions of the selection variables in the signal region for muons: (a) non b-tagged jet pseudorapidity, (b) difference in pseudorapidity between the b-tagged jet and the non b-tagged jet, (c) reconstructed top quark mass, and (d) sum of the transverse momentum of all selected objects. The predicted distributions are re-scaled using the values given in table 10.1 (section 10.2). The uncertainty bands correspond to the errors due to the limited size of the simulation samples added in quadrature with the data-driven normalisation uncertainty estimated for the multijet contribution. The lower panel shows the ratio of data to MC prediction.

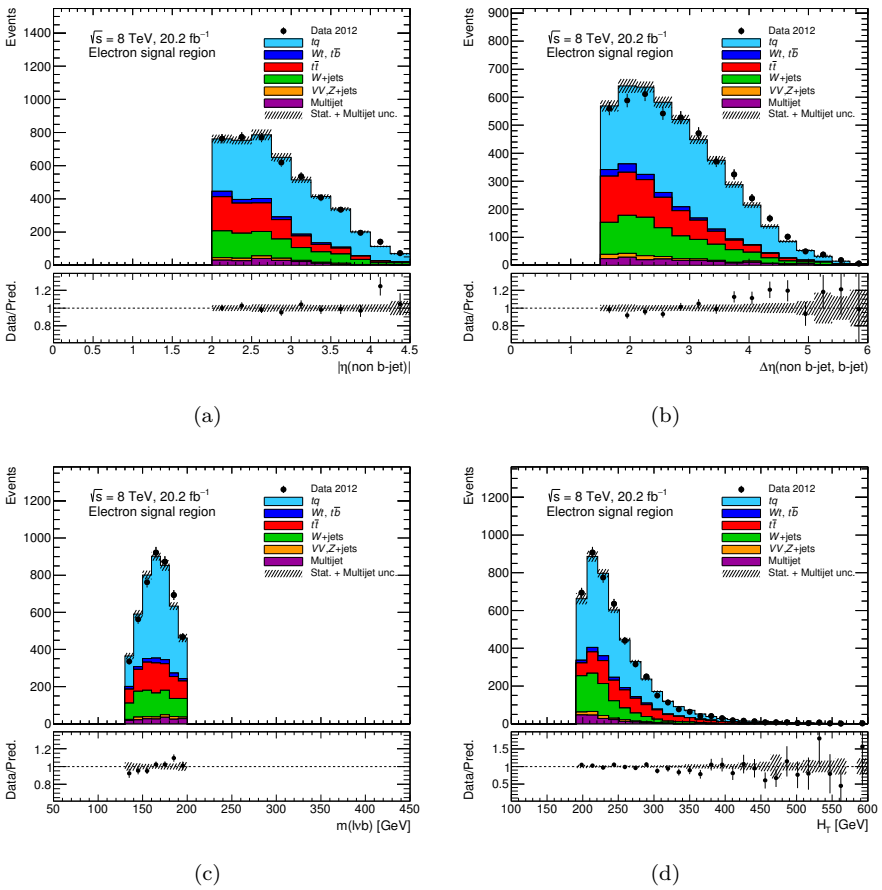

Figure C.2: Distributions of the selection variables in the signal region for electrons: (a) non b-tagged jet pseudorapidity, (b) difference in pseudorapidity between the b-tagged jet and the non b-tagged jet, (c) reconstructed top quark mass, and (d) sum of the transverse momentum of all selected objects. The predicted distributions are re-scaled using the values given in table 10.1 (section 10.2). The uncertainty bands correspond to the errors due to the limited size of the simulation samples added in quadrature with the data-driven normalisation uncertainty estimated for the multijet contribution. The lower panel shows the ratio of data to MC prediction.

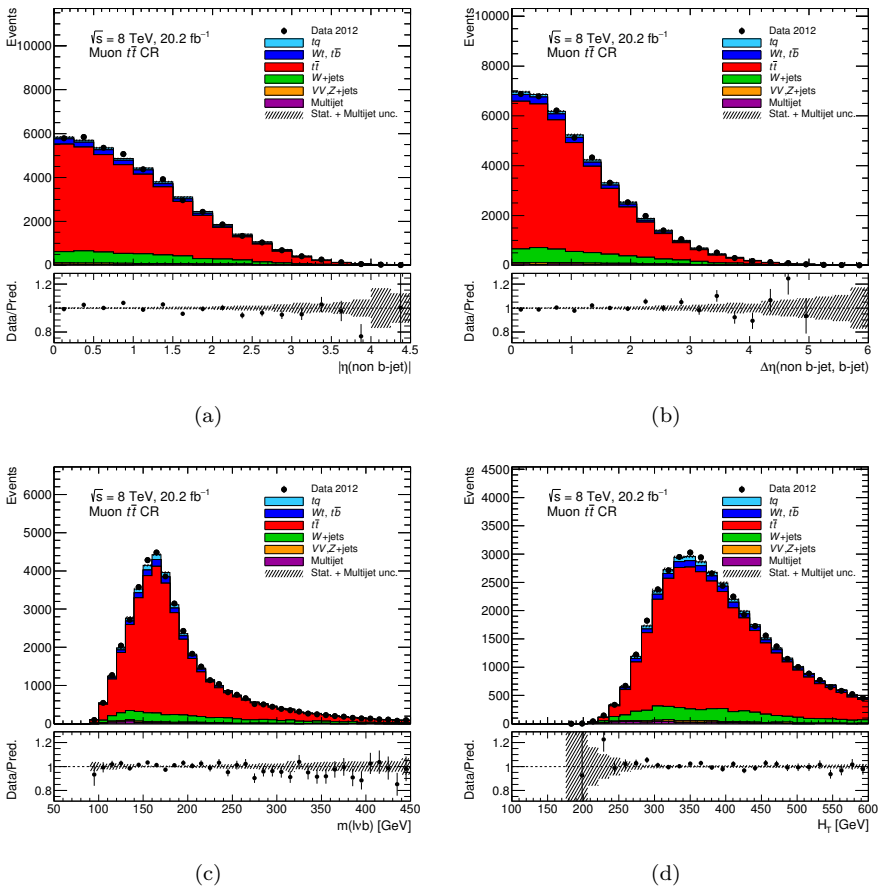

Figure C.3: Distributions of the selection variables in the $t\bar{t}$ control region for muons: (a) non b-tagged jet pseudorapidity, (b) difference in pseudorapidity between the b-tagged jet and the non b-tagged jet, (c) reconstructed top quark mass, and (d) sum of the transverse momentum of all selected objects. The predicted distributions are re-scaled using the values given in table 10.1 (section 10.2). The uncertainty bands correspond to the errors due to the limited size of the simulation samples added in quadrature with the data-driven normalisation uncertainty estimated for the multijet contribution. The lower panel shows the ratio of data to MC prediction.

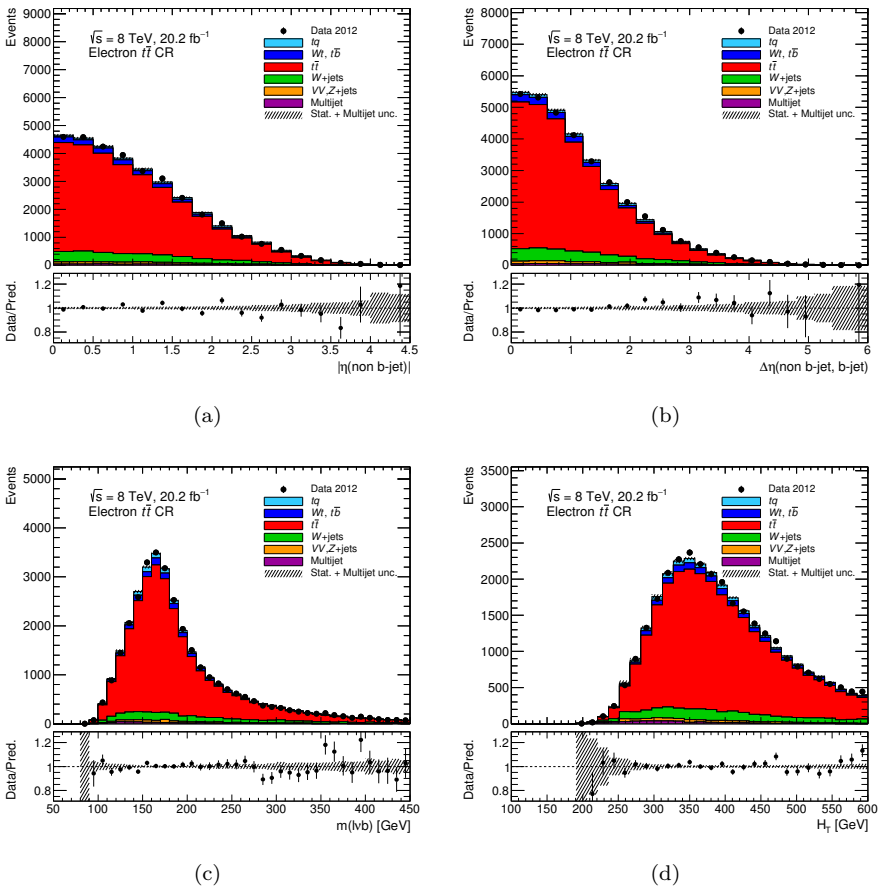

Figure C.4: Distributions of the selection variables in the $t\bar{t}$ control region for electrons: (a) non b-tagged jet pseudorapidity, (b) difference in pseudorapidity between the b-tagged jet and the non b-tagged jet, (c) reconstructed top quark mass, and (d) sum of the transverse momentum of all selected objects. The predicted distributions are re-scaled using the values given in table 10.1 (section 10.2). The uncertainty bands correspond to the errors due to the limited size of the simulation samples added in quadrature with the data-driven normalisation uncertainty estimated for the multijet contribution. The lower panel shows the ratio of data to MC prediction.

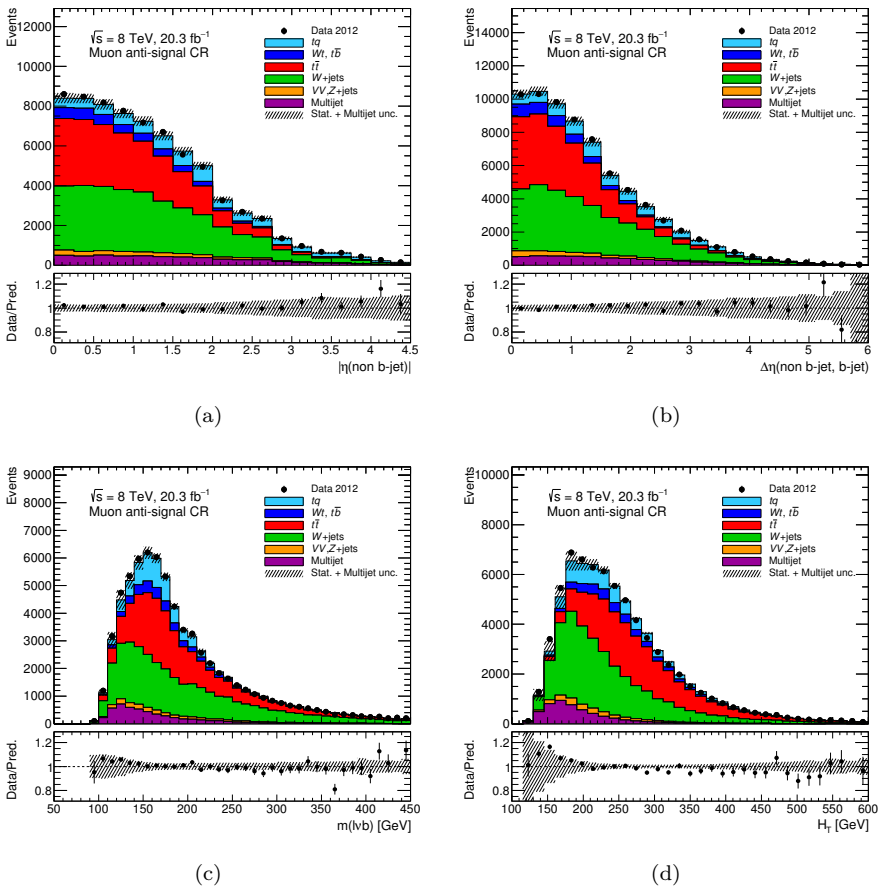

Figure C.5: Distributions of the selection variables in the anti-signal control region for muons: (a) non b-tagged jet pseudorapidity, (b) difference in pseudorapidity between the b-tagged jet and the non b-tagged jet, (c) reconstructed top quark mass, and (d) sum of the transverse momentum of all selected objects. The predicted distributions are re-scaled using the values given in table 10.1 (section 10.2). The uncertainty bands correspond to the errors due to the limited size of the simulation samples added in quadrature with the data-driven normalisation uncertainty estimated for the multijet contribution. The lower panel shows the ratio of data to MC prediction.

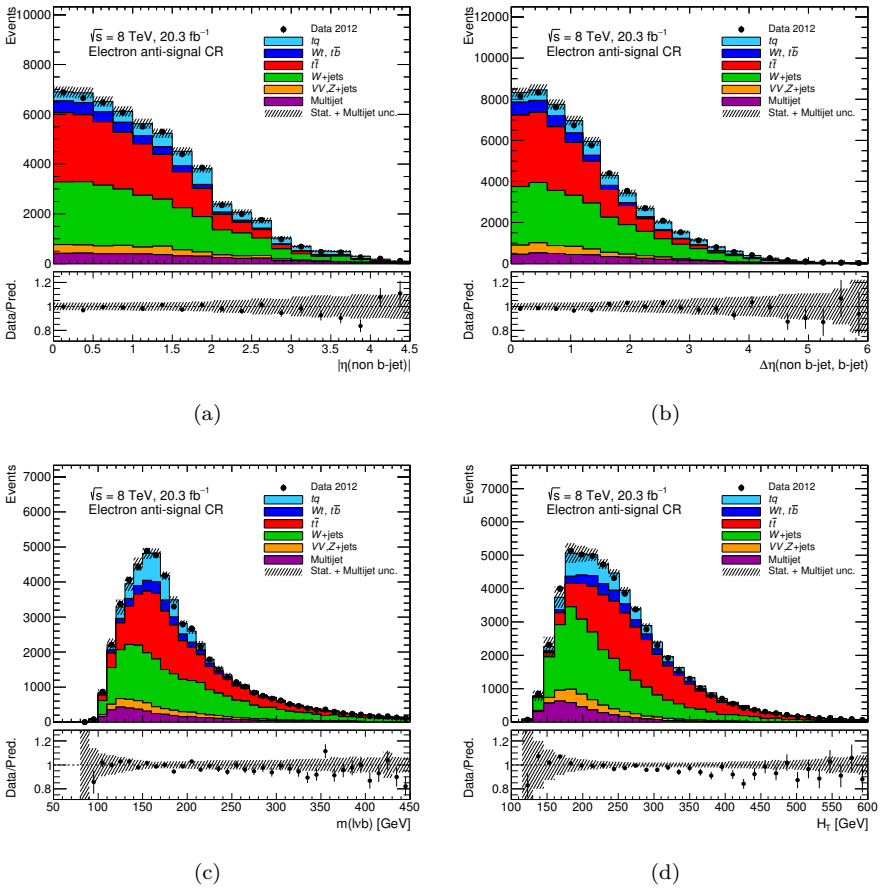

Figure C.6: Distributions of the selection variables in the anti-signal control region for electrons: (a) non b-tagged jet pseudorapidity, (b) difference in pseudorapidity between the b-tagged jet and the non b-tagged jet, (c) reconstructed top quark mass, and (d) sum of the transverse momentum of all selected objects. The predicted distributions are re-scaled using the values given in table 10.1 (section 10.2). The uncertainty bands correspond to the errors due to the limited size of the simulation samples added in quadrature with the data-driven normalisation uncertainty estimated for the multijet contribution. The lower panel shows the ratio of data to MC prediction.

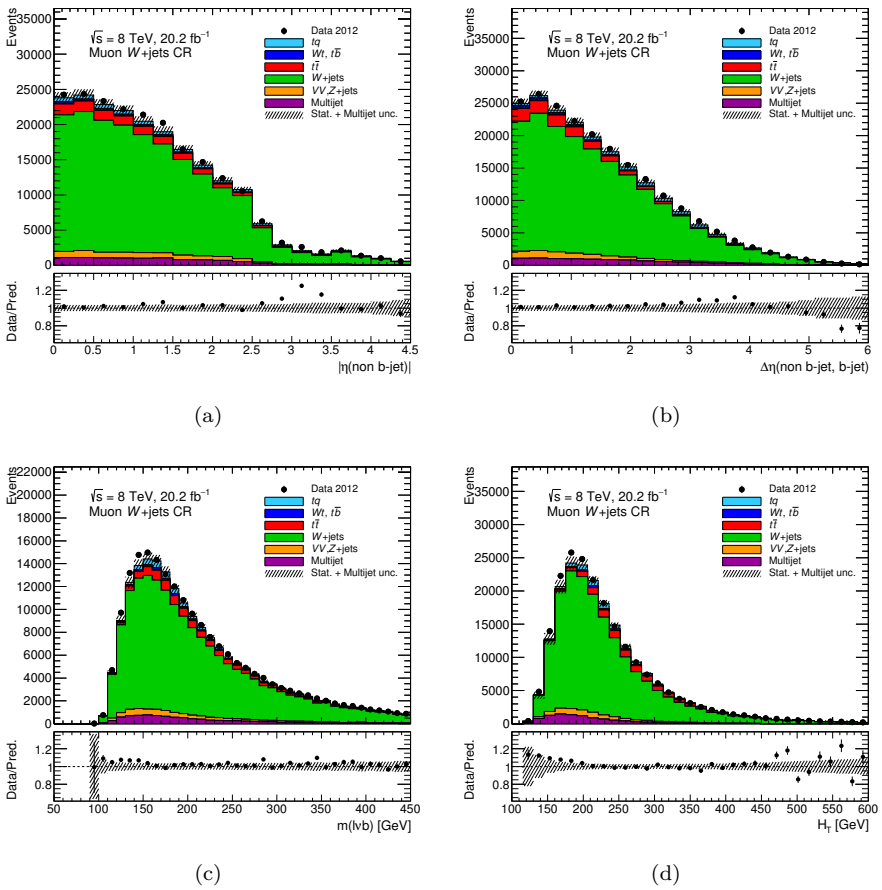

Figure C.7: Distributions of the selection variables in the W+jets validation region for muons: (a) non b-tagged jet pseudorapidity, (b) difference in pseudorapidity between the b-tagged jet and the non b-tagged jet, (c) reconstructed top quark mass, and (d) sum of the transverse momentum of all selected objects. The predicted distributions are re-scaled using the values given in table 10.1 (section 10.2). The uncertainty bands correspond to the errors due to the limited size of the simulation samples added in quadrature with the data-driven normalisation uncertainty estimated for the multijet contribution. The lower panel shows the ratio of data to MC prediction.

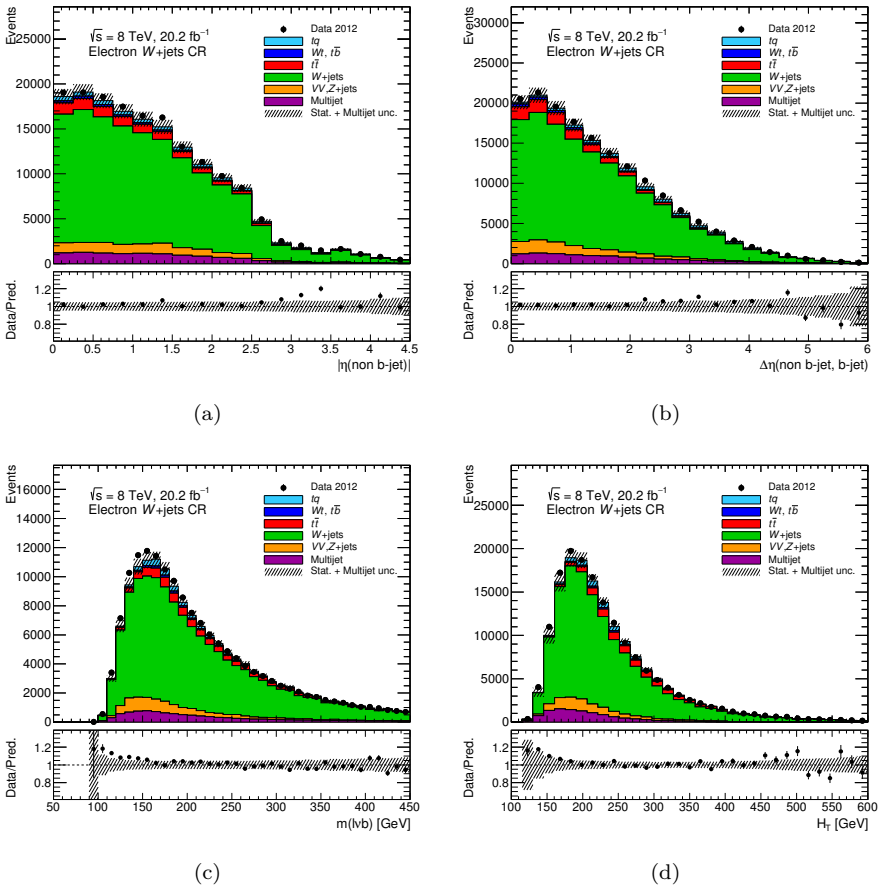

Figure C.8: Distributions of the selection variables in the W+jets validation region for electrons: (a) non b-tagged jet pseudorapidity, (b) difference in pseudorapidity between the b-tagged jet and the non b-tagged jet, (c) reconstructed top quark mass, and (d) sum of the transverse momentum of all selected objects. The predicted distributions are re-scaled using the values given in table 10.1 (section 10.2). The uncertainty bands correspond to the errors due to the limited size of the simulation samples added in quadrature with the data-driven normalisation uncertainty estimated for the multijet contribution. The lower panel shows the ratio of data to MC prediction.

Bibliography

[1] M Kobayashi and T Maskawa,
CP Violation in the Renormalizable Theory of Weak Interaction,
Prog. Theor. Phys. **49** (1973) p. 652.

[2] CDF Collaboration, *Observation of top quark production in $p\bar{p}$ collisions with the Collider Detector at Fermilab*,
Phys. Rev. Lett. **74** (1995) p. 2626, arXiv: 9503002 [hep-ex].

[3] D0 Collaboration, *Search for High Mass Top Quark Production in $p\bar{p}$ collisions at $\sqrt{s} = 1.8$ TeV*, Phys. Rev. Lett. **74** (1995) p. 2422,
arXiv: 9411001 [hep-ex].

[4] The ATLAS Collaboration,
Observation of a new particle in the search for the Standard Model Higgs boson with the ATLAS detector at the LHC,
Phys. Lett. B **716** (2012) p. 1, arXiv: 1207.7214 [hep-ex].

[5] The ATLAS Collaboration, *Observation of a new boson at a mass of 125 GeV with the CMS experiment at the LHC*,
Phys. Lett. B **716** (2012) p. 30, arXiv: 1207.7235 [hep-ex].

[6] S. Glashow, *Partial Symmetries of Weak Interactions*,
Nuclear Physics **22** (1961) p. 579.

[7] A. Salam and J. Ward, *Electromagnetic and weak interactions*,
Phys. Lett. **13** (1964) p. 168.

[8] F Englert and R Brout,
Broken symmetry and the mass of gauge vector mesons,
Phys. Rev. Lett. **13** (1964) p. 321.

[9] P. Higgs, *Broken symmetries and the masses of gauge bosons*,
Phys. Rev. Lett. **13** (1964) p. 508.

[10] Pich, A, *The Standard Model of Electroweak Interactions*, (2012),
arXiv: 1201.0537 [hep-ph].

[11] N Cabibo, *Unitary symmetry and leptonic decays*,
Phys. Rev. Lett. **10** (1963) p. 531.

[12] The ATLAS Collaboration,
Atlas Standard Model Physics public web page, (),
URL: https://twiki.cern.ch/twiki/bin/view/AtlasPublic/StandardModelPublicResults.

[13] Project GFitter, *Results for the Global Electroweak Standard Model Fit*, (), URL: http://project-gfitter.web.cern.ch/project-gfitter/Standard_Model.

[14] S. S. D. Willenbrock and D. A. Dicus, *Production of heavy quraks from W–gluon fusion*, Phys. Rev. D **34** (1986) p. 155.

[15] G. Mahlon and S. Parke, *Single Top Quark Production at the LHC: Understanding Spin*, Phys. Lett. B **476** (2000) p. 323, arXiv: hep-ph/9912458.

[16] R. Schwienhorst et al., *Single top quark production and decay in the t-channel at next-to-leading order at the LHC*, Phys. Rev. D **83** (2011) p. 034019, arXiv: 1012.5132 [hep-ph].

[17] J. A. Aguilar-Saavedra and S. Amor dos Santos, *New directions for top quark polarization in the t-channel process*, Phys. Rev. D **89** (2014) p. 114009, arXiv: 1404.1585 [hep-ph].

[18] G. Mahlon and S. Parke, *Angular Correlation in Top Quark Pair Production and Decay at Hadron Colliders*, Phys. Rev. D **53** (1996) p. 4886, arXiv: hep-ph/9512264.

[19] G Mahlon, *Observing Spin Correlations in Single Top Production and Decay*, (), arXiv: hep-ph/0011349.

[20] J. A. Aguilar-Saavedra and J. Bernabéu, *W polarisation beyond helicity fractions in top quark decays*, Nucl. Phys. B **840** (2010) p. 349, arXiv: 1005.5382 [hep-ph].

[21] J. A. Aguilar-Saavedra and J. Bernabéu, *Breaking down the entire W boson spin observables from its decay*, (), arXiv: 1508.04592 [hep-ph].

[22] The ATLAS Collaboration, *Search for anomalous couplings in the Wtb vertex from the measurement of double differential angular decay rates of single top quarks produced in the t-channel with the ATLAS detector*, JHEP **04** (2016) p. 023, arXiv: 1510.03764 [hep-ex].

[23] The CMS Collaboration, *Measurement of top quark polarization in t-channel single top quark production*, JHEP **1604** (2016) p. 073, arXiv: 1511.02138 [hep-ex].

[24] The CMS Collaboration, *Measurement of the W boson helicity in events with a single reconstructed top quark in pp collisions at* $\sqrt{s} = 8$ *TeV*, JHEP **1501** (2015) p. 053, arXiv: 1410.1154 [hep-ex].

[25] CERN, *LHC: the guide (faq)*, CERN-Brochure-2017-002-Eng (2017), URL: http://cds.cern.ch/record/2255762.

[26] CERN, *Computer-generated diagram of an LHC dipole Schéma d'un dipôle du LHC*, (1998), URL: https://cds.cern.ch/record/39731.

[27] The ATLAS Collaboration, *Atlas luminosity public web page*, (), URL: https://twiki.cern.ch/twiki/bin/view/AtlasPublic/LuminosityPublicResultsRun2.

[28] The ATLAS Collaboration,
The ATLAS Experiment at the CERN Large Hadron Collider,
J. Inst. **3** (2008) S08003.

[29] CERN, *Computer generated image of the whole ATLAS detector*, (),
URL: cds.cern.ch/record/1095924.

[30] The ATLAS Collaboration,
A computer generated image representing how ATLAS detects particles,
(), URL: cds.cern.ch/record/1505342.

[31] The ATLAS Collaboration, *ATLAS Inner Detector Alignment Performance with February 2015 Cosmic Rays Data*,
ATL-PHYS-PUB-2015-009 (2015),
URL: http://cdsweb.cern.ch/record/2008724.

[32] M Capeans et al., *ATLAS Insertable B-Layer Technical Design Report*,
ATLAS-TDR-019 (2010),
URL: https://cds.cern.ch/record/1291633/.

[33] The ATLAS Collaboration, *ATLAS Calorimeter gallery*, (),
URL: http://atlasexperiment.org/photos/calorimeters-combined-barrel.html.

[34] The ATLAS Collaboration, *ATLAS Calorimeter gallery*, (), URL: http://atlasexperiment.org/photos/calorimeters-lar-barrel.html.

[35] The ATLAS Collaboration, *ATLAS Calorimeter gallery*, (),
URL: http://atlasexperiment.org/photos/muons-combined.html.

[36] C. Eck et al., *LHC computing Grid : Technical Design Report*,
CERN-LHCC-2005-024 (2005),
URL: https://cds.cern.ch/record/840543.

[37] Worldwide LHC Computing Grid, (),
URL: http://wlcg.web.cern.ch/.

[38] The ATLAS Collaboration, *The ATLAS Simulation Infrastructure*,
Eur. Phys. J. C **70** (2010) p. 823,
arXiv: 1005.4568 [physics.ins-det].

[39] The ATLAS Collaboration, *The simulation principle and performance of the ATLAS fast calorimeter simulation FastCaloSim*, (),
URL: http://cds.cern.ch/record/1300517.

[40] B. Acharya et al.,
Object selection and calibration, background estimations and MC samples for the Winter 2013 Top Quark analyses with 2012 data, (),
URL: http://cds.cern.ch/record/1509562.

[41] B. Acharya et al.,
Object selection and calibration, background estimations and MC samples for top quark analyses using the full 2012 data set, (),
URL: http://cds.cern.ch/record/1563201.

[42] The ATLAS Collaboration,
Electron reconstruction and identification efficiency measurements with the ATLAS detector using the 2011 LHC proton–proton collision data,
Eur. Phys. J. C **74** (2014) p. 2941, arXiv: 1404.2240 [hep-ex].

[43] The ATLAS Collaboration,
Muon reconstruction efficiency and momentum resolution of the ATLAS experiment in proton-proton collisions at $\sqrt{s} = 7$ TeV in 2010,
Eur. Phys. J. C **74** (2014) p. 3034, arXiv: 1404.4562 [hep-ex].

[44] The ATLAS Collaboration,
Measurement of the muon reconstruction performance of the ATLAS detector using 2011 and 2012 LHC proton-proton collision data,
Eur. Phys. J. C **74** (2014) p. 3130.

[45] M. Cacciari, G. P. Salam, and G. Soyez,
The anti-k_t jet clustering algorithm, JHEP **0804** (2008) p. 063,
arXiv: 0802.1189 [hep-ph].

[46] The ATLAS Collaboration, *Jet energy measurement with the ATLAS detector in proton–proton collisions at $\sqrt{s} = 7$ TeV*,
Eur. Phys. J. C **73** (2013) p. 2304, arXiv: 1112.6426 [hep-ex].

[47] The ATLAS Collaboration,
Jet energy measurement and its systematic uncertainty in proton–proton collisions at TeV with the ATLAS detector,
Eur. Phys. J. C **75** (2015) p. 17, arXiv: 1406.0076 [hep-ex].

[48] The ATLAS Collaboration, *Calibration of the performance of b-tagging for c and light-flavour jets in the 2012 ATLAS data*, (),
URL: http://cds.cern.ch/record/1741020.

[49] The ATLAS Collaboration,
Measurement of the b-tag Efficiency in a Sample of Jets Containing Muons with 5 fb^{-1} of data from the ATLAS detector, (),
URL: http://cds.cern.ch/record/1435197.

[50] The ATLAS Collaboration, *Performance of algorithms that reconstruct missing transverse momentum in $\sqrt{s} = 8$ TeV proton-proton collisions in the ATLAS detector*, Eur. Phys. J. C **77** (2017) p. 241,
arXiv: 1609.09324 [hep-ex].

[51] C Escobar Ibáñez, C García García, and S Martí García, *Alignment of the ATLAS silicon tracker and measurement of the top quark mass*,
PhD Thesis, University of Valencia (2010),
URL: https://cds.cern.ch/record/1277903.

[52] V Lacuesta Miquel, S Martí García, and J. E. García Navarro,
Alignment of the ATLAS Inner Detector and Single Top studies,
PhD Thesis, University of Valencia (2015),
URL: http://mobiroderic.uv.es/handle/10550/49883.

[53] The ATLAS Collaboration, *Study of alignment-related systematic effects on the ATLAS Inner Detector tracking*,
ATLAS-CONF-2012-141 (2012),
URL: http://cdsweb.cern.ch/record/1483518.

[54] C. Patrignani *et al.*(Particle Data Group), *Review of Particle Physics*,
Chin. Phys. C **40** (2016), URL: http://pdg.lbl.gov/index.html.

[55] The ATLAS Collaboration,
Studies of radial distortions of the ATLAS Inner Detector,

ATL-PHYS-PUB-2018-003 (2018),
URL: http://cdsweb.cern.ch/record/2309785.

[56] J Beringer et al.,
Offline beam spot reconstruction in ATLAS during Run 1,
ATL-COM-DAPR-2014-013 (2014),
URL: https://cds.cern.ch/record/1978679.

[57] The ATLAS Collaboration,
Alignment of the ATLAS Inner Detector and its Performance in 2012,
ATLAS-CONF-2014-047 (2014),
URL: http://cdsweb.cern.ch/record/1741021.

[58] The ATLAS Collaboration,
Performance plots for dynamic alignment in the pixel detector,
IDTR-2016-009 (2016), URL:
https://atlas.web.cern.ch/Atlas/GROUPS/PHYSICS/PLOTS/IDTR-2016-009/.

[59] The ATLAS Collaboration, *Pixel vertical position evolution*,
IDTR-2016-005 (2018), URL:
https://atlas.web.cern.ch/Atlas/GROUPS/PHYSICS/PLOTS/IDTR-2018-003/.

[60] The ATLAS Collaboration, *ATLAS Inner Detector Alignment Performance with 2015 Cosmic Ray Data*, IDTR-2015-002 (2015), URL:
https://atlas.web.cern.ch/Atlas/GROUPS/PHYSICS/PLOTS/IDTR-2015-002/.

[61] The ATLAS Collaboration,
Study of the mechanical stability of the ATLAS Insertable B-Layer,
ATL-INDET-PUB-2015-001 (2015),
URL: http://cdsweb.cern.ch/record/2022587.

[62] The IBL Distortion Task Force,
IBL Distortion Task Force: An Internal Report,
ATL-INDET-INT-2016-002 (2016),
URL: https://cds.cern.ch/record/2126927.

[63] The ATLAS Collaboration,
Impact of IBL distortion on impact parameter resolution in MC,
IDTR-2015-010 (2015), URL:
https://atlas.web.cern.ch/Atlas/GROUPS/PHYSICS/PLOTS/IDTR-2015-010/.

[64] The ATLAS Collaboration,
Time dependent alignment corrections to IBL distortions,
IDTR-2015-011 (2015), URL:
https://atlas.web.cern.ch/Atlas/GROUPS/PHYSICS/PLOTS/IDTR-2015-011/.

[65] The ATLAS Collaboration,
Drift of IBL LV current and its consequence in IBL distortion,
PIX-2015-007 (2015), URL:
https://atlas.web.cern.ch/Atlas/GROUPS/PHYSICS/PLOTS/PIX-2015-007/.

[66] The ATLAS Collaboration, *IBL Alignment Performance in 2016*, IDTR-2016-005 (2016), URL: https://atlas.web.cern.ch/Atlas/GROUPS/PHYSICS/PLOTS/IDTR-2016-005/.

[67] E. M et al., *The ATLAS Tier-0: Overview and operational experience*, Journal of Physics: Conference Series **219** (2010), URL: http://iopscience.iop.org/article/10.1088/1742-6596/219/7/072011/meta.

[68] The ATLAS Collaboration, *Tier-0 transformations twiki*, (), URL: https://twiki.cern.ch/twiki/bin/view/AtlasComputing/TierZeroTransformations.

[69] The ATLAS Collaboration, *Tier-0 alignment twiki*, (), URL: https://twiki.cern.ch/twiki/bin/view/AtlasComputing/Tier0AlignmentTutorial.

[70] The ATLAS Collaboration, *Inner Detector residuals from first 2017 alignment*, IDTR-2017-004 (2017), URL: https://atlas.web.cern.ch/Atlas/GROUPS/PHYSICS/PLOTS/IDTR-2017-004/.

[71] The ATLAS Collaboration, *Luminosity Determination in pp Collisions at $\sqrt{s} = 8$ TeV using the ATLAS Detector at the LHC*, Eur. Phys. J. C **75** (2016) p. 653, arXiv: 1608.03953 [hep-ex].

[72] S. Frixione, P. Nason, and C. Oleari, *Matching NLO QCD computations with Parton Shower simulations: the POWHEG method*, JHEP **0711** (2007) p. 070, arXiv: 0709.2092 [hep-ph].

[73] R. Frederix, E. Re, and P. Torrielli, *Single-top t-channel hardproduction in the four-flavour scheme with POWHEG and aMC@NLO*, JHEP **1209** (2012) p. 130, arXiv: hep-ph/01207.5391.

[74] H.-L. Lai et al., *New parton distributions for collider physics*, Phys. Rev. D **82** (2010) p. 074024, arXiv: 1007.2241 [hep-ph].

[75] J. A. Aguilar-Saavedra, *Single top quark production at LHC with anomalous Wtb couplings*, Nucl. Phys. B **804** (2008) p. 160, arXiv: 0803.3810.

[76] J Pumplin et al., *New Generation of Parton Distributions with Uncertainties from Global QCD Analysis*, JHEP **0207** (2002) p. 012, arXiv: hep-ph/0201195.

[77] P Nadolsky et al., *Implications of CTEQ global analysis for collider observables*, Phys. Rev. D **78** (2008) p. 013004, arXiv: 0802.0007.

[78] ATLAS Collaboration, *Comparison of Monte Carlo generator predictions to ATLAS measurements of top pair production at 7 TeV*, 2015, URL: https://cds.cern.ch/record/1981319.

[79] T. Sjöstrand, S. Mrenna, and P. Z. Skands, *PYTHIA 6.4 Physics and Manual*, JHEP **0605** (2006) p. 026, arXiv: hep-ph/0603175.

[80] P. Z. Skands, *Tuning Monte Carlo generators: The Perugia tunes*, Phys. Rev. D **82** (2010) p. 074018, arXiv: 1005.3457 [hep-ph].

[81] T. Gleisberg et al., *Event generation with SHERPA 1.1*, JHEP **0902** (2009) p. 007, arXiv: 0811.4622 [hep-ph].

[82] S. Hoeche et al., *QCD matrix elements and truncated showers*, JHEP **0905** (2009) p. 053, arXiv: hep-ph/0903.1219.

[83] The ATLAS Collaboration, *Measurement of the top quark pair production cross-section with ATLAS in the single lepton channel*, Phys. Lett. B **711** (2012) p. 244, arXiv: 1201.1889 [hep-ex].

[84] K. A. Olive et al., *Review of Particle Physics*, Chin. Phys. C **38** (2014) p. 090001.

[85] I.C. Brock, D. Hirschbuehl, P. Seema, P. Tepel, W. Wagner, *Measurement of the Inclusive and Fiducial Cross-Section in Single Top-Quark Events in pp Collisions at* $\sqrt{s} = 8$ *TeV*, (), URL: https://cds.cern.ch/record/1999237.

[86] R Moles Valls and S Martí García, *Inner detector alignment and top-quark mass measurement with the ATLAS detector*, PhD Thesis, University of Valencia (2014), URL: https://cds.cern.ch/record/1955105.

[87] O.M. Kind, A. Lleres, T. Lohse, P. Rieck and S. Stamm, *Measurement of single top-quark production in the s-channel in proton–proton collisions at* $\sqrt{s} = 8$ *TeV with the ATLAS detector using the matrix element method*, (), URL: https://cds.cern.ch/record/1974821.

[88] The ATLAS Collaboration, *Measurement of the t-channel single top-quark production cross section in pp collisions at* $\sqrt{s} = 7$ *TeV with the ATLAS detector*, Phys. Lett. B **717** (2012) p. 330, arXiv: 1205.3130 [hep-ex].

[89] N. Kidonakis, *Next-to-next-to-leading-order collinear and soft gluon corrections for t-channel single top quark production*, Phys. Rev. D **83** (2011) p. 091503, arXiv: 1103.2792 [hep-ph].

[90] N. Kidonakis, *Two-loop soft anomalous dimensions for single top quark associated production with a* W^- *or* H^-, Phys. Rev. D **82** (2010) p. 054018, arXiv: 1005.4451 [hep-ph].

[91] N. Kidonakis, *NNLL resummation for s-channel single top quark production*, Phys. Rev. D **81** (2010) p. 054028, arXiv: 1001.5034 [hep-ph].

[92] A. D. Martin et al., *Parton distributions for the LHC*, Eur. Phys. J. C **63** (2009) p. 189, arXiv: 0901.0002 [hep-ph].

[93] P. Bärnreuther, M. Czakon, and A. Mitov, *Percent Level Precision Physics at the Tevatron: First Genuine NNLO QCD Corrections to* $q\bar{q} \to t\bar{t} + X$, Phys. Rev. Lett. **109** (2012) p. 132001, arXiv: 1204.5201 [hep-ph].

[94] M. Czakon and A. Mitov, *Top++: A Program for the Calculation of the Top-Pair Cross-Section at Hadron Colliders*,

Comput. Phys. Commun. **185** (2014) p. 2930, arXiv: 1112.5675 [hep-ph].

[95] M. Czakon and A. Mitov, *NNLO corrections to top-pair production at hadron colliders: the all-fermionic scattering channels*, JHEP **1212** (2012) p. 054, arXiv: 1207.0236 [hep-ph].

[96] M. Czakon and A. Mitov, *NNLO corrections to top pair production at hadron colliders: the quark-gluon reaction*, JHEP **1301** (2013) p. 080, arXiv: 1210.6832 [hep-ph].

[97] M. Czakon, P. Fiedler, and A. Mitov, *The total top quark pair production cross-section at hadron colliders through $O(alpha_S^4)$*, Phys. Rev. Lett. **110** (2013) p. 252004, arXiv: 1303.6254 [hep-ph].

[98] M. Cacciari et al., *Top-pair production at hadron colliders with next-to-next-to-leading logarithmic soft-gluon resummation*, Phys. Lett. B **710** (2012) p. 612, arXiv: 1111.5869 [hep-ph].

[99] M. Botje et al., *The PDF4LHC Working Group Interim Recommendations*, (2011), arXiv: 1101.0538 [hep-ph].

[100] J. Gao et al., *The CT10 NNLO Global Analysis of QCD*, Phys. Rev. D **89** (2014) p. 033009, arXiv: 1302.6246 [hep-ph].

[101] R. Ball et al., *Parton distributions with the LHC data*, Nucl. Phys. B **867** (2013) p. 244, arXiv: 1207.1303 [hep-ph].

[102] C. Anastasiou et al., *High-precision QCD at hadron colliders: electroweak gauge boson rapidity distributions at NNLO*, Phys. Rev. D **69** (2004) p. 094008, arXiv: hep-ph/0312266.

[103] J. M. Campbell, R. K. Ellis, and C. Williams, *Vector boson pair production at the LHC*, JHEP **1107** (2011) p. 018, arXiv: 1105.0020 [hep-ph].

[104] T. A. Collaboration, *Measurements of the W production cross sections in association with jets with the ATLAS detector*, The European Physical Journal C **75** (2015) p. 82, ISSN: 1434-6052, URL: https://doi.org/10.1140/epjc/s10052-015-3262-7.

[105] K. Becker et al., *Estimation of Fake Lepton Background for Top Analyses Using the $\sqrt{s} = 8$ TeV Dataset*, (), URL: http://cds.cern.ch/record/1571043.

[106] The ATLAS Collaboration, *Estimation of non-prompt and fake lepton backgrounds in final states with top quarks produced in proton-proton collisions at $\sqrt{s} = 8$ TeV with the ATLAS detector*, (), URL: https://cds.cern.ch/record/1951336.

[107] A. Brandenburg, Z. G. Si, and U. P., *QCD-corrected spin analysing power of jets in decays of polarized top quarks*, Phys. Lett. B **539** (2002) p. 235, arXiv: hep-ph/0205023.

[108] G. Mahlon and S. Parke, *Improved Spin Basis for Angular Correlation Studies in Single Top Quark Production at the Tevatron*, Phys. Rev. D **55** (1997) p. 7249, arXiv: hep-ph/9611367.

[109] A. Czarnecki, J. G. Korner, and J. H. Piclum,
Helicity fractions of W bosons from top quark decays at NNLO in QCD,
Phys. Rev. D **81** (2010) 111503(R), arXiv: 1005.2625 [hep-ph].

[110] J. M. Campbell et al., *Next-to-leading-order predictions for t-channel single-top production at hadron colliders*,
Phys. Rev. Lett. **102** (2009) p. 182003, arXiv: 0903.0005 [hep-ph].

[111] J. Aguilar-Saavedra, *TopFit - a program to fit the Wtb vertex*, (), URL: http://jaguilar.web.cern.ch/jaguilar/topfit.

[112] J. A. Aguilar-Saavedra and R. V. Herrero-Hahn,
Model-independent measurement of the top quark polarization, (),
arXiv: 1208.6006 [hep-ph].

[113] G. D'Agostini,
A Multidimensional unfolding method based on Bayes' theorem,
Nucl. Instrum. Meth. A **362** (1995) p. 487.

[114] T. Adye, *Unfolding algorithms and tests using RooUnfold*, (),
arXiv: 1105.1160 [physics.data-an].

[115] The ATLAS Collaboration, *Probing the Wtb vertex structure in t-channel single-top-quark production and decay in pp collisions at* $\sqrt{s}$ *= 8 TeV with the ATLAS detector*, JHEP **04** (2017) p. 124,
arXiv: 1702.08309 [hep-ex].

[116] C. Bernardo et al.,
Studying the Wtb vertex structure using recent LHC results,
Phys. Rev. D **90** (2014) p. 113007, arXiv: 1408.7063 [hep-ex].

[117] The ATLAS Collaboration,
Measurement of the W boson polarisation in $t\bar{t}$ *events from pp collisions at* $\sqrt{s}$ *= 8 TeV in the lepton + jets channel with ATLAS*,
Eur. Phys. J. C **77** (2017) p. 264, arXiv: 1612.02577 [hep-ex].

[118] The CMS Collaboration, *Search for anomalous Wtb couplings and flavour-changing neutral currents in t-channel single top quark production in pp collisions at* $\sqrt{s} = 7$ *and 8 TeV*,
JHEP **02** (2017) p. 028, arXiv: 1610.03545 [hep-ex].

[119] O. Arslan, I. Brock, C. Friedrich, D. Hirschbuehl, T. Velz, W. Wagner, *Search for single top quark production via strong FCNC in* $\sqrt{s} = 8$ *TeV ATLAS data*, (), URL: https://cds.cern.ch/record/1745904.

[120] B. Efron, *Bootstrap Methods: Another Look at the Jackknife*,
Ann. Statist. **07** (1979) p. 1.

[121] The ATLAS Collaboration,
Analysis of the Wtb vertex from the measurement of triple-differential angular decay rates of single top quarks produced in the t-channel at $\sqrt{s}$ *= 8 TeV with the ATLAS detector*, JHEP **12** (2017) p. 017,
arXiv: 1707.05393 [hep-ex].

[122] ATLAS single-top sub-group,
SgTop-D3PDs for 8 TeV, Lepton+Jets Selection, (), URL:
http://twiki.cern.ch/twiki/bin/view/AtlasProtected/SgTop-D3PDs8TeVLeptonJets.

[123] ATLAS top-reconstruction sub-group, *TopRootCoreRelease*, (), URL: http://twiki.cern.ch/twiki/bin/view/AtlasProtected/TopRootCoreRelease.

[124] ATLAS top-reconstruction sub-group, *TopCommonObjects*, (), URL: http://twiki.cern.ch/twiki/bin/view/AtlasProtected/TopCommonObjects.

[125] J. Alwall et al., *The automated computation of tree-level and next-to-leading order differential cross sections, and their matching to parton shower simulations*, JHEP **1407** (2014) p. 079, arXiv: 1405.0301 [hep-ph].

[126] G. Marchesini et al., *HERWIG 5.1 - a Monte Carlo event generator for simulating hadron emission reactions with interfering gluons*, Comput. Phys. Commun. **67** (1992) p. 465.

[127] G. Corcella et al., *HERWIG 6.5: an event generator for Hadron Emission Reactions With Interfering Gluons (including supersymmetric processes)*, JHEP **0101** (2001) p. 010, arXiv: hep-ph/0011363.

[128] J. M. Butterworth, J. R. Forshaw, and M. H. Seymour, *Multiparton Interactions in Photoproduction at HERA*, Z. Phys. C **72** (1996) p. 637, arXiv: hep-ph/9601371.

[129] ATLAS Collaboration, *New ATLAS event generator tunes to 2010 data*, (), URL: http://cds.cern.ch/record/1345343.

[130] S. Frixione and B. R. Webber, *Matching NLO QCD computations and parton shower simulations*, JHEP **0206** (2002) p. 029, arXiv: hep-ph/0204244.

[131] S. Frixione, P. Nason, and B. R. Webber, *Matching NLO QCD computations and parton showers in heavy flavour production*, JHEP **0308** (2003) p. 007, arXiv: hep-ph/0305252.

[132] S. Frixione et al., *Single-top production in MC@NLO*, JHEP **0603** (2006) p. 092, arXiv: hep-ph/0512250.

[133] S. Frixione et al., *Single-top hadroproduction in association with a W boson*, JHEP **0807** (2008) p. 029, arXiv: 0805.3067 [hep-ph].